Graduate School for Cellular and Biomedical Sciences
University of Bern

Experimental, theoretical and numerical investigation of the nonlinear micromechanical properties of bone

PhD Thesis submitted by

Johann Jakob Schwiedrzik

from **Germany**

for the degree of

PhD in Biomedical Engineering

Supervisor
Prof. Dr. Philippe Kurt Zysset
Institute for Surgical Technology and Biomechanics
Faculty of Medicine
University of Bern

Co-advisor
Prof. Dr. Edoardo Mazza
Institute of Mechanical Systems
Department of Mechanical and Process Engineering
Swiss Federal Institute of Technology (ETH) Zürich

Accepted by the Faculty of Medicine, the Faculty of Science and the Vetsuisse Faculty of the University of Bern at the request of the Graduate School for Cellular and Biomedical Sciences

Bern,	Dean of the Faculty of Medicine
Bern,	Dean of the Faculty of Science
Bern,	Dean of the Vetsuisse Faculty Bern

PhD Committee

Supervisor
Prof. Dr. Philippe Kurt Zysset
Institute for Surgical Technology and Biomechanics
Faculty of Medicine
University of Bern

Co-advisor
Prof. Dr. Edoardo Mazza
Institute of Mechanical Systems
Department of Mechanical and Process Engineering
Swiss Federal Institute of Technology (ETH) Zürich

Mentor
PD Dr. med. Richard Nyffeler
FMH Orthopaedic Surgery and Traumatology
of the Musculoskletal System
Sonnenhof AG

External Co-Referee
Prof. Dr. Franz-Josef Ulm
Concrete Sustainability Hub
Department of Civil and Environmental Engineering
Massachussets Institute of Technology

Abstract

Aging societies suffer from an increasing incidence of bone fractures. Bone strength depends on the amount of mineral measured by clinical densitometry, but also on the micromechanical properties of the bone hierarchical organization. A good understanding has been reached for elastic properties on several length scales, but up to now there is a lack of reliable postyield data on the lower length scales.

In order to be able to describe the behavior of bone at the microscale, an anisotropic elastic-viscoplastic damage model was developed using an eccentric generalized Hill criterion and nonlinear isotropic hardening. The model was implemented as a user subroutine in Abaqus and verified using single element tests. A FE simulation of microindentation in lamellar bone was finally performed showing that the new constitutive model can capture the main characteristics of the indentation response of bone.

As the generalized Hill criterion is limited to elliptical and cylindrical yield surfaces and the correct shape for bone is not known, a new yield surface was developed that takes any convex quadratic shape. The main advantage is that in the case of material identification the shape of the yield surface does not have to be anticipated but a minimization results in the optimal shape among all convex quadrics. The generality of the formulation was demonstrated by showing its degeneration to classical yield surfaces. Also, existing yield criteria for bone at multiple length scales were converted to the quadric formulation.

Then, a computational study to determine the influence of yield surface shape and damage on the indentation response of bone using spherical and conical tips was performed. The constitutive model was adapted to the quadric criterion and yield surface shape and critical damage were varied. They were shown to have a major impact on the indentation curves. Their influence on indentation modulus, hardness, their ratio as well as the elastic to total work ratio were found to be very well described by multilinear regressions for both tip shapes. For conical tips, indentation depth was not a significant factor, while for spherical tips damage was insignificant.

All inverse methods based on microindentation suffer from a lack of uniqueness of the found material properties in the case of nonlinear material behavior. Therefore, monotonic and cyclic micropillar compression tests in a scanning electron microscope allowing a straightforward interpretation complemented by microindentation and macroscopic uniaxial compression tests were performed on dry ovine bone to identify modulus, yield stress, plastic deformation, damage accumulation and failure mechanisms. While the elastic properties were highly consistent, the postyield deformation and failure mechanisms differed between the two length scales. A majority of the micropillars showed a ductile behavior with strain hardening until failure by localization in a slip plane, while the macroscopic samples failed

in a quasi-brittle fashion with microcracks coalescing into macroscopic failure surfaces. In agreement with a proposed rheological model, these experiments illustrate a transition from a ductile mechanical behavior of bone at the microscale to a quasi-brittle response driven by the growth of preexisting cracks along interfaces or in the vicinity of pores at the macroscale.

Subsequently, a study was undertaken to quantify the topological variability of indentations in bone and examine its relationship with mechanical properties. Indentations were performed in dry human and ovine bone in axial and transverse directions and their topography measured by AFM. Statistical shape modeling of the residual imprint allowed to define a mean shape and describe the variability with 21 principal components related to imprint depth, surface curvature and roughness. The indentation profile of bone was highly consistent and free of any pile up. A few of the topological parameters, in particular depth, showed significant correlations to variations in mechanical properties, but the correlations were not very strong or consistent. We could thus verify that bone is rather homogeneous in its micromechanical properties and that indentation results are not strongly influenced by small deviations from the ideal case.

As the uniaxial properties measured by micropillar compression are in conflict with the current literature on bone indentation, another dissipative mechanism has to be present. The elastic-viscoplastic damage model was therefore extended to viscoelasticity. The viscoelastic properties were identified from macroscopic experiments, while the quasistatic postelastic properties were extracted from micropillar data. It was found that viscoelasticity governed by macroscale properties has very little influence on the indentation curve and results in a clear underestimation of the creep deformation. Adding viscoplasticity leads to increased creep, but hardness is still highly overestimated. It was possible to obtain a reasonable fit with experimental indentation curves for both Berkovich and spherical indentation when abandoning the assumption of shear strength being governed by an isotropy condition. These results remain to be verified by independent tests probing the micromechanical strength properties in tension and shear.

In conclusion, in this thesis several tools were developed to describe the complex behavior of bone on the microscale and experiments were performed to identify its material properties. Micropillar compression highlighted a size effect in bone due to the presence of preexisting cracks and pores or interfaces like cement lines. It was possible to get a reasonable fit between experimental indentation curves using different tips and simulations using the constitutive model and uniaxial properties measured by micropillar compression. Additional experimental work is necessary to identify the exact nature of the size effect and the mechanical role of interfaces in bone. Deciphering the micromechanical behavior of lamellar bone and its evolution with age, disease and treatment and its failure mechanisms on several length scales will help preventing fractures in the elderly in the future.

Contents

List of Figures

List of Tables

1

Introduction

1.1 Motivation

Aging societies suffer from an increasing incidence of bone fractures. Bone strength depends on the mineral density measured by clinical densitometry, but also on the micromechanical properties of bone's hierarchical organization. Contemporary prevention and treatment strategies of metabolic conditions like osteoporosis benefit from a better understanding of the micromechanical behavior of bone and its relation to cell- and drug-mediated adaptation processes [Bajaj et al., 2014].

The mechanical properties of bone have been subject to intensive research since the first half of the 20th century, when modern medicine started to demand a more scientific approach on muskoloskeletal mechanics. However, many challenges remain, mostly due to spatial, inter-subject, age, and disease variation of mechanical properties [Cowin, 2001, Keaveny et al., 2003]. Analysis of bone as a hierarchical composite is an important field in biomechanics [Fratzl and Weinkamer, 2007, Wagner and Weiner, 1992, Weiner and Wagner, 1998] trying to better understand and predict whole bone properties based on knowledge of composition, microstructure, and properties on the lower length scales.

While considerable progress has been made in the prediction and understanding of elastic properties on several length scales [Crolet et al., 1993, Fritsch and Hellmich, 2007, Grimal et al., 2008, Hellmich et al., 2011, Reisinger et al., 2010], up to now there is a lack of reliable postyield data on the lower length scales [Choi and Goldstein, 1992]. The aim of this thesis is therefore to obtain a more thorough understanding of the deformation mechanisms and the postelastic mechanical properties on the microscale.

1.2 Bone

1.2.1 Hierarchical structure

Bone is a hierarchical composite material featuring a cell-seeded mineralized collagen matrix with a hierarchical structure. Its main constituents are mineral (50-60 wt. %), collagen (30-40 wt. %) and water (10-20 wt. %, both bound and free) [Rho et al., 1998]. It is designed for mechanical support, metabolizing minerals and storing bone marrow [Fratzl and Weinkamer, 2007, Weiner et al., 1999] and mostly loaded in compression in everyday activities [Currey, 2002]. The hierarchical structure of bone is described in the following paragraphs and illustrated in Fig. 1.1.

The collagen molecules self-assemble into fibrils which are periodically reinforced by mineral platelets [Fratzl and Weinkamer, 2007, Weiner and Wagner, 1998], empty pore space is filled with water and non-collageneous proteins. The mineralized collagen fibrils surrounded by extrafibrillar mineral particles [Currey, 1969, 2002, Lees et al., 1990] combine into fibril

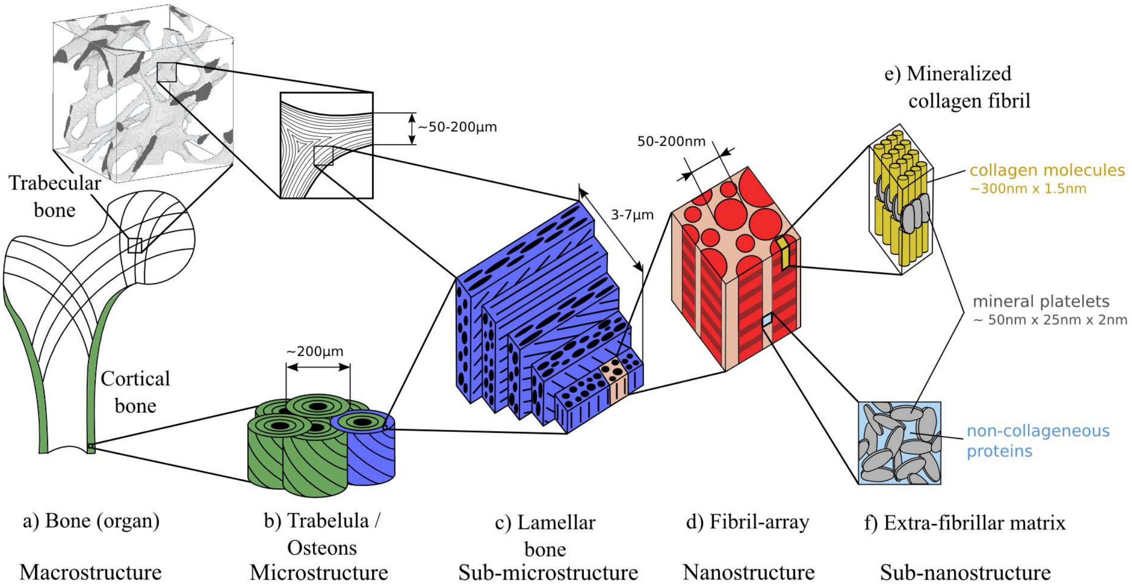

Figure 1.1: The hierarchical structure of bone [Reisinger, 2011, Varga, 2009].

arrays. In lamellar bone, parallel fibril arrays form lamellae in a rotated plywood pattern [Giraud-Guille, 1988, Reznikov et al., 2014, Varga et al., 2013, Weiner et al., 1997].

Osteocytes and their processes inhabit the lacuno-canalicular network which makes up for about 1 % of whole bone porosity [Martin, 1984]. The outer compact shell of bones is called cortex, which in humans consists of lamellae arranged concentrically around blood vessels forming osteons [Fratzl and Weinkamer, 2007]. It features a porosity of around 5-15 %, mainly made up of Haversian and Volkmann channels, which contain blood vessels and are oriented in and perpendicular to the main osteon direction (Fig. 1.2). Osteons result from a continuous remodeling process that counteracts the development of microcracks and decrease in mechanical properties over time due to fatigue and are separated from the surrounding tissue by a cement interface [Burr et al., 1988]. Old bone is resorbed by osteoclasts forming a resorption cavity, which is subsequently filled with new tissue by osteoblast cells. During this process, some of the osteoblasts get trapped in the newly formed tissue thus becoming osteocytes. Freshly deposited tissue has a lower mineral content and is mineralized over time [Currey, 2002]. A schematic drawing of the microstructure of osteonal bone may be seen in Fig. 1.2.

In large, fast growing animals an alternative tissue type, the so called fibrolamellar bone, is laid out first and converted to osteonal bone through a remodeling process [Currey, 2002]. In this bone type, fast-growing and weak woven bone is filled with stronger and more slowly deposited lamellar bone resulting in a layered structure.

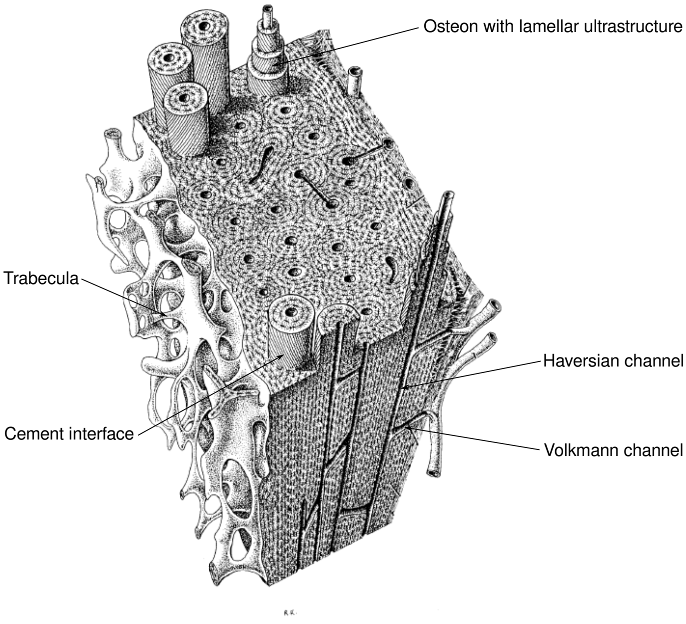

Figure 1.2: Cortical bone structure in humans [Kristic, 1991]

The inside of epiphyses of long bones and vertebral bodies is filled with a spongy bone structure called trabecular bone, which features porosities ranging from 50% to > 95%. It is made of lamellar bone organized into a network of connected plate- and beam-like structures called trabeculae (Fig. 1.1,1.2). The pores of trabecular bone are filled with bone marrow, which plays an important role in hematopoiesis and the production of lymphocytes. This work mainly focuses on the micromechanical properties of cortical bone.

1.2.2 Mechanical behavior

Mechanical tests have been performed on bone for more than a century. It has been shown to exhibit anisotropy, i.e. direction-dependence of material properties on several length scales [Currey, 2002, Franzoso and Zysset, 2009, Reisinger et al., 2011]. Also, it features a rate-and time-dependent behavior in both the elastic [Bargren et al., 1974, Eberhardsteiner et al., 2014, Lakes et al., 1979, Lakes and Katz, 1979] and the postyield regime [Caler and Carter, 1989, Fondrk et al., 1988] as well as poroelastic effects [Cowin, 1999]. When loaded quasistatically past the yield point on the macroscale, there is evidence that bone shows two simultaneous mechanisms of energy dissipation [Garcia, 2006, Zysset, 1994]: inelastic deformation and damage, i.e. reduction of stiffness due to the formation of microcracks [O'Brien et al., 2002, Sun et al., 2010, Zioupos et al., 2008]. Negative fibril strains following macroscopic tensile yielding [Gupta et al., 2006] could be interpreted as a sign of decohesion or damage on a lower length scale. Cracking in bone has been shown to be strongly associated to microstructural interfaces such as cement lines [Carter and Hayes, 1977, Diab and Vashishth, 2007, Ebacher et al., 2012, Martin and Burr, 1989, Nalla et al., 2003], which is why it may be considered as quasi-brittle [Bažant, 2004]. Materials of this class exhibit failure by developments of cracks, but the size of the plastic process zone at the crack tips is similar to the characteristic length of the microstructure. While the elastic properties of bone have been shown to be very consistent over several length scales [Hengsberger et al., 2003, Spiesz et al., 2011, Wolfram et al., 2010b], the postelastic behavior could be scale-dependent [Bažant, 2004, Bigley et al., 2007, 2008]. Evidence has been presented [Tai et al., 2006] that bone behaves like a cohesive-frictional material on the lower length scales due to its nanogranular structure. It was suggested that the increased yield properties in compression compared to tension reported in the literature [Yeni et al., 2004] may be explained by nanogranular friction between mineral particles and cohesion originating from the organic phase [Tai et al., 2006]. Other proposed nanoscale mechanisms are dissipation at the interface between mineral platelets and the organic phase [Mercer et al., 2006, Gupta et al., 2013], dilatational bands of unfolding proteins between adjacent mineral aggregates [Poundarik et al., 2012], or ductile sliding of mineral platelets followed by rupture of collagen crosslinks [Fritsch et al., 2009]. Finite element simulations of nanoindentation experiments using coupled plasticity and damage models have shown that the presence of damage may explain some of the experimental findings for mineralized tissues like reduced unloading stiffness [Zhang et al., 2010, Lucchini et al., 2011]. Fig. 1.3 shows the response of macroscopic bone samples to quasistatic loading [Gibson and Ashby, 1999] and creep tests [Fondrk et al., 1988].

For brittle materials, failure is associated with the growth of cracks originating from pores, surface scratches, or other preexisting defects and exhibits a size effect. When testing smaller specimens, the probability that a defect of a certain critical size is present in the material decreases, which leads to an increased failure stress [Griffith, 1921]. When reaching very small sample sizes, no defects of critical size may be present and alternative dissipative processes like dislocation based plasticity dominate even in ceramics [Michler et al., 2007]. In bone, the hierarchical structure leads to a macroscopically quasi-brittle behavior where plasticity and cracking both play a significant role and size effects have been reported in the past [Bigley et al., 2007, 2008]. However, the associated scaling laws spanning several levels of hierarchy remain to be investigated. Therefore, assessment of the micromechanical postelastic properties is important for understanding the nature of the size effect in bone.

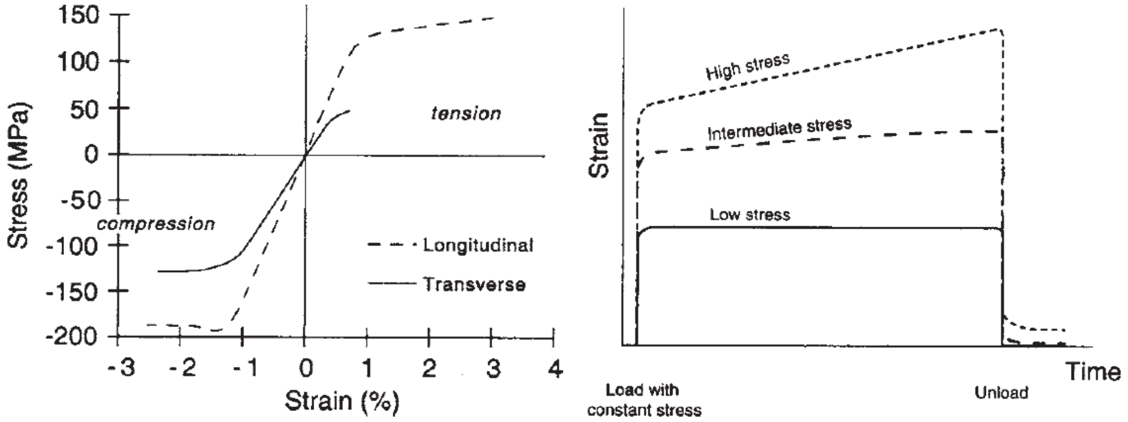

Figure 1.3: Quasistatic uniaxial (left) [Gibson and Ashby, 1999] and creep behavior (right) [Fondrk et al., 1988] of bone on the macroscale

1.3 Nanoindentation

Nanoindentation is an experimental technique allowing to assess the micromechanical properties of thin films and materials. The method originates in hardness testing, which was developed in the 19th century. In traditional mechanical testing, specimens of macroscopic dimensions and standardized shape are fixed to a testing device and subsequently loaded. In this case, the size of the tested volume is similar to the specimen size and the stress state is mostly homogeneous. In nanoindentation a diamond tip with a known geometry is pushed onto a flat surface and tip displacement as well as reaction force are measured. In this case the tested volume is much smaller than the sample and a heterogeneous stress state governed by contact mechanics develops. Therefore, local micromechanical properties are measured in contrast to properties homogenized over a large volume. A typical nanoindentation tester consists of four main components: x-y-z-table, microscope, measurement head and indenter tip. Fig. 1.4 shows a scheme of the measurement head of the Ultra Nanohardness Tester (CSM Instruments SA, Peseux, Switzerland) in use at the biomechanics laboratory of the Institute for Surgical Technology and Biomechanics of the University of Bern.

In order to make accurate measurements of indentation depth, the position of the sample surface needs to be known during the test. Therefore, the UNHT features an additional tip that acts as a reference by lowering it onto the sample surface and applying a small force to ensure continuous contact throughout the whole measurement. Tip displacements are measured differentially between reference and indenter thus minimizing load frame compliance and measurement artefacts due to piezo drift or thermal expansion.

Sneddon first published a solution for the Boussinesq problem of an axisymmetric body

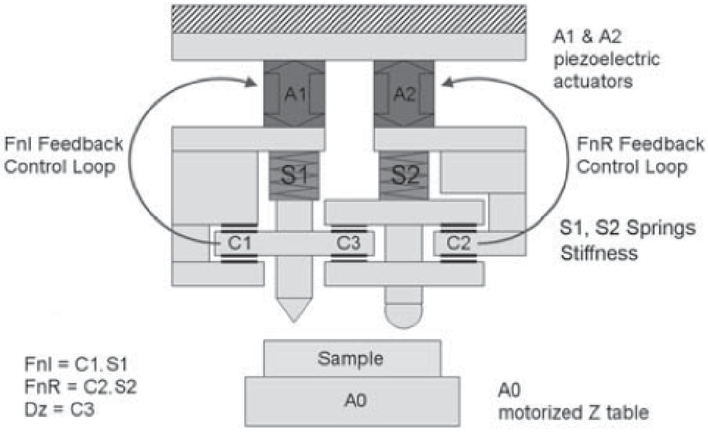

Figure 1.4: Schematic drawing of the measurement head of the UNHT nanoindentation system featuring a second tip for surface referencing. Figure adapted from CSM UNHT user manual.

in contact with an elastic halfspace in 1948 [Sneddon, 1948, 1965], which can be used to determine the elastic modulus from indentation curves provided that the contact is strictly elastic and the material's Poisson's ratio is known. However, most materials do not deform in a purely elastic way when indented. Therefore experimental techniques had to be developed that allow to extract elastic properties from real indentation experiments involving plasticity and other dissipative processes.

For elasto-plastic materials, permanent deformation takes place during the loading phase, the extent of which depends on the shape of the indenter. For sharp indenters like Berkovich or Vickers indenters, the onset of plasticity is immediate. Therefore there is a superposition of local elastic and plastic deformation making it difficult to interpret the resulting load-displacement curve. However, at the beginning of the unloading curve the behavior can be assumed to be purely elastic making it possible to extract elastic properties based on the methodology first proposed by Oliver and Pharr [Oliver and Pharr, 1992]. A typical indentation curve for bone is shown in Fig. 1.5.

The response can be divided into three parts: An elasto-plastic loading (A) followed by creep deformation at constant load (B-C) and finally elastic unloading (C-D). The method of Oliver and Pharr [Oliver and Pharr, 1992, 2004] allows to measure elastic properties based on the unloading curve and was later extended to anisotropic media [Swadener and Pharr, 2001]. A power law function is fitted to the upper 60 % of the unloading curve and its derivative $S = \frac{dP}{dh}$ computed at the maximum depth. The reduced modulus E_r may then

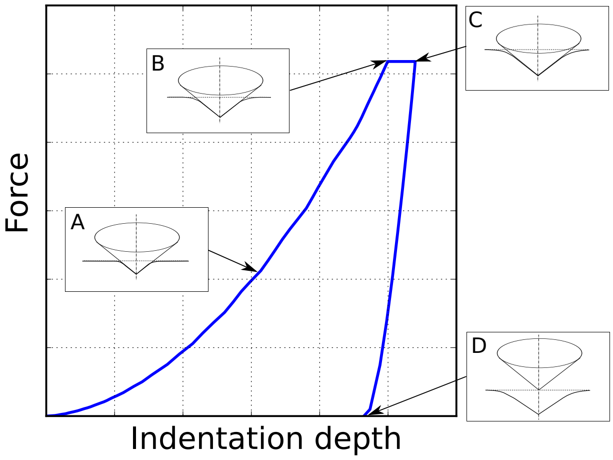

Figure 1.5: Typical load-displacement curve of an indentation experiment. Elasto-plastic loading (A) followed by creep at a constant force (B-C) and elastic unloading (C-D).

be determined using the general relation [Oliver and Pharr, 1992, Herbert et al., 2001]

$$E_r = \frac{\sqrt{\pi}}{2} S \frac{1}{\sqrt{A_c}} \tag{1.1}$$

with the slope of the unloading curve at maximum depth S, and the projected contact area A_c. Measuring the indentation depth at a high accuracy gives the possibility to approximate the actual contact area at a given depth with the help of the indenter shape function. This method is much more precise than the optical measurement of the residual imprint used in classical hardness testing. A calibration of the system determining the shape function and system compliance is done by indenting fused silica specimens with a known plain strain modulus. The indentation modulus may be recovered from the reduced modulus E_r [Herbert et al., 2001, Oliver and Pharr, 1992, 2004] by the equation

$$E^* = \left(\frac{1}{E_r} - \frac{1 - \nu_i^2}{E_i} \right)^{-1} \tag{1.2}$$

for known isotropic constants E_i and ν_i of the indenter tip. The indentation hardness H_{ind} is defined as the maximum force divided by the contact area at maximum depth:

$$H_{ind} = \frac{P_{max}}{A_{c,max}} \tag{1.3}$$

The elastic and total energies are defined as

$$W_{elast} = \int_{h_{max}}^{h_{res}} Pdh, \quad W_{tot} = \int_{0}^{h_{max}} Pdh \tag{1.4}$$

with the maximum depth h_{max} and the residual depth h_{res}. It should be noted that indentation modulus is a material property, while hardness and energies strongly depend on indenter shape and indentation depth.

Nanoindentation may also be used to extract nonlinear properties. However, it is very difficult to find a unique set of nonlinear material parameters based on one indentation curve. For materials featuring dissipative mechanisms, several inverse methods to back-calculate mechanical properties based on nanoindentations have been developed in the past [Bocciarelli et al., 2005, Bolzon et al., 2004, Bucaille et al., 2003, Ganneau et al., 2006]. These methods have been shown to provide a good estimation of the yield envelope of a material provided that the underlying dissipative mechanism is known a priori and well understood in terms of its mathematical description. However, there are additional problems when several dissipative mechanisms are at work simultaneously or their nature is not fully understood. Indentations in materials with different behaviors can result in very similar force-depth curves [Chen et al., 2007] and can thus not be used to find a unique set of nonlinear material properties. Therefore, it has been proposed in the past to increase the reliability of the obtained results by assessing mechanical properties extracted from force-depth curves of indentations with several different indenters complemented by information on the residual imprint [Bocciarelli et al., 2005, Bolzon et al., 2004, Bucaille et al., 2003, Mullins et al., 2009].

Indentation in bone with depths up to 1 µm mainly aims at characterizing the anisotropic mechanical properties on the level of single to multiple lamellae, which have a thickness of 3-7 µm [Franzoso and Zysset, 2009, Hengsberger et al., 2002, Lewis and Nyman, 2008, Olesiak et al., 2010, Oyen and Ko, 2008, Reisinger et al., 2011, Spiesz et al., 2013, Ulm et al., 2007, Zysset et al., 1999, Zysset, 2009]. Inverse methods based on conical yield surfaces have been used to extract yield properties of bone in the past [Carnelli et al., 2010, 2011, Mullins et al., 2009, Tai et al., 2006, Wang et al., 2008]. Also, finite element calculations of indentations using constitutive models coupling plasticity and damage have shown that damage could explain some of the experimental findings for bone like a reduced unloading stiffness [Lucchini et al., 2011, Zhang et al., 2010]. Nanoindentation has been used as part of validation strategies involving elastic µFE models of trabecular bone [Wolfram et al., 2010b] and mineralized tendon [Spiesz et al., 2011] and micromechanical homogenization schemes explaining the scale-dependent elastic properties of bone [Reisinger et al., 2011]. In general, it was shown that the elastic properties measured by nanoindentation are rather robust with standard deviations around 10 % of the mean value [Zysset, 2009]. The variation may most probably be explained by inhomogeneous fiber orientation, mineralization and porosity. However, correlation of indentation modulus with respect to fiber orientation and mineral mass fraction have been reported to be rather weak [Spiesz et al., 2013].

1.4 Micropillar compression

A complementary experimental setup for micromechanical testing that has emerged in the past years is micropillar compression [Dubach et al., 2009, Michler et al., 2007, Östlund et al., 2009, Uchic and Dimiduk, 2005]. Micron sized pillars are produced by erosion of material using a focused ion beam (FIB) and compressed by a flat punch indenter. Fig. 1.6 shows scanning electron microscope (SEM) images of a micropillar and a flat punch indenter from Uchic and Dimiduk [2005].

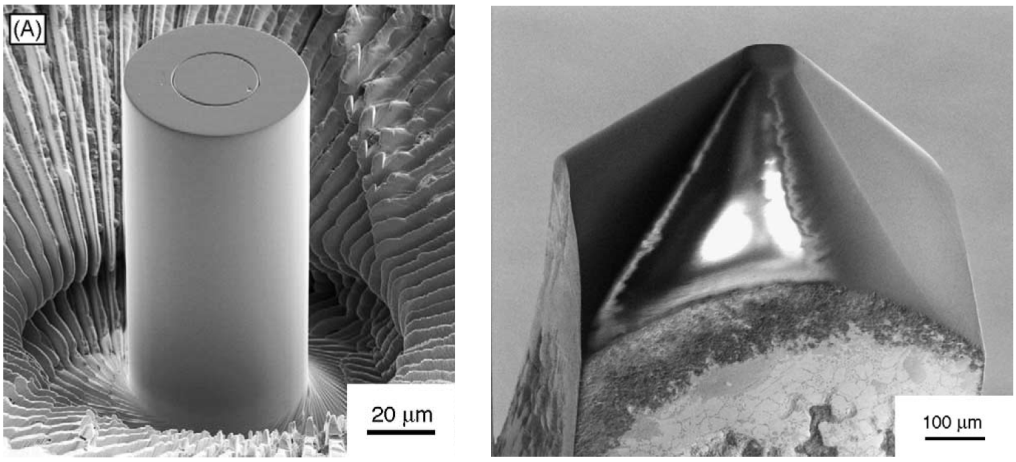

Figure 1.6: SEM images of a micropillar machined with a focused ion beam into a Ni_3(Al, Hf) single crystal (left) and a flat punch indenter used for the compression tests (right). Both figures are taken from Uchic and Dimiduk [2005].

The compression of individual pillars leads to a predominantly uniaxial stress state, which allows a straightforward interpretation of the force-displacement data similar to macroscopic uniaxial tests on dogbone-shaped specimens. This technique is ideal for studying the effects of sample size in quasi-brittle materials [Bažant, 2004] in terms of determining the postyield properties and deformation mechanisms without premature fracture [Howie et al., 2012, Michler et al., 2007, Östlund et al., 2009, 2011]. As the pillar is usually eroded from a bulk specimen, it is supported by the same material and sinks in during the test. Therefore, the solution of Sneddon for the contact of a flat punch on an elastic half space [Sneddon, 1965] was modified to include the effect of a finite fillet radius at the bottom of the pillar [Zhang et al., 2006], which may be used in order to obtain reasonably reliable strain data from the indenter displacement signal. An unwanted side effect of the focused ion beam erosion is that the impinging ions disrupt the atomic order in the sample not only by sputtering atoms, but also by displacing atoms from their original position (known as FIB damage), and Gallium implantation. These are common problems in micropillar compression studies leading to changes in the apparent properties of the tested material [El-Awady et al., 2009] and their extent may be assessed by Monte Carlo simulations [Ziegler and Biersack, 1985]. For pillars with a diameter that is considerably larger than the afflicted zone, the effect on the measured mechanical properties is negligible [Michler et al., 2007]. For mineralized tissues, this effect seems to be minor, as no significant FIB damage was reported in TEM lamellae of human dentin [Nalla et al., 2005].

1.5 Aims and Outline

The aim of this thesis was to investigate the nonlinear behavior of bone on the microscale. It focused on anisotropy, time- and rate-effects, yield and postyield properties, the presence of a damage mechanism, and the shape of the yield envelope for bone on the microscale. In order to investigate these questions, six studies were performed, three of them of a mostly theoretical nature, one numerical, and two experimental.

Chapter 2 of the thesis describes a three-dimensional material model featuring anisotropy, elasto-viscoplasticity, and damage based on a Tsai-Wu like criterion in strain space. This material model features most of the characteristics of bone that we originally aimed to investigate in this thesis.

In chapter 3, a new yield surface was proposed that may take the form of any convex quadric including ellipsoids, paraboloids, half hyperboloids and cones. Implementation of the new formulation allows to vary the yield surface shape in order to find the correct behavior for bone on the microscale instead of hypothesizing about the nature of the yield envelope a priori.

Chapter 4 deals with the influence of the yield surface shape and the presence of damage on the response of bone to indentations using Berkovich and spherical indenters in a numerical parameter study. Yield surface shape and maximum damage were varied while keeping the uniaxial yield properties constant allowing to identify the influence of the tested parameters.

Chapter 5 descibes an experimental campaign that aimed at measuring the uniaxial postelastic properties of bone on the microscale by means of *in situ* micropillar compression. The experiments allowed to determine the yield and ultimate points, postyield behavior, and to test for the presence of a damage mechanism on this length scale. The results were compared to macroscopic experiments in order to highlight the influence of microstructure as well as defects and interfaces such as preexisting cracks, pores and cement lines on the postelastic properties of bone.

In chapter 6 the residual imprint of Berkovich indentations in bone were assessed in a quantitative fashion. Mean shapes of residual imprints for dry human and ovine bone in axial and transverse direction were determined and the variability of the datasets was described by a set of principal components. Finally, the variation of the imprint shape was correlated to the measured mechanical properties in order to investigate the influence of geometry on the experimental results.

In chapter 7 the existing material model was extended to include viscoelasticity in order to test whether the discrepancies found between the micropillar compression experiments and the properties reported based on nanoindentation in the literature could be overcome by inclusion of a dissipative mechanism in the elastic regime.

The last chapter presents concluding remarks on the six studies of this thesis and an outlook on possible future work.

2

From the manuscript published in:
Biomechanics and Modeling in Mechanobiology, 12(2), 201-213, 2012

An anisotropic elastic-viscoplastic damage model for bone tissue

J.J. Schwiedrzik[1], P.K. Zysset[1]

[1]Institute for Surgical Technology and Biomechanics, University of Bern, Stauffacherstr. 78, CH-3014 Bern, Switzerland

2.1 Abstract

A new anisotropic elastic-viscoplastic damage constitutive model for bone is proposed using an eccentric elliptical yield criterion and nonlinear isotropic hardening. A micromechanics-based multiscale homogenization scheme proposed by Reisinger et al. is used to obtain the effective elastic properties of lamellar bone. The dissipative process in bone is modeled as viscoplastic deformation coupled to damage. An eccentric elliptical isotropic yield surface was defined in strain space, which is transformed to a stress based criterion by means of the damaged compliance tensor. Viscoplasticity is implemented by means of the continuous Perzyna formulation. Damage is modeled by a scalar function of the accumulated plastic strain $D(\kappa)$, reducing all elements of the stiffness matrix. A polynomial flow rule is proposed in order to capture the rate-dependent post-yield behavior of lamellar bone. A numerical algorithm to perform the backprojection on the rate-dependent yield surface has been developed and implemented in the commercial Finite Element solver Abaqus/Standard as a user subroutine UMAT. A consistent tangent operator has been derived and implemented in order to ensure quadratic convergence. Correct implementation of the algorithm, convergence and accuracy of the tangent operator were tested by means of strain- and stress-based single element tests. A finite element simulation of nanoindentation in lamellar bone was finally performed in order to show the abilities of the newly developed constitutive model.

2.2 Introduction

Bone is a biomaterial exhibiting complex mechanical behavior, especially in the post-yield regime. In order to be able to make quantitative predictions of bone stiffness and failure, realistic constitutive models of its mechanical behavior are needed. Due to the hierarchical nature of bone, the apparent mechanical properties at different length scales vary. Micromechanical approaches have been applied in the past to predict elastic and strength properties of bone on several length scales. Many of the nonlinear constitutive models proposed so far have concentrated on bone at the macroscopic organ level [Charlebois et al., 2010, Fondrk et al., 1999, Garcia et al., 2009, Keyak and Rossi, 2000, Natali et al., 2008, Zysset, 1994]. Recently, several models have been proposed that describe the behavior of bone during nanoindentation [Carnelli et al., 2010, Lucchini et al., 2011, Tai et al., 2006, Zhang et al., 2008, 2010]. Most of these models have been restricted to rate-independent post-yield behavior. It has been shown, though, that bone exhibits a strong strain-rate dependency after yielding [Gupta et al., 2007, Gupta and Zioupos, 2008], a phenomenon also seen during nanoindentation experiments at the ultrastructural level where creep behavior may be observed during holding periods [Bushby et al., 2004, Wolfram et al., 2010a, Zysset et al., 1999]. In this work, a constitutive model for bone has been developed that has the potential to be used on different length scales ranging from the ultrastructural to the macroscopic level. A micromechanical approach to assess the elastic properties was combined with a phenomenological constitutive law describing the viscoplastic and damage post-yield behavior of bone. It features anisotropic elasticity, an eccentric elliptical yield surface, viscoplasticity and damage, i.e. progressive degradation of the stiffness tensor. The purpose of this model is to be able to predict experimental force-displacement curves on several length scales from the ultrastructural to the macroscopical level by using finite element simulation and appropriate material properties. The mathematical formulation of the model is performed within the framework of thermodynamics of irreversible processes. The proposed model uses the internal state variable approach common in continuum mechanics and allows a straightforward interpretation of the constitutive behavior of cortical bone in terms of plastic deformation and damage. It does not account for the damage and inelastic deformation mechanisms in the molecular regime. Instead, several assumptions are made on the shape of the yield surface and the validity of the theory of plasticity and continuum damage mechanics. These assumptions will be listed and justified during the course of this article.

Bone is a hierarchical material with three main constituents: Collagen, mineral and water. Collagen molecules self-assemble into fibrils which are periodically reinforced by mineral platelets [Fratzl and Weinkamer, 2007, Weiner and Wagner, 1998], the empty pore space is filled with water. This basic unit forms fibril arrays, bundles of parallel mineralized fibrils embedded in a extra-fibrillar mineral matrix with a foam-like structure [Hellmich and Ulm, 2002, Reisinger et al., 2010]. In lamellar bone, parallel fibril arrays form lamellae in a rotated-plywood-like manner [Weiner et al., 1997, 1999]. Multiple bone lamellae arranged around a blood vessel make up an osteon, which features microporosity of up to 10%, mainly of the lacunar-canalicular network [Sugawara et al., 2005]. Cortical bone consists mainly of parallel arrays of osteons going in the axial direction of the bone with blood vessels making up for a macroporosity of about 6% [Fratzl and Weinkamer, 2007]. For a more thorough description, see e.g. Fratzl and Weinkamer [2007].

As shown in the previous paragraph, there is a considerable amount of porosity present on every hierarchical level of bone from the nano- to the macro-scale. Tai et al. [Tai et al., 2006] showed evidence that bone behaves as a cohesive-frictional material due to its nanogranular structure. They proposed that the increased yield properties reported in the literature [Yeni et al., 2004] in compression compared to tension may be explained by nanogranular friction between mineral particles and cohesion that originates from within the organic phase itself. Finite element simulations using plasticity models featuring a Drucker-Prager type yield surface were able to capture some of the characteristics of nanoindentation experiments on bone [Carnelli et al., 2010, Tai et al., 2006]. Micromechanical considerations by Maghous et al. [Maghous et al., 2009] on strength of porous geomaterials showed that the yield surface of cohesive-frictional materials featuring porosity takes an eccentric elliptical shape. This is also consistent with findings on the macroscopic level, where Cowin proposed a Tsai-Wu yield surface for cortical bone [Cowin, 1979]. Due to the considerable amount of porosity present on every hierarchical level in bone, we chose to base the model on an eccentric elliptical yield surface in order to make it compatible with multiple length scales from the ultrastructural to the macroscopic level. This is consistent with the notion of bone consisting of a porous mineral nanogranular matrix with organic glue reinforced by collagen fibers.

When loaded past the yield point, bone shows two mechanisms of energy dissipation: inelastic deformation and damage, i.e. reduction of the elastic properties. The formation of plastic and damage behavior is well documented on the macroscopic scale [Garcia et al., 2009]. Furthermore, it has been shown that bone exhibits a strong strain rate dependency after yielding on the macroscale [Gupta et al., 2007, Gupta and Zioupos, 2008] that may be captured by a viscoplastic approach. However, there is evidence that these mechanisms exist from the nanoscale upwards [Gupta et al., 2005, 2006, Hansma et al., 2005]. Gupta et al proposed a model where inelastic deformation at the fibril level takes place by viscous flow of the interfibrillar matrix past the fibrils transmitting shear flow stresses, once a certain strain level is reached. This process may be described by viscoplasticity taking into account the time- and rate-dependency of the post yield process and a strain-based yield criterion. One possible approach is the continuous Perzyna formulation, first proposed by Ponthot [Ponthot, 1995] allowing for a smooth transition from rate-independent elasto-plasticity to viscoplasticity. Gupta et al also interpreted their findings of negative fibril strains after macroscopical inelastic strains in tension as a sign for additional internal decohesion taking place between the mineral and the collagen molecules [Gupta et al., 2006] which may be interpreted as a formation of damage from a continuum mechanics point of view. Another experimental finding supporting the notion of damage mechanisms present at the ultrastructural level is the decrease of indentation modulus with increasing indentation depth reported in instrumented nanoindentation experiments performed on bone [Hengsberger et al., 2002, Voyiadjis and Peters, 2010, Zhang et al., 2008] and the presence of transverse microcracks around the indentation site reported by Hengsberger et al. [Hengsberger et al., 2002]. Finite element simulations of nanoindentation experiments using coupled plasticity and damage models have shown that the presence of damage may explain some of the experimental findings for mineralized tissues like size-effects [Lucchini et al., 2011, Zhang et al., 2010]. Therefore both dissipative mechanisms were included in the model by means of a plastic strain tensor and a scalar damage variable reducing all elements of the stiffness tensor as a function of accumulated plastic strain.

A strain-based formulation that is isotropic in strain space was formulated as an approximation of the yield surface of cortical bone. The advantage of this approach is the ability of the model to deal with general anisotropy and the low number of material constants needed. Experimental findings of Gupta et al support the hypothesis that the yield properties of bone can be described by a surface in strain space on the ultrastructural as well as the macroscopic level [Gupta et al., 2006]. Due to the current lack of reliable experimental data on strength properties of lamellar bone on several length scales that would allow us to refine the model, an isotropic eccentric criterion in strain space was postulated that is transformed to stress space using the damaged compliance tensor for use in the stress integration algorithm.

2.3 Constitutive model

The rheological model is a damageable elastic spring in series with a plastic pad and a dashpot element in parallel. In the purely elastic regime, the model behaves independently of the strain rate. The plastic strains are accumulating viscously using a Perzyna-type viscoplasticity formulation. The model is based on the internal variables $\boldsymbol{E}^p$ and κ. The state variable $\boldsymbol{E}^p$ is a 2nd order tensor including the inelastic strains, κ is the accumulated plastic strain. Damage accumulation is assumed to be coupled to the plasticity using a damage function $D(\kappa)$ reducing all elements of the stiffnes tensor. D is limited between 0 (no damage) and 1 (failure). Fig. 2.1 shows the rheological model for the implemented constitutive law.

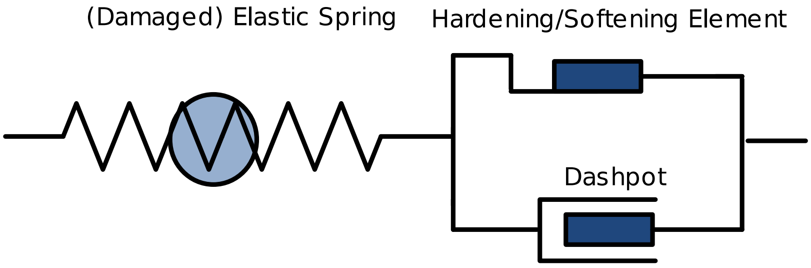

Figure 2.1: Rheological model of an elasto-viscoplastic solid with damage

2.3.1 Free energy potential and dissipation

In the notation used in the following chapters, scalars are written as X, 2^{nd} order tensors as $\boldsymbol{X}$, and 4^{th} order tensors as $\mathbb{X}$, ':' denotes the double contraction operation. In case of compositions of two 4^{th} order tensors ($\mathbb{X}_{ijkl} = \mathbb{Y}_{ijmn}\mathbb{Z}_{mnkl}$) and of transformations of a 2^{nd} order tensor with a 4^{th} order tensor ($\boldsymbol{X}_{ij} = \mathbb{Y}_{ijkl}\boldsymbol{Z}_{kl}$), the ':' sign is not written. The operator $\otimes$ denotes the dyadic product $\mathbb{X}_{ijkl} = \boldsymbol{Y}_{ij}\boldsymbol{Z}_{kl}$, $\overline{\underline{\otimes}}$ the symmetric product $\mathbb{X}_{ijkl} = \frac{1}{2}(\boldsymbol{Y}_{ik}\boldsymbol{Z}_{jl} + \boldsymbol{Y}_{il}\boldsymbol{Z}_{jk})$.

The finite total strain tensor is split additively into an elastic and a plastic part using the Green-Naghdi decomposition [Green and Naghdi, 1965]:

$$\boldsymbol{E} = \boldsymbol{E}^e + \boldsymbol{E}^p \tag{2.1}$$

The cumulated plastic strain κ is defined as:

$$\kappa = \int_0^t ||\dot{\boldsymbol{E}}^p||d\tau \tag{2.2}$$

In this model, damage is modeled as a scalar D reducing all components of the stiffness tensor. Damage is assumed to be dependent on the history of permanent deformation and therefore defined as a function of the accumulated plastic strain κ [Charlebois et al., 2010, Zysset, 1994]:

$$D(\kappa) = 1 - e^{-k_p\kappa} \tag{2.3}$$

The constant k_p was set to 10.5 following the findings of Zysset [Zysset, 1994]. The free energy potential for this material model was defined as:

$$\Psi(\boldsymbol{E}, \boldsymbol{E}^p, \kappa) = \frac{1}{2}(1 - D(\kappa))(\boldsymbol{E} - \boldsymbol{E}^p) : \mathbb{S}(\boldsymbol{E} - \boldsymbol{E}^p) \tag{2.4}$$

with the stiffness tensor $\mathbb{S}$, the total strains $\boldsymbol{E}$ and the plastic strains $\boldsymbol{E}^p$. The corresponding state laws become:

$$\boldsymbol{S}_\Psi = \nabla_{\boldsymbol{E}}\Psi = (1 - D(\kappa))\mathbb{S}(\boldsymbol{E} - \boldsymbol{E}^p) \tag{2.5}$$

and

$$\boldsymbol{S}^p_\Psi = -\nabla_{\boldsymbol{E}^p}\Psi = (1 - D(\kappa))\mathbb{S}(\boldsymbol{E} - \boldsymbol{E}^p) \tag{2.6}$$

and

$$W^\kappa_\Psi = -\nabla_{\boldsymbol{\kappa}}\Psi = \begin{cases} \frac{1}{2}D'(\kappa)(\boldsymbol{E} - \boldsymbol{E}^p) : \mathbb{S}(\boldsymbol{E} - \boldsymbol{E}^p) & \text{if } \kappa \in]0, \infty[, \\ 0 & \text{if } \kappa = 0. \end{cases} \tag{2.7}$$

where $\boldsymbol{S}$ is the stress tensor. The conjugate variables are $\boldsymbol{S}$ and $\boldsymbol{E}$, $\boldsymbol{S}^p$ and $\boldsymbol{E}^p$ as well as

W^κ and κ. For the model to be thermodynamically admissible, the dissipation Φ needs to be positive at all times. The dissipation can be expressed as the difference between the stress power density and the rate of the free energy density:

$$\Phi = \boldsymbol{S} : \dot{\boldsymbol{E}} - \dot{\Psi} \tag{2.8}$$

The dissipation becomes therefore:

$$\Phi = \boldsymbol{S} : \dot{\boldsymbol{E}} - \boldsymbol{S} : \dot{\boldsymbol{E}} + \boldsymbol{S}^p : \dot{\boldsymbol{E}}^p + W^\kappa \dot{\kappa} \tag{2.9}$$

The first two terms cancel each other out and the dissipation becomes

$$\Phi = (1 - D(\kappa))\mathbb{S}(\boldsymbol{E} - \boldsymbol{E}^p) : \dot{\boldsymbol{E}}^p + \frac{1}{2}D'(\kappa)(\boldsymbol{E} - \boldsymbol{E}^p) : \mathbb{S}(\boldsymbol{E} - \boldsymbol{E}^p)\dot{\kappa} \tag{2.10}$$

with a plastic and a damage contribution to the overall dissipation.

2.3.2 Viscoplastic formulation

Similar to the governing equations of the flow theory in rate-independent plasticity, the constitutive relations of an elastic-viscoplastic material of the Perzyna type can be written as [Etse and Carosio, 1999, Perzyna, 1966]:

$$\boldsymbol{S} = (1 - D(\kappa))\mathbb{S}(\boldsymbol{E} - \boldsymbol{E}^p) \tag{2.11}$$

$$\dot{\boldsymbol{E}}^p = \frac{1}{\eta}\langle\psi(Y)\rangle\boldsymbol{M}^p \tag{2.12}$$

$$\boldsymbol{M}^p = \nabla_{\boldsymbol{S}} Y \tag{2.13}$$

with the yield function $Y = Y(\boldsymbol{S}, \kappa)$. The $\langle\rangle$ are the McAuley brackets in their usual meaning $\langle f(x)\rangle = \frac{1}{2}(f(x)+|f(x)|)$. Following the suggestion of Ponthot [Ponthot, 1995], a viscoplastic consistency parameter $\dot{\lambda}$ is introduced. This approach is known as the continuous Perzyna formulation.

$$\dot{\lambda} = \frac{1}{\eta}\langle\psi(Y)\rangle \tag{2.14}$$

$\psi(Y)$ is a monotonously increasing, invertible function. By substituting the consistency parameter into the viscoplastic flow rules, they take a form well known from rate-independent plasticity:

$$\dot{\boldsymbol{E}}^p = \dot{\lambda}\boldsymbol{M}^p \tag{2.15}$$

For viscoplastic materials of the Perzyna type, the stress state can lie outside of the rate-independent yield surface during viscoplastic flow. In the inelastic regime ($Y \geq 0$), the overstress function $\psi(Y)$ is invertible and the yield function follows its inverse:

$$Y = \psi^{-1}(\dot{\lambda}\eta) \tag{2.16}$$

Therefore, we can define a new condition constraining the viscoplastic flow:

$$\bar{Y} = Y - \psi^{-1}(\dot{\lambda}\eta) = 0 \tag{2.17}$$

According to Etse and Carrosio [Carosio et al., 2000, Etse and Carosio, 1999], this condition represents a generalization of the rate-independent yield condition $Y = 0$ for viscoplastic materials of the Perzyna type. It allows the use of generalized Kuhn-Tucker conditions [Kuhn and Tucker, 1951] for viscoplastic flow in the form of

$$\bar{Y} \leq 0, \qquad \dot{\lambda} \geq 0, \qquad \dot{\lambda}\bar{Y} = 0 \tag{2.18}$$

which assure that the inelastic process satisfies $\bar{Y} = 0$ during viscoplastic deformation and that no permanent deformation occurs in the elastic regime. This means that during viscoplastic deformation the generalized consistency condition [Chaboche, 2008, Simo and Ju, 1987] holds true:

$$\dot{\bar{Y}} = 0 \tag{2.19}$$

It should be noted that in this approach for $\eta \rightarrow 0$ the rate-dependent yield surface $\bar{Y}$ degenerates to the rate-independent Y, transforming the elasto-viscoplastic model to an elastoplastic one.

2.3.3 Continuum tangent operator

The continuum tangent stiffness operator gives the relation between the stress rate $\dot{\boldsymbol{S}}$ and the strain rate $\dot{\boldsymbol{E}}$ in the continuum rate equation:

$$\dot{\boldsymbol{S}} = \mathbb{S}_C \dot{\boldsymbol{E}} \tag{2.20}$$

In the elastic case ($\bar{Y} < 0$), the continuum tangent has the form

$$\mathbb{S}_{C,el} = (1 - D(\kappa))\mathbb{S} \tag{2.21}$$

Differentiation of (1), (11), (14) and (17) with respect to time provides the following set of equations to evaluate the tangent in the case $\bar{Y} = 0$:

$$\dot{\boldsymbol{E}} = \dot{\boldsymbol{E}}^e + \dot{\boldsymbol{E}}^p \tag{2.22}$$

$$\dot{\boldsymbol{S}} = -D'(\kappa)\mathbb{S}(\boldsymbol{E} - \boldsymbol{E}^p)\dot{\kappa} + (1 - D(\kappa))\mathbb{S}(\dot{\boldsymbol{E}} - \dot{\boldsymbol{E}}^p) \tag{2.23}$$

$$\dot{\bar{Y}} = \dot{Y} - \dot{\psi}^{-1} = (\nabla_{\boldsymbol{S}} Y)\dot{\boldsymbol{S}} + \frac{\partial Y}{\partial \kappa}\dot{\kappa} - \frac{\partial \psi^{-1}}{\partial \dot{\lambda}}\ddot{\lambda} = 0 \tag{2.24}$$

$$\ddot{\lambda} = \frac{1}{\eta}\psi'(Y)\dot{Y} = \frac{1}{\eta}\psi'(Y)\Big((\nabla_{\boldsymbol{S}} Y)\dot{\boldsymbol{S}} + \frac{\partial Y}{\partial \kappa}\dot{\kappa}\Big) \tag{2.25}$$

For the exact form of the gradients and derivatives, see the appendix. By combining (22) and (23) with (11) and substituting $\dot{\lambda} = \frac{\dot{\kappa}}{||\nabla_{\boldsymbol{S}} Y||}$, we get:

$$\dot{\boldsymbol{E}} = \frac{\mathbb{E}\dot{\boldsymbol{S}}}{1 - D(\kappa)} + \frac{\mathbb{E}\boldsymbol{S}}{(1 - D(\kappa))^2} D'(\kappa)\dot{\kappa} + \dot{\kappa}\boldsymbol{N}^p \tag{2.26}$$

with the compliance tensor $\mathbb{E} = \mathbb{S}^{-1}$ and

$$\boldsymbol{N}^p = \frac{\nabla_{\boldsymbol{S}} Y}{||\nabla_{\boldsymbol{S}} Y||} \tag{2.27}$$

Combining (24) and (25) provides the following equation:

$$\Big(\nabla_{\boldsymbol{S}} Y \dot{\boldsymbol{S}} + \frac{\partial Y}{\partial \kappa}\dot{\kappa}\Big)\Big(1 - \frac{1}{\eta}\frac{\partial \psi^{-1}}{\partial \dot{\lambda}}\frac{\partial \psi}{\partial Y}\Big) = 0 \tag{2.28}$$

For $\eta \to 0$, the first expression has to vanish due to the consistency condition $\dot{Y} = 0$ for rate-independent materials. This provides a relationship between $\dot{\kappa}$ and $\dot{\boldsymbol{S}}$. Substituting this into (26) and accounting for (11) leads to:

$$\dot{\boldsymbol{E}} = \Big(\frac{\mathbb{E}}{1 - D(\kappa)} - (\boldsymbol{N}^p \otimes \boldsymbol{N}^p + \frac{D'(\kappa)}{1 - D(\kappa)}(\boldsymbol{E} - \boldsymbol{E}^p) \otimes \boldsymbol{N}^p)\frac{||\nabla_{\boldsymbol{S}} Y||}{\frac{\partial Y}{\partial \kappa}}\Big)\dot{\boldsymbol{S}} \tag{2.29}$$

The continuum tangent operator for the rate-independent material is therefore given by:

$$\mathbb{S}_C = \Big(\frac{\mathbb{E}}{1 - D(\kappa)} - (\boldsymbol{N}^p \otimes \boldsymbol{N}^p + \frac{D'(\kappa)}{1 - D(\kappa)}(\boldsymbol{E} - \boldsymbol{E}^p) \otimes \boldsymbol{N}^p)\frac{||\nabla_{\boldsymbol{S}} Y||}{\frac{\partial Y}{\partial \kappa}}\Big)^{-1} \tag{2.30}$$

It features a damaged elastic stiffness, a rank one correction term connected to the associated plasticity and a second correction term accounting for the damage accumulation. The presence of damage makes the problem non-associated, the tangent operator loses major symmetry. By applying the Sherman-Morrison formula, a straightforward expression for the continuum tangent stiffness of the rate-independent case may be obtained:

$$\mathbb{S}_C = (1 - D(\kappa))\mathbb{S} - \frac{(1 - D(\kappa))^2 \mathbb{S}(\boldsymbol{N}^p + \frac{D'(\kappa)}{1 - D(\kappa)}(\boldsymbol{E} - \boldsymbol{E}^p)) \otimes \boldsymbol{N}^p \mathbb{S}}{(1 - D(\kappa))\boldsymbol{N}^p \mathbb{S}(\boldsymbol{N}^p + \frac{D'(\kappa)}{1 - D(\kappa)}(\boldsymbol{E} - \boldsymbol{E}^p)) - \frac{1}{||\nabla_{\boldsymbol{S}} Y||}\frac{\partial Y}{\partial \kappa}} \tag{2.31}$$

If damage and isotropic hardening are turned off, the tangent degenerates to:

$$\mathbb{S}_{C,ep} = \mathbb{S} - \frac{\mathbb{S}\boldsymbol{N}^p \otimes \boldsymbol{N}^p \mathbb{S}}{\boldsymbol{N}^p \mathbb{S} \boldsymbol{N}^p} \tag{2.32}$$

which is equivalent to the classical tangent elastoplastic tensor [Rakatomanana et al., 1991, Zinkiewicz et al., 1969]. For the viscoplastic material ($\eta \neq 0$), the first expression of (27) does not vanish and therefore the second one has to be equal to 0. This leads to a differential equation that can be solved for special cases as demonstrated by Carrosio and Etse [Carosio et al., 2000]. A general solution for this problem is beyond the scope of this article. However, an algorithmic tangent will be presented for the rate-dependent case later in this article.

2.3.4 Elastic stiffness

The proposed constitutive model can handle elastic tensors with material symmetries ranging from isotropy to general anisotropy. In this work, we based the elastic properties on a multiscale homogenization scheme for lamellar bone proposed by Reisinger et al [Reisinger et al., 2010, 2011]. The scheme starts by modeling the mineralized fibrils as a collagen matrix reinforced by ellipsoid mineral inclusions and the extrafibrillar matrix as a mineral matrix with spherical pores. In a second homogenization step the fibril array is modeled as an extra-fibrillar matrix reinforced by mineralized collagen fibrils. Both homogenization steps are performed using a Mori-Tanaka scheme [Nemat-Nassar and Mori, 1993]. The resulting stiffness tensor for a single fibril array is transversely isotropic. In a third step, a laminate unit cell describing a single bone lamella is built and periodic boundary conditions are applied. The stiffness tensor of the unit cell is determined by applying 6 independent load cases. The resulting stiffness operator can have material symmetries ranging from isotropy to general anisotropy depending on the sublamellar arrangement of fibril arrays. For further details see Reisinger et al. [Reisinger et al., 2010, 2011]. Recently, an attempt has been made to validate the fibril array model experimentally on mineralized turkey leg tendon by Spiesz et al [Spiesz, 2011, Spiesz et al., 2011]. Comparison to experimental results on two length scales obtained through nanoindentation and comparison of macroscopical tension tests to μFE simulations showed that the model is able to predict the anisotropic stiffness of uniaxially aligned fibril arrays if the needed parameters are obtained locally at a sufficient accuracy.

2.3.5 Yield criterion

The model is based on an eccentric elliptical criterion in stress space featuring isotropic hardening and a back stress $\boldsymbol{A}$. It takes the form of:

$$Y(\boldsymbol{S},\kappa) := \sqrt{(\boldsymbol{S} - r(\kappa)\boldsymbol{A}) : \mathbb{A}(\boldsymbol{S} - r(\kappa)\boldsymbol{A})} - r(\kappa) \tag{2.33}$$

The fourth order tensor $\mathbb{A}$ and the back stress $\boldsymbol{A}$ can be determined from an equivalent orthotropic Tsai-Wu Criterion using a transformation introduced by Shih [Shih and Lee, 1978]:

$$\mathbb{A} = \frac{\mathbb{F}}{1 + \boldsymbol{A}\mathbb{F}\boldsymbol{A}} \tag{2.34}$$

$$\boldsymbol{A} = -\frac{1}{2}\mathbb{F}^{-1}\boldsymbol{F} \tag{2.35}$$

The general forms of the tensors $\mathbb{F}$ and $\boldsymbol{F}$ defining the Tsai-Wu criterion are:

$$\mathbb{F} = \sum_{i=1}^{3} \frac{1}{\sigma_i^+ \sigma_i^-} \boldsymbol{M}_i \otimes \boldsymbol{M}_i + \sum_{i,j=1;i\neq j}^{3} \frac{\zeta_{ij}}{\sigma_i^+ \sigma_i^-} \boldsymbol{M}_i \otimes \boldsymbol{M}_j + \sum_{i,j=1;i\neq j}^{3} \frac{1}{2\tau_{ij}^2} \boldsymbol{M}_i \underline{\overline{\otimes}} \boldsymbol{M}_j \tag{2.36}$$

and

$$\boldsymbol{F} = \sum_{i=1}^{3} \left(\frac{1}{\sigma_i^+} - \frac{1}{\sigma_i^-} \right) \boldsymbol{M}_i \tag{2.37}$$

with

$$\boldsymbol{M}_i = \boldsymbol{m}_i \otimes \boldsymbol{m}_i \tag{2.38}$$

The $\boldsymbol{m}_i$ are the vectors describing the material orientation. Twelve orthotropic constants are needed to define the criterion: σ_1^+, σ_1^-, σ_2^+, σ_2^-, σ_3^+, σ_1^-, ζ_{12}, ζ_{23}, ζ_{31}, τ_{12}, τ_{23} and τ_{31}. It shows isotropic hardening with respect to the midpoint of the ellipse rather than the origin of stress space . This is done in order to ensure that the tension/compression yield stress ratio is not altered by the isotropic hardening. In this formulation, the hardening function is hypothesized to be an explicit function of the accumulated plastic strain.

$$r(\kappa) := 1 + ({}^{y}r - 1)g(\kappa) \tag{2.39}$$

with $g(\kappa)$ being an arbitrary (nonlinear) function of κ. The scalar ${}^{y}r$ describes the ratio of the yield and ultimate properties. In the case of exponential hardening, $g(\kappa)$ takes the form of:

$$g(\kappa) := 1 - e^{-k_s \kappa} \tag{2.40}$$

In order to simplify material identification, it was hypothesized that an eccentric isotropic elliptical yield surface in strain space can describe the yield limit of cortical behavior accurately. It features an offset between the isotropic tensile and compressive yield strains. The criterion is given by:

$$Y_{TW}^{Strain}(\boldsymbol{E}^e) := (1-D(\kappa))\boldsymbol{P} : \boldsymbol{E}^e + \boldsymbol{E}^e : (1-D(\kappa))^2 \mathbb{P}\boldsymbol{E}^e - 1 \tag{2.41}$$

The general form of the fourth order tensor $\mathbb{P}$ is:

$$\mathbb{P} = \sum_{i=1}^{3} \frac{1}{\epsilon_0^+ \epsilon_0^-} \boldsymbol{M}_i \otimes \boldsymbol{M}_i + \sum_{i,j=1;i\neq j}^{3} \frac{\xi_0}{\epsilon_0^+ \epsilon_0^-} \boldsymbol{M}_i \otimes \boldsymbol{M}_j + \sum_{i,j=1;i\neq j}^{3} \frac{2}{\gamma_0^2} \boldsymbol{M}_i \overline{\underline{\otimes}} \boldsymbol{M}_j \tag{2.42}$$

The general form of the second order tensor $\boldsymbol{P}$ is:

$$\boldsymbol{P} = \sum_{i=1}^{3} \left(\frac{1}{\epsilon_0^+} - \frac{1}{\epsilon_0^-} \right) \boldsymbol{M}_i \tag{2.43}$$

The constants defining the elliptical strain-based criterion for cortical bone were estimated from the experimental findings of Garcia [Garcia, 2006]. The isotropy condition $\mathbb{P}_{1122} = \mathbb{P}_{1111} - \mathbb{P}_{1212}$ [Cowin and Mehrabadi, 1995] yields:

Table 2.1: Yield constants for lamellar bone

ϵ_0^+	ϵ_0^-	ξ_0
0.006	0.009	0.25

$$\gamma_0 = \sqrt{\frac{2\epsilon_0^+ \epsilon_0^-}{1-\xi_0}} \tag{2.44}$$

The resulting yield surface for lamellar bone in strain space is shown in Fig. 2.2. The yield criterion is then transformed to stress space using the damaged compliance tensor:

$$Y_{TW}^{Stress}(\boldsymbol{S}) = \boldsymbol{P} : \mathbb{E}\boldsymbol{S} + \boldsymbol{S} : \mathbb{E}\mathbb{P}\mathbb{E}\boldsymbol{S} - 1 \tag{2.45}$$

Clearly, the shape of the criterion in stress space is highly dependent on the elasticity tensor. Fig. 2.3 shows an example of a yield surface in stress space for lamellar bone. The formulation of the elliptical criterion in stress space is similar to the Tsai-Wu criterion, which is originally a failure criterion for composite materials. It is therefore transformed to the Hill criterion defined in (33) by an adaption of the methodology proposed by Shih [Shih

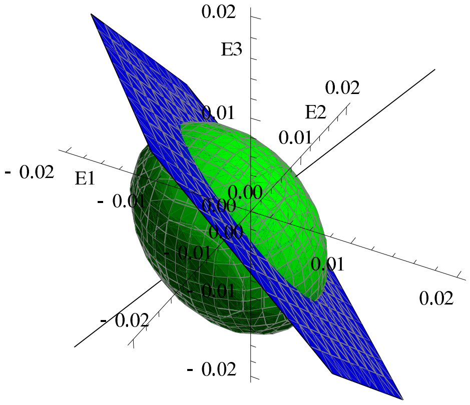

Figure 2.2: Elliptical yield criterion for lamellar bone in strain space

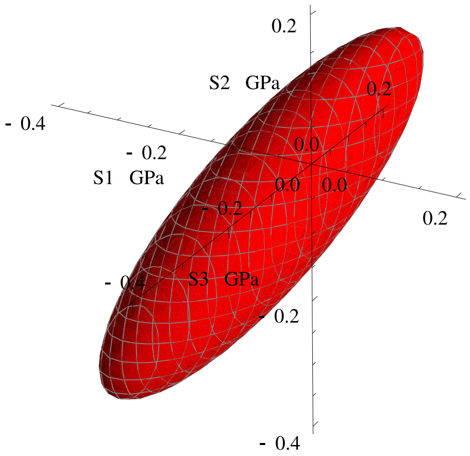

Figure 2.3: Elliptical failure criterion for lamellar bone in stress space

and Lee, 1978]:

$$\mathbb{A} = \frac{\mathbb{EPE}}{1 + \boldsymbol{A} : \mathbb{EPE}\boldsymbol{A}} \tag{2.46}$$

$$\boldsymbol{A} = -\frac{1}{2}(\mathbb{EPE})^{-1}\boldsymbol{P}\mathbb{E} \tag{2.47}$$

2.3.6 Numerical algorithm

In the following chapter, the local iteration number will be called i and should not be mistaken with the increment number n. For the sake of simplicity, all state variables at the end of the increment X_{n+1} will be called X and state variables at the beginning of the increment X_n will be called X_0 from now on. The commercial finite element solver Abaqus uses an updated Lagrangian mapping technique with the Cauchy stress tensor and an approximation of the integral of the rate of deformation $\int \boldsymbol{D}dt$ as the conjugate strain tensor for simulations involving large deformations and rotations. These stress and strain measures were therefore used in this implementation. In principle, the model is consistent for any conjugate pair of stress and strain measures, though.

First, the elastic trial stress is calculated:

$$\boldsymbol{S}_T = (1 - D(\kappa_0))\mathbb{S}(\boldsymbol{E} - \boldsymbol{E}^p_0) \tag{2.48}$$

If the yield criterion evaluated using the elastic trial stress and the old damage state is $Y(\boldsymbol{S}_T; \kappa_0) < 0$, the stress increment is purely elastic and no further damage is taking place. Therefore the state variables are updated as follows:

$$\begin{aligned} \kappa &= \kappa_0 \\ \boldsymbol{E}^p &= \boldsymbol{E}^p_0 \\ \boldsymbol{S} &= \boldsymbol{S}_T \end{aligned}$$

The tangent stiffness operator in the elastic case is given by:

$$\mathbb{S}_{CA,el} = \nabla_E \boldsymbol{S} = (1 - D(\kappa))\mathbb{S} \tag{2.49}$$

If the yield criterion $Y(\boldsymbol{S}_T; \kappa_0) \geq 0$, an implicit backprojection on the rate-dependent yield surface $\bar{Y}(\boldsymbol{S}, \kappa; \dot{\lambda})$ is performed. The following set of nonlinear equations needs to be solved using the Newton-Raphson algorithm:

$$\boldsymbol{S} = (1 - D(\kappa))\mathbb{S}(\boldsymbol{E} - \boldsymbol{E}^p)$$

$$\bar{Y}(\boldsymbol{S}, \kappa, \dot{\lambda}) = Y(\boldsymbol{S}, \kappa) - \psi^{-1}(\dot{\lambda}\eta) = 0$$

$$\dot{\boldsymbol{E}}^p = \dot{\lambda}\boldsymbol{M}^p(\boldsymbol{S}, \kappa), \qquad \boldsymbol{M}^p(\boldsymbol{S}, \kappa) = \nabla_{\boldsymbol{S}}\bar{Y}$$

$$\dot{\kappa} = h(\boldsymbol{S}, \kappa)\dot{\lambda}, \quad h(\boldsymbol{S}, \kappa) = ||\boldsymbol{M}^p||$$

constrained by the generalized Kuhn-Tucker conditions

$$\bar{Y} \leq 0, \qquad \dot{\lambda} \geq 0, \qquad \dot{\lambda}\bar{Y} = 0.$$

The gradients and derivatives can be found in the appendix. The viscoplastic consistency parameter $\dot{\lambda}$ is discretized and approximated by $\dot{\lambda} = \frac{\Delta\lambda}{\Delta t}$. The incremental consistency parameter can be written in terms of the incremental change of cumulated plastic strain:

$$\Delta\lambda = \frac{\Delta\kappa}{h(\boldsymbol{S}, \kappa_0 + \Delta\kappa)} \tag{2.50}$$

The total strains can be rewritten as:

$$\boldsymbol{E} = \boldsymbol{E}_0 + \Delta\boldsymbol{E} \tag{2.51}$$

The stress is linearized and expressed in incremental form as:

$$\begin{aligned} \boldsymbol{S} &= (1 - D(\kappa_0) - (D(\kappa) - D(\kappa_0)))\mathbb{S}(\boldsymbol{E}_0 + \Delta\boldsymbol{E} - \boldsymbol{E}_0^p - \Delta\boldsymbol{E}^p) \\ &= \boldsymbol{S}_T - (D(\kappa) - D(\kappa_0))\mathbb{S}(\boldsymbol{E} - \boldsymbol{E}_0^p) - (1 - D(\kappa))\mathbb{S}\Delta\kappa\boldsymbol{N}^p \end{aligned} \tag{2.52}$$

By bringing all expressions onto one side and multiplying with $\frac{-\mathbb{E}}{1-D}$, a tensor function expressing the residual error of elastic strains is introduced:

$$\boldsymbol{R}(\boldsymbol{S}, \Delta\kappa) = \frac{\mathbb{E}}{1 - D(\kappa_0 + \Delta\kappa)}(\boldsymbol{S}^T - \boldsymbol{S}) - \frac{D(\kappa_0 + \Delta\kappa) - D(\kappa_0)}{1 - D(\kappa_0 + \Delta\kappa)}(\boldsymbol{E} - \boldsymbol{E}_0^p) - \Delta\kappa\boldsymbol{N}^p \tag{2.53}$$

The rate-dependent yield function $\bar{Y}$ is approximated by

$$\bar{Y}(\boldsymbol{S}, \Delta\kappa) = Y(\boldsymbol{S}, \kappa_0 + \Delta\kappa) - \Psi^{-1}\Big(\frac{\Delta\kappa}{h(\boldsymbol{S}, \kappa_0 + \Delta\kappa)\Delta t}\Big) = 0 \tag{2.54}$$

The discretized equations for $\bar{Y}$, $\boldsymbol{R}$ are linearized with respect to their variables $\boldsymbol{S}$ and $\Delta\kappa$. The total strain at the end of the increment $\boldsymbol{E}$ is known a priori. This provides a linearized system of equations for the Newton-Raphson algorithm:

$$\boldsymbol{R}_{i+1} = \boldsymbol{R}_i + \nabla_{\boldsymbol{S}}\boldsymbol{R}_i : \delta\boldsymbol{S} + \frac{\partial\boldsymbol{R}_i}{\partial\Delta\kappa}\delta\Delta\kappa = \boldsymbol{0} \tag{2.55}$$

$$\bar{Y}_{i+1} = \bar{Y}_i + \nabla_{\boldsymbol{S}} \bar{Y}_i \delta \boldsymbol{S} + \frac{\partial \bar{Y}_i}{\partial \Delta \kappa} \delta \Delta \kappa = 0 \tag{2.56}$$

The set of equations is solved by determining

$$\delta \Delta \kappa = -\frac{\frac{1}{||\nabla_{\boldsymbol{S}} \bar{Y}_i||} \bar{Y}_i + \boldsymbol{N}_i^p \mathbb{S}_a \boldsymbol{R}_i}{\boldsymbol{N}_i^p \mathbb{S}_a^E \frac{\partial \boldsymbol{R}_i}{\partial \Delta \kappa} + \frac{1}{||\nabla_{\boldsymbol{S}} \bar{Y}_i||} \frac{\partial \bar{Y}_i}{\partial \Delta \kappa}} \tag{2.57}$$

$$\delta \boldsymbol{S} = \mathbb{S}_a (\boldsymbol{R}_i + \frac{\partial \boldsymbol{R}_i}{\partial \Delta \kappa} \delta \Delta \kappa) \tag{2.58}$$

with the algorithmic stiffness tensor

$$\mathbb{S}_a = -(\nabla_{\boldsymbol{S}} \boldsymbol{R})^{-1} \tag{2.59}$$

in an iterative fashion until the norm of the residual in elastic strains $\boldsymbol{R}$ and the rate dependent yield function $\bar{Y}$ are smaller than a predefined tolerance. After each iteration, the following update is performed:

$$\boldsymbol{S}_{i+1} = \boldsymbol{S}_i + \delta \boldsymbol{S} \tag{2.60}$$

$$\Delta \kappa_{i+1} = \Delta \kappa_i + \delta \Delta \kappa \tag{2.61}$$

This algorithm corresponds to a normal projection on the rate-dependent yield criterion $\bar{Y}$. Fig. 2.4 shows a schematic sketch of the implemented stress return algorithm. After convergence of the algorithm, the state variables at the end of the increment are obtained:

$$\boldsymbol{S} = \boldsymbol{S}_{i+1}$$

$$\kappa = \kappa_0 + \Delta \kappa_{i+1}$$

$$\boldsymbol{E}^p = \boldsymbol{E} - \frac{\mathbb{E} \boldsymbol{S}}{1 - D(\kappa)}$$

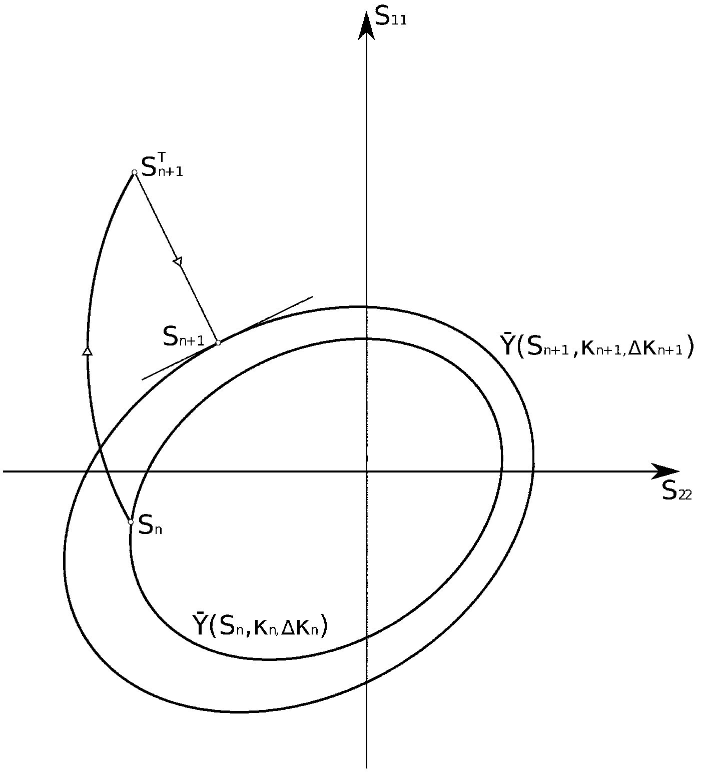

Figure 2.4: Schematic sketch of the stress return algorithm

2.3.7 Algorithmic tangent operator

The algorithmic stiffness tensor $\mathbb{S}_a$ relates infinitesimal changes of the strain increment $\delta\Delta\boldsymbol{E}$ to corresponding infinitesimal changes in the stress increment $\delta\Delta\boldsymbol{S}$. In order to find the tangent, a linearization of the stress-strain relationship has to be performed around the current solution. In this case, the consistency condition has to be applied to the algorithmic form of the rate equations. This was already done during the stress integration and does not need to be repeated. After convergence of the Newton scheme, the rate-dependent yield function $\bar{Y}$ is equal to 0 and the residual strain tensor $\boldsymbol{R}$ may be interpreted as an infinitesimal change in strain. Therefore the tensor relating infinitesimal changes of strain $\delta\boldsymbol{R} = \delta\Delta\boldsymbol{E}$ to infinitesimal changes of the stress increment $\delta\Delta\boldsymbol{S}$ is the sought algorithmic tangent stiffness tensor. In order to find it, the solution for $\delta\Delta\kappa|_{\bar{Y}=0}$ has to be substituted into the equation for $\delta\boldsymbol{S}$. The resulting algorithmic tangent stiffness operator is:

$$\mathbb{S}_{CA} = \mathbb{S}_a - \frac{\mathbb{S}_a(\frac{\partial \boldsymbol{R}}{\partial \Delta\kappa} \otimes \boldsymbol{N}^p)\mathbb{S}_a}{\boldsymbol{N}^p \mathbb{S}_a \frac{\partial \boldsymbol{R}}{\partial \Delta\kappa} - \frac{1}{||\nabla_{\boldsymbol{S}} \bar{Y}_i||} \frac{\partial \bar{Y}_i}{\partial \Delta\kappa}} \tag{2.62}$$

The gradients and derivatives appearing in this expression can be found in the appendix. For $\frac{\eta}{\Delta t} \rightarrow 0$, the inverse overstress function $\psi^{-1}(\dot{\lambda}\eta) = 0$ and the rate-dependent yield surface $\bar{Y}$ degenerates to the rate-independent Y. In this case, the tangent stiffness tensor degenerates to the rate-independent one:

$$\mathbb{S}_{CA}|_{\frac{\eta}{\Delta t}\rightarrow 0} = \mathbb{S}_a - \frac{\mathbb{S}_a(\frac{\partial \boldsymbol{R}}{\partial \Delta\kappa} \otimes \boldsymbol{N}^p)\mathbb{S}_a}{\boldsymbol{N}^p : \mathbb{S}_a \frac{\partial \boldsymbol{R}}{\partial \Delta\kappa} - \frac{1}{||\nabla_{\boldsymbol{S}} Y_i||} \frac{\partial Y_i}{\partial \Delta\kappa}} \tag{2.63}$$

The difference between the algorithmic and the continuum tangent should vanish when the plastic increment $\Delta\kappa \rightarrow 0$. In the case of $\frac{\eta}{\Delta t} \rightarrow 0$, the following relations hold:

$$\nabla_{\boldsymbol{S}} \bar{Y}|_{\frac{\eta}{\Delta t}\rightarrow 0, \Delta\kappa\rightarrow 0} = \nabla_{\boldsymbol{S}} Y \tag{2.64}$$

$$\frac{\partial \bar{Y}}{\partial \Delta\kappa}|_{\frac{\eta}{\Delta t}\rightarrow 0, \Delta\kappa\rightarrow 0} = \frac{\partial Y}{\partial \kappa} \tag{2.65}$$

$$\frac{\partial \boldsymbol{R}}{\partial \Delta\kappa}|_{\frac{\eta}{\Delta t}\rightarrow 0, \Delta\kappa\rightarrow 0} = \boldsymbol{N}^p + \frac{D'(\kappa)}{1 - D(\kappa)}(\boldsymbol{E} - \boldsymbol{E}^p) \tag{2.66}$$

Therefore, as expected, the algorithmic tangent degenerates to the continuum operator for a rate-independent material and infinitesimal plastic strain increments.

$$\mathbb{S}_{CA}|_{\Delta\kappa\rightarrow 0} = \mathbb{S}_C \tag{2.67}$$

For $\frac{\eta}{\Delta t} \rightarrow \infty$, the expression $\frac{1}{||\nabla_{\boldsymbol{S}} \bar{Y}_i||} \frac{\partial \bar{Y}_i}{\partial \Delta\kappa} \rightarrow \infty$. In this case, the tangent operator degenerates to the elastic one:

$$\mathbb{S}_{CA}|_{\frac{\eta}{\Delta t}\rightarrow \infty} = -(\nabla_{\boldsymbol{S}} \boldsymbol{R})^{-1}|_{\frac{\eta}{\Delta t}\rightarrow \infty} = (\frac{\mathbb{E}}{1 - D})^{-1} = (1 - D)\mathbb{S} \tag{2.68}$$

The implemented material model therefore shows a smooth transition from rate-independent plasticity to viscoplasticity and ultimately elasticity.

2.4 Verification

2.4.1 Single Element Tests

Different boundary conditions were imposed in strain- and stress-controlled single element tests using an orthotropic elasticity tensor and an exponential hardening function. Uniaxial tension and compression in all main directions as well as triaxial compression and shear were tested. The strain/stress was increased at a linear rate until a maximum, followed by linear unloading. Stiffness and yield point were checked to verify the correct implementation of the algorithm. The post-yield behavior was checked qualitatively. The model showed the expected behavior. The tests converged up to large strains for all load cases in strain control. Also, the algorithmic tangent operator was checked by running tests in stress control. The solution converged in one iteration in elastic increments and two to four iterations after the yield point.

2.4.2 Indentation in Bone

In order to show the abilities of the new constitutive model, a nanoindentation experiment using a Berkovich tip in cortical bone was simulated and compared to experimental results from a previous indentation study on cortical shell of human vertebral bone by Mazza [Mazza, 2008]. The tip geometry was modeled by an equivalent conical tip with a semivertical angle of 70,3°. The tip of the cone was rounded with a radius of 100nm. This coincides with a realistic tip geometry of common indenters. Only one quarter of the bone halfspace was modeled by a sufficiently large hexahedron with the dimensions $100\mu m \times 100\mu m \times 100\mu m$ following the suggestions of Poon [Poon et al., 2008b] and symmetry boundary conditions were applied in the y-z and x-z planes. The bottom nodes were constrained in the testing direction (z). The conical indenter is modeled as an analytical rigid body of revolution. Contact was defined between the conical tip and the surface of the tested bone specimen. The rigid tip acts as master surface, the bone surface as slave. In direction normal to the surfaces, hard contact was implemented using a penalty method. No friction was defined in the tangential direction.

The halfspace was meshed using linear hexahedral elements with reduced integration and enhanced hourglass control. As large deformations and rotations were anticipated to appear in the vicinity of the nanoindentation, geometrically nonlinear analysis was activated. In order to avoid numerical problems due to element distortion, arbitrary lagrangean eulerian (ALE) remeshing was activated. In this technique, the displacement is mapped in the lagrangean, the eulerian and the ALE domain. The displacement increments take place in the lagrangean configuration. In order to avoid excessive mesh distortion, the nodes are allowed to move with respect to the material during mesh sweeps. An advection step is then performed in the eulerian domain to map the solution from the old to the new mesh.

The model contains approximately 9250 elements. As the gradients of the field variables are comparatively large near the indentation and low with increasing distance to the tip, the edges of the cube were seeded with a bias towards the indentation. This allowed to have a finer mesh near the indenter tip while maintaining a relatively small number of elements.

Fig. 4.2 shows the setup of the indentation model.

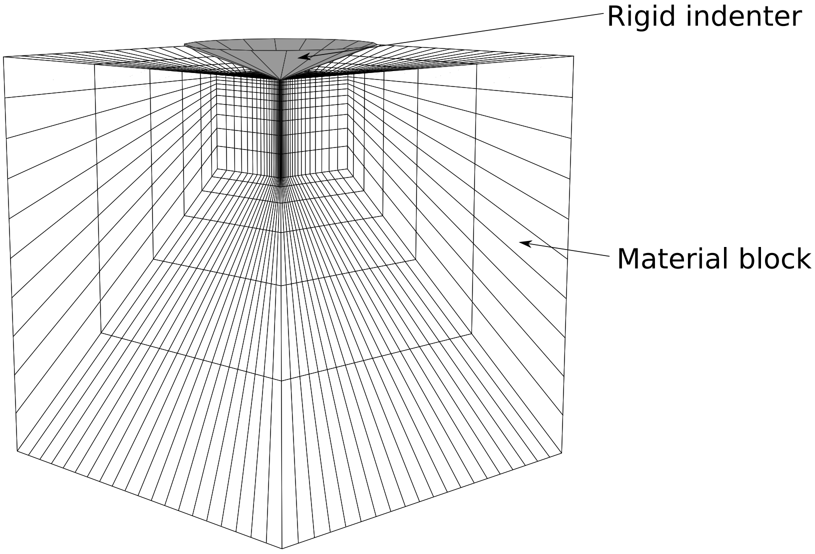

Figure 2.5: Finite element indentation model

The simulations were run in load control with the same parameters as the experimental setup. The load in z-direction on the conical tip was increased linearly at a rate of $60mN/min$ until the holding force was reached. The linear loading was followed by a holding time of $60s$ and a linear unloading at the same rate. An average orthotropic stiffness tensor for cortical bone measured during the experimental indentation study [Mazza, 2008] was used as stiffness input for the model. The rate-dependent yield criterion was implemented using a polynomial flow rule (see appendix for details). Fig. 4.3 compares the resulting force-depth curve for the simulation of a nanoindentation in bone using the newly proposed constitutive model with the experimental results of Mazza [Mazza, 2008].

The simulation was able to reach indentation depths of 2.5 μm with convergence of the solution after two to six equilibrium iterations in increments where plastic deformation occurred. Large deformations were handled by the model without the occurrence of instabilities. Table 2.2 compares the experimentally measured indentation modulus E_{IT}, maximum depth h_{max}, residual depth h_{res}, elastic work W_{elast} and the ratio of elastic to plastic work W_{elast}/W_{plast} for cortical bone with the numerical results.

The resulting force-displacement curve is consistent with the experimental findings on bone showing inelastic deformation, creep and reduced unloading stiffness. Indentation modulus, residual depth, elastic work and the ratio of elastic to plastic work of the simulated indentation were within the experimental range reported by Mazza [Mazza, 2008]. Maximum depth was slightly underestimated. No pile-up occurred around the indentation site in the

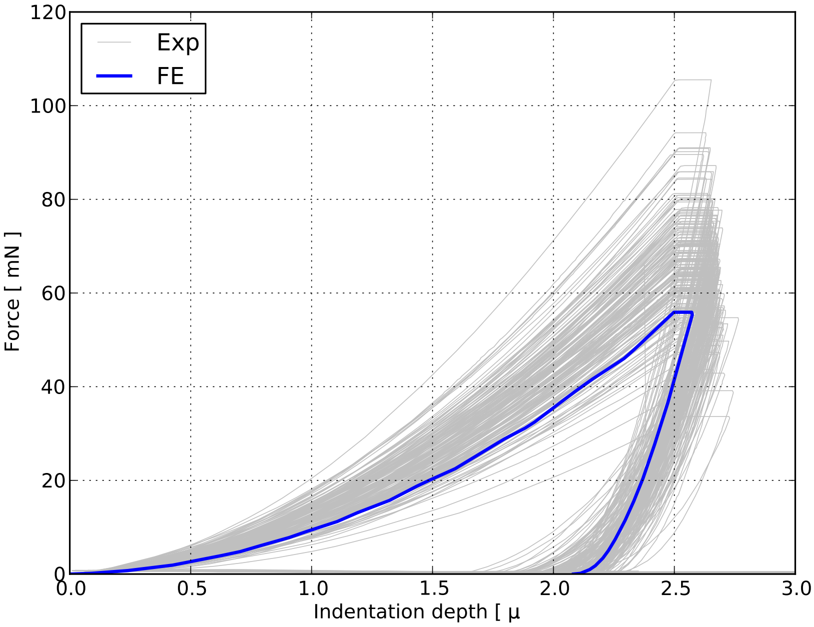

Figure 2.6: Indentation curve for the tested material model

Table 2.2: Comparison of experimental [Mazza, 2008] with numerical results

Measurement	Exp. Median	Exp. Min.	Exp. Max.	Model
E_{IT} $[GPa]$	15.79	8.76	21.79	14.88
h_{max} $[\mu m]$	2.68	2.61	2.77	2.58
h_{res} $[\mu m]$	1.94	0.85	2.21	2.08
W_{elast}	13664	6100	23807	9652
W_{elast}/W_{plast}	0.256	0.16	0.44	0.232

model, which is also consistent with the behavior of bone seen in nanoindentation. The polynomial viscoplasticity proved to be a fast and stable constitutive model.

2.5 Discussion

An new anisotropic constitutive model for bone has been proposed that is able to capture both the elastic and the post-yield mechanical behavior of lamellar bone. It features anisotropic elasticity based on a multiscale homogenization scheme, viscoplasticity and damage. After yielding, bone shows two mechanisms of energy dissipation: rate-dependent inelastic deformation and damage. There is evidence that these mechanisms exist already at the fibril level [Gupta et al., 2005, 2006, Hansma et al., 2005]. Therefore we believe that the proposed phenomenological model can potentially capture the post-yield behavior of bone at length scales from the fibril array to the organ level. It was hypothesized that, due to the nanogranular nature of the mineral matrix, the cohesive behavior caused by the organic phase [Tai et al., 2006] and the porosity present at all length scales [Fratzl and Weinkamer, 2007], an eccentric elliptical yield criterion [Maghous et al., 2009] is the best choice for bone. Nonlinear isotropic hardening was implemented in order to capture the post-yield behavior. This is a reasonable choice as long as the applied loads are proportional. A micromechanics-based multiscale homogenization scheme proposed by Reisinger et al. [Reisinger et al., 2010, 2011] has been used to obtain the elastic properties. Viscoplasticity was implemented by means of the continuous Perzyna formulation [Ponthot, 1995] allowing for a smooth transition from rate-independent elasto-plasticity to viscoplasticity. Damage is modeled by a scalar function coupled to the plastic loading history. A polynomial flow rule was proposed in order to describe the rate-dependent post-yield behavior of lamellar bone. A numerical algorithm to perform the backprojection on the rate-dependent yield surface was developed and implemented in the commercial Finite Element solver Abaqus/Standard as a user subroutine UMAT. A consistent tangent operator has been derived and implemented in order to assure rapid convergence.

The correct implementation of the algorithm as well as the convergence of the model were tested by means of strain- and stress-based single element tests. The model showed the expected stress-strain behavior and converged up to large strains for all applied load cases. A finite element simulation of a Berkovich indentation in bone was performed in order to show the abilities of the newly developed constitutive model. Comparison to experimental results [Mazza, 2008] verified that the model is able to capture the behavior of bone during indentation experiments.

Advantages of the model include: The presented formulation is very general. Due to the introduction of an isotropic yield surface in strain space, only three independent material properties are needed in addition to the elastic properties to define an anisotropic yield surface for bone thus simplifying material identification. The combination of anisotropic elasticity with viscoplasticity and damage based on an elliptical yield surface makes the model feasible for use at multiple levels of bone hierarchy reaching from the fibril to the macroscopic level. By coupling a phenomenological post-yield model to a multiscale homogenization approach predicting elastic properties, an efficient and powerful tool has been proposed to assess the mechanical behavior of bone at several length scales. The inclusion of viscoplasticity makes it possible to account for strain rate effects as reported by Gupta et al [Gupta et al., 2007, Gupta and Zioupos, 2008] and to assess creep or relaxation behavior as seen during nanoindentation experiments.

Limitations of the model include the modeling of damage by a scalar function. As the model is supposed to work on several length scales that show different mechanisms reducing the elastic stiffness tensor most of which are not completely understood, this seemed to be a reasonable approach. Also, the model describes the post-yield behavior of bone in a continuum mechanics framework, it does not account for the exact mechanisms at the submicron scale. However, as the activated volume of the dissipative processes in bone was reported in the range from $0.64nm^3$ to $1.0nm^3$ by Gupta et al. [Gupta et al., 2007] and the model is supposed to reflect the mechanical behavior of bone starting at the fibril array level with representative volumes several orders of magnitude larger, this approach is justified. The assumption of an isotropic yield surface in strain space is very strong, however given the lack of reliable data at several length scales it is a reasonable starting point. A second limitation is the use of isotropic hardening that might not be able to catch some effects, especially during cyclic testing combining tension and compression. This limits the model's predictive capabilities to proportional loading, which are however the most common types of loading encountered in the body. Introduction of mixed hardening in the future would be desirable.

Both cortical and trabecular bone show inelastic deformation and a reduction of the elastic stiffness tensor after the yield point as well as pressure dependent yield properties that differ in tension and compression [Yeni et al., 2004]. The porosity in trabecular bone is considerably higher than in cortical bone, however the underlying dissipative mechanisms remain similar. There is evidence that the yield strains for trabecular bone can be captured rather well by an eccentric isotropic elliptical yield criterion in strain space [Gross, 2010]. Therefore the proposed model may be expanded to describe the homogenized response of trabecular bone in the future using fabric elasticity relationships [Zysset and Curnier, 1995] and a different set of parameters for the yield surface and post-yield properties. Since a general nonlinear hardening function may be implemented in the model, hardening/softening behavior characteristic of the mechanical response of trabecular bone to compression [Charlebois et al., 2010] may be implemented in the current model.

2.6 Gradients and derivatives

2.6.1 Polynomial flow rule

$$\dot{\lambda} = \frac{1}{\eta}\Big(Y^2 + mY\Big)$$

$$\psi^{-1}(\eta\dot{\lambda}) = -\frac{m}{2} + \Big(\frac{m^2}{4} + \eta\dot{\lambda}\Big)^{\frac{1}{2}}$$

2.6.2 Residual of elastic strains

$$\boldsymbol{R}(\boldsymbol{S}, \Delta\kappa) = \frac{\mathbb{E}}{1 - D(\kappa_0 + \Delta\kappa)}(\boldsymbol{S}^T - \boldsymbol{S}) - \frac{D(\kappa_0 + \Delta\kappa) - D(\kappa_0)}{1 - D(\kappa_0 + \Delta\kappa)}(\boldsymbol{E} - \boldsymbol{E}_0^p) - \Delta\kappa \boldsymbol{N}^p$$

$$\nabla_{\boldsymbol{S}} \boldsymbol{R} = -\frac{\mathbb{E}}{1 - D} - \Delta\kappa \nabla_{\boldsymbol{S}} \boldsymbol{N}^p$$

$$\frac{\partial \boldsymbol{R}}{\partial \Delta\kappa} = \frac{D'}{(1 - D)^2}\Big(\mathbb{E}(\boldsymbol{S}^T - \boldsymbol{S}) - (1 - D_0)(\boldsymbol{E} - \boldsymbol{E}_0^p)\Big) - \boldsymbol{N}^p - \Delta\kappa \frac{\partial \boldsymbol{N}^p}{\partial \Delta\kappa}$$

2.6.3 Direction of plastic flow

$$\boldsymbol{N}^p(\boldsymbol{S}, \Delta\kappa) = \frac{\mathbb{A}(\boldsymbol{S} - r(\kappa_0 + \Delta\kappa)\boldsymbol{A})}{||\mathbb{A}(\boldsymbol{S} - r(\kappa_0 + \Delta\kappa)\boldsymbol{A})||}$$

$$\nabla_{\boldsymbol{S}} \boldsymbol{N}^p = \frac{\mathbb{A} - \boldsymbol{N}^p \otimes \mathbb{A}\boldsymbol{N}^p}{||\mathbb{A}(\boldsymbol{S} - \boldsymbol{A})||}$$

$$\frac{\partial \boldsymbol{N}^p}{\partial \Delta\kappa} = -\frac{r'\mathbb{A}\boldsymbol{A} - \boldsymbol{N}^p(r'\mathbb{A}\boldsymbol{A} : \boldsymbol{N})}{||\mathbb{A}(\boldsymbol{S} - r\boldsymbol{A})||}$$

2.6.4 Continuum rate-independent yield surface

$$Y(\boldsymbol{S}, \kappa) = \sqrt{(\boldsymbol{S} - r(\kappa)\boldsymbol{A}) : \mathbb{F}(\boldsymbol{S} - r(\kappa)\boldsymbol{A})} - r(\kappa)$$

$$\nabla_{\boldsymbol{S}} Y = \frac{\mathbb{A}(\boldsymbol{S} - r\boldsymbol{A})}{\sqrt{(\boldsymbol{S} - r\boldsymbol{A}) : \mathbb{A}(\boldsymbol{S} - r\boldsymbol{A})}}$$

$$\frac{\partial Y}{\partial \kappa} = -\frac{r'\boldsymbol{S}\mathbb{A}\boldsymbol{A} - rr'\boldsymbol{A}\mathbb{A}\boldsymbol{A}}{\sqrt{(\boldsymbol{S} - r\boldsymbol{A}) : \mathbb{A}(\boldsymbol{S} - r\boldsymbol{A})}} - r'$$

2.6.5 Algorithmic rate-dependent yield surface

$$\bar{Y}(\boldsymbol{S},\Delta\kappa) = Y(\boldsymbol{S},\kappa_0+\Delta\kappa) + \frac{m}{2} - \Big(\frac{m^2}{4} + \frac{\eta}{\Delta t}\frac{\Delta\kappa}{h}\Big)^{\frac{1}{2}}$$

$$\nabla_{\boldsymbol{S}}\bar{Y} = \frac{\mathbb{A}(\boldsymbol{S}-r\boldsymbol{A})}{\sqrt{(\boldsymbol{S}-r\boldsymbol{A}):\mathbb{A}(\boldsymbol{S}-r\boldsymbol{A})}} + \frac{1}{2}\frac{\eta}{\Delta t}\frac{\Delta\kappa}{h^2}\nabla_{\boldsymbol{S}}h\Big(\frac{m^2}{4} + \frac{\eta}{\Delta t}\frac{\Delta\kappa}{h}\Big)^{-\frac{1}{2}}$$

$$\frac{\partial\bar{Y}}{\partial\Delta\kappa} = -\frac{r'\boldsymbol{S}\mathbb{A}\boldsymbol{A} - rr'\boldsymbol{A}\mathbb{A}\boldsymbol{A}}{\sqrt{(\boldsymbol{S}-r\boldsymbol{A}):\mathbb{A}(\boldsymbol{S}-r\boldsymbol{A})}} - r' - \frac{1}{2}\frac{\eta}{\Delta t}\frac{h-\Delta\kappa\frac{\partial h}{\partial\Delta\kappa}}{h^2}\Big(\frac{m^2}{4} + \frac{\eta}{\Delta t}\frac{\Delta\kappa}{h}\Big)^{-\frac{1}{2}}$$

2.6.6 Norm of the gradient on the yield surface

$$h(\boldsymbol{S},\Delta\kappa) = \frac{||\mathbb{A}(\boldsymbol{S}-r(\kappa_0+\Delta\kappa)\boldsymbol{A})||}{\sqrt{(\boldsymbol{S}-r(\kappa_0+\Delta\kappa)\boldsymbol{A})\mathbb{A}(\boldsymbol{S}-r(\kappa_0+\Delta\kappa)\boldsymbol{A})}}$$

$$\nabla_{\boldsymbol{S}}h = \frac{\mathbb{A}\boldsymbol{N}^p}{\sqrt{(\boldsymbol{S}-r\boldsymbol{A})\mathbb{A}(\boldsymbol{S}-r\boldsymbol{A})}} - \frac{||\mathbb{F}(\boldsymbol{S}-r\boldsymbol{A})||\big(\mathbb{A}(\boldsymbol{S}-r\boldsymbol{A})\big)}{\big((\boldsymbol{S}-r\boldsymbol{A}):\mathbb{A}(\boldsymbol{S}-r\boldsymbol{A})\big)^{\frac{3}{2}}}$$

$$\frac{\partial h}{\partial\Delta\kappa} = \frac{-r'\mathbb{A}\boldsymbol{A}:\boldsymbol{N}^p}{\sqrt{(\boldsymbol{S}-r\boldsymbol{A})\mathbb{A}(\boldsymbol{S}-r\boldsymbol{A})}} - \frac{||\mathbb{F}(\boldsymbol{S}-r\boldsymbol{A})||\big(r'\boldsymbol{S}\mathbb{A}\boldsymbol{A} - rr'\boldsymbol{A}\mathbb{A}\boldsymbol{A})\big)}{\big((\boldsymbol{S}-r\boldsymbol{A}):\mathbb{A}(\boldsymbol{S}-r\boldsymbol{A})\big)^{\frac{3}{2}}}$$

3

From the manuscript published in:
Biomechanics and Modeling in Mechanobiology, 12(6), 1155-1168, 2013

A generalized anisotropic quadric yield criterion and its application to bone tissue at multiple length scales

J.J. Schwiedrzik[1], U. Wolfram[1], P.K. Zysset[1]

[1]Institute for Surgical Technology and Biomechanics, University of Bern, Stauffacherstr. 78, CH-3014 Bern, Switzerland

3.1 Abstract

Nonlinear computational analysis of materials showing elasto-plasticity or damage rely on knowledge of their yield behavior and strength under complex stress states. In this work, a generalized anisotropic quadric yield criterion is proposed that is homogeneous of degree one and takes a convex quadric shape with a smooth transition from ellipsoidal to cylindrical or conical surfaces. If in the case of material identification the shape of the yield function is not known a priori, a minimization using the quadric criterion will result in the optimal shape among the convex quadrics. The convexity limits of the criterion and the transition points between the different shapes are identified. Several special cases of the criterion for distinct material symmetries such as isotropy, cubic symmetry, fabric-based orthotropy and general orthotropy are presented and discussed. The generality of the formulation is demonstrated by showing its degeneration to several classical yield surfaces like the von Mises, Drucker-Prager, Tsai-Wu, Liu, generalized Hill and classical Hill criteria under appropriate conditions. Applicability of the formulation for micromechanical analyses was shown by transformation of a criterion for porous cohesive-frictional materials by Maghous et al. In order to demonstrate the advantages of the generalized formulation, bone is chosen as an example material, since it features yield envelopes with different shapes depending on the considered length scale. A fabric- and density-based quadric criterion for the description of homogenized material behavior of trabecular bone is identified from uniaxial, multiaxial and torsional experimental data. Also, a fabric- and density-based Tsai-Wu yield criterion for homogenized trabecular bone from *in silico* data is converted to an equivalent quadric criterion by introduction of a transformation of the interaction parameters. Finally, a quadric yield criterion for lamellar bone at the microscale is identified from a nanoindentation study reported in the literature thus demonstrating the applicability of the generalized formulation to the description of the yield envelope of bone at multiple length scales.

3.2 Introduction

Nonlinear computational analysis of materials showing elasto-plasticity or damage behavior rely on knowledge of their yield behavior and strength under complex stress states. The yield or failure criterion of a material is usually described by a convex function taking into account the influence of the shear and normal stresses as well as their interactions. Many criteria have been proposed in the past like the von Mises [von Mises, 1913] or Hill [Hill, 1951] criteria for plastically incompressible materials, especially metals, or the Drucker-Prager criterion for dilatant cohesive-frictional materials [Prager and Drucker, 1952]. These functions, although of phenomenological nature, have proven to be valuable tools in mechanics of irreversible processes, as they can often be used as closed-form approximations of the complex material strength behavior. The criteria are formulated as explicit functions of the components of the stress tensor and a set of material constants that may be identified by independent tests. When solving mechanical problems using numerical methods, it is often desirable to use smooth functions as yield surfaces as standard backprojection procedures may be used in this case [Curnier, 1994]. However, some classical criteria like the one proposed by Drucker and Prager [Prager and Drucker, 1952] feature singular points where the normal on the yield surface is non-unique. In this case, it is often desirable to use smooth approximations of the actual yield function in order to avoid the implementation of special algorithms and/or numerical instabilities. In the framework of computational mechanics, strength criteria are frequently combined with dissipation mechanisms like damage or plasticity, i.e. the accumulation of inelastic strains. These formulations often make use of hardening mechanisms such as dilatation and translation of the yield surface as a function of scalar or tensorial hardening variables. Especially in the case of isotropic hardening, the use of functions that are homogeneous of degree one as a yield criterion is beneficial, since it simplifies the implementation of numerical algorithms like implicit backprojections.

One obstacle when dealing with elasto-plasticity in a computational mechanics framework is the choice of the correct yield surface. Since the formulations are usually valid for a certain group of materials and not of a general nature, care must be taken to identify the right one for the given application. This is especially the case when strength data is available for given load directions and a yield function needs to be identified by means of minimization procedures. In this sense it would be desirable to use a formulation that describes a wide range of materials while retaining a simple and explicit form in order to obtain the optimal shape of the yield surface with respect to the data points without severe restrictions due to the formulation used.

One class of surfaces that combines simplicity of the underlying function with the ability to take a large variety of shapes is the set of convex quadrics. It spans from parallel planes to ellipsoids, paraboloids, (half) hyperboloids of two sheets, cylinders, and cones, which are popular choices for yield functions of materials like metals, geomaterials, porous foams, bone, etc. Especially in the case of bone tissue, a general formulation is desirable. Its yield envelope changes its shape drastically depending on the length scale considered and has been approximated by quadric surfaces in the past [Carnelli et al., 2011, Cowin, 1986, 2001, Wolfram et al., 2012]. Therefore it was chosen as an example material in this work.

Bone is a hierarchical material with collagen, mineral and water as well as non-collagenous proteins [Rho et al., 1998, Fratzl and Weinkamer, 2007, Wang and Gupta, 2011] as the main constituents. The collagen molecules self-assemble into fibrils which are periodically reinforced by mineral platelets [Fratzl and Weinkamer, 2007, Weiner and Wagner, 1998]. Empty pore space is filled with water and non-collageneous proteins. This basic unit then forms bundles of parallel mineralized fibrils embedded in an extra-fibrillar mineral matrix with a foam-like structure [Hellmich and Ulm, 2002, Reisinger et al., 2010] that are called fibril arrays. There is a considerable amount of porosity present on every hierarchical level from the nano- to the macro-scale [Smith et al., 2008]. Tai et al. [2006] showed some evidence that bone behaves like a cohesive-frictional material at the nanolevel due to its nanogranular structure. They suggested that increased yield properties in compression compared to tension reported in the literature [Yeni et al., 2004] may be explained by nanogranular friction between mineral particles and cohesion originating from the organic phase. Finite element simulations using plasticity and damage models featuring a conical yield surface were able to capture some of the characteristics reported from nanoindentation experiments on bone [Carnelli et al., 2010, 2011, Tai et al., 2006]. Micromechanical considerations by Maghous et al. showed that the introduction of porosity into a cohesive-frictional material leads to a decrease in uniaxial strength properties as well as a change of the shape of the criterion from a conical to an eccentric elliptical surface [Maghous et al., 2009].

When looking at bone at the macroscale, one distinguishes between two types of bone, i.e. compact and trabecular. In compact bone, parallel fibril arrays form lamellae. These lamellae are arranged in layers around blood vessels (Haversian channels) forming cylindrical structures called osteons. Arrays of parallel osteons connected by interstitial bone regions make up the cortical bone structure. Cortical bone features microporosity of up to 10%, mainly due to an interconnected network of cells and cell processes, the so called lacunar-canalicular network [Kristic, 1991, Weiner and Wagner, 1998]. On the macroscopic level, it has been proposed by Cowin [Cowin, 1979, 1986, 2001] in the past that an eccentric elliptical, i.e. a Tsai-Wu yield surface is suitable for cortical bone.

Trabecular bone is an anisotropic and highly porous mineralized tissue enclosed in compact bone in the cores of flat and small bones and the epiphyses of long bones [Kristic, 1991]. Plate- and rod-like structures of bone form an open-cell foam [Gibson, 1985]. Large efforts have been undertaken in the past to identify the mechanical properties and morphology of this highly heterogeneous tissue and their underlying relationships [Gupta and Zioupos, 2008, Keaveny et al., 2001, Zysset, 2003]. Historically, morphological parameters like volume fraction, surface density, trabecular thickness, spacing and number have been identified using quantitative stereology [Parfitt, 1984]. In order to assess the anisotropy of the trabecular structure, the mean intercept length (MIL) method was introduced by Whitehouse [Whitehouse, 1974]. Within the last 20 years, the investigation of trabecular morphology has been facilitated by the development of new technologies like micro computed tomography (μCT). Hildebrand et al. [1999] proposed a methodology to measure morphological parameters directly from 3D μCT data. The three-dimensional distribution function of trabecular orientations is then mathematically modeled by means of a second order fabric tensor [Harrigan and Mann, 1984, Kanatani, 1984].

Cowin first established a relationship between volume fraction, fabric tensor and the homogenized anisotropic elasticity tensor and strength criterion for highly porous materials such as trabecular bone [Cowin, 1985, 1986, 2001]. An alternative model for anisotropic elasticity of cancellous bone based on fabric tensors was proposed by Zysset and Curnier [1995], which reduced the number of material parameters and a priori satisfied thermodynamic admissibility. For further information on fabric-based models, see e.g. the review by Zysset [2003]. The model was extended towards yield and strength properties leading to the introduction of a halfspacewise defined fabric- and density based generalized Hill criterion [Zysset and Rincón, 2006], which was later identified by Rincón-Kohli and Zysset [2009]. Arramon et al. [2000] proposed an anisotropic criterion for bone in stress space based on Kelvin modes, while other authors introduced strain-based formulations [Bayraktar et al., 2004, Cowin and He, 2005]. Recently, a fabric- and density-based Tsai-Wu criterion has been proposed and successfully identified for trabecular bone using nonlinear µFE and homogenization techniques [Wolfram et al., 2012].

As part of this paper, the quadric yield criterion will be presented in a general anisotropic formulation and special cases of material symmetry will be discussed. This includes the case of a fabric- and density based orthotropic formulation that has been proven useful in the past in the description of anisotropic mechanical behavior of bone [Wolfram et al., 2012, Zysset and Rincón, 2006]. Additionally, it will be shown that material properties may be obtained from a known Tsai-Wu criterion by means of a straightforward transformation of the interaction coefficients. The generality of the formulation will be demonstrated by showing that the quadric criterion degenerates to several classical yield criteria including the ones of Drucker and Prager [Prager and Drucker, 1952], von Mises [von Mises, 1913], Tsai and Wu [Tsai and Wu, 1971], Liu et al. [Liu et al., 1997] and Hill [Hill, 1951] when the right conditions are met. Applicability of the formulation for micromechanical analyses will be demonstrated by identification of a quadric yield surface from a criterion for porous cohesive-frictional materials [Maghous et al., 2009], which is also applicable for the description of bone at the microscale as a cohesive-frictional material [Tai et al., 2006] in interaction with nanoporosity. Finally, the suitability of the formulation to describe the yield surface of bone at several length scales will be presented by identification of material constants for criteria of bovine lamellar bone at the microscale as well as homogenized human trabecular bone at the macroscale.

3.3 General formulation

In the notation used in the following chapter, scalars are written as X, vectors as $\boldsymbol{x}$, 2^{nd} order tensors as $\boldsymbol{X}$, 4^{th} order tensors as $\mathbb{X}$, and tensor spaces as $\mathcal{X}$. The sign ':' denotes the double contraction operation. In case of compositions of two 4^{th} order tensors ($\mathbb{X}_{ijkl} = \mathbb{Y}_{ijmn}\mathbb{Z}_{mnkl}$) and of transformations of a 2^{nd} order tensor with a 4^{th} order tensor ($\boldsymbol{X}_{ij} = \mathbb{Y}_{ijkl}\boldsymbol{Z}_{kl}$), the sign ':' is not written. The operator $\otimes$ denotes the dyadic product $\mathbb{X}_{ijkl} = \boldsymbol{Y}_{ij}\boldsymbol{Z}_{kl}$, $\underline{\otimes}$ the tensorial product $\mathbb{X}_{ijkl} = \boldsymbol{Y}_{ik}\boldsymbol{Z}_{jl}$, and $\overline{\underline{\otimes}}$ the symmetric product $\mathbb{X}_{ijkl} = \frac{1}{2}(\boldsymbol{Y}_{ik}\boldsymbol{Z}_{jl} + \boldsymbol{Y}_{il}\boldsymbol{Z}_{jk})$.

We postulate an anisotropic quadric yield criterion in stress space $\mathcal{S}$:

$$Y(\boldsymbol{S}) := \sqrt{\boldsymbol{S} : \mathbb{F}\boldsymbol{S}} + \boldsymbol{F} : \boldsymbol{S} - 1 = 0 \tag{3.1}$$

It contains a fourth order tensor $\mathbb{F}$ and a second order tensor $\boldsymbol{F}$ defining the origin, orientation and shape of the criterion. Its surface normal is given by:

$$\nabla_{\boldsymbol{S}} Y = (\boldsymbol{S} : \mathbb{F}\boldsymbol{S})^{-\frac{1}{2}}\mathbb{F}\boldsymbol{S} + \boldsymbol{F} \tag{3.2}$$

See Fig. 3.3.1 for a visualization of the possible shapes of the criterion. It is a homogeneous function of degree one ($Y(\lambda\boldsymbol{S}) = \lambda Y(\boldsymbol{S})$, $\forall\lambda \in \mathbb{R}$), which allows for a straightforward introduction of isotropic hardening, i.e. a dilatation of the yield surface with respect to the origin of stress space, in the form of

$$Y(\boldsymbol{S}, \kappa) := \sqrt{\boldsymbol{S} : \mathbb{F}\boldsymbol{S}} + \boldsymbol{F} : \boldsymbol{S} - r(\kappa) = 0 \tag{3.3}$$

with an isotropic hardening function $r(\kappa)$ of a scalar hardening variable κ. For tensorial hardening with a tensor function $\mathbb{K}(\kappa)$, the criterion takes the form

$$Y(\boldsymbol{S}, \kappa) := \sqrt{\boldsymbol{S} : \mathbb{K}(\kappa)\mathbb{F}\mathbb{K}(\kappa)\boldsymbol{S}} + \mathbb{K}(\kappa)\boldsymbol{F} : \boldsymbol{S} - 1 = 0, \tag{3.4}$$

where $\mathbb{K}(\kappa)$ features the same symmetries as $\mathbb{F}$. In order for (3.1) to be real, the fourth order tensor $\mathbb{F}$ needs to be positive semidefinite, which may be expressed as:

$$\boldsymbol{S} : \mathbb{F}\boldsymbol{S} \geq 0, \quad \forall\boldsymbol{S} \in \mathcal{S} \tag{3.5}$$

$\mathbb{F}$ has major symmetry ($\mathbb{F}_{ijkl} = \mathbb{F}_{klij}$) and both minor symmetries ($\mathbb{F}_{ijkl} = \mathbb{F}_{jikl} = \mathbb{F}_{ijlk} = \mathbb{F}_{jilk}$), which allows to project the associated space defined on $(\mathcal{R}^3 \times \mathcal{R}^3) \times (\mathcal{R}^3 \times \mathcal{R}^3)$ onto a symmetric matrix space defined on $\mathcal{R}^6 \times \mathcal{R}^6$. This is a standard procedure in continuum mechanics [Mehrabadi and Cowin, 1990, Zysset and Curnier, 1995] and simplifies the mathematical discussion of the problem. In this case, positive semidefiniteness of the fourth order tensor $\mathbb{F}$ is given if the determinants of all principal minors of its projection onto the symmetric matrix space are positive. Positive semidefiniteness as defined in (3.5) requires that

$$1 - \boldsymbol{F} : \boldsymbol{S} \geq 0, \tag{3.6}$$

which defines a half hyperspace, in order for (3.1) to hold true. In order for (3.1) to describe a convex surface, its Hessian needs to be positive semidefinite, i.e.

$$\boldsymbol{S} : \nabla^2_{\boldsymbol{S}} Y \boldsymbol{S} \geq 0, \qquad \forall \boldsymbol{S} \in \mathcal{S} \tag{3.7}$$

with the Hessian

$$\nabla^2_{\boldsymbol{S}} Y = (\boldsymbol{S} : \mathbb{F}\boldsymbol{S})^{-\frac{1}{2}}\mathbb{F} - (\boldsymbol{S} : \mathbb{F}\boldsymbol{S})^{-\frac{3}{2}}\mathbb{F}\boldsymbol{S} \otimes \mathbb{F}\boldsymbol{S}. \tag{3.8}$$

Substituting (3.8) into (3.7) leads to the requirement

$$\sqrt{\boldsymbol{S} : \mathbb{F}\boldsymbol{S}} - \sqrt{\boldsymbol{S} : \mathbb{F}\boldsymbol{S}} \geq 0, \tag{3.9}$$

which is true for all $\boldsymbol{S}$ in $\mathcal{S}$ and any positive semidefinite $\mathbb{F}$. Therefore positive semidefiniteness of the fourth order tensor $\mathbb{F}$ as required in (3.5) is a necessary and sufficient requirement for the convexity of the criterion (3.1). If the requirements (3.5) and (3.6) are met, (3.1) is convex and may be squared without loss of information.

$$\boldsymbol{S} : \mathbb{F}\boldsymbol{S} - (\boldsymbol{F} : \boldsymbol{S})^2 + 2\boldsymbol{F} : \boldsymbol{S} - 1 = 0, \qquad (\boldsymbol{F} : \boldsymbol{S})^2 = \boldsymbol{S} : (\boldsymbol{F} \otimes \boldsymbol{F})\boldsymbol{S}. \tag{3.10}$$

The mathematical discussion of the criterion within the boundaries given by (3.5) and (3.6) is therefore equivalent to the discussion of the quadratic form

$$\boldsymbol{S} : (\mathbb{F} - \boldsymbol{F} \otimes \boldsymbol{F})\boldsymbol{S} + 2\boldsymbol{F} : \boldsymbol{S} - 1 = 0 \tag{3.11}$$

within the same boundaries. In order to find the midpoint of the criterion, the quadratic form (3.11) may be rewritten as proposed by Shih and Lee [Shih and Lee, 1978]:

$$(\boldsymbol{S} - \boldsymbol{A}) : \mathbb{A}(\boldsymbol{S} - \boldsymbol{A}) - 1 = 0 \tag{3.12}$$

with a fourth order tensor $\mathbb{A}$ describing the shape and orientation

$$\mathbb{A} = \frac{\mathbb{F} - \boldsymbol{F} \otimes \boldsymbol{F}}{1 + \boldsymbol{A} : (\mathbb{F} - \boldsymbol{F} \otimes \boldsymbol{F})\boldsymbol{A}} \tag{3.13}$$

and the second order tensor $\boldsymbol{A}$ describing the shift of the quadric with respect of the origin of $\mathcal{S}$,

$$\boldsymbol{A} = -(\mathbb{F} - \boldsymbol{F} \otimes \boldsymbol{F})^{-1}\boldsymbol{F}. \tag{3.14}$$

The shape of the criterion is determined by the nature of the eigenvalues of the fourth order tensor $\mathbb{F} - \boldsymbol{F} \otimes \boldsymbol{F}$. If all six eigenvalues are positive, the quadratic form (3.11) takes an hyperellipsoidal shape. When the eigenvalue whose eigentensor points in the main direction of the quadric vanishes it becomes a hyperparaboloid. If this eigenvalue becomes negative and the others stay positive, $\mathbb{F} - \boldsymbol{F} \otimes \boldsymbol{F}$ becomes negative definite and the shift $\boldsymbol{A}$ changes its sign. In this case, the quadratic form (3.11) describes an elliptical hyperboloid of two sheets with the extreme case of a double hypercone. The negative eigenvalue results from the ambiguity of the quadratic form (3.11) and does not lead to a loss of convexity of the criterion (3.1), as it is defined in the half hyperspace (3.6) only. The boundary hyperplane of (3.6) separates the hyperboloid of two sheets described by (3.11) into two halfspace-wise convex surfaces. The criterion (3.1) then takes a hyperboloidal or hyperconical shape. The transition from hyperellipsoidal to hyperboloidal shape is a hyperparaboloid and may be found by requiring

$$Det(\mathbb{F} - \boldsymbol{F} \otimes \boldsymbol{F}) = 0. \tag{3.15}$$

The multidimensional determinant of a fourth order tensor may be evaluated as shown in, e.g. Gelfand et al. [1994]. However, the calculations may be largely simplified by requiring the determinant of the projection of $\mathbb{F} - \boldsymbol{F} \otimes \boldsymbol{F}$ onto the symmetric matrix space defined on $\mathcal{R}^6 \times \mathcal{R}^6$ to vanish. The hypercone is a limit case of the possible convex shapes of the criterion that is found when requiring

$$Det(\mathbb{F}) = 0. \tag{3.16}$$

Several special cases of material symmetry ranging from isotropy to orthotropy will be discussed in the following subsections.

3.3.1 Isotropy

In the case of isotropy, the tensors $\mathbb{F}$ and $\boldsymbol{F}$ defining (3.1) are given by

$$\mathbb{F} = -\zeta_0 F_0^2(\boldsymbol{I} \otimes \boldsymbol{I}) + (\zeta_0 + 1)F_0^2(\boldsymbol{I}\underline{\overline{\otimes}}\boldsymbol{I}) \tag{3.17}$$

and

$$\boldsymbol{F} = f_0 \boldsymbol{I}. \tag{3.18}$$

For a uniaxial test to failure in tension, the yield criterion reads:

$$F_0 \sigma_0^{+} + f_0 \sigma_0^{+} - 1 = 0 \tag{3.19}$$

For a uniaxial test in compression, the criterion yields

$$F_0 \sigma_0^{-} - f_0 \sigma_0^{-} - 1 = 0 \tag{3.20}$$

By combining these equations, we find

$$F_0 = \frac{\sigma_0^{+} + \sigma_0^{-}}{2\sigma_0^{+}\sigma_0^{-}} \tag{3.21}$$

and

$$f_0 = \frac{1}{2}\Big(\frac{1}{\sigma_0^{+}} - \frac{1}{\sigma_0^{-}}\Big) \tag{3.22}$$

The criterion has three independent parameters: σ_0^{+}, σ_0^{-} and ζ_0. The shear strength is given by

$$\tau_0 = \sqrt{\frac{2}{1+\zeta_0}\frac{\sigma_0^{+}\sigma_0^{-}}{\sigma_0^{-} + \sigma_0^{+}}} \tag{3.23}$$

For isotropic material symmetry, the stress space may be decomposed into two independent parts, shear and normal stress space. The second order tensor $\boldsymbol{F}$ is proportional to identity. The tensor $\mathbb{F}$ may be decomposed in a hydrostatic and a deviatoric part by spectral decomposition, which means that one of its eigentensors is pointing in the direction of the hydrostatic axis. Therefore, the rank-1 correction $\mathbb{F} - \boldsymbol{F} \otimes \boldsymbol{F}$ corresponds to a translation in the direction of the dyad $\boldsymbol{I} \otimes \boldsymbol{I}$ together with an isotropic dilatation and does not lead to a rotation of the eigensystem irrespective of the parameters governing $\mathbb{F}$ and $\boldsymbol{F}$. The shape of the surface in the direction of the hydrostatic axis is determined by the interaction parameter ζ_0. This may be seen in Fig. 3.3.1. Convexity of the quadric surface requires (3.5) and (3.6) to be fulfilled, which leads to the following conditions:

$$\sigma_0^{\pm} \geq 0, \qquad \tau_0 \geq 0, \qquad -1 \leq \zeta_0 \leq 0.5. \tag{3.24}$$

After finding the convexity criterion, it is interesting to examine the criterion in normal stress space in the extreme cases $\zeta_0 = 0.5$ and $\zeta_0 = -1$. Firstly, the solutions of the criterion on the trisectrix are determined by solving equation (3.11) for isotropic material symmetry and a hydrostatic stress state $\boldsymbol{S}_{hydro}$. This yields the following result:

$$\boldsymbol{S}^{\pm}_{hydro} = \frac{\sigma_0^-(3\sigma_0^-\sigma_0^+ - 3(\sigma_0^-)^2 \pm \sqrt{(\sigma_0^+)^2(\sigma_0^- + \sigma_0^+)^2(12 - 24\zeta_0)})}{(\sigma_0^- + \sigma_0^+)^2(3 + 3\zeta_0) - 18\sigma_0^+\sigma_0^-}\boldsymbol{I} \tag{3.25}$$

In the case $\zeta_0 = 0.5$ the square root in the enumerator of (3.25) vanishes, i.e. the two solutions of equation (3.25) degenerate to one. This means that the quadric yield surface takes a conical shape in this case as shown in Fig. 3.3.1. If $\zeta_0 > 0.5$, no real solution exists on the hydrostatic axis, confirming the requirements for convexity of the yield surface stated in (3.24). For $\zeta_0 = -1$, the criterion (3.1) degenerates to

$$|F_0 tr\boldsymbol{S}| - f_0 tr\boldsymbol{S} - 1 = 0 \tag{3.26}$$

which describes two parallel planes defined by the uniaxial yield points in tension and compression, respectively (see Fig. 3.3.1).

In between those extreme values, the criterion takes an elliptical, paraboloidal or hyperboloidal shape. When $\zeta_0 < 0.5$, more than one solutions exist. For $\zeta = \zeta_{0,crit}$, the criterion takes the shape of a spheroidal paraboloid. For $\zeta_{0,crit} < \zeta_0 < 0.5$, it becomes one sheet of a hyperboloid because of (3.6). A prolate spheroid in normalized stress space is obtained for $0 \leq \zeta_0 < \zeta_{0,crit}$. For $-1 < \zeta_0 < 0$, the criterion has the shape of an oblate spheroid. The variety of possible shapes in normal stress space are shown in Fig. 3.3.1.

In order to find the critical value $\zeta_{0,crit}$ at which the yield surface changes its form from ellipsoidal to hyperboloidal, equation (3.15) is considered in the case of isotropy. Solving $Det(\mathbb{F} - \boldsymbol{F} \otimes \boldsymbol{F})|_{\zeta_0 = \zeta_{0,crit}} = 0$ for $\zeta_{0,crit}$ provides the sought value of $\zeta_{0,crit}$:

$$\zeta_{0,crit} = \frac{-(\sigma_0^-)^2 + 4\sigma_0^-\sigma_0^+ - (\sigma_0^+)^2}{(\sigma_0^+ + \sigma_0^-)^2}. \tag{3.27}$$

In shear stress space, the isotropic criterion has the shape of a sphere with radius τ_0 (Fig. 3.3.1).

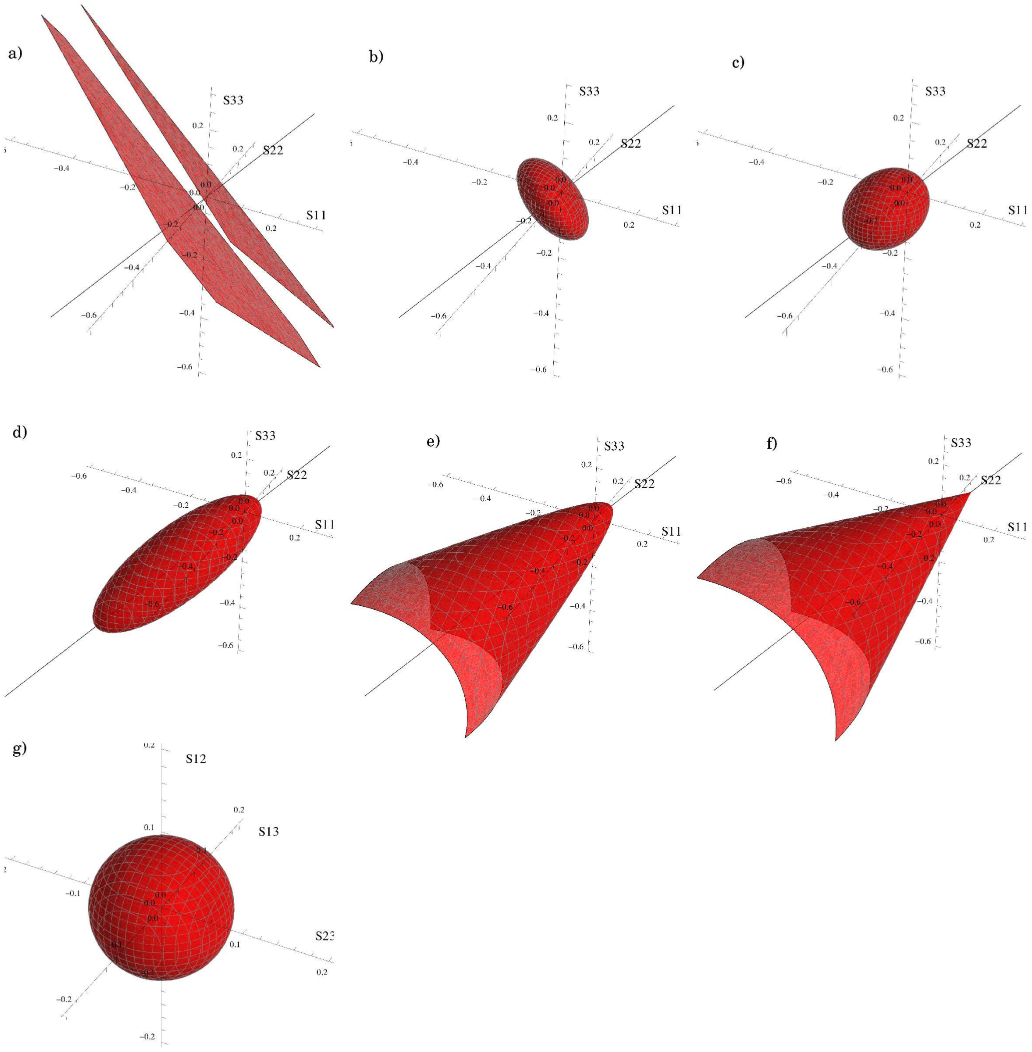

Fig. 3.3.1: Shape of the isotropic quadric yield surface in normal stress space for a) $\zeta_0 = -1$, b) $\zeta_0 = -0.5$, c) $\zeta_0 = 0.0$, d) $0 < \zeta_0 < \zeta_{0,crit}$, e) $\zeta_{0,crit} < \zeta_0 < 0.5$, and f) $\zeta_0 = 0.5$ as well as g) in shear stress space.

3.3.2 Cubic symmetry

In the case of cubic symmetry, the tensors $\mathbb{F}$ and $\boldsymbol{F}$ defining (3.1) are given by

$$\mathbb{F} = \sum_{i=1}^{3} F_0^2 \boldsymbol{M}_i \otimes \boldsymbol{M}_i - \sum_{i,j=1;i\neq j}^{3} \zeta_0 F_0^2 \boldsymbol{M}_i \otimes \boldsymbol{M}_j + \sum_{i,j=1;i\neq j}^{3} \frac{F_{ij}^2}{2} \boldsymbol{M}_i \overline{\underline{\otimes}} \boldsymbol{M}_j \tag{3.28}$$

and

$$\boldsymbol{F} = \sum_{i=1}^{3} f_0 \boldsymbol{M}_i \tag{3.29}$$

with

$$\boldsymbol{M}_i = \boldsymbol{m}_i \otimes \boldsymbol{m}_i \tag{3.30}$$

defining the main axes of the cubic symmetry. In analogy to the isotropic case, we find:

$$F_0 = \frac{\sigma_0^+ + \sigma_0^-}{2\sigma_0^+ \sigma_0^-} \tag{3.31}$$

and

$$f_0 = \frac{1}{2}\Big(\frac{1}{\sigma_0^+} - \frac{1}{\sigma_0^-}\Big). \tag{3.32}$$

When a shear test is performed to failure with shear stresses acting on plane i in direction j, the yield criterion in the case of cubic symmetry reads:

$$F_{ij}\tau_0 - 1 = 0. \tag{3.33}$$

Therefore we get

$$F_{ij} = \frac{1}{\tau_0}. \tag{3.34}$$

The criterion has four independent parameters: σ_0^+, σ_0^- and ζ_0 and τ_0. The mathematical discussion of the criterion with cubic symmetry with respect to convexity and shape of the criterion yields the same results as in the isotropic case and will not be repeated at this point.

3.3.3 Fabric-based orthotropy

When modeling a material with an internal microstructure, it is of high importance to account for its morphology. Trabecular bone may be characterized by bone volume fraction ρ and a fabric tensor $\boldsymbol{M}$ [Matsuura et al., 2008, Rincón-Kohli and Zysset, 2009, Zysset and Rincón, 2006] emerging from an approximation of its orientation distribution function by spherical harmonics [Kanatani, 1984] or by an ellipsoid [Harrigan and Mann, 1984]. In the particular case of the Zysset-Curnier model [Zysset and Curnier, 1995], the influence of these two factors on its homogenized mechanical properties is governed by two exponents p and q that need to be determined experimentally [Matsuura et al., 2008, Rincón-Kohli and Zysset, 2009, Wolfram et al., 2012, Zysset and Rincón, 2006]. The number of independent material parameters for the fabric-based orthotropy is 5 in the case of an isotropic base material (σ_0^+, σ_0^-, χ_0, p and q) or 6 in the case of cubic symmetry (σ_0^+, σ_0^-, χ_0, τ_0, p and q). Inhomogeneity and anisotropy of material properties may in this case be interpreted as a stretch of the original stress space with eigenvalues m_i and eigenvectors $\boldsymbol{m_i}$ [Wolfram et al., 2012]. The stress tensor can therefore be normalised with respect to fabric and density by an inversion of the stretch operation:

$$\hat{\boldsymbol{S}} = \frac{\boldsymbol{M}^{-q}\boldsymbol{S}\boldsymbol{M}^{-q}}{\rho^p} \tag{3.35}$$

with

$$\boldsymbol{M} = \sum_{i=1}^{3} m_i(\boldsymbol{m}_i \otimes \boldsymbol{m}_i). \tag{3.36}$$

The $\boldsymbol{m}_i$ are the vectors describing the material orientation. $\boldsymbol{M}^q$ is determined analogously to (3.36) with the same eigenvectors $\boldsymbol{m_i}$ and the eigenvalues m_i^q. $\boldsymbol{M}$ is symmetric ($\boldsymbol{M} = \boldsymbol{M}^T$) and normalized so that

$$tr\boldsymbol{M} = 3. \tag{3.37}$$

The criterion may then be rewritten in normalized stress space featuring at least cubic symmetry:

$$Y(\hat{\boldsymbol{S}}) := \sqrt{\hat{\boldsymbol{S}} : \hat{\mathbb{F}}\hat{\boldsymbol{S}}} + \hat{\boldsymbol{F}} : \hat{\boldsymbol{S}} - 1 = 0. \tag{3.38}$$

The tensors $\hat{\mathbb{F}}$ and $\hat{\boldsymbol{F}}$ are given by

$$\hat{\mathbb{F}} = \sum_{i=1}^{3} F_0^2 \boldsymbol{M}_i \otimes \boldsymbol{M}_i - \sum_{i,j=1;i\neq j}^{3} \zeta_0 F_0^2 \boldsymbol{M}_i \otimes \boldsymbol{M}_j + \sum_{i,j=1;i\neq j}^{3} \frac{1}{2\tau_0^2} \boldsymbol{M}_i \underline{\overline{\otimes}} \boldsymbol{M}_j \tag{3.39}$$

and

$$\hat{\boldsymbol{F}} = \sum_{i=1}^{3} f_0 \boldsymbol{M}_i \tag{3.40}$$

The tensors $\mathbb{F}$ and $\boldsymbol{F}$ defining the criterion (3.1) in original stress space are obtained by:

$$\mathbb{F} = \rho^{2p}(\boldsymbol{M}^q \underline{\otimes} \boldsymbol{M}^q)\hat{\mathbb{F}}(\boldsymbol{M}^q \underline{\otimes} \boldsymbol{M}^q) \tag{3.41}$$

$$\boldsymbol{F} = \rho^{p}(\boldsymbol{M}^q \underline{\otimes} \boldsymbol{M}^q)\hat{\boldsymbol{F}} = \rho^p \boldsymbol{M}^q \hat{\boldsymbol{F}} \boldsymbol{M}^q. \tag{3.42}$$

Since the fabric tensor $\boldsymbol{M}$ is strictly positive definite, the discussion of the orthotropic fabric-based criterion in stress space is equivalent to the discussion of the cubic criterion in fabric-normalized stress space. The discussion with respect to convexity and shape of the criterion is then analogous to the isotropic case and is not repeated in detail here.

In the following paragraphs, some important aspects of the fabric-based orthotropic criterion in stress space will be discussed. In the case of orthotropic material symmetry, stress space may be divided into a normal and a shear stress space. The uniaxial strengths in the main material directions are given by

$$\sigma_{ii}^{+} = \sigma_0^{+}\rho^p m_i^{2q}, \qquad \sigma_{ii}^{-} = \sigma_0^{-}\rho^p m_i^{2q}, \tag{3.43}$$

the interaction parameters of $\mathbb{F}$ and the shear strengths by

$$\zeta_{ij} = \zeta_0 \frac{m_i^{2q}}{m_j^{2q}}, \qquad \tau_{ij} = \tau_0 \rho^p m_i^q m_j^q. \tag{3.44}$$

The solutions of the criterion in stress space collinear to $\boldsymbol{M}^{2q}$, $\boldsymbol{S}_{ma}^{\pm}$, may be obtained by backtransformation of the hydrostatic solutions in normalized stress space $\hat{\boldsymbol{S}}_{hydro}$, which are equivalent to the solutions presented in (3.25):

$$\boldsymbol{S}_{ma}^{\pm} = \rho^p \boldsymbol{M}^q \hat{\boldsymbol{S}}_{hydro}^{\pm} \boldsymbol{M}^q \tag{3.45}$$

a) For $\zeta_0 = 0.5$, The two solutions $\boldsymbol{S}_{ma}^{\pm}$ and $\boldsymbol{A}$ degenerate to one solution, the apex of the generalized cone. The coordinates of the apex may be obtained by:

$$\boldsymbol{S}_{apex} = \rho^p \boldsymbol{M}^q \hat{\boldsymbol{S}}_{hydro}|_{\zeta_0=0.5} \boldsymbol{M}^q. \tag{3.46}$$

It lies on the plane $\boldsymbol{F} : \boldsymbol{S} = 1$ and therefore, according to requirement (3.6), the anisotropic generalized cone is a limiting case of the possible convex shapes of the yield function.

The only eigentensor of the dyad $\boldsymbol{F} \otimes \boldsymbol{F}$ is always collinear to $\boldsymbol{M}^{2q}$ irrespective of the value of ζ_0 as seen in (3.40) and (3.42). The eigensystem of $\mathbb{F}$, however, changes. For $\zeta_0 = 0.5$, one eigenvalue of $\mathbb{F}$ vanishes and the corresponding eigentensor is aligned with $\boldsymbol{M}^{2q}$. Therefore, $\boldsymbol{M}^{2q}$ is also an eigentensor of $\mathbb{F} - \boldsymbol{F} \otimes \boldsymbol{F}$ and determines the orientation of the hypercone in stress space.

b) In the case of $\zeta_0 = -1$, two eigenvalues of $\mathbb{F}$ with eigentensors in normal stress space vanish and $\boldsymbol{M}^{2q}$ is an eigentensor of $\mathbb{F}$ with a positive eigenvalue. The criterion therefore degenerates to two parallel hyperplanes with the hypersurface normal $\boldsymbol{M}^{2q}$ (see Fig. 3.3.3).

c) For $\zeta_0 = 0$, however, the eigensystem of $\mathbb{F}$ is aligned with the material axes themselves. Therefore, the main orientation of the quadric surface rotates from $\boldsymbol{M}^{2q}$ at $\zeta_0 = 0.5$ to a perpendicular direction for $\zeta_0 = -1$. For $-1 < \zeta_0 < 0.5$, the orientation is changing continuously with the parameter ζ_0.

The mid point of the equivalent quadratic form (3.11) may be determined using equation (3.14). If $\zeta_{0,crit} < \zeta_0 < 0.5$, $\boldsymbol{A}$ lies outside of the convex surface, as the quadratic form (3.11) of the criterion from which the midpoint $\boldsymbol{A}$ is derived describes a hyperboloid of two sheets in this case.

The change of the shape, midpoint and main orientation of the criterion as a function of the parameter ζ_0 in the case of fabric-based orthotropy is illustrated in Fig. 3.3.3. The main orientation of the criterion is the eigentensor of $\mathbb{F} - \boldsymbol{F} \otimes \boldsymbol{F}$ with the largest eigenvalue.

3.3.4 General orthotropy

In the case of general orthotropy, the fourth order tensor $\mathbb{F}$ is given by:

$$\mathbb{F} = \sum_{i=1}^{3} F_{ii}^2 \boldsymbol{M}_i \otimes \boldsymbol{M}_i - \sum_{i,j=1;i\neq j}^{3} \zeta_{ij} F_{ii}^2 \boldsymbol{M}_i \otimes \boldsymbol{M}_j + \sum_{i,j=1;i\neq j}^{3} \frac{F_{ij}^2}{2} \boldsymbol{M}_i \underline{\overline{\otimes}} \boldsymbol{M}_j \tag{3.47}$$

The general form of the second order tensor $\boldsymbol{F}$ is in this case:

$$\boldsymbol{F} = \sum_{i=1}^{3} f_i \boldsymbol{M}_i \tag{3.48}$$

For a uniaxial test to failure in tension in the direction i, the yield criterion reads:

$$F_{ii}\sigma_{ii}^{+} + f_i\sigma_{ii}^{+} - 1 = 0, \qquad i = 1, 2, 3 \tag{3.49}$$

For a uniaxial test in compression, the criterion yields

$$F_{ii}\sigma_{ii}^{-} - f_i\sigma_{ii}^{-} - 1 = 0, \qquad i = 1, 2, 3. \tag{3.50}$$

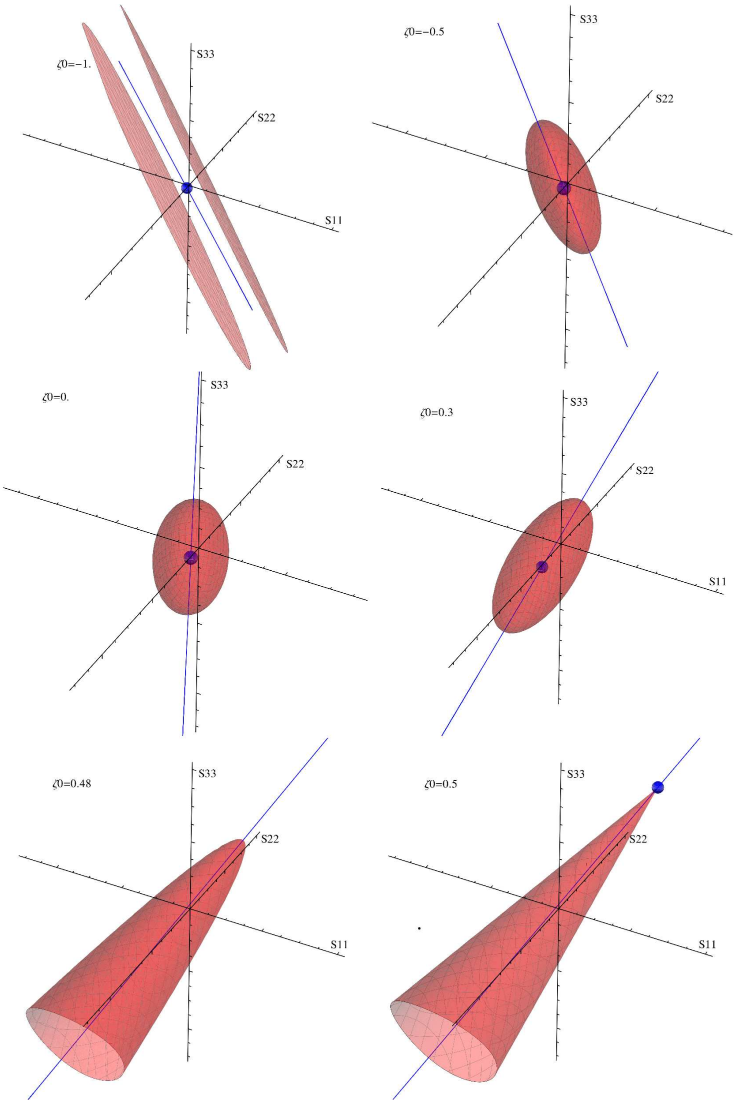

Fig. 3.3.3: Midpoint, orientation and shape of the fabric-based orthotropic quadric yield surface in normal stress space for a) $\zeta_0 = -1$, b) $\zeta_0 = -0.5$, c) $\zeta_0 = 0.0$, d) $0 < \zeta_0 < \zeta_{0,crit}$, e) $\zeta_{0,crit} < \zeta_0 < 0.5$, and f) $\zeta_0 = 0.5$.

By combining equations (3.49) and (3.50), we find that

$$F_{ii} = \frac{\sigma_{ii}^{+} + \sigma_{ii}^{-}}{2\sigma_{ii}^{+}\sigma_{ii}^{-}} \tag{3.51}$$

and

$$f_i = \frac{1}{2}\Big(\frac{1}{\sigma_{ii}^{+}} - \frac{1}{\sigma_{ii}^{-}}\Big). \tag{3.52}$$

When a shear test is performed to failure with shear stresses acting on plane i in direction j, the yield criterion reads:

$$F_{ij}\tau_{ij} - 1 = 0 \tag{3.53}$$

Therefore we get

$$F_{ij} = \frac{1}{\tau_{ij}}. \tag{3.54}$$

Twelve orthotropic constants are needed to define the criterion: the uniaxial yield stresses σ_{11}^{+}, σ_{11}^{-}, σ_{22}^{+}, σ_{22}^{-}, σ_{33}^{+} and σ_{33}^{-}, the shear yield stesses τ_{12}, τ_{23} and τ_{13} as well as interaction coefficients ζ_{12}, ζ_{23} and ζ_{13}. For a homogeneous material, the criterion may be identified by a set of 6 uniaxial tests in the 3 main material directions in tension and compression providing the uniaxial yield stresses σ_{ii}^{-} and σ_{ii}^{+}. Three additional shear tests in 23, 13 and 12 provide the shear yield strains τ_{ij}. The interaction parameters may be determined by independent biaxial tests in the 12, 13 and 23 planes as discussed by Tsai and Wu [Tsai and Wu, 1971] or triaxial tests as done, e.g., *in silico* by Wolfram et al. [Wolfram et al., 2012]. The requirements for convexity of the quadric are obtained from (3.5):

$$\sigma_{ii}^{\pm} \geq 0, \qquad \tau_{ij} \geq 0, \qquad |\zeta_{ij}| \leq \Big|\frac{F_{jj}}{F_{ii}}\Big| \tag{3.55}$$

as well as

$$F_{22}^2F_{33}^2 - F_{11}^2F_{33}^2\zeta_{12}^2 - F_{11}^2F_{22}^2\zeta_{13}^2 + 2F_{11}^2F_{22}^2\zeta_{12}\zeta_{13}\zeta_{23} - F_{22}^4\zeta_{23}^2 \geq 0. \tag{3.56}$$

The transition from ellipsoidal to paraboloidal shape in normal stress space is taking place at any triplets $\{\zeta_{12}, \zeta_{13}, \zeta_{23}\}$ satisfying (3.15). In general, there is no analytical form for the roots of a cubic equation. However, a solution may be found numerically.

3.4 Degeneration to classical yield criteria

In the subsequent sections, the generality of the formulation is demonstrated by showing its degeneration to several classical yield envelopes under appropriate conditions like the von Mises [von Mises, 1913], Drucker-Prager [Prager and Drucker, 1952], Tsai-Wu [Tsai and

Wu, 1971], Liu [Liu et al., 1997], generalized Hill [Zysset and Rincón, 2006] and classical Hill [Hill, 1951] criteria.

3.4.1 Isotropic Drucker-Prager criterion

When setting $\zeta_0 = 0.5$ in the isotropic case, the criterion (3.1) degenerates to

$$F_0\sqrt{\frac{3}{2}\boldsymbol{S} : \mathbb{I}^d\boldsymbol{S}} + f_0 tr\boldsymbol{S} - 1 = 0 \tag{3.57}$$

with the deviatoric tensor

$$\mathbb{I}^d = \boldsymbol{I}\underline{\overline{\otimes}}\boldsymbol{I} - \frac{1}{3}\boldsymbol{I}\otimes\boldsymbol{I}, \tag{3.58}$$

which descibes a cone oriented in the direction of the hydrostatic axis and is identical to the criterion first proposed by Drucker and Prager [Prager and Drucker, 1952]. In this case, the cohesion h would be given by $h = \frac{1}{F_0}$ and the friction coefficient T by $T = \frac{3f_0}{F_0}$.

3.4.2 Isotropic von Mises criterion

When setting $\zeta_0 = 0.5$ and considering yield stresses that are symmetric around the origin ($\sigma_0^+ = \sigma_0^- = \sigma_0$) in the isotropic case, then $f_0 = 0$ and the second order tensor $\boldsymbol{F}$ vanishes. In this case, the criterion (3.1) degenerates to

$$\frac{1}{\sigma_0}\sqrt{\frac{3}{2}\boldsymbol{S} : \mathbb{I}^d\boldsymbol{S}} - 1 = 0, \tag{3.59}$$

which is the classical von Mises yield criterion [von Mises, 1913].

3.4.3 Orthotropic Tsai-Wu criterion

When considering the equivalent quadratic form (3.11), there is an obvious similarity to the polynomial Tsai-Wu criterion [Cowin, 1986, Tsai and Wu, 1971, Wolfram et al., 2012], which has the form

$$Y^{TW}(\boldsymbol{S}) := \boldsymbol{S} : \mathbb{P}\boldsymbol{S} + \boldsymbol{P}\boldsymbol{S} - 1 = 0 \tag{3.60}$$

with

$$\mathbb{P} = \sum_{i=1}^{3}\frac{1}{\sigma_{ii}^-\sigma_{ii}^+}\boldsymbol{M}_i\otimes\boldsymbol{M}_i - \sum_{i,j=1;i\neq j}^{3}\frac{\chi_{ij}}{\sigma_{ii}^-\sigma_{ii}^+}\boldsymbol{M}_i\otimes\boldsymbol{M}_j + \sum_{i,j=1;i\neq j}^{3}\frac{1}{2\tau_{ij}^2}\boldsymbol{M}_i\underline{\overline{\otimes}}\boldsymbol{M}_j \tag{3.61}$$

and

$$\boldsymbol{P} = \sum_{i=1}^{3} \Big(\frac{1}{\sigma_{ii}^{+}} - \frac{1}{\sigma_{ii}^{-}}\Big) \boldsymbol{M}_i. \tag{3.62}$$

Comparison of the two criteria shows that a straightforward transformation exists from the Tsai-Wu to the quadric criterion. For known tensors $\mathbb{P}$ and $\boldsymbol{P}$, the tensors $\mathbb{F}$ and $\boldsymbol{F}$ defining the quadric surface are given by:

$$\boldsymbol{F} = \frac{\boldsymbol{P}}{2} \tag{3.63}$$

$$\mathbb{F} = \mathbb{P} + \frac{\boldsymbol{P} \otimes \boldsymbol{P}}{4} \tag{3.64}$$

The 6 uniaxial and 3 shear yield stresses are not altered by this transformation. Elementwise comparison of the tensors $\mathbb{P}$ and $(\mathbb{F} - \boldsymbol{F} \otimes \boldsymbol{F})$ shows that the interaction parameters ζ_{ij} of the quadric criterion may be determined from the known χ_{ij} of the Tsai-Wu criterion by:

$$\zeta_{ij} = \frac{1}{F_{ii}^2} \Big(\frac{\chi_{ij}}{\sigma_{ii}^{+} \sigma_{ii}^{-}} - f_i f_j \Big) \tag{3.65}$$

3.4.4 Orthotropic Liu criterion

If the interaction coefficients ζ_{ij} are determined by a specific coupling:

$$\zeta_{ij} = \frac{1}{2F_{ii}^2}(F_{ii}^2 + F_{jj}^2 - F_{kk}^2) \quad \forall\, i,j,k \in \mathcal{N},\ \ i,j,k \leq 3,\ \ i \neq j \neq k, \tag{3.66}$$

where no summation should be performed on repeated indices, Liu's criterion [Liu et al., 1997] is obtained, which is a generalization of the Drucker-Prager criterion to plastically orthotropic materials, i.e. a generalized cone in normal stress space aligned with the hydrostatic axis.

3.4.5 Orthotropic Hill criterion

If the yield stresses are symmetric around the origin ($\sigma_i^{+} = \sigma_i^{-}$), the second order tensor $\boldsymbol{F}$ vanishes and (3.1) degenerates to

$$\sqrt{\boldsymbol{S} : \mathbb{F}\boldsymbol{S}} - 1 = 0, \tag{3.67}$$

which is a generalized Hill criterion as described by e.g. Zysset and Rincon [Zysset and Rincón, 2006]. After transformation of the interaction coefficients ζ_{ij} according to (3.66), equation (3.67) describes the classical Hill criterion for plastically orthotropic materials [Hill, 1951], which is a generalized cylinder in normal stress space aligned with the hydrostatic axis.

3.5 Application to a micromechanical yield criterion for porous solids

In the following section, the applicability of the yield criterion (3.1) to micromechanical analyses will be demonstrated by identifying a quadric criterion based of an existing micromechanics-based formulation. Maghous et al. [Maghous et al., 2009] proposed a micromechanical yield criterion for isotropic porous cohesive-frictional solids based on nonlinear homogenization techniques. The matrix material is governed by a Drucker-Prager yield surface with cohesion h and friction coefficient T, ϕ denotes the pore volume fraction. This criterion is to some extend applicable to bone, which may be described at the microscale as a cohesive-frictional material [Tai et al., 2006] interacting with nanoporosity. It has the form [Maghous et al., 2009]:

$$Y_p(\boldsymbol{S}, \phi) = \frac{1 + \frac{2}{3}\phi}{T^2}\Sigma_d^2 + (\frac{3\phi}{2T^2} - 1)\Sigma_m^2 + 2(1-\phi)h\Sigma_m - (1-\phi)^2 h^2 = 0, \tag{3.68}$$

with

$$\Sigma_m = \frac{tr\boldsymbol{S}}{3}, \qquad \Sigma_d = \sqrt{(\boldsymbol{S} - \Sigma_m \boldsymbol{I}) : (\boldsymbol{S} - \Sigma_m \boldsymbol{I})}, \tag{3.69}$$

and predicts an elliptical criterion above a critical porosity $\phi_{crit} = \frac{4T^2}{3}$. Below the critical porosity, the criterion descibes a hyperboloid or a double cone and is nonconvex. It may be rewritten in the following form:

$$\boldsymbol{S} : \Big(\frac{1 + \frac{2}{3}\phi}{(1-\phi)^2 h^2 T^2}\mathbb{I}^d + \frac{\frac{3\phi}{2T^2} - 1}{9(1-\phi)^2 h^2}\boldsymbol{I} \otimes \boldsymbol{I}\Big)\boldsymbol{S} + \frac{2}{3(1-\phi)h}\boldsymbol{I} : \boldsymbol{S} - 1 = 0. \tag{3.70}$$

This is a quadratic polynomial in $\boldsymbol{S}$ and therefore the isotropic tensors $\mathbb{F}_p$ and $\boldsymbol{F}_p$ defining

(3.1) may be determined by comparison to the quadratic form (3.11). They are:

$$\mathbb{F}_p = \frac{1+\frac{2}{3}\phi}{(1-\phi)^2 h^2 T^2}(\boldsymbol{I}\underline{\overline{\otimes}}\boldsymbol{I}) - \frac{\frac{1}{3}+\frac{1}{18}\phi}{(1-\phi)^2 h^2 T^2}(\boldsymbol{I}\otimes\boldsymbol{I}) \tag{3.71}$$

and

$$\boldsymbol{F}_p = \frac{1}{3(1-\phi)h}\boldsymbol{I}. \tag{3.72}$$

The criterion rewritten in the form of (3.1) then predicts the same elliptical criteria for overcritical porosities and a conical one for the solid matrix. However, it predicts convex (half) hyperboloidal criteria for undercritical porosities, which extends the validity of the existing micromechanical formulation as presented by Maghous et al. [Maghous et al., 2009] as a yield criterion to undercritical states of pore volume fraction. Thus, a smooth transition is found from a conical criterion for the solid matrix to elliptical criteria for $\phi > \phi_{crit}$ through convex (half) hyperboloids. This is illustrated in Fig. 3.5.

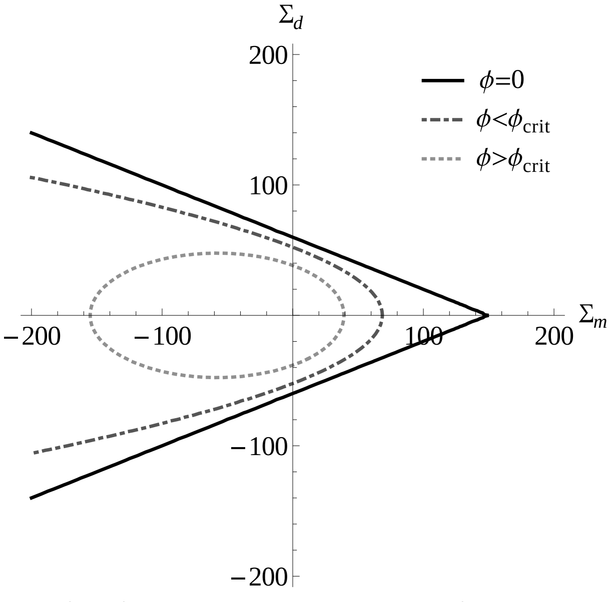

Fig. 3.5: Quadric yield surface for isotropic porous cohesive-frictional materials [Maghous et al., 2009] for friction coefficient $T = 0.4$ and cohesion $h = 150$ MPa as a function of pore volume fraction ϕ in the Σ_d-Σ_m plane showing a smooth transition from conical to elliptical surfaces.

3.6 Identification of yield criteria for bone

In the following section, the advantage in using a very general formulation like the one proposed in this work when describing a hierarchical material like bone will be demonstrated by describing the varying yield envelopes of bone at several length scales. Elliptical criteria describing the yield envelope of homogenized trabecular bone at the macroscale from experimental data and numerical homogenization techniques as well as a conical criterion for lamellar bone at the microscale will be identified.

3.6.1 Trabecular bone

A fabric- and density-based orthotropic quadric yield and strength criterion for trabecular bone was fitted to the multiaxial experimental data obtained by Rincon et al. [Rincón-Kohli and Zysset, 2009]. In this study, a multi-axial loading chamber was used to determine the compressive multi-axial yield and strength properties of cancellous bone from several anatomical locations. Cylindrical cancellous bone samples were disected from fresh frozen bones of 12 donors (5male , 7 female) with a mean age of 73.5 years (30 – 89 years). Their morphology was assessed by means of µCT scans. Then, different mechanical tests were performed such as torsion, uni-axial traction, uni-axial compression and multi-axial compression. A total of 128 bone samples were tested to failure. The yield point was determined according to the 0.2 % offset criterion, strength was defined as ultimate force before failure divided by mean area. A fabric- and density based quadric criterion was then fitted to the experimental data by means of the optimization routine Nminimize (Mathematica, Wolfram Research Inc.). The resulting constants for trabecular bone as well as the number of observations (N), standard error of the estimate (SEE) and R^2 are shown in Tables 6.1 and 6.2 for the yield and strength criteria, respectively.

Table 3.1: Tensile yield stress σ_0^+, compressive yield stress σ_0^-, interaction parameter ζ_0, shear yield stress τ_0, exponents p and q as well as number of load cases N, standard error of the estimate SEE and R^2 of a yield criterion for trabecular bone in MPa obtained from experimental data [Rincón-Kohli and Zysset, 2009].

σ_0^+	σ_0^-	ζ_0	τ_0	p	q	N	SEE	R^2
32.7	47.8	0.220	11.1	1.28	0.503	110	0.26	0.94

The quadric strength criterion is illustrated in normalized stress space in Fig. 3.6.1.

It is worth noting that even though the yield and strength criteria have a similar shape in both the normal and the shear stress space, the strength criterion is not an isotropic

Table 3.2: Tensile strength σ_0^{u+}, compressive strength σ_0^{u-}, interaction parameter ζ_0^u, shear strength τ_0^u, exponents p^u and q^u as well as number of load cases N, standard error of the estimate SEE and R^2 of a strength criterion for trabecular bone in MPa obtained from experimental data [Rincón-Kohli and Zysset, 2009].

σ_0^{u+}	σ_0^{u-}	ζ_0^u	τ_0^u	p^u	q^u	N	SEE	R^2
39.7	53.2	0.226	22.9	1.29	0.593	95	0.259	0.933

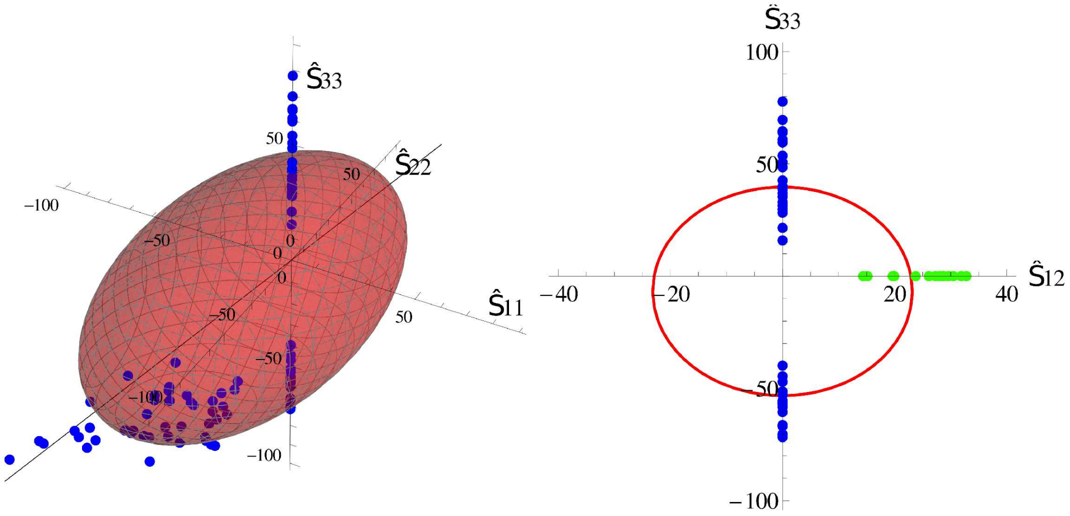

Fig. 3.6.1: Quadric strength surface for trabecular bone and experimental data [Rincón-Kohli and Zysset, 2009] in a) normalized normal stress space and b) the $\hat{S}_{33}$-$\hat{S}_{12}$ plane.

expansion of the yield criterion as defined in eq. (3.3). It may, however, be described by an expansion of the yield criterion with distinct hardening ratios $r_n = 1.1$ in normal and $r_s = 2.1$ in shear stress space. This might be accomplished by using the yield data presented in Tab. 6.1 in a criterion with a tensorial hardening rule as introduced in eq. (3.4) with a tensor function $\mathbb{K}(\kappa)$ of the form

$$\mathbb{K}(\kappa) = \sum_{i=1}^{3} \frac{\boldsymbol{M}_i \otimes \boldsymbol{M}_i}{1 + (r_n - 1) f_n(\kappa)} + \sum_{i,j=1;i\neq j}^{3} \frac{\boldsymbol{M}_i \underline{\overline{\otimes}} \boldsymbol{M}_j}{1 + (r_s - 1) f_s(\kappa)}, \tag{3.73}$$

where $f_n(\kappa)$ and $f_s(\kappa)$ are appropriate scalar hardening evolution functions bounded by $0 \leq f_n(\kappa), f_s(\kappa) \leq 1$ and the $\boldsymbol{M}_i$ are defined by (3.30). This would allow to describe both the experimental yield and strength data by one criterion.

Alternatively, a fabric- and density-based orthotropic yield criterion for trabecular bone was obtained by conversion of the Tsai-Wu criterion proposed by Wolfram et al [Wolfram et al., 2012]. In this particular study, nonlinear µFE models with cancellous bone cubes of 5.62mm edge length were generated from µCT scans. Kinematic boundary conditions were imposed testing the specimen in force control in 17 different load cases (six uniaxial, three shear and eight multiaxial) beyond yield. The yield point was determined according to the 0.2% offset rule. The study included 16 fresh frozen vertebrae (T6 to L2) from 10 donors (7 male, 3 female) with a median age of 51 y (37 – 84 y). The fabric- and density based Tsai-Wu criterion was fitted to the resulting yield data using the optimization routine Nminimize (Mathematica, Wolfram Research Inc.). The interaction parameters were then transformed using eq. (3.65). The resulting constants of the quadric yield criterion for trabecular bone as well as N, SEE and R^2 are given in Table 3.3.

Table 3.3: Tensile yield stress σ_0^+, compressive yield stress σ_0^-, interaction parameter ζ_0, shear yield stress τ_0, exponents p and q as well as number of load cases N, standard error of the estimate SEE and R^2 of a yield criterion for trabecular bone in MPa obtained by numerical homogenization techniques [Wolfram et al., 2012].

σ_0^+	σ_0^-	ζ_0	τ_0	p	q	N	SEE	R^2
74.589	111.724	0.2182	47.3314	1.686	1.02	391	0.1358	0.93

The quadric yield criterion for trabecular bone is shown in normalized stress space in Fig. 3.6.1.

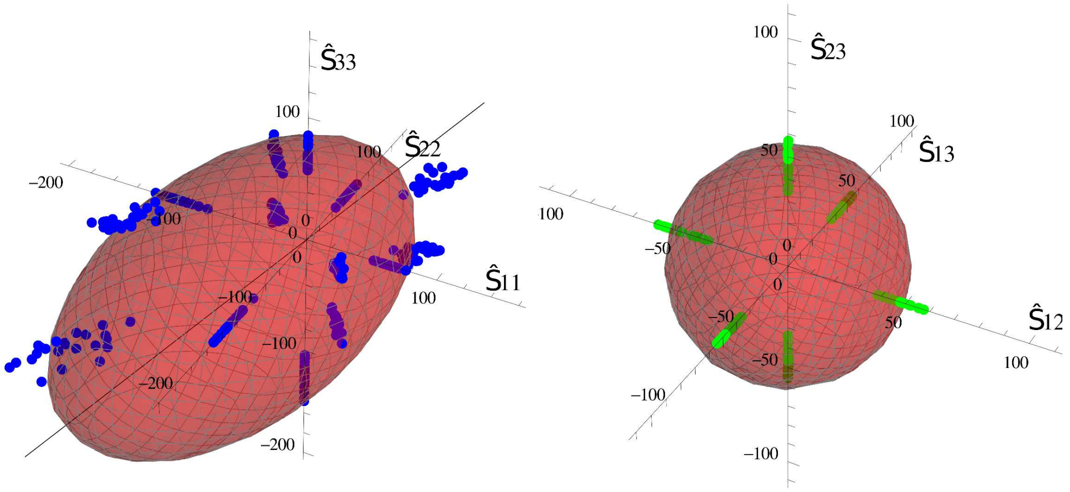

Fig. 3.6.1: Quadric yield surface for trabecular bone and *in silico* data [Wolfram et al., 2012] in normalized a) normal and b) shear stress space.

3.6.2 Lamellar bone

It has been proposed that lamellar bone behaves as a cohesive-frictional material at the nanoscale due to its nanogranular structure [Carnelli et al., 2010, Tai et al., 2006, Wang et al., 2008]. Here, the parameters of the quadric yield surface for bone tissue at the nanoscale were identified based on the work presented by Carnelli et al. [Carnelli et al., 2010, 2011]. In this particular study, transversely isotropic yield properties of bovine bone tissue were determined by means of a combination of nanoindentation experiments in axial and transverse direction with a numerical sensitivity study. Carnelli et al. [Carnelli et al., 2011] reported an axial compressive yield strength $\sigma_{33}^- = 150\,\mathrm{MPa}$, a transverse to axial ratio $R_{TA} = 0.86$ and a cone opening angle $\beta = 25°$ of an underlying fictitious isotropic material. Using the relations $\sigma_{ii}^- = \sigma_0^- \rho^p m_i^{2q}$, $R_{TA} = \frac{m_1^{2q}}{m_3^{2q}}$, $m_1 = m_2 = \frac{3-m_3}{2}$ for transverse isotropy, $tan\beta = \frac{3f_0}{F_0}$ and (3.23), and setting $p = 0.0$, $q = 1.0$, as well as $\zeta_0 = 0.5$, the yield constants provided by Carnelli et al. [Carnelli et al., 2011] were converted to a fabric-based quadric criterion. The resulting properties are shown in Table 3.4.

Table 3.4: Tensile yield stress σ_0^+, compressive yield stress σ_0^-, interaction parameter ζ_0, shear yield stress τ_0, exponents p and q as well as the eigenvalues of the fabric tensor $m1$, $m2$ and $m3$ of a yield criterion for bovine lamellar bone in MPa from a nanoindentation study [Carnelli et al., 2011].

σ_0^+	σ_0^-	ζ_0	τ_0	p	q	m1=m2	m3
100.0	136.0	0.5	66.6	0.0	1.0	0.975	1.05

The yield surface for lamellar bone is presented in Fig. 3.6.2.

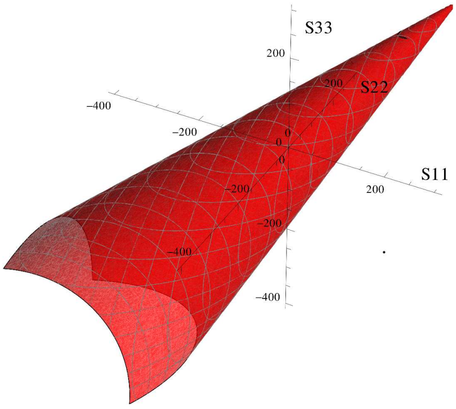

Fig. 3.6.2: Conical yield surface for lamellar bone from nanoindentation study [Carnelli et al., 2011] in normal stress space.

3.7 Discussion

In this work, a generalized anisotropic quadric yield criterion was proposed and discussed in stress space. The convexity limits of the criterion and the transition points between the different shapes were identified. The criterion was discussed for special cases of material symmetry such as isotropy, cubic symmetry, fabric-based orthotropy and general orthotropy. It was shown that the criterion degenerates to several classical yield criteria under appropriate conditions like the ones proposed by von Mises [von Mises, 1913], Drucker-Prager [Prager and Drucker, 1952], Tsai-Wu [Tsai and Wu, 1971], Liu [Liu et al., 1997], generalized Hill [Zysset and Rincón, 2006] and classical Hill [Hill, 1951] criteria. Applicability of the formulation for micromechanical analyses was shown by the identification of a quadric yield surface from a micromechanics based criterion for porous cohesive-frictional materials [Maghous et al., 2009]. This is particularly interesting for the description of bone, as it may be described on the micro-level as a cohesive-frictional material [Tai et al., 2006] interacting with nanoporosity. It was shown that the formulation as a quadric criterion extends the convexity of the original criterion [Maghous et al., 2009] to undercritical porosities. Thus, a smooth transition from the conical yield surface of the solid matrix material to an elliptical criterion of the porous composite is found. Also, a fabric- and density-based quadric strength criterion was identified for trabecular bone from multiaxial experimental data of Rincon et al. [Rincón-Kohli and Zysset, 2009]. A tensorial hardening rule was proposed allowing to fit both the experimental yield and strength data of Rincon et al. [Rincón-Kohli and Zysset, 2009] by a single criterion. Additionally, the fabric- and density-based Tsai-Wu yield criterion for trabecular bone identified by Wolfram et al [Wolfram et al., 2012] from *in silico* data was converted to an equivalent quadric criterion by a transformation of the interaction parameter. Finally, a conical yield criterion for bovine lamellar bone was identified from a nanoindentation study by Carnelli et al. [Carnelli et al., 2011].

Bone features a varying amount of porosity on every hierarchical level and a nanogranular ultrastructure. Therefore, the quadric yield criterion with its ability to take different convex quadric shapes is suitable to approximate the yield envelope at every hierarchical level starting from the extracellular matrix to the macroscopic bone tissue.

The formulation allows material symmetries ranging from isotropy to general anisotropy. It may take different convex quadratic shapes with a smooth transition from ellipsoidal to conical or cylindrical ones, making it a suitable candidate for use with a wide range of different materials such as metals, geomaterials, porous foams, bone, etc. The generality of the formulation is also beneficial in the case of material identification. If the shape of the yield function is not known a priori, a minimization using the quadric criterion will result in the optimal shape among the convex quadrics eliminating the need for several trial identifications using different formulations. It might prove especially interesting in combination with multiscale homogenization techniques in the future, as it may be used for the homogenized material description at several length scales as long as the failure envelope of the material can be approximated by a quadric surface.

The proposed criterion is a homogeneous function of degree one, which is beneficial for implementation of isotropic hardening rules in a computational mechanics framework. For isotropic hardening (3.3), its gradients with respect to stress and the hardening variable are independent of each other thus simplifying the implementation of e.g. backprojection algorithms. Also, it allows to make conservative approximations of the elastic domain of cohesive-frictional materials governed by a Drucker-Prager type conical yield surface by a smooth hyperboloid. This solves the common problem of non-uniqueness of the normal of the surface at the cone apex and allows the use of standard backprojection algorithms. The quadric criterion proved to be an effective tool in the description of bone strength at several length scales. Due to its generality and simple structure, it is well suited for the use in computational inelasticity of materials and structures.

4

From the manuscript published in:
Computer Methods in Biomechanics and Biomedical Engineering, DOI:
10.1080/10255842.2013.818665, 2013

The influence of yield surface shape and damage on the depth-dependent response of bone tissue to nanoindentation using spherical and Berkovich indenters

J.J. Schwiedrzik[1], P.K. Zysset[1]

[1] Institute for Surgical Technology and Biomechanics, University of Bern, Stauffacherstr.
78, CH-3014 Bern, Switzerland

4.1 Abstract

Prevention and treatment of osteoporosis rely on understanding of the micromechanical behavior of bone and its influence on fracture toughness and cell-mediated adaptation processes. Postyield properties may be assessed by nonlinear finite element simulations of nanoindentation using elastoplastic and damage models. This computational study aims at determining the influence of yield surface shape and damage on the depth dependent response of bone to nanoindentation using spherical and conical tips. Yield surface shape and damage were shown to have a major impact on the indentation curves. Their influence on indentation modulus, hardness, their ratio as well as the elastic to total work ratio are well described by multilinear regressions for both tip shapes. For conical tips, indentation depth was not statistically significant ($p < 0.01$). For spherical tips, damage was not a significant parameter ($p < 0.01$). The gained knowledge can be used for developing an inverse method for identification of postelastic properties of bone from nanoindentation.

4.2 Introduction

With modern societies ageing rapidly, the increasing number of fractures and falls poses a major challenge for health care systems all over the world. Modern preventive and therapeutic methods for metabolic diseases like osteoporosis rely on the results of the research on the micro-mechanical behavior of bone and its influence on fracture toughness and cell-mediated adaptation processes.

Bone is a composite material consisting of a cell seeded mineralized collagen matrix with a hierarchical structure. It is designed to provide mechanical support, store bone marrow and metabolize calcium [Fratzl and Weinkamer, 2007, Weiner et al., 1999, Zysset, 2009]. Parallel mineralized collagen fibrils surrounded by extra-fibrillar mineral particles [Currey, 1969, Lees et al., 1990, Reisinger et al., 2010] form fibril arrays. In lamellar bone, bundles of parallel fibril arrays form lamellae in a rotated-plywood-like manner [Weiner et al., 1997, 1999]. Osteocytes and their cell processes reside in the lacuno-canalicular system making up for 10 % of microporosity [Sugawara et al., 2005]. For a more thorough description, see e.g. [Fratzl and Weinkamer, 2007].

While biomechanical testing of bone has been performed on the macroscale for more than a century, there are still many challenges due to spatial, inter-subject, disease and age variation of mechanical properties [Keaveny et al., 2001]. Micromechanical analysis of bone as a hierarchical composite is a new and rapidly developing field in biomechanics [Hellmich et al., 2011] with a high clinical relevance. In order to understand and predict bone fracture more accurately, it is important to consider the yield behavior of bone on small length scales.

Nanoindentation is a micromechanical testing technique routinely used to extract mechanical properties at a high spatial resolution. A small diamond probe with a known geometry is pressed onto a flat surface and force and tip displacement are recorded. The work of Sneddon [Sneddon, 1948], Oliver and Pharr [Oliver and Pharr, 1992, 2004] and Swadener and Pharr for anisotropic media [Swadener and Pharr, 2001] allows us to extract elastic properties from the indentation curve. However, certain assumptions like an intact unloading stiffness and homogeneity of the material are made. The method has proven to be very robust for many ductile engineering materials like metals [Oliver and Pharr, 1992, 2004]. Nanoindentation in bone aims at characterizing the mechanical properties on the lamellar (2-7 µm) or the bone structural unit (BSU, 60 µm) level [Lewis and Nyman, 2008, Zysset, 2009] depending on the indentation depth [Hoffler et al., 2005]. Yield behavior may be determined from the indentation curves using inverse methods [Bolzon et al., 2004, Carnelli et al., 2010, Ganneau et al., 2006, Herbert et al., 2001], if the underlying dissipative processes are well understood. In the past, several groups have proposed experimental protocols that allow to extract yield strength [Ganneau et al., 2006, Herbert et al., 2001], if plasticity is the dominating dissipative process and the shape of the governing yield surface is known a priori. Great care must be taken when designing such a method, as it is difficult to extract unique postelastic mechanical properties from indentation curves using only one indenter shape. The reason for this is that indentation in multiple materials with significantly different properties might result in very similar curves [Chen et al., 2007]. Therefore a simultaneous analysis of indentations using different indenter geometries becomes necessary in order to be confident about the validity and uniqueness of the found parameters. Also, the method has to be designed for a specific expected behavior making it important to understand the underlying mechanics and the response of the model first.

When loaded past the yield point, bone shows two simultaneous mechanisms of energy dissipation: inelastic deformation and damage, i.e. reduction of the elastic properties through the formation of microcracks [Hengsberger et al., 2002, O'Brien et al., 2002, Zioupos et al., 2008]. The formation of plastic and damage behavior is well documented on the macroscopic scale [Garcia et al., 2009, O'Brien et al., 2002, Sun et al., 2010, Zioupos et al., 2008]. Recent studies seem to indicate that the effect of damage may also be seen on the microscale [Gupta et al., 2006, Hengsberger et al., 2002]. The assumptions of an unloading phase with intact elasticity needed for the Oliver and Pharr analysis seems not to hold true for the testing of bone tissue. Also, the question arises what mechanisms dominate yielding of the material and how the yield envelope influences the indentation curve.

Tai et al. [Tai et al., 2006] showed evidence that bone behaves as a cohesive-frictional material due to its sub-microscopic structure. They proposed that increased strength properties in compression compared to tension reported in the literature [Yeni et al., 2004] may be explained by friction between mineral particles and cohesion originating from the organic phase. Micromechanical considerations by Maghous et al. [Maghous et al., 2009] on strength of porous geomaterials showed that the yield surface of cohesive-frictional materials featuring porosity takes a hyperboloidal or elliptical shape, which would seem appropriate for bone given the nanogranular structure and the inherent porosity at all length scales. This is also consistent with findings on the macroscopic level, where Cowin proposed a Tsai-Wu yield surface for cortical bone [Cowin, 1979, 2001]. Therefore, it seems reasonable to hypothesize that the yield criterion of bone under nanoindentation loading might be of a conical, hyperboloidal or ellipsoidal shape depending on the amount of porosity. Due to the complex mechanical problem arising in the context of nanoindentation featuring both material and geometric nonlinearities combined with contact mechanics, many recent studies rely on numerical simulations and discretization of the mechanical problem instead of using analytical solutions for a simplified system [Carnelli et al., 2010, Chen et al., 2007, Mullins et al., 2009, Zhang et al., 2008, 2010]. Finite element simulations using plasticity models featuring a conical Drucker-Prager yield surface were able to capture some of the characteristics of nanoindentation experiments on bone [Carnelli et al., 2010, Tai et al., 2006]. Finite element simulations of nanoindentation experiments using coupled plasticity and damage models have shown that the presence of damage may explain some of the experimental findings for mineralized tissues like reduced unloading stiffness [Lucchini et al., 2011, Zhang et al., 2010].

Most studies trying to extract postelastic properties of bone from indentation curves so far assumed a certain shape of the yield surface and subsequently determined yield parameters like von Mises yield stress or cohesion and friction angle depending on the used formulation. However, the appropriate shape of the yield surface of bone at the microlevel is not known for certain at the moment.

Therefore, the main aim of this study is to determine the influence of the material constitutive behavior, in particular the shape of the yield surface and presence of a damage mechanism, on the depth dependent response of bone to nanoindentation using spherical and conical tips and to identify measures that would be best suited for use in an inverse method to identify yield and damage parameters of bone.

4.3 Materials and methods

4.3.1 Constitutive Model

A recently proposed elastoplastic damage model for bone tissue [Schwiedrzik and Zysset, 2013a] was implemented as a user subroutine UMAT in the commercial finite element solver ABAQUS (Dassault Systems, Vélizy-Villacoublay, France) and adapted for use in this study.

The rheological model is a damageable elastic spring in series with a plastic pad. The free energy potential is given by:

$$\Psi(\boldsymbol{E}, \boldsymbol{E}^p, \kappa) = \frac{1}{2}(1 - D(\kappa))(\boldsymbol{E} - \boldsymbol{E}^p) : \mathbb{S}(\boldsymbol{E} - \boldsymbol{E}^p) \tag{4.1}$$

with the fourth order stiffness tensor $\mathbb{S}$, the total and plastic strain tensors $\boldsymbol{E}$ and $\boldsymbol{E}^p$ and the accumulated plastic strain κ. The commercial finite element solver Abaqus uses an updated Lagrangian mapping technique with the Cauchy stress tensor and an approximation of the integral of the rate of deformation $\int \boldsymbol{D} dt$ as its conjugate strain tensor for simulations involving finite deformations and rotations. These stress and strain measures were therefore used in this implementation. The evolution of plastic strains is associated to the yield surface and damage accumulation is assumed to be coupled to the plasticity using a damage function $D(\kappa)$ reducing all elements of the stiffness tensor:

$$D(\kappa) = D_c(1 - e^{-k_p \kappa}) \tag{4.2}$$

The inverse damage rate $\frac{1}{k_p}$ was set to 9.53 % as suggested earlier [Schwiedrzik and Zysset, 2013a, Zysset, 1994]. Since the exact damage evolution is not known for bone on the microscale, the maximum damage D_c was treated as an unknown parameter in this study. D_c was varied from 0.0 to 0.6 in order to show its influence on the indentation curve and to assure that continuum damage mechanics is applicable. The primal closest point projection algorithm proposed by Perez-Foguet et al. [Armero and Pérez-Foguet, 2002, Pérez-Foguet and Armero, 2002] was implemented using a line search algorithm for constrained problems as a fail safe for the Newton algorithm used by Schwiedrzik and Zysset [2013a] in order to enlarge the region of convergence of the model. In order to verify the correct implementation of the material model, single element tests were performed and stiffness and strength compared to analytical solutions.

Elastic stiffness

A transversely isotropic stiffness tensor $\mathbb{S}$ for dry trabecular bone measured in a nanoindentation study by Wolfram et al. [Wolfram et al., 2010a] and computed using the methodology of Franzoso and Zysset [Franzoso and Zysset, 2009] was chosen as the elastic input for this study. Using a fabric elasticity model [Zysset and Curnier, 1995] with an isotropic base material, the following constants were obtained to define the stiffness tensor:

E_0 is the elastic modulus, ν_0 the Poisson ratio, and μ_0 the shear modulus of the base material. The parameter ρ is the volume fraction, the m_i are the eigenvalues of the fabric tensor describing the anisotropy of the material and k and l are exponents of the fabric-

Table 4.1: Constants for fabric-based elasticity [Zysset and Curnier, 1995] of bone tissue identified from Wolfram et al [Wolfram et al., 2010a].

E_0 $[GPa]$	ν_0	μ_0 $[GPa]$	ρ	$m1 = m2$	m3	k	l
13.846	0.32	5.245	0.9	0.971	1.058	1.0	1.0

based model. For further details see Zysset and Curnier [1995]. Due to the isotropy of the base material, the relation $\mu_0 = \frac{E_0}{2(1+\nu_0)}$ holds true. Theoretical indentation moduli for the given stiffness tensor were determined using the method of Swadener and Pharr [Swadener and Pharr, 2001] in axial and transverse direction as 14.9 GPa and 13.4 GPa, respectively.

Yield criterion

A recently proposed fabric-based orthotropic quadric yield criterion [Schwiedrzik et al., 2013] was used to define the yield surface of bone. It allows strength differences in tension and compression and may take an ellipsoidal, hyperboloidal or conical shape depending on the chosen interaction parameters (see Fig. 4.1). The material model [Schwiedrzik and Zysset, 2013a] was adapted to accomodate the new yield function. The criterion is defined in stress space as

$$Y(\boldsymbol{S}) := \sqrt{\boldsymbol{S} : \mathbb{F}\boldsymbol{S}} + \boldsymbol{F}\boldsymbol{S} - 1. \tag{4.3}$$

It features no postyield hardening/softening behavior in this study. The general form of the fourth order tensor $\mathbb{F}$ is

$$\mathbb{F} = \sum_{i=1}^{3} F_i^2 \boldsymbol{M}_i \otimes \boldsymbol{M}_i - \sum_{i,j=1;i\neq j}^{3} \zeta_{ij} F_i^2 \boldsymbol{M}_i \otimes \boldsymbol{M}_j + \sum_{i,j=1;i\neq j}^{3} \frac{1}{2\tau_{ij}^2} \boldsymbol{M}_i \underline{\overline{\otimes}} \boldsymbol{M}_j \tag{4.4}$$

with

$$F_i = \frac{\sigma_i^- + \sigma_i^+}{2\sigma_i^+ \sigma_i^-} \tag{4.5}$$

and

$$\boldsymbol{M}_i = \boldsymbol{m}_i \otimes \boldsymbol{m}_i. \tag{4.6}$$

In this case, the general form of the second order tensor $\boldsymbol{F}$ is

$$\boldsymbol{F} = \sum_{i=1}^{3} \frac{1}{2} \left(\frac{1}{\sigma_{ii}^{+}} - \frac{1}{\sigma_{ii}^{-}} \right) \boldsymbol{M}_i. \tag{4.7}$$

The $\boldsymbol{m}_i$ are the vectors describing the material orientation. Twelve orthotropic constants are needed to define the criterion: The uniaxial yield stresses σ_1^+, σ_1^-, σ_2^+, σ_2^-, σ_3^+, σ_3^-, interaction coefficients ζ_{12}, ζ_{23}, ζ_{13}, and the shear yield stresses τ_{12}, τ_{23} and τ_{13}. When using a fabric based model [Schwiedrzik et al., 2013, Wolfram et al., 2012, Zysset and Rincón, 2006], the orthotropic constants are given by

$$\sigma_{ii}^{+} = \sigma_0^{+} \rho^p m_i^{2q}, \qquad \sigma_{ii}^{-} = \sigma_0^{-} \rho^p m_i^{2q}, \tag{4.8}$$

$$\zeta_{ij} = \zeta_0 \frac{m_i^{2q}}{m_j^{2q}}, \qquad \tau_{ij} = \tau_0 \rho^p m_i^q m_j^q. \tag{4.9}$$

In the case of an isotropic base material, the number of independent constants thus reduces to five: σ_0^+, σ_0^-, ζ_0 as well as two exponents p and q. The parameter ζ_0 is an interaction parameter and determines the shape of the criterion in normal stress space. As for the elastic domain, an isotropic base material was defined. The yield strength in tension and compression of the base material were determined by

$$\sigma_0^{+} = E_0 \varepsilon_0^{+}, \tag{4.10}$$

$$\sigma_0^{-} = E_0 \varepsilon_0^{-}, \tag{4.11}$$

using the modulus of the base material E_0. The principal yield strains for the base material were taken from Bayrakthar et al. [Bayraktar et al., 2004] to be 0.41 % in tension and 0.83 % in compression. The shear strength was determined using the isotropy condition $\mathbb{F}_{1122} = \mathbb{F}_{1111} - \mathbb{F}_{1212}$ for the base material:

$$\tau_0 = \sqrt{\frac{2}{1+\zeta_0} \frac{\sigma_0^{+}\sigma_0^{-}}{\sigma_0^{-} + \sigma_0^{+}}} \tag{4.12}$$

It was assumed that the influence of the fabric eigenvalues on the yield surface is similar to its influence on the elastic properties, which is consistent with previous studies of indentation on bone conducted by other groups [Carnelli et al., 2010, 2011, Lucchini et al., 2011]. Therefore q was set equal to 1. The constants defining the fabric-based yield surface of bone are given in Table 4.2.

Table 4.2: Yield constants for bone tissue, stresses in GPa.

Name	σ_0^+	σ_0^-	ζ_0	p	q
Mat1	0.057	0.115	0.30	1.0	1.0
Mat2	0.057	0.115	0.35	1.0	1.0
Mat3	0.057	0.115	0.49	1.0	1.0

It is important to note that the yield surface is defined in stress space and not effective stress space, as is sometimes the case in continuum damage mechanics. Therefore, damage will not lead to softening in this model. Instead, a constant yield surface was used for both the purely elasto-plastic and the elasto-plastic case with damage leading to an ideal plasticity or ideal plasticity and damage model in order to guarantee that the changes in the indentation response originate from the dissipative mechanisms themselves and not the resulting postyield hardening/softening curve. Fig. 4.1 illustrates the yield surfaces for $\zeta_0 = 0.30$ (ellipsoidal, left), $\zeta_0 = 0.35$ (hyperboloidal, middle) and $\zeta_0 = 0.49$ (conical, right) in normal stress space.

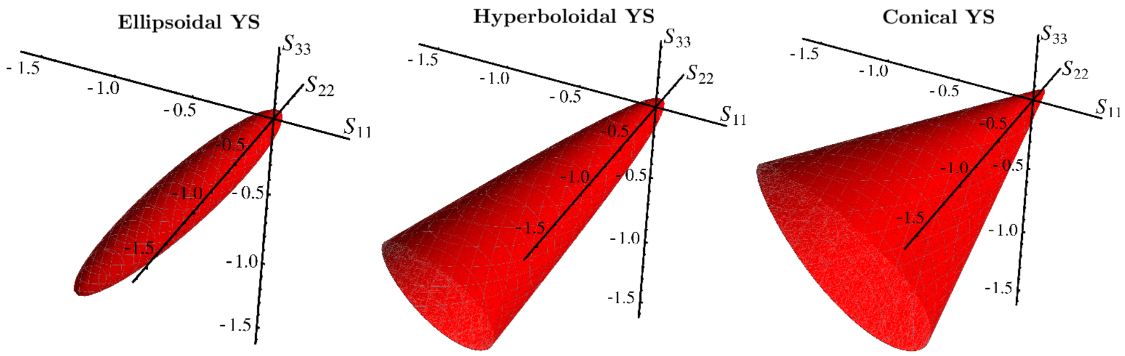

Figure 4.1: Quadric yield surfaces for $\zeta_0 = 0.30$ (ellipsoidal, left), $\zeta_0 = 0.35$ (hyperboloidal, middle) and $\zeta_0 = 0.49$ (conical, right) in normal stress space.

4.3.2 Finite Element Model

The tip geometry of the Berkovich indenter was modeled by a rigid cone with a semivertical angle of 70,3°. The tip was not blunted, since this has been shown to have an effect only for indentations smaller than 200 nm [Lucchini et al., 2011]. The spherical indenter was modeled as rigid with a radius $R = 50\mu m$. Only one quarter of the bone halfspace was meshed by a sufficiently large cube with a side length of $100\mu m$ following the suggestions of Poon [Poon et al., 2008b] and symmetry boundary conditions were applied. The bottom nodes were constrained in the testing direction. Hard, frictionless contact was defined between the conical tip and the surface of the tested bone specimen.

The halfspace was meshed using linear fully integrated hexahedral elements. As large deformations and rotations were anticipated to appear in the vicinity of the nanoindentation, geometrically nonlinear analysis was activated. In order to avoid numerical problems due to element distortion, reduced integration with enhanced hourglass control and arbitrary lagrangean eulerian (ALE) remeshing was activated for the elements within 5 µm of the contact surface.

The model contains 36474 elements. As the gradients of the field variables are comparatively large near the indentation and low with increasing distance to the tip, the edges of the cube were seeded with a bias towards the indentation allowing to have a fine mesh near the indenter tip while maintaining a relatively small number of elements. Fig. 4.2 shows the setup of the indentation model using a conical indenter.

In order to validate the finite element mesh, it was verified that the influence of the discretization on the indentation simulation is negligible for the range of indentation depths used in this study. Conical and spherical indentations into an elastic halfspace were simulated to a maximum depth of 2.5 µm and compared to analytical and empirical solutions [Hertz, 1881, Poon et al., 2008a, Sneddon, 1965, Swadener and Pharr, 2001] using isotropic materials with varying Poisson's ratio as well as transversely isotropic materials. As expected, the indentation curve was close to the analytical solution and the measured indentation modulus was independent of the indentation depth for indentation depths larger than 300 nm. Additionally, a mesh convergence study (h-refinement) was performed for conical indentations into an isotropic elastoplastic halfspace governed by a von Mises yield surface to depths of $1\mu m$ and $2.5\mu m$. This showed that the mesh has also converged in the case of material nonlinearity.

4.3.3 Parameter study and data analysis

Simulations of conical indentations to depths of 0.5, 1.0, 1.5, 2.0 and $2.5\mu m$ as well as spherical indentations to 0.5, 0.75 and 1.0 µm were run in displacement control for each

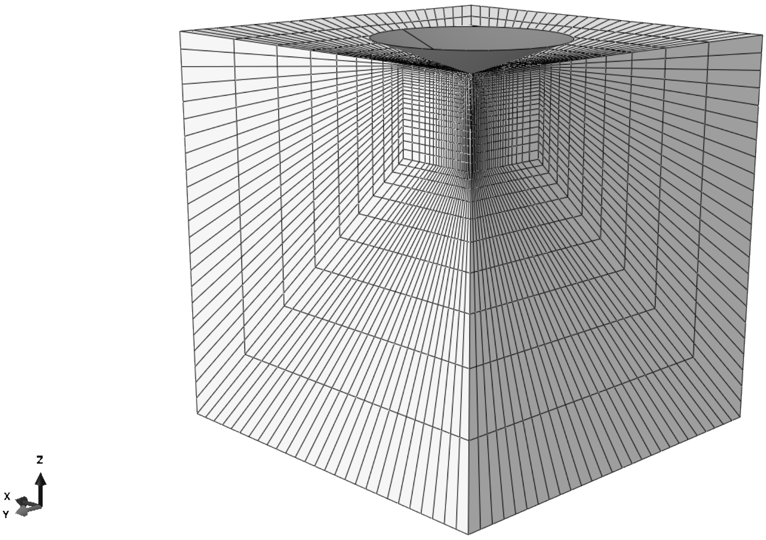

Figure 4.2: Finite element indentation model using a conical indenter.

yield surface ($\zeta_0 = 0.3,\ 0.35,\ 0.49$). In order to show the influence of damage on the indentation curve, each simulation was run with different values of D_c (0.0, 0.4, 0.6). A total of 90 conical and 54 spherical indentations were performed in axial and transverse direction. The force-depth ($P - h$) curves were extracted and analyzed according to the Oliver and Pharr method [Oliver and Pharr, 1992]. A power law function was fitted to the upper 60 % of the unloading curve and its derivative $S = \frac{dP}{dh}$ computed at the maximum depth. Then, the indentation modulus was determined using the general relation [Herbert et al., 2001, Oliver and Pharr, 1992]

$$E_{ind} = \frac{\sqrt{\pi}}{2} S \frac{1}{\sqrt{A_c}} \tag{4.13}$$

with the indentation modulus E_{ind} and the projected contact area A_c. The contact area was determined using

$$A_c = 24.5 h_c^2 \tag{4.14}$$

in the case of conical indenters [Oliver and Pharr, 1992] and

$$A_c = (R h_c - h_c^2)\pi \tag{4.15}$$

for spherical indenters [Herbert et al., 2001] with the sphere radius R and the contact depth h_c. Contact depth was found using the relation

$$h_c = h - \beta \frac{P}{S} \tag{4.16}$$

with an empirical factor β, which is 0.72 for conical and 0.75 for spherical indenters [Herbert et al., 2001, Oliver and Pharr, 1992]. The indentation hardness H_{ind} is defined as the maximum force divided by the contact area at maximum depth:

$$H_{ind} = \frac{P_{max}}{A_{c,max}} \tag{4.17}$$

The elastic and total energies are defined as

$$W_{elast} = \int_{h_{max}}^{h_{res}} P dh, \quad W_{tot} = \int_{0}^{h_{max}} P dh \tag{4.18}$$

with the maximum depth h_{max} and the residual depth h_{res}. A pair of dimensionless parameters, H_{ind}/E_{ind} and W_{elast}/W_{tot}, was defined to characterize the indentation curves. Indentation modulus, hardness, elastic and total energy were analyzed as a function of ζ_0, i.e. yield surface shape, maximum damage D_c, and indentation depth h. For both indenters, trilinear regressions describing the influence of h, ζ_0 and D_c on E_{ind} and H_{ind} were fitted separately to the axial and the transverse data and regressions for the dimensionless measures H_{ind}/E_{ind} and W_{elast}/W_{tot} to the pooled axial and transverse data. Subsequently, the regressions were reduced to the significant parameters.

4.4 Results

A total of 90 conical and 54 spherical indentations were performed in axial and transverse direction. Indentation curves of conical and spherical indentations with $\zeta = 0.3$, 0.35 and 0.49 for elasto-plasticity ($D_c = 0$) and for elasto-plasticity with damage ($D_c = 0.6$) may be seen in Fig. 4.3. The extracted E_{ind}, H_{ind} and W_{elast}/W_{tot} for the axial indentations may be seen in Fig. 4.4. The extracted depth profiles are shown in Fig. 4.5.

The indentations for the conical yield surface ($\zeta_0 = 0.49$) are the most elastic. Pile-up is visible, but very broad around conical indentations in Fig. 5, leading to an overestimation of the indentation modulus. Measured indentation modulus is not significantly dependent on depth for both indenters, while hardness and elastic to plastic work ratio change within the assessed depth range for the spherical indentations.

The hyperboloidal yield surface ($\zeta_0 = 0.35$) leads to a lower elastic to total work ratio.

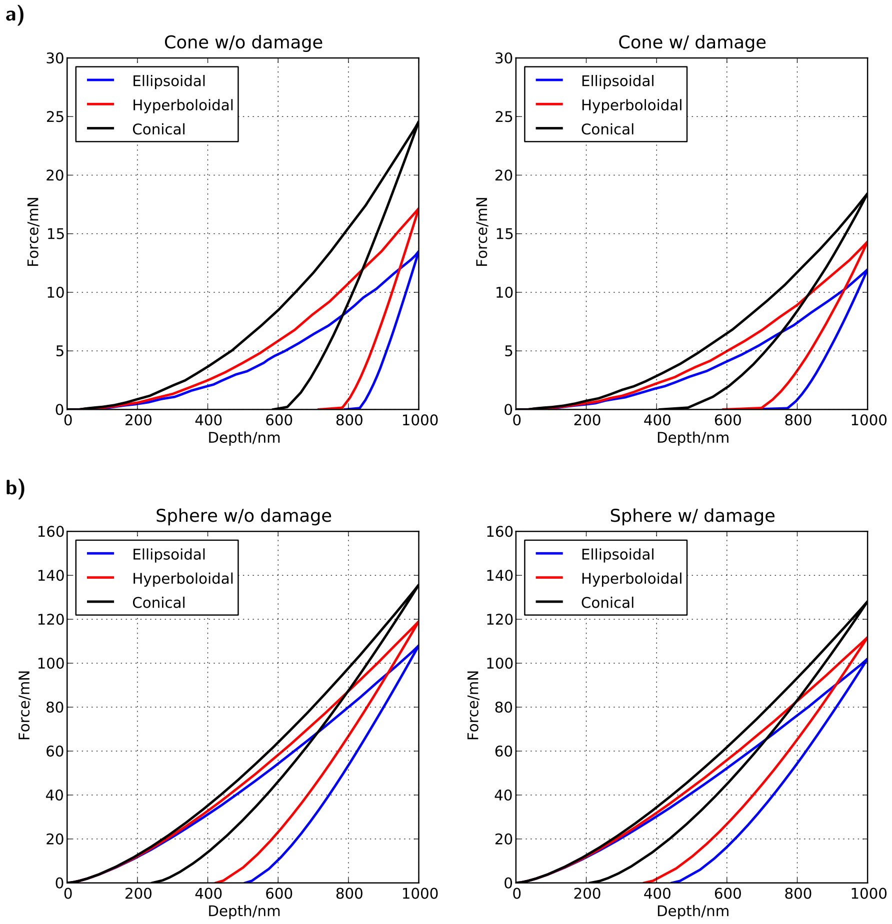

Figure 4.3: Axial indentation curves with $\zeta_0 = 0.3$, 0.35 and 0.49 using a) conical and b) spherical indenters to a depth of $1\mu m$ for elasto-plasticity ($D_c = 0$, left) and elasto-plasticity with damage ($D_c = 0.6$, right).

Hardness reduces compared to the conical surface. Pile-up forms near the conical indentations leading to an overestimation of the measured indentation modulus. The amount of pile-up around the conical indentation is decreasing monotonously with increased D_c. For spherical indentations, no pile-up is visible, indentation modulus is constant, hardness increases and elastic to total work ratio decrease with depth.

For the ellipsoidal yield surface ($\zeta_0 = 0.3$), the indentations are even more dissipative. Hardness is substantially reduced in comparison to the other yield surfaces for both conical and spherical indenters. Pile-up around the conical indentation leads to an overestimation of the indentation modulus in the case of $D_c = 0$. The amount of pile-up seen in the conical indentations decreases monotonously with growing D_c. For spherical indentations, there was no pile-up. The trends for hardness and elastic to total work ratio are similar to the other yield surfaces.

For conical indentations, indentation depth h was not a significant parameter. Table 4.3 shows the significant parameters of bilinear regressions describing the influence of the parameters ζ_0 and D_c on indentation modulus E_{ind} and hardness H_{ind} for axial indentations (N=45) and transverse indentations (N=45) as well as the dimensionless measures H_{ind}/E_{ind} and W_{elast}/W_{tot} for pooled axial and transverse indentations (N=90) using a conical tip.

As table 4.3 shows, the bilinear regressions for the conical indentations are significant for both the absolute as well as the dimensionless measures and have a high predictability.

Table 4.3: Significant parameters of bilinear regressions describing the influence of ζ_0 and D_c on indentation modulus E_{ind} and hardness H_{ind} for axial indentations (N=45) and transverse indentations (N=45) as well as H_{ind}/E_{ind} and elastic to total work ratio W_{elast}/W_{tot} for pooled axial and transverse indentations (N=90) using a conical tip. Absolute measures in GPa.

Measurement	Intercept	Slope ζ_0	Slope D_c	Slope $\zeta_0 D_c$	p-value	Adj. R^2	N
$E_{ind,ax}$	24.796	-11.0864	-9.3162	–	< 0.0001	0.939	45
$H_{ind,ax}$	−0.780	4.875	0.746	-2.663	< 0.0001	0.986	45
$E_{ind,tv}$	20.4934	-6.1804	-9.0019	-	< 0.0001	0.950	45
$H_{ind,tv}$	−0.638	3.996	0.550	-2.003	< 0.0001	0.989	45
H_{ind}/E_{ind}	−0.048	0.257	0.019	–	< 0.0001	0.990	90
W_{elast}/W_{tot}	−0.181	1.355	–	0.384	< 0.0001	0.988	90

Table 4.4: Significant parameters of bilinear regressions describing the influence of ζ_0 and h/R on hardness H_{ind} for axial indentations (N=27) and transverse indentations (N=27) as well as H_{ind}/E_{ind} and elastic to total work ratio W_{elast}/W_{tot} for pooled axial and transverse indentations (N=54) using a spherical tip. Absolute measures in GPa.

Measurement	Intercept	Slope h/R	Slope ζ_0	Slope $\zeta_0 h/R$	p-value	Adj. R^2	N
$H_{ind,ax}$	0.366	-12960	–	61610	< 0.0001	0.981	27
$H_{ind,tv}$	0.313	-13090	–	56430	< 0.0001	0.982	27
H_{ind}/E_{ind}	0.023	-975.9	–	4056	< 0.0001	0.951	54
W_{elast}/W_{tot}	0.343	-986.9	1.221	–	< 0.0001	0.946	54

For spherical indentations, the critical damage D_c was not a significant parameter. The indentation modulus E_{ind} showed an intercept but no significant slope ($p < 0.0001$). H_{ind} had significant slopes in the directions h/R and $\zeta_0 h/R$ only. H_{ind}/E_{ind} and W_{elast}/W_{tot} were also not significantly affected by D_c. Therefore, only bilinear models of H_{ind}, H_{ind}/E_{ind} and

W_{elast}/W_{tot} as a function of h/R and ζ_0 are reported here. Table 4.4 shows the significant parameters of bilinear models describing the influence of h/R and ζ_0 on indentation modulus E_{ind} and hardness H_{ind} for axial indentations (N=45) and transverse indentations (N=45) hardness H_{ind} for axial indentations (N=27) and transverse indentations (N=27) and for the dimensionless measures H_{ind}/E_{ind} and W_{elast}/W_{tot} for spherical indentations using pooled axial and transverse data (N=54).

4.5 Discussion

The main aim of this study was to determine the influence of the material constitutive behavior, in particular the shape of the yield surface and presence of a damage mechanism on the depth dependent indentation behavior by means of a parametric study using conical and spherical indenters and to identify suitable measures on which to base an inverse method for identification of yield and damage properties.

The results of the parameter study showed that the shape of the yield surface has a major impact on pile-up and the indentation curve. Both conical and spherical indentations became more plastic with decreasing ζ_0. In the absence of damage, elastoplastic indentations using a conical tip showed considerable pile-up leading to an overestimation of indentation modulus and hardness when using the Oliver-Pharr method [Oliver and Pharr, 1992], which is consistent with the literature [Bolshakov and Pharr, 1998, Hay et al., 1999]. The introduction of damage consistently lead to a reduction of pile-up and thus the measured indentation modulus and hardness as well as an increase in the elastic to total work ratio.

The scalar damage mechanics approach used in this study allows higher volume changes in the vicinity of the indent than a pure elastoplastic model thus reducing the formation of pile-up around conical indentations. The damaged region itself is very localized around the indentation and much smaller than the elastic stress field limiting its influence on the measurement of the elastic properties of the tested volume. However, interpretation of elastic measurements from conical indentations in the presence of damage and plasticity is problematic, as the measured modulus, which should in theory be an elastic material property and thus constant, was shown to be a function of the critical damage and the yield surface shape. On the other hand, spherical indents showed no pile-up and constant indentation moduli. From the results of this study, it may be concluded that elastic moduli measured by spherical indentation give correct results irrespective of the presence of a damage mechanism or the yield surface shape, which makes them an interesting alternative to the current practice.

As expected, conical indentations were self-similar. The introduction of damage leads to reduced unloading stiffness, a reduced residual imprint, realistic values of indentation modulus and a clear reduction of pile-up, which is consistent with experimental findings in nanoindentation on bone [Mullins et al., 2009, Zhang et al., 2010, Wolfram et al., 2010a]. For $D_c = 0.6$, all measured indentation moduli were within 10 % to the theoretical value of 14.9 GPa in the axial and 13.4 GPa in the transverse direction for all implemented yield surface shapes. The consistency of the elastic properties with the experimental results of Wolfram et al. [Wolfram et al., 2010a], the reduced plastic imprint and the absence of pile-up suggest that a damage mechanism is present and $D_c = 0.6$ is a realistic value for bone tissue. This is consistent with the findings of Gupta et al. [Gupta et al., 2006], who reported negative fibril strains after macroscopic tests in tension past the yield point as a sign of internal decohesion between mineral platelets and collagen molecules as well as the presence of transverse microcracks around the indentation site reported by Hengsberger et al. [Hengsberger et al., 2002]. Wolfram et al. reported indentation hardness values for Berkovich indentations of dry trabecular bone to 2.5 μm of 0.527±0.078 GPa in axial and 0.459±0.057 GPa in transverse direction. The pooled elastic to total work ratio W_{elast}/W_{tot} was 0.232±0.025, H_{ind}/E_{ind} was 0.037±0.004. A qualitative comparison ignoring the effects of creep and other time-dependent effects seen in experiments on bone with the results of this study suggests that a D_c of 0.6 and a ζ_0 of 0.3 gives a reasonable correspondence with the experimental indentation data for dry human trabecular bone, which would suggest that damage is present and the yield surface of bone could be of an elliptical shape. This needs to be investigated further by a rigorous quantitative comparison using several tips and indentation depths as well as time-dependent material behavior in the constitutive model.

In general, pile-up, hardness and W_{elast}/W_{tot} varied significantly with D_c and ζ_0 and are well suited for use in an identification strategy. Bilinear regressions were fitted highlighting the influence of D_c and ζ_0 for conical and h/R and ζ_0 for spherical indentation on E_{ind} and H_{ind} as well as the dimensionless parameters H_{ind}/E_{ind} and W_{elast}/W_{tot}. It was found that linear regressions are describing the observables very well, with the regressions showing a high significance ($p < 0.0001$) and adjusted coefficient of determination ($R^2 > 0.93$). While the linear regressions of the absolute and relative measures with respect to the studied parameters are equally predictive, the main advantage of H_{ind}/E_{ind} and W_{elast}/W_{tot} compared to the absolute measures is that they are normalized and dimensionless and thus may be computed on pooled data if the anisotropy of the yield surface and the elastic stiffness is the same. The linear relationships can be inverted easily. This makes them usable in an identification strategy with sought parameters D_c and ζ_0 and experimental observables H_{ind}/E_{ind} and W_{elast}/W_{tot} of the conical and their evolution with depth for the spherical indenter. It may be therefore concluded that these measures are well suited for identification of the yield surface shape and critical damage using different indenter geometries. The fact that two different indenter types are used and that the spherical indenter is not self-similar increases the number of observables substantially, which improves the robustness of the final identification scheme.

The formation of pile-up in combination with a FE mesh with finite characteristic element lengths lead to a slight depth-dependence of the results in the case of conical indentation and elastoplasticity ($D_c = 0$). However, the induced variability was small enough that statistically significant changes could be detected as a function of the studied parameters. Self-similarity of the conical indentations was confirmed for all yield surfaces, as indentation depth was found not to be a significant parameter in the linear models fitted to the data. As expected, the spherical tip showed a clear depth dependence for both hardness and elastic to total work ratio. The lack of self similarity makes it an interesting tip geometry for an inverse method to identify postelastic properties, as indentations to different depths may be treated as independent experiments.

There are several limitations to this study: Bone was modeled as a homogeneous material with constant anisotropic material properties. The lamellar structure, differences in mineralization, fibril orientation as well as the lacuno-canalicular system, which are of the same length scale as the indentation, were not included explicitly in the model, but modeled in a homogenized, average way. Therefore, these results are only valid for average properties and may not be used for explaining the variability of reported experimental results. Frictionless, hard contact was assumed between the rigid indenter and the surface. Also, the material was modeled using time- and rate-independent constitutive behavior and damage was described using a scalar variable reducing all elements of the stiffness tensor. These modeling assumptions were necessary to keep the computational costs at a reasonable level and to highlight the influence of the two parameters studied in this work, i.e. the shape of the yield surface and the presence of a damage mechanism. Therefore they were justified in this case. No quantitative comparison to experimental data was performed with respect to hardness, work or pile-up. The modeling assumptions like rate-independent material behavior needed to highlight the influence of the chosen parameters did not allow to do a rigorous quantitative comparison to experimental data, which shows strong time-dependent behavior. A qualitative comparison of indentation modulus, hardness and elastic to total work ratio of the conical indentations to the experimental data of Wolfram et al. [Wolfram et al., 2010a] of Berkovich indentations in dry human trabecular bone was performed. The significance of these findings is limited by the missing time-dependency of the model and the fact that the comparison was done using only one indenter shape.

4.6 Conclusion

It was shown in this work that pile-up, measured indentation modulus E_{ind}, hardness H_{ind}, the dimensionless parameters H_{ind}/E_{ind} and W_{elast}/W_{tot} of conical indentations are highly sensitive to both yield surface shape and critical damage. For the spherical indenter, no pile-up occurs and the other measures are not significantly correlated to D_c, but to h/R. These measures are well suited for use in the identification process.

The indentation modulus E_{ind} extracted using the Oliver-Pharr method, which should be an elastic material constant in theory, was found to be a function of yield surface shape and damage for conical indentations while being constant for spherical indentations. This means that the interpretation of indentation moduli extracted from sharp indentations by the Oliver-Pharr method as virgin elastic material properties is problematic, at least for the material descriptions used in this study. On the other hand, the use of spherical indenters is a good alternative since they do not suffer from the same shortcomings.

The major advantages of H_{ind}/E_{ind} and W_{elast}/W_{tot} over their absolute counterparts lies in their normalization and nondimensionality allowing the evaluation of pooled data from several directions if the anisotropy of the elastic and plastic properties are similar. The advantage of using an additional indenter that is not self-similar lies in the increase of independent observables, which will help to improve the robustness and uniqueness of the identified parameters. A qualitative comparison of experimental data to the results of this study ignoring the effects of creep suggests the presence of a damage mechanism and an elliptical shape of the yield surface, which needs to be further investigated. The knowledge on the influence of the yield surface shape and the presence of damage gained from this parametric study may subsequently be used for the development of an identification strategy for the yield surface of bone tissue at the microlevel based on indentation with sharp and spherical indenters.

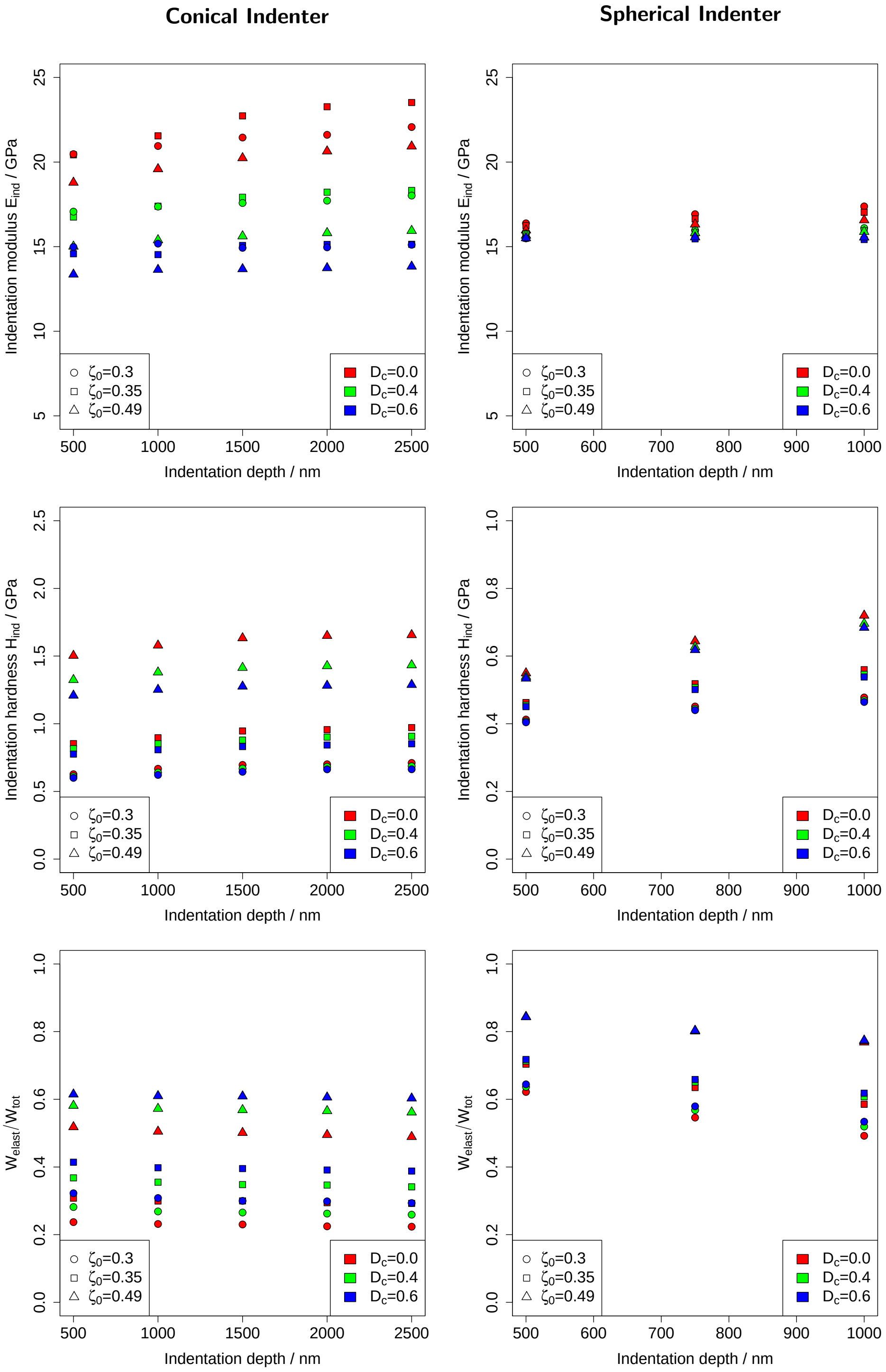

Figure 4.4: Indentation modulus E_{ind} (top), hardness H_{ind} (middle) and elastic to total work ratio W_{elast}/W_{tot} (bottom) in axial direction as a function of indentation depth using conical (left) and spherical indenters (right) for varying ζ_0 and D_c. The symbol shape depends on ζ_0, the color coding on D_c.

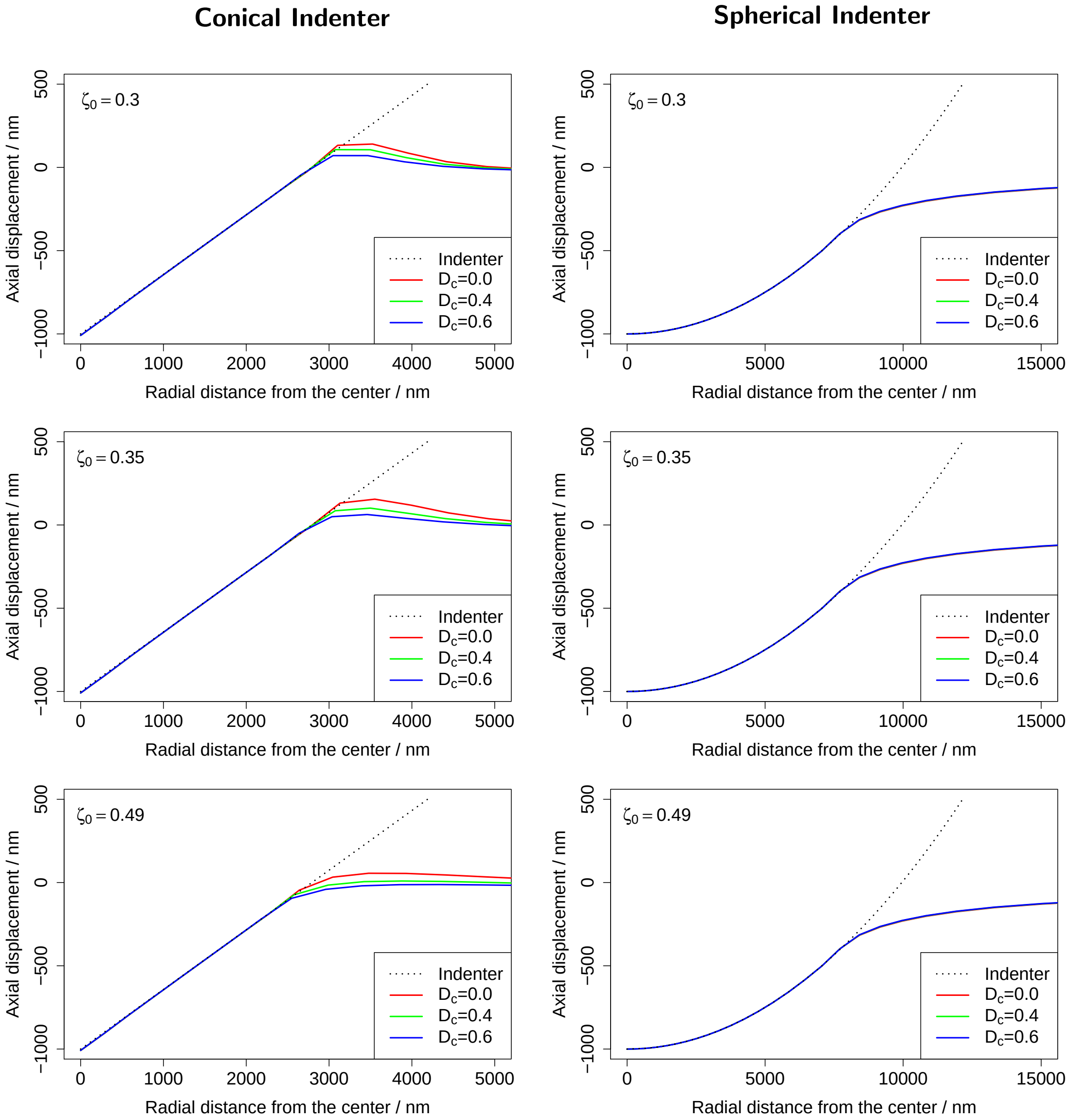

Figure 4.5: Depth profile at maximum load for conical (left) and spherical indentation (right) in axial direction for $\zeta_0 = 0.3$ (top), $\zeta_0 = 0.35$ (middle) and $\zeta_0 = 0.49$ (bottom) and varying D_c.

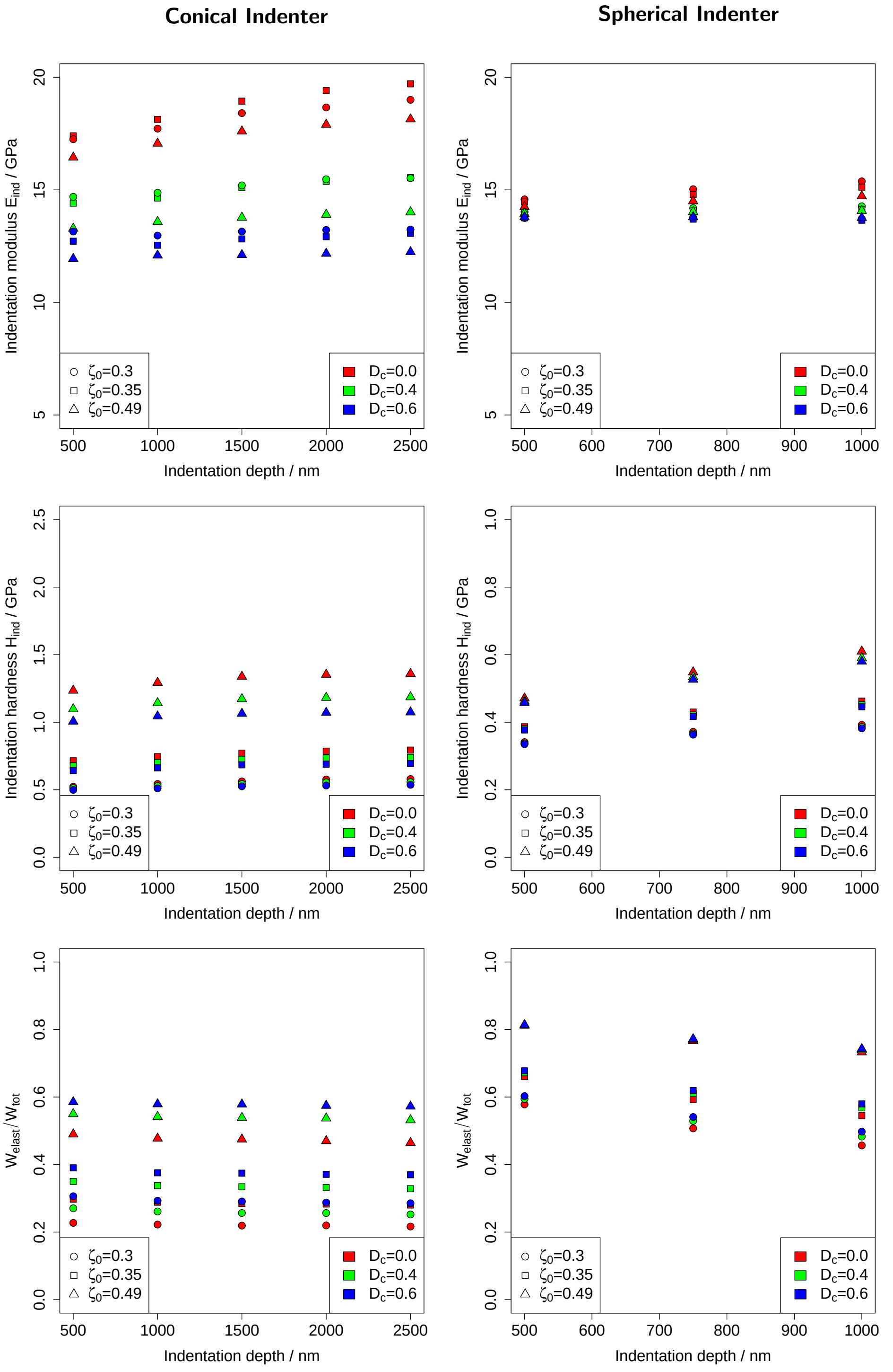

Figure 4.6: Indentation modulus E_{ind} (top), hardness H_{ind} (middle) and W_{elast}/W_{tot} (bottom) in transverse direction as a function of indentation depth using conical (left) and spherical indenters (right) for varying ζ_0 and D_c.

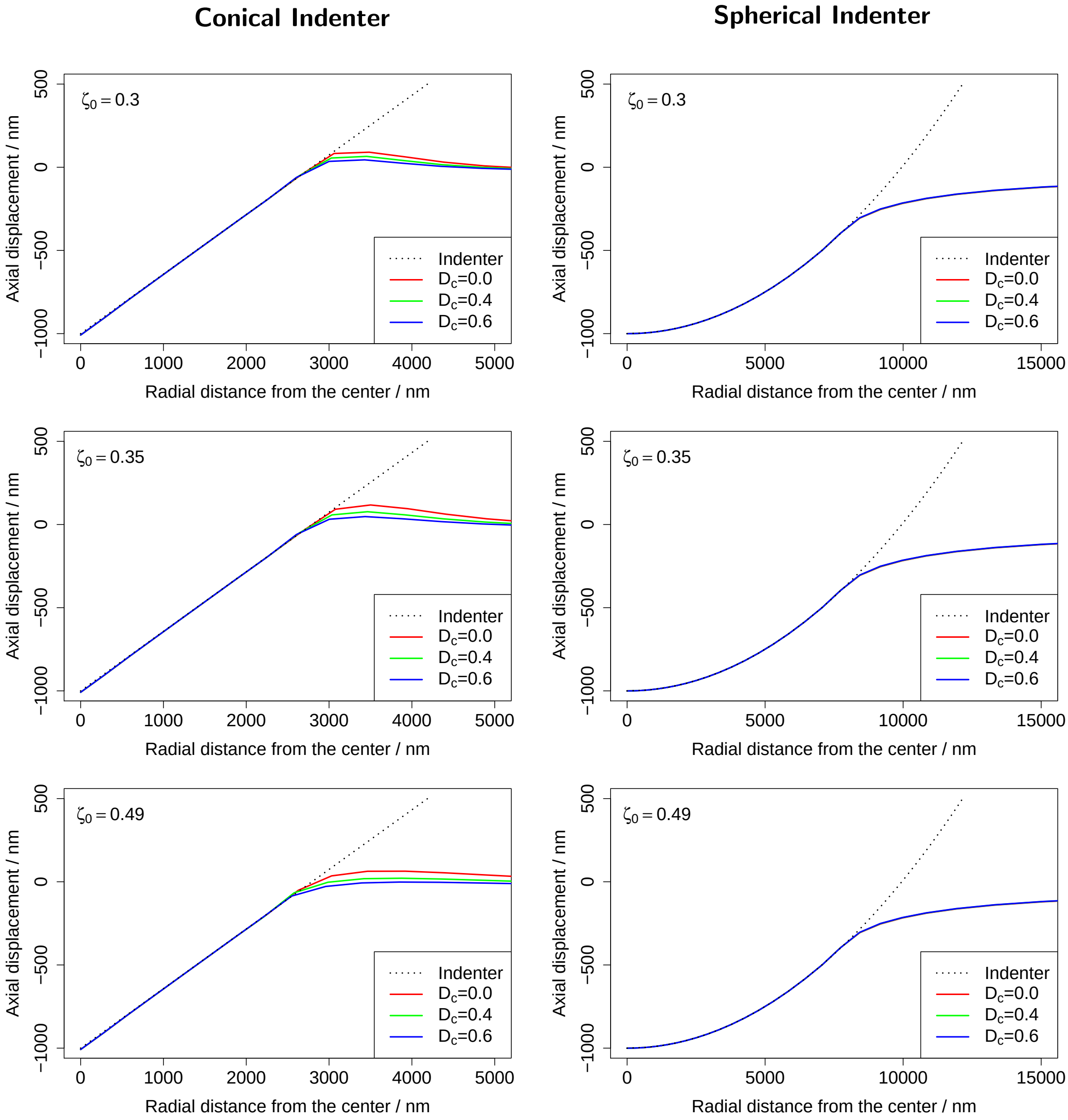

Figure 4.7: Depth profile at maximum load for conical (left) and spherical indentation (right) in transverse direction for $\zeta_0 = 0.3$ (top), $\zeta_0 = 0.35$ (middle) and $\zeta_0 = 0.49$ (bottom) and varying D_c.

5

From the manuscript published in:
Nature Materials 13, 740–747, 2014

In situ micropillar compression of lamellar bone reveals superior strength and ductility but no damage

J.J. Schwiedrzik[1], R. Raghavan[2,3], A. Bürki[1], V. LeNader[2], U. Wolfram[1], J. Michler[2],
P.K. Zysset[1]

[1]Institute for Surgical Technology and Biomechanics, University of Bern, Stauffacherstr. 78, CH-3014 Bern, Switzerland
[2]EMPA, Swiss Federal Laboratories for Materials Science and Technology, Laboratory of Mechanics of Materials and Nanostructures, Feuerwerkerstr 39, CH-3602 Thun, Switzerland
[3]Max-Planck-Institut für Eisenforschung, Structure and Nano/Micromechanics of Materials, Max-Planck-Str. 1, D-40237 Düsseldorf, Germany

5.1 Abstract

Aging societies suffer from an increasing incidence of bone fractures. Bone strength depends on the amount of mineral measured by clinical densitometry, but also on the micromechanical properties of the bone hierarchical organization. Here, we investigated the mechanical response under monotonic and cyclic compression of both single osteonal lamellae and macroscopic samples containing numerous osteons. Micropillar compression tests in a scanning electron microscope, microindentation and macroscopic compression tests were performed on dry ovine bone to identify elastic modulus, yield stress, plastic deformation, damage accumulation and failure mechanisms. We found that isolated lamellae exhibit a plastic behavior with higher yield stress and ductility but no damage. In agreement with a proposed rheological model, these experiments illustrate a transition from a ductile mechanical behavior of bone at the microscale to a quasi-brittle response driven by the growth of cracks along interfaces or in the vicinity of pores at the macroscale.

5.2 Introduction

Bone is a hierarchical composite material featuring a cell-seeded mineralized collagen matrix. It is designed for mechanical support, metabolizing minerals and storing bone marrow [Fratzl and Weinkamer, 2007, Weiner et al., 1999] and mostly loaded in compression in everyday activities [Currey, 2002]. Mineralized collagen fibrils surrounded by extrafibrillar mineral particles [Currey, 1969, 2002, Lees et al., 1990] combine into fibril arrays. In lamellar bone, parallel fibril arrays form lamellae in a rotated plywood pattern [Giraud-Guille, 1988, Weiner et al., 1997]. Osteocytes and their processes inhabit the lacuno-canalicular network which makes up for about 1 % of whole bone porosity [Martin, 1984]. Human compact bone consists of lamellae arranged concentrically around blood vessels forming osteons with a porosity of around 6 % [Fratzl and Weinkamer, 2007]. In large, fast growing animals an alternative tissue type, the so called fibrolamellar bone, is laid out first and converted to osteonal bone through a remodeling process [Currey, 2002].

Biomechanical testing of bone on the macroscale has been performed for more than a century. However, many challenges remain, mostly due to spatial, inter-subject, age, and disease variation of mechanical properties [Cowin, 2001, Keaveny et al., 2003]. Analysis of bone as a hierarchical composite is an important field in biomechanics [Fratzl and Weinkamer, 2007, Hellmich et al., 2011, Rho et al., 1998] trying to understand and predict whole bone properties more accurately by considering its mechanical behavior on the lower length scales. However, so far it suffers from a lack of direct measurements of postyield properties on the microscale.

There is evidence on the continuum level that bone shows two simultaneous mechanisms of energy dissipation on the macroscale when loaded quasi-statically past the yield point: inelastic deformation of the material and damage (i.e. reduction of stiffness through the formation of microcracks) [O'Brien et al., 2002, Sun et al., 2010, Zioupos et al., 2008]. Negative fibril strains following macroscopic tensile yielding found by Gupta et al. [Gupta et al., 2006] hint at damage as a dissipation mechanism on a lower length scale. However, these findings on the microscale were reported following macroscopic tests and are therefore influenced by the microstructure of the tested specimens. Therefore, it is necessary to perform tests directly on the microscale in order to decouple material and structural effects.

Indentation is a mechanical testing technique in which a tip with known geometry is pressed into a flat sample surface and force and tip displacement are recorded. The pioneering work of Oliver and Pharr [Oliver and Pharr, 1992] allows us to extract elastic properties from the unloading part of the indentation curve. Indentation in bone with depths up to 1 µm mainly aims at characterizing the mechanical properties on the lamellar (3-7 µm) level [Lewis and Nyman, 2008, Zysset et al., 1999]. Finite element simulations of indentations using coupled plasticity and damage models have shown that damage may explain some of the experimental findings for bone like a reduced unloading stiffness [Lucchini et al., 2011, Zhang et al., 2010] and that strength on the microlevel seems to be similar to the macroscopic values. However, it is very difficult to uniquely interpret such experimental data in materials featuring dissipative processes, as indentations in materials with different behaviors can result in very similar curves [Chen et al., 2007]. Therefore, independent experiments allowing a straightforward interpretation are necessary in order to assess the deformation mechanisms and postyield behavior of bone at the microscale.

Such an experimental setup for micromechanical testing is micropillar compression. Micron sized pillars are produced by erosion of material using a focused ion beam (FIB) and used to extract mechanical properties of all classes of materials [Howie et al., 2012, Michler et al., 2007]. Due to the uniaxial loading conditions as opposed to the complex stress states during indentations, the setup allows a straightforward interpretation of the data. Also, this technique is ideal for studying the effects of size in quasi-brittle materials [Bažant, 2004] in terms of determining the postyield properties and deformation mechanisms by circumventing premature fracture [Howie et al., 2012, Michler et al., 2007, Östlund et al., 2009, 2011].

For brittle materials like ceramics failure is associated with the growth of cracks originating from pores, surface scratches or other preexisting defects. When testing smaller specimens, the probability that a defect of a certain critical size is present in the material decreases, which leads to an increased failure stress [Griffith, 1921]. When reaching very small sample sizes, no defects of critical size may be present and alternative dissipative processes like dislocation based plasticity dominate [Michler et al., 2007]. In bone, the hierarchical structure leads to a macroscopically quasi-brittle behavior where plasticity and cracking both play a significant role and the associated scaling law remains to be investigated.

The aim of this study was therefore to investigate: what is the anisotropic uniaxial compressive strength of lamellar bone at the microscale; what are the dominating deformation and failure mechanisms under compression in the postyield regime on the microscale; and how do these properties compare to the macroscopic response? Based on the reviewed literature [Carnelli et al., 2011, Gupta et al., 2006, Hengsberger et al., 2002, Lucchini et al., 2011, Zhang et al., 2010], we intend to test two hypotheses: 1. The compressive strength of bone is similar on the lamellar and macroscopic level. 2. Under compression, bone deforms inelastically in a quasi-brittle fashion by formation of cracks on several length scales, which lead to a reduction of stiffness at both levels.

In order to test these hypotheses, *in situ* micropillar compression tests using monotonic and cyclic loading protocols and microindentation tests were performed on dry ovine osteonal bone in axial and transverse direction and compared to macroscopic uniaxial compression tests using the same sample geometry and loading protocol.

5.3 Materials and Methods

Sheep tibiae were acquired from a local butcher shop. Ovine bone is mostly primary, features less porosity and a more homogeneous but similar mineralization to human bone [Pearce et al., 2007, Ravaglioli et al., 1996], making it an attractive model for human bone on the microlevel. Axial and transverse specimens were cut from the diaphyses with a diamond-coated band saw (Exact, Germany). They were embedded in, but not infiltrated by, polymethylmethacrylate (PMMA) and subsequently air-dried [Wolfram et al., 2010a] for more than 48 h. Finally, they were ultramilled (Polycut E, Reichert-Jung, Germany) to obtain a flat surface for the Raman, microindentation and micropillar compression experiments.

Raman spectroscopy was performed on a transverse control sample in dry condition using an upright Raman microscope (Nova Spectra, ND-MDT, Russia) featuring a laser source with a wavelength of 633 nm, 5 mW power and a 100x objective with a numerical aperture of 0.95. Spectra were recorded at a spectral resolution of 3 cm^{-1}. The exposure time was 1 s.

The Raman spectra corresponded well to the literature [Morris and Mandair, 2011] and all characteristic peaks could be identified. Based on previous work on bone quality assessment using vibrational spectroscopy [Akkus et al., 2004, Yerramshetty et al., 2006], three physicochemical properties of the tissue were investigated: mineralization, i.e. the ratio

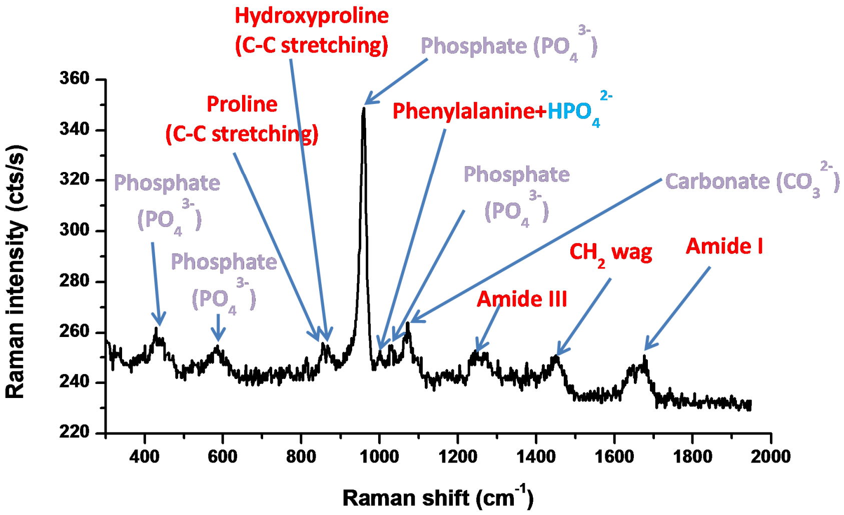

Figure 5.1: Raman spectrum of ovine cortical bone. Representative spectrum from an osteonal region with identified peaks.

of mineral to organic components, substitution of carbonate ions in phosphate positions, and mineral cristallinity, i.e. the orderliness of the crystal lattice. The calculation of these properties is explained in Fig. 5.2. Mineralization was found to be 11.0 ± 1.1, carbonate substitution 7.6 ± 0.8, and crystallinity 19.6 ± 0.4 cm^{-1} (N=10). This is reasonably similar to the results of Yerramshetty et al. [Yerramshetty et al., 2006], who found a mineralization of 8.0 to 10.0, carbonation of 4.5 to 5.3 and crystallinity of 16.7 to 19.2 cm^{-1} in hydrated human femoral bone. It can therefore be concluded that the chemical composition of the tested samples was in the expected range and that ovine bone is indeed a reasonable model for human bone on the microscale.

Microindentations were performed in dry and wet state in osteonal regions with an Ultra Nano Hardness Tester (UNHT, CSM Instruments, Switzerland). For the wet nanoindentations, control samples were rehydrated for at least 1.5 h in Hank's balanced saline solution (HBSS) following the protocol of Wolfram et al. [Wolfram et al., 2010a] and subsequently indented in a HBSS submersion. A trapezoidal protocol in load control up to a maximum depth of 1 µm with a loading rate of 100 mN/min, holding time of 30 s [Wolfram et al., 2010a] and unloading rate of 400 mN/min was chosen to minimize the effects of creep. Indentation modulus and hardness, elastic and total work were extracted using standard methods [Oliver and Pharr, 1992, Reisinger et al., 2011, Wolfram et al., 2010a]. Indentation modulus is recovered from the reduced modulus E_r [Oliver and Pharr, 1992] by the equation

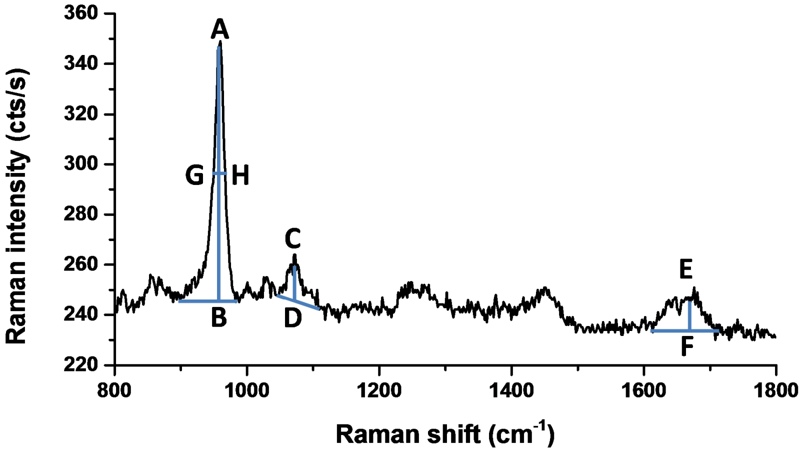

Figure 5.2: Measurements on Raman spectrum of ovine cortical bone in order to measure mineralization, carbonate substitution and crystallinity based on [Akkus et al., 2004]. Mineralization=AB/EF, Substitution=AB/CD, Crystallinity=GH.

$$E^* = \left(\frac{1}{E_r} - \frac{1-\nu_i^2}{E_i}\right)^{-1} \tag{5.1}$$

for known isotropic constants E_i and ν_i of the indenter tip. Indentation hardness is defined as the maximum load divided by the contact area at maximum depth, elastic and total work as the area under the unloading curve and the loading and holding curves. A transversely isotropic stiffness tensor was fitted to the indentation moduli using the method of Franzoso et al. [Franzoso and Zysset, 2009] to obtain estimates for apparent moduli. For the wet indentations in transverse direction, a swelling effect similar to the one reported in [Spiesz et al., 2012] was found that increases surface roughness and affects the experimental curves. This data was therefore not used for further analysis.

After indentation, the samples were extracted from the embedding material and glued on SEM stubs using silver adhesive. A 50 nm thick Au-Pd film was sputtered on the specimens to minimize drift due to charging. A dual beam FIB workstation (Tescan Lyra, Czech Republic) operated at 30 kV was used to machine micropillars of 5 µm diameter and aspect ratio of 2 in osteonal regions, and to section them after testing. Micropillars were aligned with the longitudinal and circumferential directions of the respective osteons. The micropillars were machined to the desired dimensions in three major steps: First, circular trenches of 50 µm diameter were machined with 6000 pA to obtain 10 µm diameter posts, which were milled down to 6 µm with 1000 pA and polished to 5 µm with 300 pA.

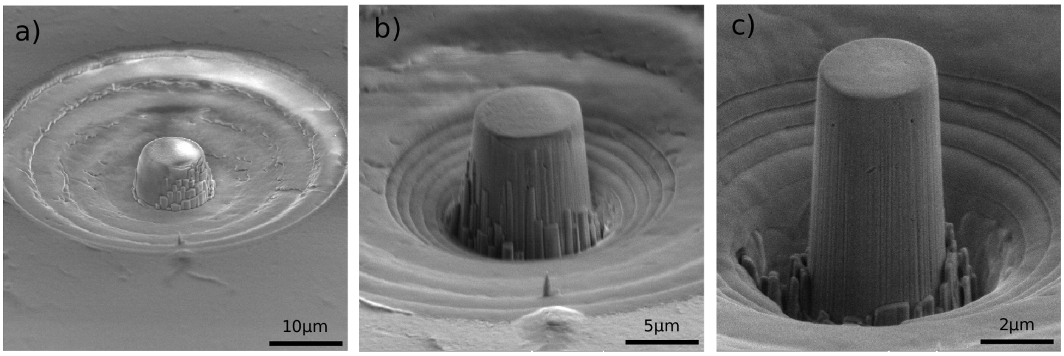

Figure 5.3: SEM micrographs showing the micropillar machining process. a) Micropillar after trench milling with 6000 pA, b) after intermediate step with 1000 pA, c) after final polishing step with 300 pA.

FIB induced damage and Gallium implantation at the surface are common problems in micropillar compression studies. In order to assess these effects, Monte Carlo simulations using the software SRIM [Ziegler and Biersack, 1985] with an incidence angle of 3°, 30 keV Ga^+ ions, and the material composition for cortical bone ICRU-119 from the software's compound library were performed. They showed that damage on the side of the pillars are confined to a layer of 25 nm and can therefore be neglected [Michler et al., 2007] from a mechanical point of view. The calculated ion range is 8.7 ± 5.9 nm and therefore also neglectable. These results are in line with the study of Nalla et al. [Nalla et al., 2005], who report no significant FIB damage for mineralized tissues.

A total of 60 micropillars were fabricated, out of which 40 were used for quasi-static, monotonic tests and 10 for cyclic loading tests. Micropillars were compressed using an *in situ* indenter (Alemnis, Switzerland) [Rabe et al., 2004] inside a SEM (Zeiss, Germany) operated at 5 kV, allowing precise alignment and tracking of the deformation. A diamond flat punch (Synton-MDP, Switzerland) of 10 µm diameter and cone angle of 45° was used to compress the micropillars in displacement control at a rate of 5 nm/s, corresponding to a strain rate of $\sim 5 \times 10^{-4}$ s^{-1}. A schematic drawing of the experimental setup is shown below.

Post-failure micrographs were taken using a HRSEM (Hitachi, Japan) operated at 3 kV and 55° specimen tilt. The displacement data was corrected for instrument frame compliance and sink-in of the micropillar using the so called Sneddon approach proposed by Zhang et al. [Zhang et al., 2006] with a fillet radius of 300 nm.

Engineering stress-strain data was obtained by dividing force by the average cross sectional area and compliance-corrected displacement by the height of each micropillar and converted

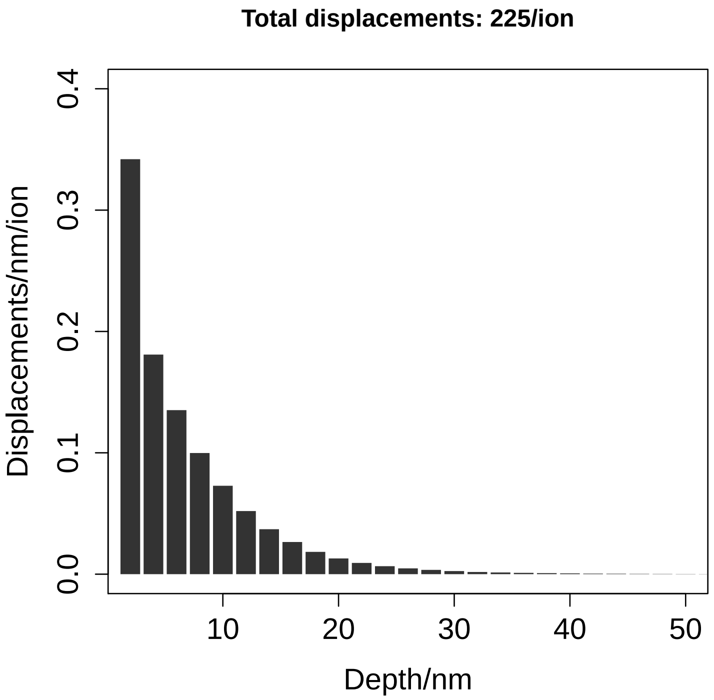

Figure 5.4: FIB damage distribution determined by means of a Monte Carlo simulation using the software SRIM. Atomar displacements/nm/ion due to ion bombardment and damage cascade as a function of radial distance from the surface/nm.

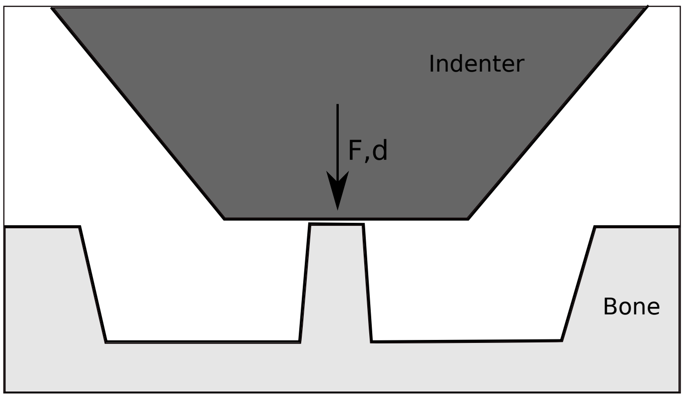

Figure 5.5: Sketch of the experimental setup of the micropillar compression experiments. A flat punch indenter is placed on top of the micropillar that is surrounded by a trench. The indenter is then moved downward and tip displacement as well as the axial force are recorded.

to true stress-strain measures, i.e. Cauchy stress σ and logarithmic stretch lnU, using the assumption of negligible volume change [Ashby and Jones, 1980].

$$\sigma = \sigma_{Eng}(1 + \epsilon_{Eng}) \tag{5.2}$$

$$lnU = ln(1 + \epsilon_{Eng}) \tag{5.3}$$

For the monotonic tests, samples were loaded in displacement control until failure. Yield stress was determined using the 0.2 % offset rule, ultimate stress is the maximum stress in the true stress-strain curve. For cyclic loading, samples were loaded in displacement control with 5 intermittent cycles with an amplitude of 100 nm after every 200 nm of loading until failure. The apparent modulus E_{app} was determined by fitting a line to the last of each 5 cycles. Modulus was normalized with respect to the one measured during the second cycle to minimize the influence of the toe region. A schematic drawing explaining the cyclic micropillar compression analysis is shown below.

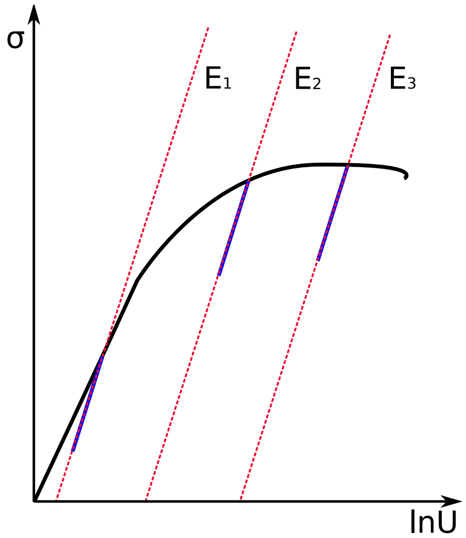

Figure 5.6: Sketch depicting the analysis of cyclic experiments. Monotonic loading phases are drawn in black, intermittent cycles in blue. Apparent moduli E_i were measured during every cycle and divided by the apparent modulus of the intermittent cycle in the elastic phase E_1.

Plastic strains were determined using

$$lnU_{33}^{p} = lnU_{33} - \frac{\sigma_{33}}{E_{app}}. \tag{5.4}$$

For the macroscopic tests, samples were cut from the diaphyses of ovine tibiae using a diamond-coated bandsaw and subsequently lathed to a dumbbell-shaped form with a diameter of 3 mm and an aspect ratio of 2 for the reduced section using a desktop lathe. The samples were dried for more than 48 h and subsequently tested in a servo-hydraulic testing device (858 Mini Bionix, MTS, USA). The machine was operated displacement controlled at a rate of 18 µm/s (strain rate $\approx 5 \times 10^{-4}\,\mathrm{s}^{-1}$) with 5 intermittent cycles with an amplitude of 0.125 % after every 0.25 % of strain until failure. An extensometer (Epsilon Tech., USA) was attached to the reduced section with an initial gauge length of 6 mm. True stress-strain data and moduli were obtained the same way as described for the cyclic micropillar experiments.

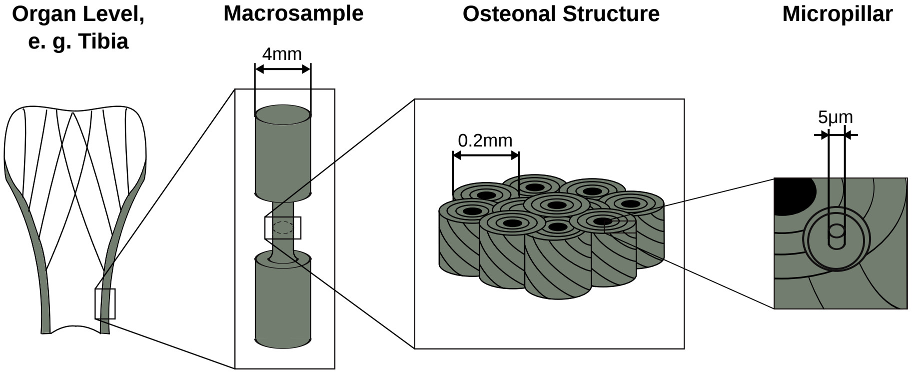

Figure 5.7: Tested samples and relevant bone structures. Dumb-bell shaped macrosamples extracted from the diaphysis of ovine tibiae and micropillars on the length scale of osteonal lamellae.

All data manipulations and statistical analysis were performed using R [R Development Core Team, 2008]. Normality of distributions was tested by visual inspection of normalized quantile-quantile plots against the standard normal distribution and the Shapiro-Wilk normality test [R Development Core Team, 2008, Shapiro and Wilk, 1965]. Measurements are reported as mean ± standard deviation. Significant differences were tested using two-tailed t-tests. Influence of measured parameters on the data was tested by ANOVA and linear regressions using dummy coding for categorical variables. The significance threshold was chosen as $p = 0.01$.

5.4 Rheological model

The rheological model consists of an elastic spring in series with a plastic slider that breaks beyond a given ultimate plastic strain. The series arrangement leads to an additive decomposition of the elastic and plastic strains

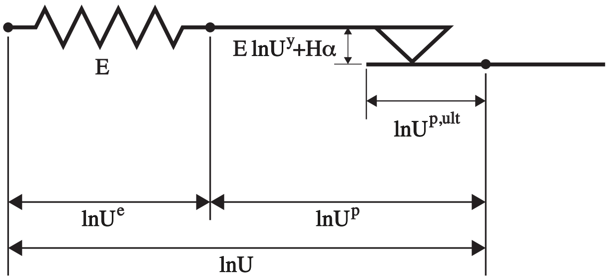

Figure 5.8: Underlying rheological model and constitutive law. Elasto-plastic material with linear hardening and brittle failure when the slider quits the support after passing $\ln U^{p,ult}$.

$$\ln U = \ln U^e + \ln U^p \tag{5.5}$$

The spring represents a proportional relationship between the stress and the elastic strain and leads to the free energy:

$$\begin{aligned} \psi(\ln U, \ln U^p) &= (1 - \mathcal{H}(-\ln U^p - \ln U^{p,ult}))\frac{1}{2}E(\ln U - \ln U^p)^2 \\ &\quad -\mathcal{H}(\ln U^p - \ln U^{p,ult})\frac{1}{2}E(\ln U - \ln U^p)^2 \end{aligned} \tag{5.6}$$

where E is Young's modulus, $\ln U^{p,ult}$ is the ultimate or failure strain of the plastic slider and $\mathcal{H}$ is the Heaviside unit step function.

Remark 1. *This formulation of the free energy corresponds to a discontinuous damage model with*

$$D = \mathcal{H}(-\ln U^p - \ln U^{p,ult}) + \mathcal{H}(\ln U^p - \ln U^{p,ult})$$

The total stress is given by the derivative of the free energy with respect to the total strain:

$$\begin{aligned}\sigma(\ln U, \ln U^p) &= \frac{\partial \psi}{\partial \ln U} \\ &= (1 - \mathcal{H}(-\ln U^p - \ln U^{p,ult}))E(\ln U - \ln U^p) \\ &\quad -\mathcal{H}(\ln U^p - \ln U^{p,ult})E(\ln U - \ln U^p)\end{aligned} \tag{5.7}$$

The plastic stress is the derivative of the free energy with respect to plastic strain:

$$\begin{aligned}\sigma^p(\ln U, \ln U^p) &= -\frac{\partial \psi}{\partial \ln U^p} \\ &= \delta(-\ln U^p - \ln U^{p,ult})\frac{1}{2}E(\ln U - \ln U^p)^2 \\ &\quad +\delta(\ln U^p - \ln U^{p,ult})\frac{1}{2}E(\ln U - \ln U^p)^2 + \sigma\end{aligned} \tag{5.8}$$

where δ is the Dirac delta function.

The behavior of the plastic slider is described by a yield function for the plastic stress,

$$f(\sigma^p) = |\sigma^p| - E \ln U^y - H\alpha \tag{5.9}$$

with the classical Kuhn-Tucker conditions for f and $\dot{\lambda} = |\ln \dot{U}^p|$

$$f \leq 0 \qquad \dot{\lambda} \geq 0 \qquad f\dot{\lambda} = 0 \tag{5.10}$$

where $\ln U^y$ is the yield strain, H is the hardening modulus and the accumulated plastic strain α is expressed by:

$$\alpha = \int_0^t |\ln \dot{U}^p| d\tau \tag{5.11}$$

The plastic stress is finally given by

$$\sigma^p = \begin{cases} -E \ln U^y - H\alpha & \text{if } \ln \dot{U}^p < 0 \\ [-E \ln U^y - H\alpha; E \ln U^y + H\alpha] & \text{if } \ln \dot{U}^p = 0 \\ E \ln U^y + H\alpha & \text{if } \ln \dot{U}^p > 0 \end{cases} \tag{5.12}$$

From an algorithmic point of view, computation of the plastic strain flow for a new total strain $\ln U_{n+1}$ can be initiated with a trial stress based on the plastic strain of the previous step n:

$$\sigma_t^p = E(\ln U_{n+1} - \ln U_n^p) \tag{5.13}$$

If the yield criterion is respected for that plastic state

$$f(\sigma_t^p) \leq 0 \tag{5.14}$$

then the total stress reduces to

$$\sigma_{n+1} = \sigma_t^p \tag{5.15}$$

If the yield criterion is violated

$$f(\sigma_t^p) > 0 \tag{5.16}$$

then the implicit projection of the plastic stress on the yield criterion provides an equation for $\ln U_{n+1}^p$

$$f(\sigma^p(\ln U_{n+1}, \ln U_{n+1}^p)) = 0 \tag{5.17}$$

The solution of the above equation is:

$$\ln U_{n+1}^p = \ln U_n^p + \mathrm{sign}(\sigma_t^p)\frac{|\sigma_t^p| - (E \ln U^y + H\alpha_n)}{E + H} \tag{5.18}$$

and the total stress is updated with

$$\sigma_{n+1} = E(\ln U_{n+1} - \ln U_{n+1}^p) \tag{5.19}$$

In case of failure of the plastic slider, i.e. $|\ln U_{n+1}^p| \geq \ln U^{p,ult}$, the total stress vanishes abruptly

$$\sigma_{n+1} = 0 \tag{5.20}$$

The dissipation of the model is the usual dissipation of the plastic slider plus the elastic energy of the spring released by breakage of the slider when $|\ln U^p| = \ln U^{p,ult}$,

$$\begin{aligned} \phi(\ln \dot{U^p}) &= \sigma^p \ln \dot{U^p} \\ &= \sigma \ln \dot{U^p} + \delta(\ln U^p + \ln U^{p,ult})\frac{1}{2}E(\ln U - \ln U^p)^2 \\ &\quad + \delta(\ln U^p - \ln U^{p,ult})\frac{1}{2}E(\ln U - \ln U^p)^2 \end{aligned} \tag{5.21}$$

and vanishes beyond failure of the plastic slider.

Remark 2. *The model degenerates into an elastic material for* $\ln U^y \to \infty$*, a perfectly* *elasto-plastic material for* $\ln U^{p,ult} \to \infty$ *or into an elastic and perfectly brittle material for* $\ln U^{p,ult} = 0$*. In the case of* $\ln U^{p,ult} = 0$*, the damage model of Krajcinovic [Krajcinovic et al., 1987] is obtained for a homogeneous distribution governing the yield stress.*

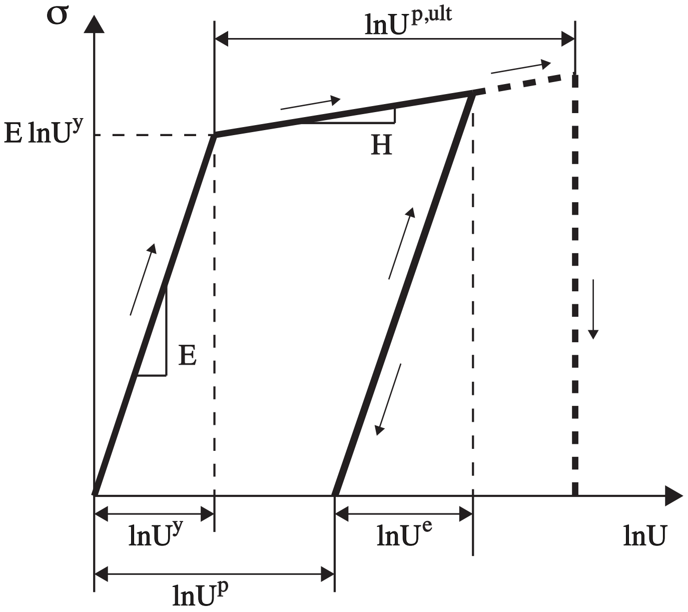

Figure 5.9: Stress-strain behavior. Elasto-plastic material response with linear hardening and subsequent failure.

The model consists of a parallel array of 100 parallel elements. The total response is given by the summation over all elements. For the micropillars, all material properties are governed by the experimentally measured normal distributions. On the other hand, a macroscopic bone sample will contain bone structural units with a distribution of microcracks along cement lines, at the vicinity of lacunae, vascular pores or other defects. Since micro-cracks develop continuously with fatigue loading of the bone tissue, uniform distributions of yield strain and ultimate plastic strain up to the mean values observed in micro-pillar compression tests were assumed, which is in line with the argument made by Krajcinovic [Krajcinovic et al., 1987] in a damage model for bone under tension.

Table 5.1: Material constants of extracellular bone matrix.

	E/GPa	H/GPa	$\ln U^{y}$	$\ln U^{p,ult}$
Axial	31.2 ± 3.12	0.0312 ± 0.0031	0.0241 ± 0.0019	0.08 ± 0.008
Transv.	16.5 ± 1.65	3.5 ± 0.35	0.0182 ± 0.0015	0.1 ± 0.01

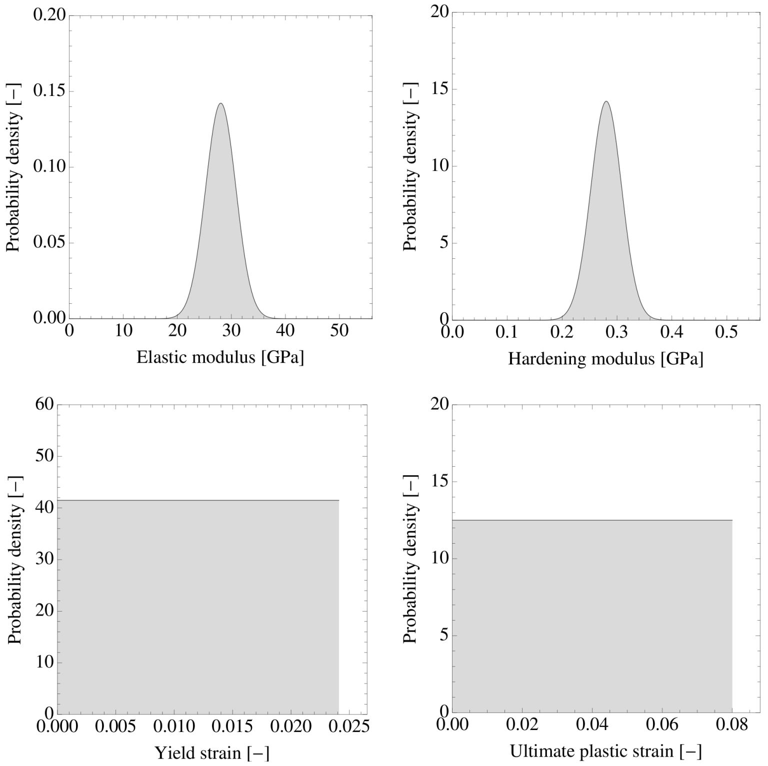

Figure 5.10: Distributions of material properties for a macroscopic sample. Distributions of elastic modulus, hardening modulus, yield strain and ultimate plastic strain for the axial direction of bone structural units.

5.5 Results

Micropillar diameter and aspect ratio before testing were determined by scanning electron microscopy (SEM) to be 5.21 ± 0.14 µm (mean ± standard deviation) and 2.13 ± 0.10. Based on the *in situ* observation of the micropillar compression tests in a SEM and high resolution SEM (HRSEM) pictures taken after testing (Fig. 5.11), the failure modes were classified into three groups: shearing, mushrooming, and axial splitting. Under axial compression, 55 % of the pillars failed by development of shear planes, 25 % by mushrooming, i.e. failure on the top of the pillar leading to localized cracking and delamination, and 15 % by an axial split. One pillar failed by compression of a relatively large pore and was removed from the study. All of the pillars oriented in transverse direction failed by shearing.

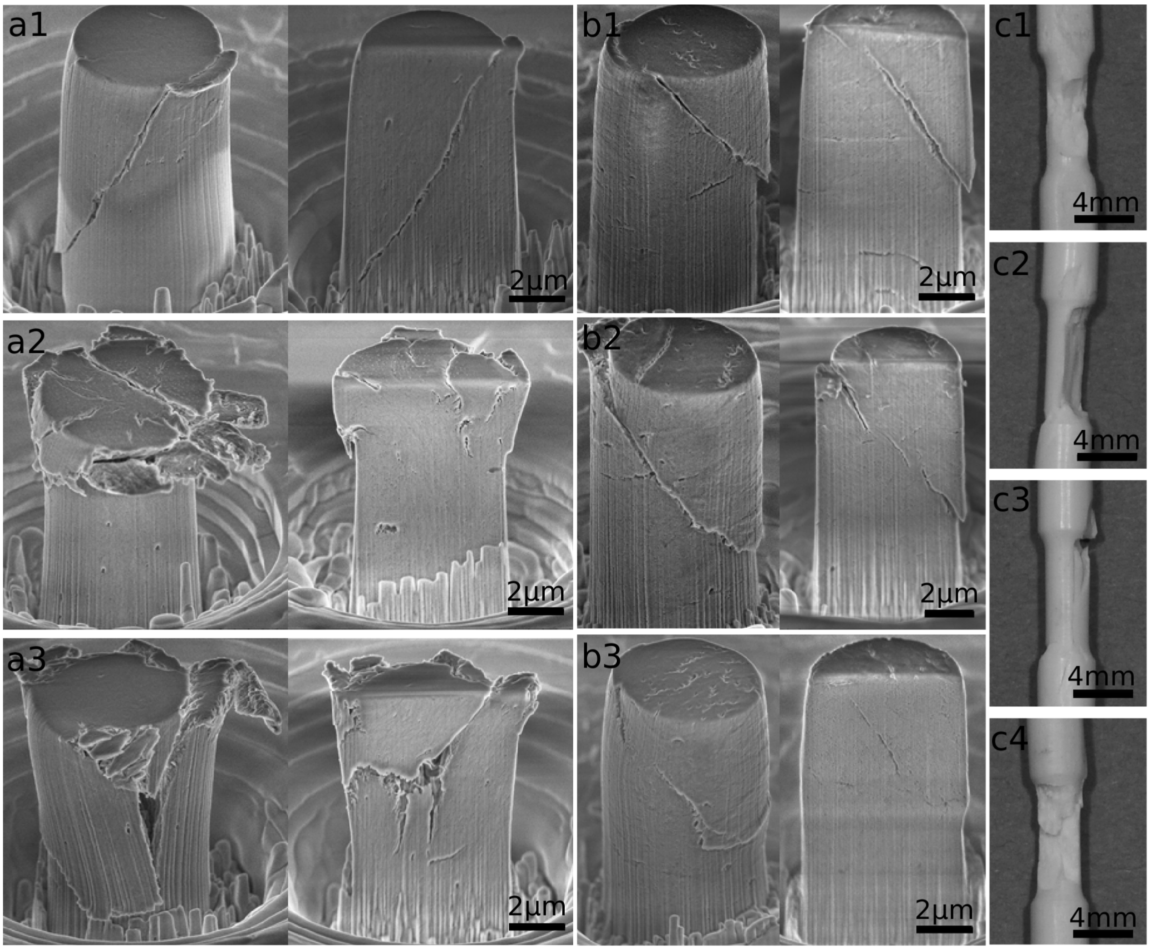

Figure 5.11: Observed failure modes of bone on the micro- and macroscale. HRSEM micrographs taken after testing, FIB cross-sections and photographs showing failure modes encountered in compression tests a) of micropillars in axial and b) transverse directions as well as c) of macroscopic specimens. Micropillars mostly deformed homogeneously and failed by development of slip planes (a1, b1-b3). A minority of the axial pillars failed by mushrooming (a2) or axial splitting (a3), which is a brittle failure mode. Scale bars for a1-a3 and b1-b3 represent 2 µm, for c1-c4 4 mm.

The true stress-strain curves resulting from the analysis of the quasi-static micropillar compression as well as normalized postyield behavior may be seen in Fig. 5.12. For the micropillars, yield stress was found to be 0.49 ± 0.1 GPa in axial ($N = 19$) and 0.30 ± 0.02 GPa in transverse direction ($N = 20$), strength was 0.75 ± 0.06 GPa and 0.59 ± 0.04 GPa, respectively. The postyield behavior depended on the failure mode. Strain hardening/softening behavior was observed in the case of mushrooming and splitting, continuous hardening until failure in the case of shearing (Fig. 5.12 bottom). A linear regression model showed that testing direction was a significant parameter ($p = 9 \times 10^{-10}$) and could explain 71.9 % of the variation of strength and 63.8 % of the yield stresses, while failure mode was not a significant parameter ($p = 0.1$). When assessing the pillars that showed shear failure only, direction alone accounts for 84 % of the variation of strength and 74.8 % of the yield stresses. For 22 out of the 31 pillars that failed by localization in a single shear plane, the inclination angle could be measured and was found to have a mean of $46.63 \pm 8.94°$, with no significant difference between axial and transverse directions ($p = 0.63$). For this data subset, the critical shear stress along the plane of failure was computed and analyzed using analysis of variance (ANOVA). It was found that only loading direction was a significant parameter ($p = 2 \times 10^{-6}$) with critical shear stresses of 0.356 ± 0.028 GPa in axial and 0.280 ± 0.026 GPa in the transverse direction. HRSEM micrographs of the slip planes of micropillars failed by shearing revealed three main toughening mechanisms of bone: isolated fibril bridging as well as ligament bridging and crack deflection. Fibril bridging was almost exclusively observed in axial micropillars.

The apparent modulus measured during the cyclic micropillar compression (Fig. 5.13) was found to be 31.16 ± 6.46 GPa in axial ($N = 5$) and 16.5 ± 1.50 GPa in transverse direction ($N = 5$). Analysis of the normalized apparent modulus as a function of plastic strain showed that the stiffness is not reduced after overloading of the sample to up to 8 % plastic strain (Fig. 5.13). A linear regression showed no significant change of normalized apparent modulus as a function of plastic strain ($p = 0.188$, RMS error = 0.032, $N = 50$) for the pillars that failed by development of a slip plane. When fitting only the axial pillars that failed in shear, a non-significant slope was found ($p = 0.026$) predicting a 5 % modulus reduction at 8 % of plastic strain, which is 20 times smaller than for the macroscopic data reported later in this manuscript.

Microindentation showed also a clear anisotropy of mechanical properties. The measured values for indentation modulus, hardness and work in wet and dry state may be seen in Tab. 5.2 and are in accordance with values for dry human osteonal bone of Reisinger et al. [Reisinger et al., 2011], who reported indentation moduli of 27.6 ± 3.3 GPa and 20.5 ± 1.9 GPa in the axial and transverse directions. A mean stiffness tensor was fitted to the average dry indentation moduli using the methodology of Franzoso and Zysset [Franzoso and Zysset, 2009]. The resulting predicted apparent moduli were found to be 28.97 GPa in axial and 16.07 GPa in transverse direction, respectively.

Visual inspection of 2 cross sections in 15 of the macroscopic samples showed that $\sim 50\%$

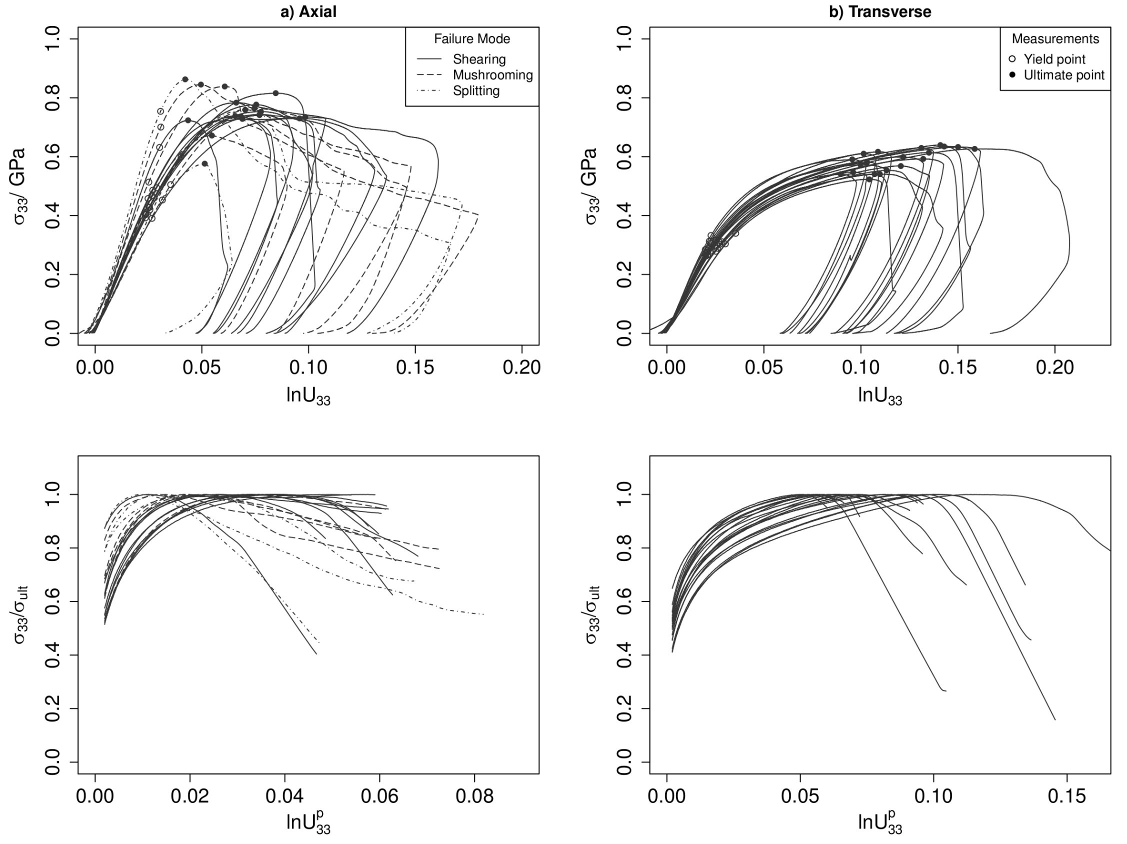

Figure 5.12: Experimental curves and postyield behavior of monotonic micropillar compression tests. True stress-strain (σ_{33}-lnU_{33}) curves (top) and postyield behavior normalized with ultimate stress as a function of plastic strain (bottom) of monotonic micropillar compression in a) axial and b) transverse direction. Observed yield points are indicated by hollow circles and ultimate points by full circles.

Table 5.2: Mean ± standard deviation of the indentation modulus E^*, indentation hardness H_{IT}, elastic W_{el} and total Work W_{tot} as well as number of experiments N for wet and dry indentations in axial and transverse directions.

Hydr.	Direct.	E^*/GPa	H_{IT}/GPa	W_{el}/pJ	W_{tot}/pJ	N
Dry	Axial	27.5 ± 2.2	1.01 ± 0.13	1837 ± 258	8069 ± 1012	50
Dry	Transv.	19.0 ± 1.8	0.67 ± 0.08	1636 ± 214	6482 ± 745	72
Wet	Axial	22.8 ± 1.6	0.60 ± 0.11	1083 ± 249	4849 ± 907	67
Wet	Transv.	14.5 ± 1.6	0.51 ± 0.08	1313 ± 204	4125 ± 756	83

of them were entirely secondary osteonal, the others showed a mixture of fibrolamellar and osteonal bone. During the macroscopic cyclic tests apparent moduli of 25.74 ± 3.71 GPa and strength of 0.314 ± 0.043 GPa were measured ($N = 26$). The stress-strain curves and normalized modulus evolution as a function of plastic strain are shown in Fig. 5.13. The macroscopic samples showed a significantly lower strength than the micropillars ($p < 2 \times 10^{-16}$) and a much more brittle behavior. The samples failed mostly at less than 1.2 % of plastic strain, which is 6 times less than on the microscale and consistent with the literature [Chamay, 1970]. Ductility of the osteonal samples was not higher than for the rest of the group. It was found that modulus was significantly reduced as a function of plastic strain (Fig. 5.13, $p = 2.4 \times 10^{-10}$, $adj.\ R^2 = 0.3, N = 116$), which is consistent with reports for tension [Keaveny et al., 2003, Zioupos et al., 2008].

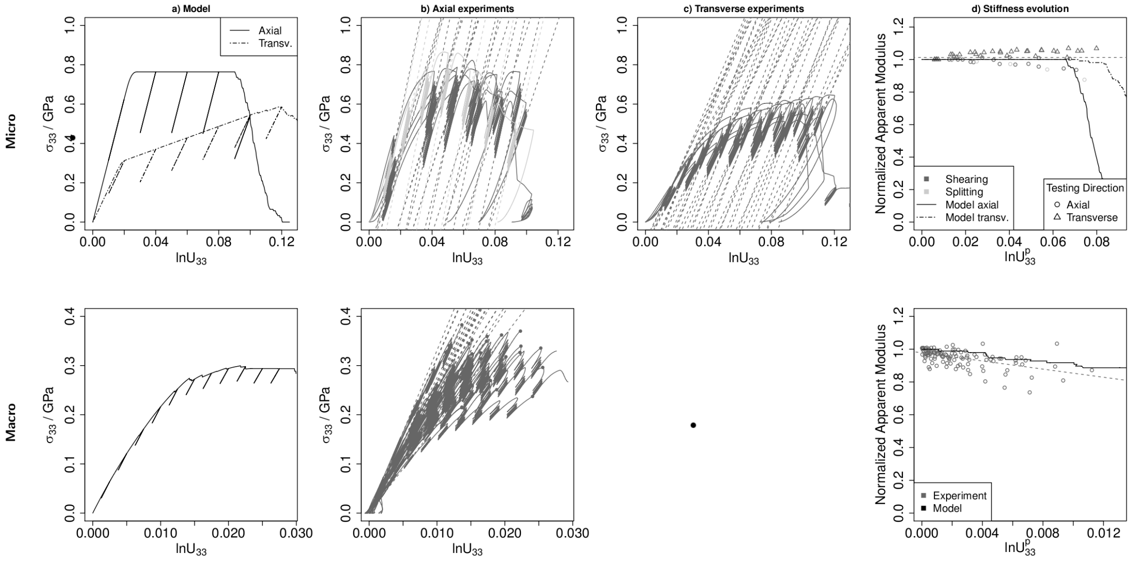

Figure 5.13: Model predictions, experimental curves and normalized apparent modulus evolution of cyclic compression tests on the micro- and macroscale. a) Model predictions, experimental true stress-strain curves in b) axial and c) transverse direction and d) normalized apparent modulus evolution as a function of plastic strain of cyclic micropillar (top) and macroscopic (bottom) compression.

A one dimensional rheological model based on elasto-plasticity with failure (Fig. 5.8, 5.9, 5.14) representing bone at the microscale was fed with the means and standard deviations of the elastic modulus, yield stress and maximal plastic strain measured in the micropillar experiments (Tab. 5.1). Using an appropriate plastic hardening law, the resulting stress-strain curves match the experimental data in both axial and transverse directions very well (Fig. 5.13) and no stiffness reduction is observed below 8 % of plastic strain. In order to account for the existing cracks and defects between bone structural units in the macroscopic samples, the rheological model was fed with a homogenous distribution of yield stress and maximum plastic strain bounded by microscale properties (Fig. 5.10). With this single assumption that is in line with the argument made by Krajcinovic [Krajcinovic et al., 1987] in a damage model for bone under tension, the model predicted a strength of 0.3 GPa and a modulus reduction of 11.5 % at a plastic strain of 1.2 %. Also, the predicted stress-strain curve matched the experimental data very well (Fig. 5.13).

5.6 Discussion

The microindentation measurements were in very good agreement with the results reported by Reisinger et al. [Reisinger et al., 2011] for dry human osteonal bone. This confirms that ovine bone is an acceptable model for human tissue at the lamellar level as indicated by [Pearce et al., 2007, Ravaglioli et al., 1996]. The macroscopic strength measured in this study was slightly higher than the 0.272 ± 0.003 GPa reported by Reilly and Burstein [Reilly and Burstein, 1975] for Haversian bovine bone. This is in line with the fact that Haversian systems tend to reduce the strength of primary bone [Currey, 2002]. The depth of the microindentations and the dimensions of the micropillars were chosen to be consistent with the average lamellar thickness of 3-7 µm. Consequently, the apparent modulus of the cyclic tests after correction using the Sneddon approach [Zhang et al., 2006] corresponded very well to the apparent moduli predicted from the microindentation data. Also, the high consistency of the micropillar compressions demonstrated the homogeneity of ovine bone at this length scale in the absence of interfaces such as cement lines. The macroscopic tests were designed with the same aspect ratio and strain rate as the micropillar tests, which allowed to do a direct comparison of the two length scales.

Three distinct failure modes could be identified on the microlevel from the *in situ* observation and post-failure HRSEM micrographs: shearing, mushrooming, and axial splitting. The dominating failure mode was shearing with almost 80 % of the samples showing a highly ductile behavior with continuous hardening until failure by localization in a slip plane. This observed behavior is consistent with oblique or cross-hatched slip lines reported for compressive yielding of compact bone on the macroscale [Chamay, 1970, Currey, 2002]. A minority of the axial micropillars failed by mushrooming associated with boundary effects such as indenter-sample friction or axial splitting, which is a brittle failure mode [Östlund et al., 2011].

The observed postyield behavior of the sheared micropillars was anisotropic: axial pillars had a higher yield to ultimate stress ratio and reached their strength at lower strains than transverse pillars, but failed less rapidly after the maximum stress had been passed.

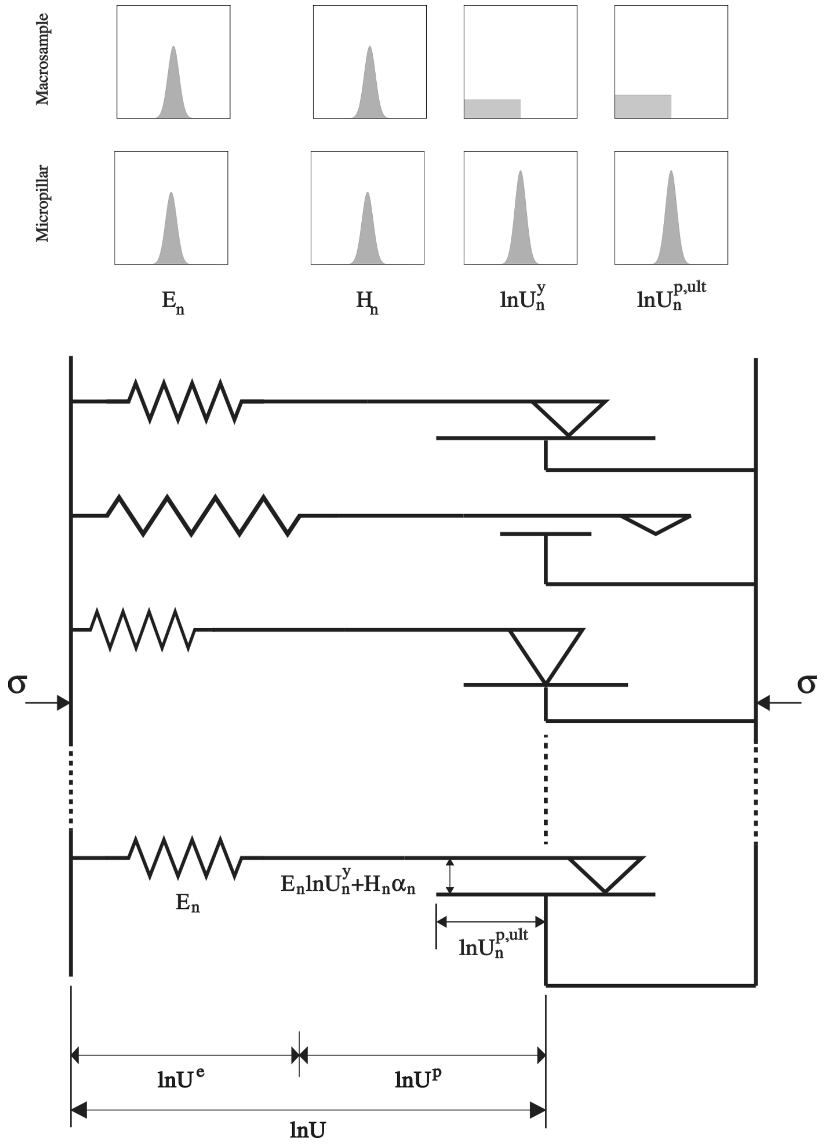

Figure 5.14: Rheological model describing the mechanical response of bone under compression. A parallel array of elastic springs in series with plastic pads failing at a ultimate plastic strain (Fig. 5.8 and 5.9). On the microscale, heterogeneity is governed by Gaussian distributions of the material properties modulus, yield strain, hardening modulus and ultimate plastic strain (Tab. 5.1) identified from the micropillar compression tests. For the macroscale, the presence of cracks, defects and interfaces increases tissue heterogeneity leading to a reduction of strength and ductility. Therefore, uniform distributions between 0 and the microscopic properties are used (Fig. 5.10) to describe variability in strength and ultimate plastic strain corresponding to the pre-existence of defects and microcracks with different lengths from 0 to a critical length.

HRSEM pictures revealed failure planes with ligament bridging, crack deflection, and, almost exclusively for axial pillars, isolated fibril bridging. These phenomena act as toughening mechanisms and are consistent with similar findings of other groups [Fantner et al., 2006, Koester et al., 2008, Peterlik et al., 2006, Poundarik et al., 2012]. Measurement of the inclination angles showed that on average the failure occurred in the plane of maximum shear stress. The critical shear stress in the slip plane was significantly anisotropic. The direction-dependence of the observed postyield behavior and the critical shear stress hints at a difference in the failure mechanism and may be explained by a nonlinear rotated plywood model: For the axial pillars, the majority of the fibrils are oriented at small angles to the loading direction. The observed slip planes are a result of a combined fibril and extra-fibrillar mineral failure. In this case, isolated fibrils that have not yet failed act as a toughening mechanism leading to an increased post strength ductility. For the transverse micropillars, most of the fibrils are oriented at angles close to 90° to the loading direction. Therefore, one orientation exists for which the number of fibers going across the plane is minimal. In this case, a slip plane may form by failure of the extra-fibrillar mineral only, which explains the absence of fibrils spanning the gap and the rapid failure once strength had been passed in most of the transverse micropillars (Fig. 5.15). It was found that an elastoplastic model with failure (Fig. 5.14) is able to represent the microscale data very accurately (Fig. 5.13). The observed plasticity could be explained by different nanoscale mechanisms, e.g. nanogranular friction between mineral particles [Tai et al., 2006] or dissipation at the interface between mineral platelets and the organic phase [Gupta et al., 2013, Mercer et al., 2006].

When comparing the two length scales, only a small difference in stiffness of $\sim 10\ \%$ was found. When applying an equal strain model, this difference could be explained by a porosity of 10 %, which is in the range of the lacunar-canalicular and Haversian porosity [Fratzl and Weinkamer, 2007]. On the other hand, the strength and failure behavior differed strongly at the two length scales. The response on the microlevel was highly ductile with maximum plastic strains in the order of 8 %, while the dry macroscopic samples failed mostly in a quasi-brittle fashion with plastic strains below 1.2 %. The measured strength on the microscale was higher by a factor of 2.4 than the macroscopic tests. When applying the quadratic relationship between strength and porosity proposed by Carter and Hayes [Hayes and Carter, 1976], a change in strength by a factor of only 1.23 would be expected, therefore the first hypothesis that ultimate stresses are similar on the micro- and macroscale was falsified. The unaccounted difference in strength and ductility is attributed to a size effect, more specifically to the existing cracks and defects located between osteons [Schaffler et al., 1995], and is in line with the scaling theory of quasi-brittle failure [Bažant, 2004]. The yield stress and ultimate plastic strain associated with the growth of pre-existing cracks

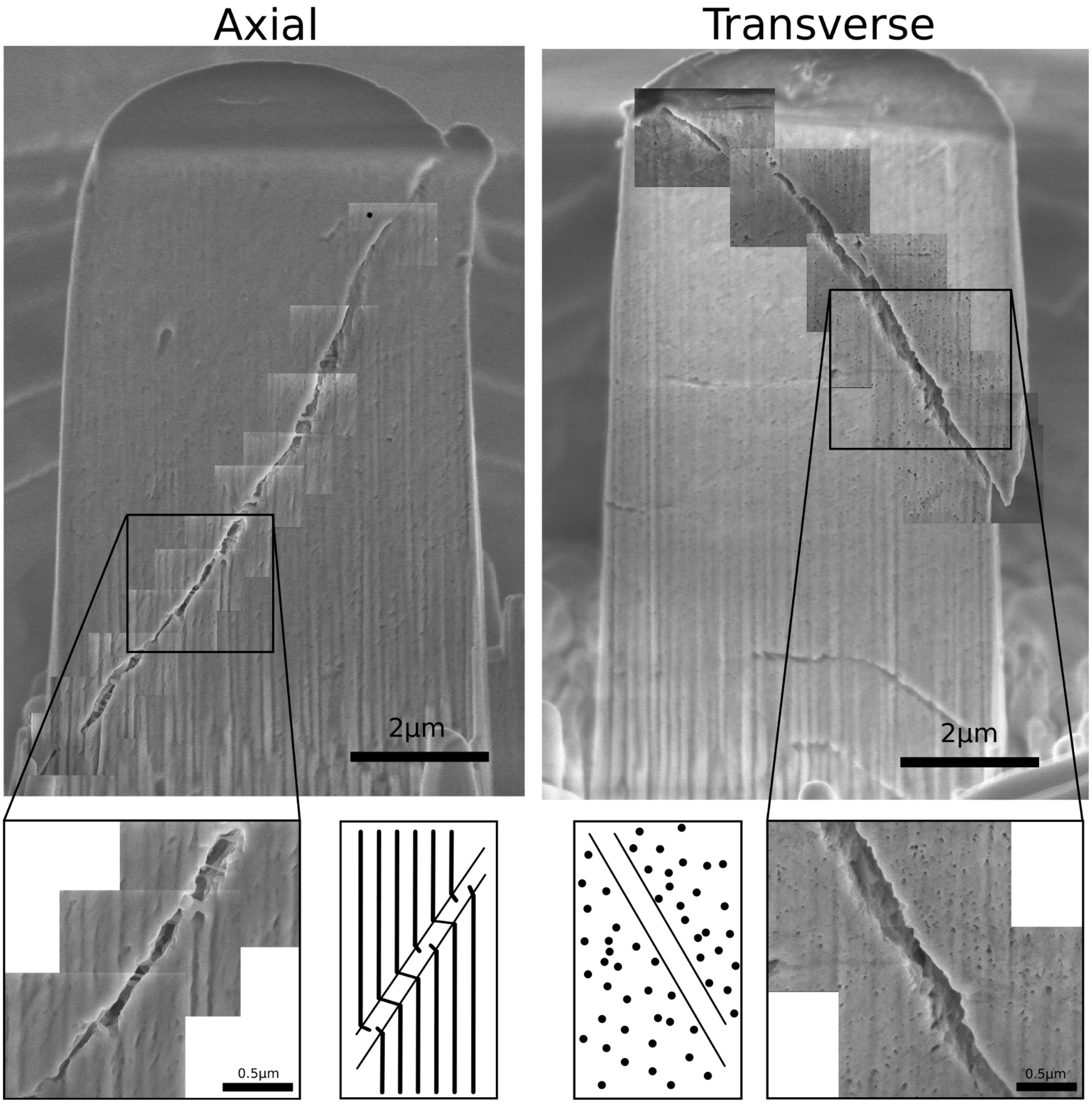

Figure 5.15: Dominant failure mechanism observed on the microscale. Overlay of SEM micrographs of micropillars in axial (top, left) and in transverse (top, right) direction failed by shearing with HR images of the slip planes and schematical drawings (bottom) depicting the distinct failure mechanisms depending on the fibrillar orientation. Scale bars on the top represent 2 µm, on the bottom 0.5 µm.

near interfaces [Carter and Hayes, 1977, Martin and Burr, 1989] or pores [Currey, 1962] on the macroscale are substantially lower than the ones necessary to initiate and propagate a new crack through a micropillar made of a single osteonal lamella (Fig. 5.7). The proposed rheological model (Fig. 5.14) illustrates this difference very well as it was found to be in excellent agreement with the experimental data at both length scales (Fig. 5.13). The model is thus able to build a bridge between the newly observed ductile behavior on the lamellar level and the well-documented quasi-brittle behavior of bone on the macroscale characterized by a reduction of stiffness that increases with plastic deformation [Zysset, 1994]. Similar size effects are known for other material like ceramics [Griffith, 1921], which show brittle failure due to crack growth near preexisting defects that are homogeneously distributed in the material. In the case of bone, these defects are concentrated in interstitial tissue and near cement lines [Schaffler et al., 1995], which causes the macroscopic response to be a combination of plastic deformation and cracking, while isolated osteonal lamellae show plasticity only.

Due to the setup of the *in situ* indenter in a conventional SEM and the preparation of the micropillars using a FIB, the tests were performed in a vacuum environment. Therefore, the specimens had to be dried before testing, which affects the mechanical properties of the organic phase and the surface chemistry of the mineral platelets. Raman spectroscopy confirmed that the composition was not significantly different from hydrated human samples reported in the literature (Fig. 5.1 and 5.2). To assess the mechanical influence of hydration on the microscale, microindentations were performed in wet and dry condition. Indentation modulus increased by 20 % in the axial direction, hardness and work by as much as 65 % after drying. Hardness has been shown to scale with yield strength [Fischer-Cripps, 2002], which implies that stiffness and strength of hydrated micropillars would be reduced as compared to the dry setup. This is consistent with findings on the macroscale [Nyman et al., 2006] . However, the ratio of plastic to total indentation work did not change significantly ($p = 0.23$), which is consistent with data for human bone [Wolfram et al., 2010a] and suggests that the underlying dissipative mechanism remains the same after dehydration. Macroscopically, it has been reported that toughness is reduced by dehydration [Nyman et al., 2006]. Nevertheless, the micropillars showed a highly ductile behavior up to failure. Therefore it might be argued that reduced toughness after drying is caused by its influence on interfaces and preexisting defects rather than on the bone matrix itself. This effect needs further investigation.

The yield and ultimate properties on the lamellar level reported in this study were also significantly higher than values reported in previous studies based on microindentation [Carnelli et al., 2011]. However, these studies had to rely on assumptions regarding the nonlinear material behavior and inverse methods to back-calculate material properties, while the data of the micropillar compression tests may be interpreted in a straightforward manner due to the uniaxial stress state. Finally, previous indentation studies suggested that a damage mechanism at the ultrastructural level might be responsible for some of the characteristics of indentation experiments in bone such as a reduced unloading stiffness [Lucchini et al., 2011, Zhang et al., 2010]. However, most of the monotonic tests did not show the strain softening behavior that is characteristic of a mechanical damage process. Additionally, unlike those performed on the macroscale, the cyclic micropillar compression tests did not show a significant reduction of apparent modulus following overloading of the sample. This is an indication that no diffuse cracks were opening inside the micropillars until failure and falsifies the second hypothesis that bone deforms inelastically by formation of microcracks reducing its stiffness at both length scales.

This study showed that unlike the consistent elastic properties, the postyield properties and failure mechanisms of bone under compression differ significantly at the two length scales. Isolated bone lamellae show a high strength and ductility but no damage and fail mostly by development of shear planes, while the response of macroscopic specimens containing numerous osteons is quasi-brittle with low strength and ductility, substantial damage and longitudinal cracks. The data supports the thesis that, under compressive loading, multiple slip planes emerging at the weak interfaces or in the vicinity of pores in the interstitial bone coalesce into microcracks, the statistical distribution and growth of which lead to a quasi-brittle failure at the macroscopic level. These findings highlight the importance of studying interface properties of cement lines and the stress concentration effect of pores in the interstitial tissue more closely. Also, they remain to be extended to human lamellar bone tissue, physiological testing conditions and further loading modes. Deciphering the micromechanical behavior of lamellar bone and its evolution with age, disease and treatment will help preventing bone fractures in the elderly.

5.7 Author contributions

The initial planning of the study was done by JS, RR, JM and PZ. FIB was operated by RR. Micropillar compressions and SEM imaging were performed by JS and RR, Raman measurements and interpretation by VL, Monte Carlo simulations and microindentations by JS, macroscopic tests by JS, UW and AB. Data analysis was performed by JS and RR with assistance of UW, interpretation in cooperation with JM and PZ. Modeling was performed by JS and PZ. The manuscript was written by JS with contributions of all coauthors. JM and PZ share senior authorship for this work.

6

This manuscript was submitted to: Journal of Biomechanics

Quantitative analysis of imprint shape and its relation to mechanical properties measured by microindentation in bone

J.J. Schwiedrzik[1], P.K. Zysset[1]

[1]Institute for Surgical Technology and Biomechanics, University of Bern, Stauffacherstr. 78, CH-3014 Bern, Switzerland

6.1 Abstract

Microindentation in bone is a micromechanical testing technique routinely used to extract material properties related to bone quality. As the analysis of microindentation data is based on assumptions about the contact between sample and surface, the aim of this study was to quantify the topological variability of indentations in bone and examine its relationship with mechanical properties. Indentations were performed in dry human and ovine bone in axial and transverse directions and their topography was measured by atomic force microscopy. Statistical shape modelling of the residual imprint allowed to define a mean shape and to describe the variability in terms of 21 principal components related to imprint depth, surface curvature and roughness. The indentation profile of bone was found to be highly consistent and free of any pile up while differing mostly by depth between species and direction. A few of the topological parameters, in particular depth, showed significant but rather weak and inconsistent correlations to variations in mechanical properties. The mechanical response of bone as well as the residual imprint shape were highly consistent within each category. We could thus verify that bone is rather homogeneous in its micromechanical properties and that indentation results are not strongly influenced by small deviations from an ideally flat surface.

6.2 Introduction

Bone is a hierarchical material that features a cell-seeded mineralized collagen matrix and provides mechanical support, metabolizes minerals and stores bone marrow [Fratzl and Weinkamer, 2007, Weiner et al., 1999] for hematopoiesis. Fibril arrays form by combination of parallel mineralized collagen fibrils surrounded by extrafibrillar mineral particles [Currey, 1969, 2002, Lees et al., 1990]. Parallel fibril arrays group into lamellae in a rotated plywood pattern [Giraud-Guille, 1988, Weiner et al., 1997] in lamellar bone. Osteocytes and their cell processes reside in the lacuno-canalicular network which makes up for about 1 % of macroscopic bone porosity [Martin, 1984]. Human compact bone consists of lamellae arranged concentrically around blood vessels forming osteons with a porosity of approximately 6 % [Fratzl and Weinkamer, 2007]. Fibrolamellar bone is an alternative tissue type that is laid out in large, fast growing animals and converted later to osteonal bone through a remodeling process [Currey, 2002]. Bone sections lying outside of secondary osteons are usually older than the newly remodeled osteonal bone and referred to as interstitial bone [Cowin, 2001, Currey, 2002].

Biomechanical testing of macroscopic bone samples has been performed for more than a century. Up to now many challenges remain, mostly due to spatial, inter-subject, age, and disease variation of mechanical properties [Cowin, 2001, Keaveny et al., 2003]. Analysis of bone as a hierarchical composite material is therefore an important area of research [Fratzl and Weinkamer, 2007, Fritsch and Hellmich, 2007, Fritsch et al., 2009, Rho et al., 1998] aiming to understand and predict whole bone properties by considering its hierarchical microstructure and mechanical behavior on the lower length scales.

Indentation is a micromechanical testing technique in which a well defined diamond tip is pressed onto a flat sample surface and force and tip displacement are recorded simultaneously. Based on the pioneering work of Oliver and Pharr [Oliver and Pharr, 1992, Swadener and Pharr, 2001] elastic properties may be extracted from the unloading part of the force-depth curve. Indentation in bone with depths up to 1 µm mainly aims at characterizing the mechanical properties on the level of single to multiple lamellae, which have a thickness of 3-7 µm [Hengsberger et al., 2002, Lewis and Nyman, 2008, Oyen and Ko, 2008, Zysset et al., 1999, Zysset, 2009]. Finite element calculations of indentations using constitutive models coupling plasticity and damage have shown that damage can explain some of the experimental findings for bone like the reduced unloading stiffness [Lucchini et al., 2011, Zhang et al., 2010]. However, it is very difficult to find a unique set of material parameters for complex materials based on such data [Bocciarelli et al., 2005, Bolzon et al., 2004, Bucaille et al., 2003, Ganneau et al., 2006], as indentations in materials with different behavior can result in very similar force-depth curves [Chen et al., 2007]. Therefore, it is of high interest to increase the reliability of the obtained results by assessing not only mechanical properties extracted from force-depth curves, but also the residual imprint in a quantitative way [Bocciarelli et al., 2005, Bolzon et al., 2004, Bucaille et al., 2003, Mullins et al., 2009, Schwiedrzik and Zysset, 2013b].

As the extraction of material properties from indentation curves is based on the assumption of a flat sample surface, deviations of the real surface topography from this ideal shape will lead to a variability in the data that does not reflect the heterogeneity of the underlying tissue. Quantitative analysis of the residual imprint shape and the surrounding bone surface can help to separate these two effects thereby allowing to quantify the inherent heterogeneity in bone more accurately.

Atomic force microscopy (AFM) is a method combining the principles of scanning tunneling microscopy (STM) and profilometry [Binnig et al., 1986] that is routinely used to determine surface topography [Jalili and Laxminarayana, 2004] and has been used to visualize the residual imprints of microindentations in bone in the past [Hengsberger et al., 2001, 2002]. However, the raw AFM data is not suitable for a direct quantitative analysis, while the usual measurements such as pile-up, residual depth and surface roughness [Fischer-Cripps, 2002] do not capture the full geometrical information. A powerful tool for mathematical description of the variability of surface shapes is statistical shape modeling

(SSM) [Goodall, 1991, Lüthi et al., 2012] using principal components analysis (PCA) [Pearson, 1901]. This method, routinely used in image analysis [Blanc et al., 2009, Heimann and Meinzer, 2009, Lüthi et al., 2012], allows to define a mean shape and to describe variation in shape of a dataset by variations of principal components or eigenmodes. This reduces the amount of variables defining the shape substantially while retaining a high accuracy of the description.

The aim of this work was to quantify the topography of indents in bone and its variability using PCA in order to analyze the shape as a function of direction and species and to explore its correlation with mechanical data. This information can be used to define mean imprint shapes for use as additional observables in inverse methods as well as a more precise quantification of the inherent heterogeneity of bone.

6.3 Materials and Methods

Ovine femora were acquired from a local butcher shop and human samples from a 73 yrs old female were provided by the Department of Applied Anatomy of the Medical University of Vienna. Ethics approval (175/2011) based on informed consent of the donors has been obtained. Axial and transverse samples were cut using a diamond-coated bandsaw (Exakt, Norderstedt, Germany), air-dried following the protocol of Wolfram et al. [Wolfram et al., 2010a], and embedded in, but not infiltrated by polymethylmethacrylate (PMMA). Samples were then ultramilled (Polycut E, Reichert-Jung, Germany) to obtain flat and parallel surfaces. Microindentations were performed in interstitial and osteonal tissue using a Berkovich tip on a Ultra Nano Hardness Tester (UNHT, CSM Instruments, Switzerland) in force control up to a depth of to 1µm. A trapezoidal loading protocol was used with a loading rate of 100 mN/min, 30 s holding time at maximum force, and an unloading rate of 400 mN/min in order to minimize effects of creep on the measured properties. The indenter tip was cleaned using 99 % ethanol as well as by indentations in copper and calibrated using a fused silica reference specimen before starting the measurements. Before each test, it was confirmed by focusing a light microscope with a 100× objective ($NA = 0.95$) underneath the surface that no lacuna was present within a radius of 40 µm from the indentation site in order to minimize the effect of lacunar porosity on the measurements. The force-depth ($P - h$) curves were analyzed using the Oliver and Pharr method [Oliver and Pharr, 1992]. The reduced modulus E_r is given by [Oliver and Pharr, 1992, Reisinger et al., 2011]:

$$E_r = \frac{\sqrt{\pi}}{2} S \frac{1}{\sqrt{A_c}}. \tag{6.1}$$

The indentation modulus takes into account the elastic deformation of the indenter tip [Reisinger et al., 2011]:

$$E^* = \Big(\frac{1}{E_r} - \frac{1-\nu_{tip}^2}{E_{tip}}\Big)^{-1}. \tag{6.2}$$

The indentation hardness H_{IT} is defined as the maximum force divided by the contact area at maximum depth:

$$H_{IT} = \frac{P_{max}}{A_c} \tag{6.3}$$

The total and plastic energies are defined as [Wolfram et al., 2010a]

$$W_{tot} = \int_0^{h_m} Pdh, \quad W_{plast} = \int_0^{h_m} Pdh - \int_{h_m}^{h_p} Pdh \tag{6.4}$$

with the maximum depth h_m and the residual depth h_p.

Following each indentation the residual imprint topography was measured using an AFM (CSM Instruments, Switzerland) in static force contact mode using a silicon tip. The misalignment between the sample and the AFM reference frames was determined to be 0.788° in x- and 0.188° in y-direction on a reference sample and subsequently corrected. An image size of 512 × 512 pixels was chosen with a pixel spacing of 25 nm resulting in an image size of $12.8 \mu m \times 12.8\ \mu m$. The image was convoluted with a Gauss kernel with a standard deviation of 25 nm to filter high frequency noise. Afterwards, the image data was converted to a 3D point cloud, rigidly registered by moving the tip apex for all indents to (0,0,0) and cropped to a size of $10\mu m \times 10\mu m$. A surface mesh was created using the VTK Delauney 2D triangulation algorithm and saved as VTK polydata.

Principal component analysis (PCA) and statistical shape modeling on the registered datasets was performed using STATISMO [Lüthi et al., 2012]. STATISMO determines eigenvalues that are normalized by their standard deviations, which ensures that there are no large numerical differences in the data. The eigenvalues were extracted for all bone samples and statistical analysis of the eigenvalues as well as the measured mechanical properties was performed using R [R Development Core Team, 2008]. Normality was tested using the Shapiro-Wilk normality test [Shapiro and Wilk, 1965] and visual inspection of normalized quantile-quantile (Q-Q) plots [R Development Core Team, 2008] against the standard normal distribution. Experimental data is reported as mean ± standard deviation. Differences between groups were tested using two-sided t-tests. The significance level was chosen as $p = 0.01$. Categorical variables were handled using dummy coding. All multilinear regressions using the eigenmodes as predictor variables did not include interaction terms, as the eigenmodes determined by PCA are by definition orthogonal. The isolated influence of groups of eigenmodes was reported as adjusted R^2 of linear regressions using only the significant eigenmodes in the group as predictor variables.

6.4 Results

First, the mechanical properties were analyzed by analysis of variance (ANOVA) as a function of direction, tissue type and species. It was found that direction and species are significant factors ($p < 0.01$). The properties measured by microindentation are therefore reported in Tab. 1 and mean imprint shapes in Fig. 6.1 separately for human and ovine bone in axial and transverse direction. Fig. 6.1 also shows mean indent shapes for indentations in copper (N=10) and PMMA (N=10) for comparison.

Table 6.1: Mean ± standard deviation of the indentation modulus E^*, indentation hardness H_{IT}, plastic W_{pl} and total Work W_{tot}, and residual depth h_p determined by the method of Oliver and Pharr [Oliver and Pharr, 1992], the dimensionless measures h_p/h_m, W_{pl}/W_{tot}, and H_{IT}/E^*, as well as eigenvalue λ_1 and number of experiments N for microindentations in ovine and human tissue and axial and transverse direction. The other eigenmodes were not significantly different for direction alone and are not reported here.

	E^*/GPa	H_{IT}/GPa	W_{pl}/pJ	W_{tot}/pJ	h_p/nm	N
Ov. Ax.	25.92 ± 1.73	0.815 ± 0.067	6139 ± 404	7722 ± 489	810.1 ± 22.5	50
Hu. Ax.	24.64 ± 1.56	0.771 ± 0.086	5876 ± 554	7439 ± 731	785.7 ± 19.0	21
Ov. Tv.	15.82 ± 0.93	0.545 ± 0.038	4097 ± 336	5509 ± 442	493.0 ± 60.0	24
Hu. Tv.	17.03 ± 1.88	0.540 ± 0.091	4479 ± 581	5759 ± 804	685.2 ± 64.3	12

	h_p/h_m	W_{pl}/W_{tot}	H_{IT}/E^*	λ_1	N
Ov. Ax.	0.759 ± 0.017	0.795 ± 0.011	0.0315 ± 0.0016	0.817 ± 0.259	50
Hu. Ax.	0.732 ± 0.017	0.790 ± 0.007	0.0312 ± 0.0020	0.220 ± 0.397	21
Ov. Tv.	0.453 ± 0.055	0.744 ± 0.009	0.0345 ± 0.0015	-1.534 ± 0.252	24
Hu. Tv.	0.624 ± 0.055	0.779 ± 0.021	0.0316 ± 0.0028	-0.720 ± 0.303	12

The complexity of the shape model was reduced from 107 to 21 eigenmodes λ_i by setting the represented variance to 99%. Independence of the eigenvalues was confirmed by calculation of the correlation matrix for the complete dataset, which showed off-diagonal correlation coefficients that were $< 10^{-4}$. Next, samples were drawn from the model showing 3 standard deviations in positive and negative direction for each eigenmode in order to

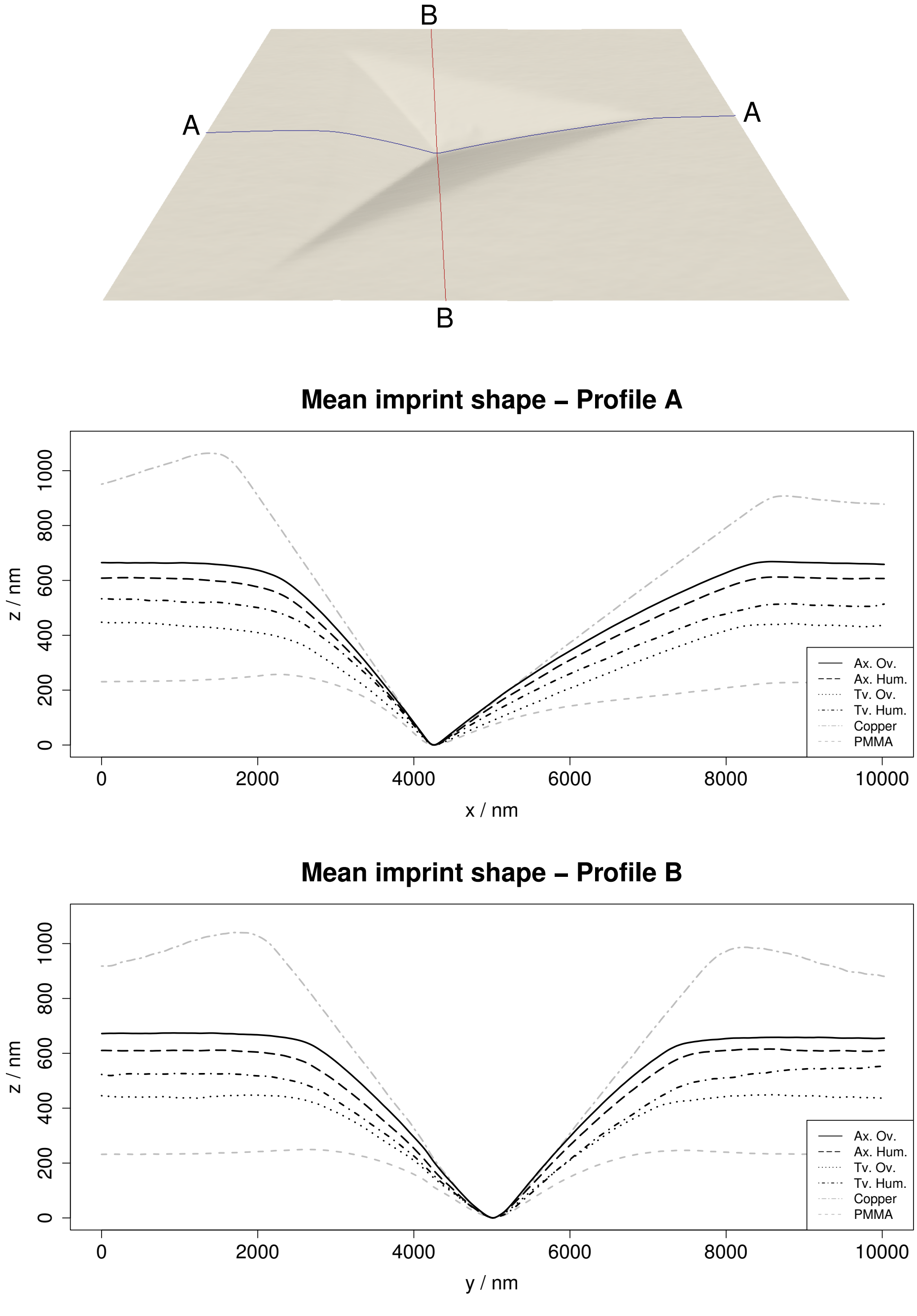

Figure 6.1: Mean residual imprint shape for ovine bone in axial direction (N=50, top) and extracted mean depth profiles along an axis of symmetry (Profile A, middle) and perpendicular to it (Profile B, bottom) for human and ovine bone in axial and transverse direction as well as copper and PMMA as reference materials.

Table 6.2: Interpretation of the first 21 eigenmodes of the statistical shape model.

Eigenmode	Interpretation
1	Depth
2-7	1^{st} and 2^{nd} order warping
8-21	Higher order warping, Roughness

identify the meaning of the remaining eigenmodes. The interpretation based on a visual inspection of the resulting surfaces for each eigenmode (see Fig. 6.2) is given in Tab. 2.

Based on the interpretation shown in Tab. 2, the eigenmodes were divided into three main groups: imprint depth (λ_1), surface curvature (λ_2 to λ_7), and roughness (λ_8 to λ_{21}). STATISMO sorts the eigenmodes in decending order for the included variance, which means that eigenmode λ_i reflects a higher percentage of shape variation than λ_{i+1}. All individual datasets were tested for normality using the Shapiro-Wilk normality test. In those cases where the Shapiro-Wilk normality test showed a significant deviation from a normal distribution, a visual inspection of normalized Q-Q plots against the standard normal distribution showed a mostly linear dependence with some outliers. It was therefore concluded that all variables may be regarded as normally distributed.

As expected, correlation of the plastic depth h_p obtained from the indentation curve with λ_1 representing the imprint depth in the AFM data yielded a significant positive slope ($p < 0.01$) with an R^2 of 0.83. Regression of the mechanical properties with respect to the significant factors direction and species explained 89% of the variation of E^*, 76% for H_{IT}, 80% for W_{pl} and 73% for W_{tot}. In order to test whether the residual shape can be used to account for these differences as well, the pooled data of both species, tissue types and directions was regressed as a function of the shape model only and subsequently reduced to the significant eigenmodes. It was found that the residual imprint shape alone explains 88% of the variation of E^*, 84% for H_{IT}, 84% for W_{pl} and 80% for W_{tot}, which is in the same range as the regression with respect to direction and species.

ANOVA of the imprint shape showed that for λ_1, direction and species were significant ($p < 0.01$), while for the other eigenvalues direction alone was not. Apart from λ_3, λ_4, λ_5 and λ_{19}, for which either species or the interaction of direction and species were significant ($p < 0.01$), the other eigenvalues did not differ signifficantly between directions or species. Fig. 6.1 shows the mean imprint profiles as a function of direction and species that differ mainly in the depth of the imprint. However, some subtle differences in surface curvature are visible due to eigenvalues 3 to 5. As significant differences were found for the mechanical properties between the two directions, the correlation analysis was performed for each

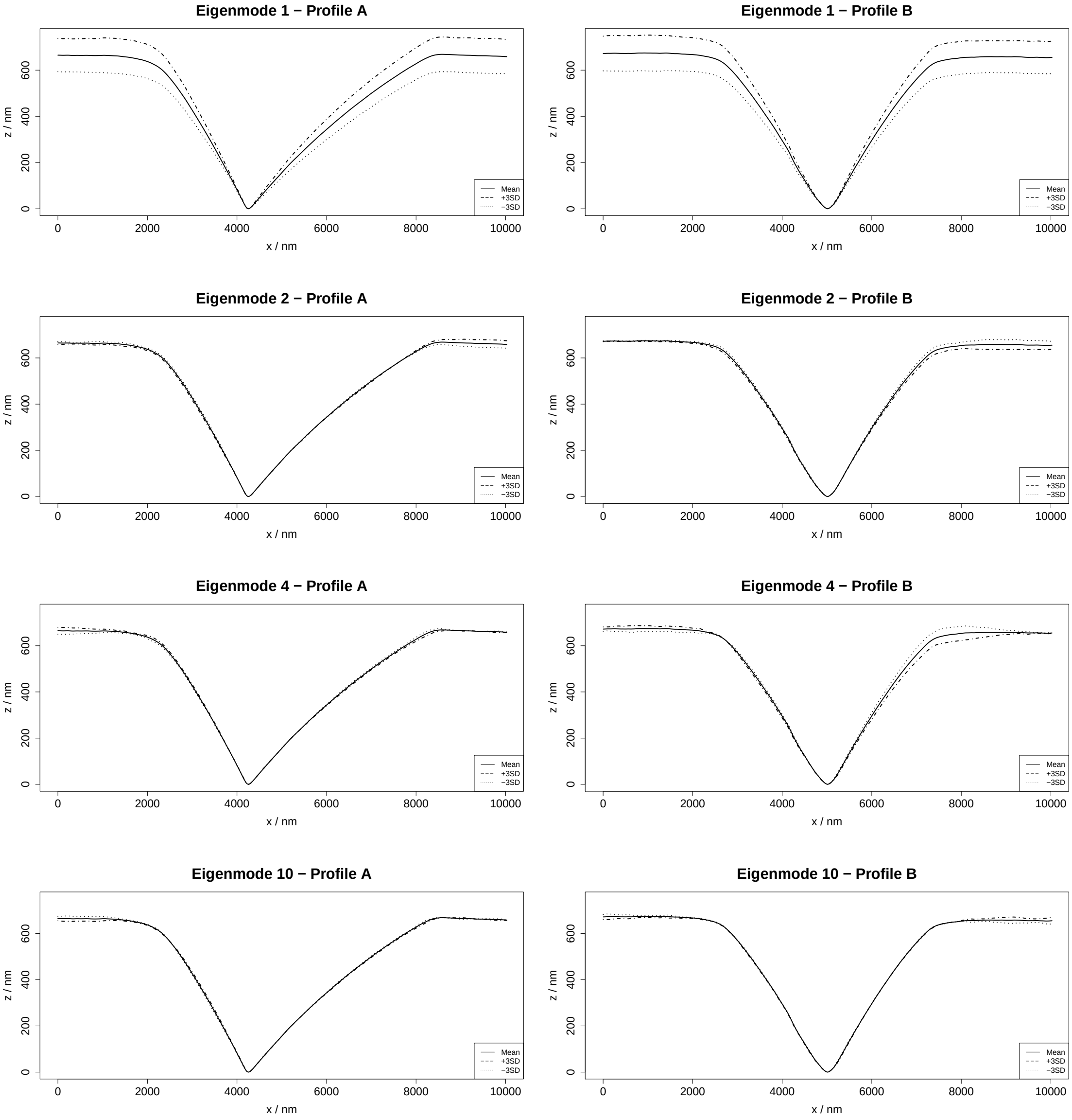

Figure 6.2: Mean ± 3 standard deviations for profiles A and B (Fig. 6.1) of selected eigenmodes for the ovine axial dataset. For a representation of all eigenmodes, the reader is referred to the supplementary material.

direction separately.

6.4.1 Axial data

For the axial indentations, the area surface roughness R_a was measured by AFM in the vicinity of each indent and found to be 10.7 ± 3.2 nm for ovine and 15.6 ± 4.5 nm for human tissue, which is similar to values for samples prepared by polishing or microtoming [Lewis and Nyman, 2008, Mullins et al., 2009]. A line roughness measurement on a control scan of an area of 51.2×51.2 µm in the ovine sample with the same lateral resolution yielded an average surface roughness R_a of 4.8 nm. T-test of the mechanical properties and eigenmodes for osteonal/interstitial differences were not significant ($p < 0.01$). However, t-tests between human and ovine tissue showed significant differences ($p < 0.01$) for the measurements E^*, h_p/h_m, as well as the major eigenmodes λ_1 and λ_3 representing indent depth and surface warping. The mean imprint profiles of human and ovine bone are shown in Fig. 6.1. Therefore, the correlation was performed on the ovine data only, but both indents in interstitial and osteonal tissue were included. After reduction to the significant eigenmodes ($p < 0.01$), the following correlations were obtained:

$$E^* = 22.87 + 3.73\lambda_1, adj.R^2 = 0.30, SEE = 1.45 \text{ GPa}$$

$$H_{IT} = 0.680 + 0.167\lambda_1 + 0.034\lambda_{11}, adj.R^2 = 0.53, SEE = 0.046 \text{ GPa}$$

$$W_{pl} = 5294.1 + 1032.9\lambda_1 + 189.0\lambda_{21}, adj.R^2 = 0.50, SEE = 286.1 \text{ pJ}$$

$$W_{tot} = 6643.9 + 1319.6\lambda_1, adj.R^2 = 0.48, SEE = 352.9 \text{ pJ}$$

Analysis of the dimensionless parameters yielded the following regressions:

$$h_p/h_m = 0.762 - 0.007\lambda_3 + 0.006\lambda_8 - 0.012\lambda_{20}, adj.R^2 = 0.28, SEE = 0.014$$

$$W_{pl}/W_{tot} = 0.794 + 0.005\lambda_8 + 0.005\lambda_{18}, adj.R^2 = 0.31, SEE = 0.009$$

$$H_{IT}/E^* = 0.0315 - 0.0007\lambda_8 - 0.0009\lambda_{16} - 0.0009\lambda_{18}, adj.R^2 = 0.43, SEE = 0.001$$

All dimensionless parameters were not significantly correlated to imprint depth.

6.4.2 Transverse data

For the transverse indentations, area surface roughness R_a was found to be 14.5 ± 2.4 nm for ovine and 32.7 ± 11.1 nm for human tissue, which is considerably smaller than 5% of the indentation depth and should therefore not influence the results significantly [Fischer-Cripps, 2002]. A line roughness measurement on a control scan of an area of 51.2×51.2 µm in the transverse ovine sample with the same lateral resolution yielded an average surface roughness R_a of 19.9 nm. The mean indent shapes for the human and ovine transverse datasets are shown in Fig. 6.1. T-test for human/ovine differences were not significant ($p < 0.01$) for all mechanical properties and eigenmodes except for h_p, the dimensionless measures W_{pl}/W_{tot} and h_p/h_m as well as λ_1. The residual imprints in human tissue were significantly deeper by 86 nm, even though the fraction of dissipated to total work was significantly smaller. The mean imprint profiles of human and ovine bone are shown in Fig. 6.1. After reduction to the significant eigenmodes ($p < 0.01$), the following correlations were obtained for the transverse microindentations in ovine bone:

$$E^* = 19.04 + 2.10\lambda_1, adj.R^2 = 0.29, SEE = 0.78 \text{ GPa}$$

$$H_{IT} = 0.647 + 0.066\lambda_1, adj.R^2 = 0.15, SEE = 0.035 \text{ GPa}$$

$$W_{pl} = 4191.3 + 293.2\lambda_5 - 203.3\lambda_8, adj.R^2 = 0.25, SEE = 290.9 \text{ pJ}$$

$$W_{tot} = 5637.0 + 399.6\lambda_5 - 273.0\lambda_8, adj.R^2 = 0.27, SEE = 377.1 \text{ pJ}$$

The regressions for H_{IT} and W_{pl} were only just insignificant (p=0.034 and p=0.018) and are therefore still reported here. Analysis of the dimensionless parameters yielded the following regressions:

$$h_p/h_m = 0.473 - 0.060\lambda_2 - 0.048\lambda_3, adj.R^2 = 0.53, SEE = 0.038$$

$$W_{pl}/W_{tot} = 0.771 + 0.016\lambda_1 + 0.006\lambda_4 - 0.005\lambda_7, adj.R^2 = 0.56, SEE = 0.006$$

$$\begin{aligned} H_{IT}/E^* = 0.0303 - 0.0031\lambda_1 + 0.0013\lambda_5 - 0.0011\lambda_8 \\ - 0.0010\lambda_{14} - 0.0005\lambda_{15}, adj.R^2 = 0.37, SEE = 0.001 \end{aligned}$$

The regression for H_{IT}/E^* was only just insignificant ($p = 0.018$) and is therefore still reported here.

6.5 Discussion

The aim of the study was to quantify the topological variability of indentations in bone and examine its relationship with mechanical parameters extracted from the indentation curve.

The indentation profile of bone was situated between the ones of copper and PMMA and was found to be free of any pile up. This represents a quantitative confirmation of an argument made in the bone indentation literature [Mullins et al., 2009]. In the PCA, three types of topological eigenvalues were identified: depth, warping and roughness of the surface. Indentation shape in bone was found to be highly consistent and differed mostly by depth among species (ovine/human) and direction (axial/transverse). Some of the eigenmodes representing surface warping, which is a result of the sample preparation, also differed between the two species. No significant differences in mechanical properties or imprint shape were found between osteonal and interstitial tissue for both ovine and human tissue in axial direction. As expected, the residual depth extracted from the indentation curve correlated well with the associated eigenvalue.

The mechanical properties derived from bone indentation differed also with species and direction and exhibited a rather low standard deviation within these categories. This was aided by avoiding indentations near lacunae. The data of this study suggests that bone tissue is in fact remarkably homogeneous with respect to its inherent indentation properties when the influence of porosity is limited to canaliculi, which are much smaller and more homogeneously distributed than lacunae [Kerschnitzki et al., 2011]. This is in line with the study of Spiesz et al. [Spiesz et al., 2013], who reported a lack of correlation of a micromechanical model based on the fibril angle and mineralization with the indentation modulus measured by microindentation in human bone and concluded that other factors like porosity might dominate the variability in the indentation data.

A higher elastic and post-yield anisotropy was found in ovine bone than human bone. This may be related to the underlying fibril architecture. A recent study reported a strongly oriented fibrillar ultrastructure in ovine bone [Schwiedrzik et al., 2014], while the fibrillar orientation pattern in human bone is believed to follow a rotated plywood pattern [Giraud-Guille, 1988], which results in a less anisotropic response. The fact that H_{IT}, which has been shown to scale with yield stress [Fischer-Cripps, 2002], as well as h_p/h_m and W_{pl}/W_{tot} of ovine bone were significantly lower in transverse than in axial direction suggests that the fibril orientation pattern leads to a direction-dependent dissipative mechanism at the microscale. It seems that the material is storing a higher fraction of energy elastically when tested in transverse direction, even though the yield stress is reduced. This is highly consistent with the fact that bone lamellae have a lower yield and maximum stress in transverse direction but a more pronounced hardening behavior compared to the axial direction as recently shown in micropillar compression tests [Schwiedrzik et al., 2014].

A few topological parameters, in particular depth in the axial direction, showed significant associations with variations in mechanical properties, but the correlations were not very strong (adj. R^2 0.15 to 0.56) or consistent and the standard errors were quite low. In principle, only depth could be exploited by a direct inverse method to identify differences in material properties, but this variable is related to the plastic depth that can be extracted from the indentation curve. However, the high consistency of the extracted mean shapes suggests that they may be used as an additional observable for identification of material properties based on comparison of both indentation curves and imprint shape with Finite Element calculations [Bocciarelli et al., 2005, Bolzon et al., 2004, Bucaille et al., 2003, Mullins et al., 2009, Schwiedrzik and Zysset, 2013b] in order to increase the reliability of the found parameters.

A limitation of this work is that it was performed on dry bone, as no AFM was available at the time of the study that could be used under liquid immersion and also be mounted on the indenter frame. Dehydration of bone has been shown to influence the properties of human and ovine bone measured by indentation significantly [Schwiedrzik et al., 2014, Wolfram et al., 2010a]. Indentation modulus was reported to increase by about 20 % in axial direction, hardness and work by as much as 65 % [Schwiedrzik et al., 2014]. However, the ratio of plastic to total indentation work was shown to remain constant after drying for both ovine [Schwiedrzik et al., 2014] and human bone [Wolfram et al., 2010a] suggesting that the underlying dissipative mechanisms could remain the same. This effect needs further investigation. The main strength of this study is that a large number of high precision measurements using an AFM were performed on two species and in two directions allowing a rigorous quantitative analysis of the shape as well as the mechanical data.

In conclusion, we show a highly consistent imprint shape upon indentation in bone and the absence of pile up. Except depth, the principal component eigenvalues are dominated by warping and roughness of the bone surface that are essentially independent of bone material properties. An inverse method based on indentation shape alone appears to be a difficult pathway to identify subtle differences in post-yield properties. However the residual imprint shape is well suited as an additional observable in an identification strategy combining mechanical data and residual imprint shape [Bolzon et al., 2004, Mullins et al., 2009] to circumvent problems regarding uniqueness of the found parameters [Chen et al., 2007]. Also, we could verify that if the surface is prepared well with roughness values comparable to the existing literature [Lewis and Nyman, 2008, Mullins et al., 2009], slight deviations hardly affect the indentation measurements. The study highlighted the value of using statistical shape models and exploratory data analysis to analyze geometry and its effects on mechanical measurements. This could be also interesting in other fields of biomechanics in the future such as macroscopic testing of whole bones or soft tissues, where the variability in both shape and measured properties is much more pronounced than in the case of microindentations in bone.

7

An extension of the elasto-viscoplastic damage model to viscoelasticity

J.J. Schwiedrzik[1], A. Bürki[1], P.K. Zysset[1]

[1]Institute for Surgical Technology and Biomechanics, University of Bern, Stauffacherstr. 78, CH-3014 Bern, Switzerland

7.1 Introduction

As the uniaxial strength values for dry bone measured by micropillar compression presented in Chapter 5 of this dissertation [Schwiedrzik et al., 2014] were considerably higher than the values reported based on inverse methods and microindentations in the literature [Mullins et al., 2009, Carnelli et al., 2010, 2011, Lucchini et al., 2011], the current models are not able to capture all of the characteristics of bone on the microscale. It could be that this is due to the fact that there is another dissipative mechanism at work affecting the indentation curves. Indentation tests performed at the Institute for Surgical Technology and Biomechanics showed that if a holding time is included in the indentation protocol during the unloading phase, an elastic recovery takes place (Fig. 7.1).

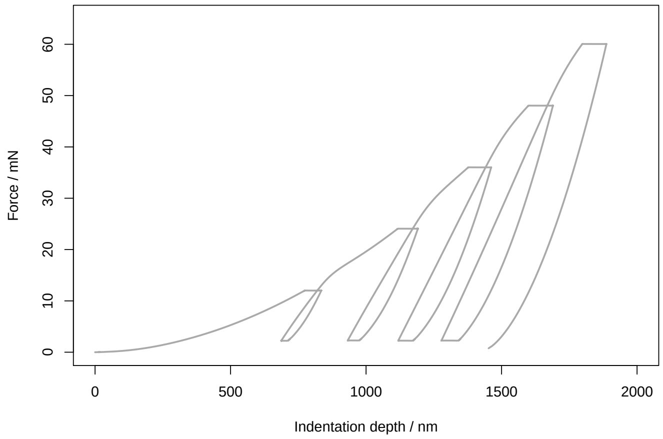

Figure 7.1: Mean curve of cyclic indentation experiments in the axial direction of an ovine tibia using a Berkovich tip ($N = 45$).

This can be interpreted as an indication of a viscoelastic process, which is also consistent with reports for microindentation in bone [Olesiak et al., 2010, Spampatti, 2013] and the presence of viscoelastic effects reported on the macroscale [Bargren et al., 1974, Lakes et al., 1979, Lakes and Katz, 1979, Sasaki et al., 1993, Iyo et al., 2004]. Analytical solutions exist for indentations of cones and spheres [Cheng et al., 2005, Spampatti, 2013, Vandamme and Ulm, 2006] into linear viscoelastic materials, but these do not incorporate other dissipative mechanisms such as plasticity or damage. Therefore, linear viscoelasticity was added to the existing viscoplastic damage model. Viscoelastic parameters were identified using macroscopic experiments, postelastic properties based on the uniaxial properties reported in Chapter 5. Then, simulations of microindentations using both Berkovich and spherical indenters were performed and compared to experiments. The hypothesis tested in this chapter was that with the addition of viscoelasticity to the constitutive model it should be possible to reconcile the differences between the predicted indentation responses using spherical and Berkovich indenters and the uniaxial strength properties measured by micropillar compression.

7.2 Constitutive model

The rheological model is a linear spring in series with a finite number of viscoelastic Kelvin elements in series followed by a viscoplastic Kelvin element, i.e. a plastic slider and a nonlinear damper in parallel. In the elastic regime, it shows a viscoelastic response by combination of the instantaneous response and creep of the Kelvin elements. Damage and plastic strains are accumulating viscously as well. The model is based on the internal variables $\boldsymbol{E}^p$, $\boldsymbol{E}^v$, and κ. $\boldsymbol{E}^p$ is a 2^{nd} order tensor of plastic strains, $\boldsymbol{E}^v$ the viscous strains, κ the accumulated plastic strain. The rheological model is illustrated in Fig. 7.2 for the case of a single viscous Kelvin element.

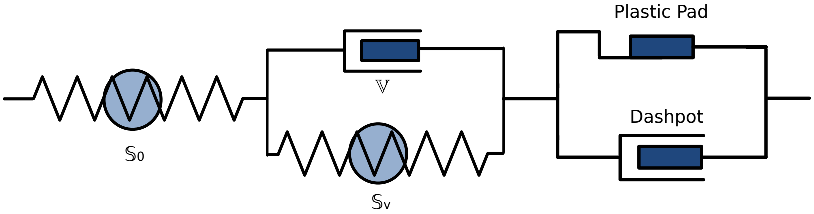

Figure 7.2: Rheological model of a viscoelastic-viscoplastic solid with damage in case of a single viscous Kelvin element

7.2.1 Free energy potential and dissipation

In the notation used in the following chapter, scalars are written as X, 2^{nd} order tensors as $\boldsymbol{X}$, and 4^{th} order tensors as $\mathbb{X}$. The sign ':' denotes the double contraction operation. In case of compositions of two 4^{th} order tensors ($\mathbb{X}_{ijkl} = \mathbb{Y}_{ijmn}\mathbb{Z}_{mnkl}$) and of transformations of a 2^{nd} order tensor with a 4^{th} order tensor ($\boldsymbol{X}_{ij} = \mathbb{Y}_{ijkl}\boldsymbol{Z}_{kl}$), the sign ':' is omitted. The operator $\otimes$ denotes the dyadic product $\mathbb{X}_{ijkl} = \boldsymbol{Y}_{ij}\boldsymbol{Z}_{kl}$, $\underline{\otimes}$ the tensorial product $\mathbb{X}_{ijkl} = \boldsymbol{Y}_{ik}\boldsymbol{Z}_{jl}$, and $\underline{\overline{\otimes}}$ the symmetric product $\mathbb{X}_{ijkl} = \frac{1}{2}(\boldsymbol{Y}_{ik}\boldsymbol{Z}_{jl} + \boldsymbol{Y}_{il}\boldsymbol{Z}_{jk})$.

The finite total strain tensor is split additively into an elastic, plastic and a viscous part following the Green-Naghdi [Green and Naghdi, 1965] decomposition:

$$\boldsymbol{E} = \boldsymbol{E}^e + \boldsymbol{E}^v + \boldsymbol{E}^p \tag{7.1}$$

The viscous strains tensor is split additively into m parts corresponding to the viscoelastic Kelvin elements in the model.

$$\boldsymbol{E}^v = \sum_{m=1}^{n} \boldsymbol{E}^v_m \tag{7.2}$$

The accumulated plastic strain κ is defined as:

$$\kappa = \int_0^t ||\dot{\boldsymbol{E}}^p|| d\tau \tag{7.3}$$

The rate of the accumulated plastic strain is equal to the norm of the rate of the plastic strain tensor:

$$\dot{\kappa} = ||\dot{\boldsymbol{E}}^p|| \tag{7.4}$$

This way the rates of the two variables are coupled while the variables itself are independent of each other. In this model, damage is defined as a scalar function D of the cumulated plastic strain κ (compare Charlebois et al. [2010], Lucchini et al. [2011], Schwiedrzik and Zysset [2013a], Zysset [1994]):

$$D(\kappa) = D_c(1 - e^{-k_p\kappa}) \tag{7.5}$$

The free energy potential for this material model was therefore defined as:

$$\Psi(\boldsymbol{E}, \boldsymbol{E}^v_m, \boldsymbol{E}^p, \kappa) = \frac{1}{2}(1-D(\kappa))\big((\boldsymbol{E}-\boldsymbol{E}^v-\boldsymbol{E}^p) : \mathbb{S}_0(\boldsymbol{E}-\boldsymbol{E}^v-\boldsymbol{E}^p)+\sum_{m=1}^{n} \boldsymbol{E}^v_m \mathbb{S}_{v,m} \boldsymbol{E}^v_m\big) \tag{7.6}$$

The corresponding state laws become:

$$\boldsymbol{S} = \nabla_{\boldsymbol{E}}\Psi = (1 - D(\kappa))\mathbb{S}_0(\boldsymbol{E} - \boldsymbol{E}^v - \boldsymbol{E}^p),$$

$$\boldsymbol{S}^p = -\nabla_{\boldsymbol{E}^p}\Psi = (1 - D(\kappa))\mathbb{S}_0(\boldsymbol{E} - \boldsymbol{E}^v - \boldsymbol{E}^p),$$

$$\boldsymbol{S}^v_m = -\nabla_{\boldsymbol{E}^v_m}\Psi = (1 - D(\kappa))\big(\mathbb{S}_0(\boldsymbol{E} - \boldsymbol{E}^v - \boldsymbol{E}^p) + \mathbb{S}_{v,m}\boldsymbol{E}^v_m\big),$$

$$W^{\kappa} = \begin{cases} \frac{1}{2}D'(\kappa)\left((\boldsymbol{E} - \boldsymbol{E}^{v} - \boldsymbol{E}^{p}) : \mathbb{S}_0(\boldsymbol{E} - \boldsymbol{E}^{v} - \boldsymbol{E}^{p}) + \sum \boldsymbol{E}^{v}_{m}\mathbb{S}_{v,m}\boldsymbol{E}^{v}_{m}\right) & \forall\kappa \in \,]0, \infty[\\ 0 & \forall\kappa = 0 \end{cases}$$

The conjugate variables are $\boldsymbol{S}$ and $\boldsymbol{E}$, $\boldsymbol{S}^p$ and $\boldsymbol{E}^p$, $\boldsymbol{S}^v_m$ and $\boldsymbol{E}^v_m$ as well as W^κ and κ. For the model to be thermodynamically admissible, the dissipation rate Φ needs to be positive at all times. The dissipation can be expressed as the difference of the stress power density and the rate of the free energy density

$$\Phi = \boldsymbol{S} : \dot{\boldsymbol{E}} - \dot{\Psi}, \tag{7.7}$$

which gives

$$\Phi = \boldsymbol{S} : \dot{\boldsymbol{E}} - \boldsymbol{S} : \dot{\boldsymbol{E}} + \boldsymbol{S} : \dot{\boldsymbol{E}}^p + \sum_{m=1}^{n} \boldsymbol{S}^v_m : \dot{\boldsymbol{E}}^v_m + W^\kappa \dot{\kappa}. \tag{7.8}$$

The first two terms cancel each other out and the dissipation is therefore equal to

$$\Phi = \Phi^p + \Phi^v + \Phi^\kappa \tag{7.9}$$

with the plastic dissipation Φ^p:

$$\Phi^p = (1 - D(\kappa))\mathbb{S}_0(\boldsymbol{E} - \boldsymbol{E}^v - \boldsymbol{E}^p) : \dot{\boldsymbol{E}}^p, \tag{7.10}$$

the viscoelastic dissipation Φ^v

$$\Phi^v = \sum_{m=1}^{n} (1 - D(\kappa))\left(\mathbb{S}_0(\boldsymbol{E} - \boldsymbol{E}^v - \boldsymbol{E}^p) - \mathbb{S}_{v,m}\boldsymbol{E}^v_m\right) : \dot{\boldsymbol{E}}^v_m, \tag{7.11}$$

and the damage dissipation Φ^κ

$$\Phi^\kappa = \frac{1}{2}D'(\kappa)\left((\boldsymbol{E} - \boldsymbol{E}^v - \boldsymbol{E}^p) : \mathbb{S}_0(\boldsymbol{E} - \boldsymbol{E}^v - \boldsymbol{E}^p) + \sum_{m=1}^{n} \boldsymbol{E}^v_m\mathbb{S}_{v,m}\boldsymbol{E}^v_m\right)\dot{\kappa}. \tag{7.12}$$

7.2.2 Elasticity and viscoelastic formulation

The instantaneous stiffness tensor $\mathbb{S}_0$ may in principle be of general anisotropy in this model. In this implementation, a fabric-based stiffness tensor was chosen [Zysset and Curnier, 1995]. The elastic constants were identified based on the indentation results presented in Chapter 5 using the methodology of Franzoso [Franzoso and Zysset, 2009].

Table 7.1: Constants for fabric-based elasticity [Zysset and Curnier, 1995] of ovine cortical bone.

E_0 $[GPa]$	ν_0	μ_0 $[GPa]$	ρ	$m1 = m2$	m3	k	l
19.951	0.3	7.67	1.0	0.898	1.205	1.0	1.0

The total stress in each Kelvin element is composed of an elastic and a viscous part:

$$\boldsymbol{S} = (1 - D(\kappa))\mathbb{S}_{v,m}\boldsymbol{E}^v_m + \mathbb{V}_m\dot{\boldsymbol{E}}^v_m \tag{7.13}$$

with an anisotropic stiffness tensor $\mathbb{S}_{v,m}$ and an anisotropic fourth order tensor $\mathbb{V}_m$ describing the direction-dependent behavior of the viscous damper of the m^{th} Kelvin element. A flow rule for the viscous strains $\boldsymbol{E}^v_m$ in each Kelvin element may be determined from this relation:

$$\dot{\boldsymbol{E}}^v_m = \mathbb{V}^{-1}_m(\boldsymbol{S} - (1 - D(\kappa))\mathbb{S}_{v,m}\boldsymbol{E}^v_m) \tag{7.14}$$

The flow rule for the total viscous strains is then given by:

$$\dot{\boldsymbol{E}}^v = \sum_{m=1}^{n} \dot{\boldsymbol{E}}^v_m \tag{7.15}$$

The characteristic times τ_m and stiffness ratios λ_m were identified by relaxation tests of dry cylindrical ovine bone specimens under uniaxial compression (Fig. 7.3) in a servohydraulic testing device (858 Mini Bionix, MTS, USA). A total of 14 dry ovine samples with a diameter of 3 mm were loaded uniaxially to three different strain levels in the elastic range and stress relaxation curves were recorded for 300 s followed by a pause of 600 s before reloading. The one-dimensional creep function for the rheological model presented in Fig. 7.2 for n Kelvin elements can be determined analytically and is given by:

$$J(t) = \frac{1}{E_0} + \sum_{m=1}^{n} \frac{1 - e^{-\frac{t}{\tau_m}}}{\lambda_m E_0} \tag{7.16}$$

The 1D relaxation function is related to the creep function by

$$G(t) = \mathcal{L}^{-1}\{\mathcal{L}\{J(t)\}^{-1}(s)\} \tag{7.17}$$

with the Laplace transform $\mathcal{L}$ and may be determined analytically for $n \leq 2$. The analytical form is rather long and therefore not reported here. The relaxation function was fitted to the uniaxial experimental data (Fig. 7.3, Tab. 7.2). The found behavior corresponds well to results of Fondrk et al. [1988] on bovine cortical bone and Rincón et al. [2001] for bovine trabecular bone, who reported a stress relaxation of ∼ 10%.

Table 7.2: Viscoelastic constants for dry ovine bone from macroscopic relaxation experiments.

τ_1	λ_1	τ_2	λ_2
2.0 ± 1.5 s	30.5 ± 19.9	69.4 ± 30.1	14.7 ± 5.0

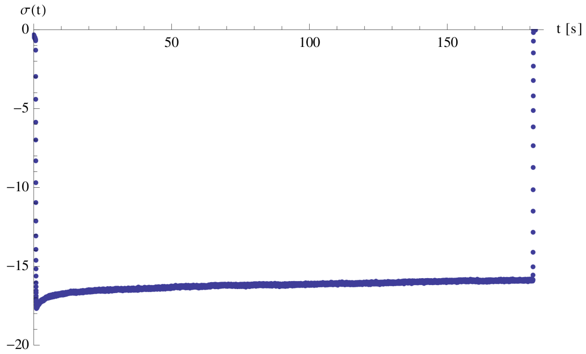

Figure 7.3: Stress over time during a macroscopic relaxation experiment on dry ovine cortical bone.

In the three-dimensional implementation, two Kelvin elements were included and it was hypothesized that the tensors governing the Kelvin elements $\mathbb{S}_{v,m}$ and $\mathbb{V}_m$ are proportional to the initial stiffness tensor $\mathbb{S}_0$ and may be determined by multiplication with the respective uniaxial constants.

$$\mathbb{V}_m = \tau_m \mathbb{S}_{v,m} = \tau_m \lambda_m \mathbb{S}_0, \qquad \mathbb{S}_{v,m} = \lambda_m \mathbb{S}_0.$$

7.2.3 Yield criterion, damage and viscoplastic formulation

A recently proposed fabric-based orthotropic quadric failure criterion [Schwiedrzik et al., 2013] was used to define the yield surface of bone. It allows strength differences in tension and compression and may take an ellipsoidal, hyperboloidal or conical shape depending on the chosen interaction parameters. The yield function is defined in stress space as:

$$Y(\boldsymbol{S}) := \sqrt{\boldsymbol{S} : \mathbb{F}\boldsymbol{S}} + \boldsymbol{F} : \boldsymbol{S} - 1 \tag{7.18}$$

The general form of the fourth order tensor $\mathbb{F}$ is then:

$$\mathbb{F} = \sum_{i=1}^{3} S_i^2 \boldsymbol{M}_i \otimes \boldsymbol{M}_i - \sum_{i,j=1;i\neq j}^{3} \zeta_{ij} S_i^2 \boldsymbol{M}_i \otimes \boldsymbol{M}_j + \sum_{i,j=1;i\neq j}^{3} \frac{1}{2\tau_{ij}^2} \boldsymbol{M}_i \underline{\otimes} \boldsymbol{M}_j \tag{7.19}$$

with

$$S_i = \frac{1}{2}\left(\frac{1}{\sigma_{ii}^{+}} + \frac{1}{\sigma_{ii}^{-}}\right) \tag{7.20}$$

In this case, the general form of the second order tensor $\boldsymbol{F}$ is:

$$\boldsymbol{F} = \sum_{i=1}^{3} \frac{1}{2}\left(\frac{1}{\sigma_{ii}^{+}} - \frac{1}{\sigma_{ii}^{-}}\right) \boldsymbol{M}_i \tag{7.21}$$

The criterion may be formulated based on fabric and density information. In this case, the number of independent constants reduces to six: σ_0^{+}, σ_0^{-}, ζ_0, τ_0, p and q. The orthotropic constants are then given by:

$$\sigma_{ii}^{+} = \sigma_0^{+} \rho^p m_i^{2q} \qquad \sigma_{ii}^{-} = \sigma_0^{-} \rho^p m_i^{2q}$$

$$\zeta_{ij} = \zeta_0 \frac{m_i^{2q}}{m_j^{2q}} \qquad \tau_{ij} = \tau_0 \rho^p m_i^q m_j^q$$

In this case, the parameter ζ_0 determines the shape of the criterion, which may be cylindrical, ellipsoidal, hyperboloidal or conical. The uniaxial parameters governing the surface and hardening were identified using the micropillar tests reported in Chapter 5. The tensile yield stress was approximated using the tensile/compression ratio of 1.5 reported by Gross [Gross, 2014]. Interaction parameter ζ_0 and shear strength τ_0 were regarded as unknown variables and determined by fitting the simulated curves to the experimental data of the Berkovich indentations. In the case of $m_1 = m_2 \neq m_3$ and an independent shear strength τ_0, the material features tetragonal symmetry. Isotropic hardening was introduced as a function of the cumulated plastic strain κ and the equivalent viscous strain rate $\dot{\epsilon}^v$. The criterion then reads:

$$Y(\boldsymbol{S}, \kappa, \dot{\epsilon^v}) := \sqrt{\boldsymbol{S} : \mathbb{F}\boldsymbol{S}} + \boldsymbol{F} : \boldsymbol{S} - r(\kappa) - r_v(\dot{\epsilon}^v). \tag{7.22}$$

In this implementation, viscoelastic hardening and damage were turned off and plastic hardening was approximated using an exponential function based on the experimental results of the micropillar compression experiments reported in Chapter 5. The final constants determining the strength and postyield behaviour are reported in the results section of this chapter.

Similar to the governing equations of the flow theory in rate-independent plasticity, the constitutive relations of a viscoplastic material may be written as [Etse and Carosio, 1999, Heeres et al., 2002, Perzyna, 1966]:

$$\boldsymbol{S} = (1 - D(\kappa))\mathbb{S}_0(\boldsymbol{E} - \boldsymbol{E}^v - \boldsymbol{E}^p)$$

$$\dot{\boldsymbol{E}}^p = \frac{1}{\eta}\langle\psi(Y)\rangle\frac{\boldsymbol{M}^p}{||\boldsymbol{M}^p||}$$

$$\boldsymbol{M}^p = \nabla_{\boldsymbol{S}} G$$

$$\dot{\kappa} = \frac{1}{\eta}\langle\psi(Y)\rangle$$

with a plastic potential G. In this implementation, the plastic potential G was set equal to the yield surface Y, therefore the plastic flow is associated when no hardening is present. The $\langle\rangle$ are the Macauley brackets in their usual meaning $\langle f(x)\rangle = \frac{1}{2}(f(x)+|f(x)|)$. Following the suggestion of Ponthot [Ponthot, 1995], a viscoplastic consistency parameter $\dot{\lambda}$ is introduced as known from the continuous Perzyna formulation.

$$\dot{\lambda} = \frac{1}{\eta}\langle\psi(Y)\rangle\frac{1}{||\boldsymbol{M}^p||} \tag{7.23}$$

By substituting the consistency parameter into the viscoplastic flow rules, they take a form well known from rate-independent plasticity [Hill, 1951]:

$$\dot{\boldsymbol{E}}^p = \dot{\lambda}\boldsymbol{M}^p \tag{7.24}$$

$$\dot{\kappa} = \dot{\lambda}||\boldsymbol{M}^p|| \tag{7.25}$$

For viscoplastic materials of the Perzyna type, the stress state can lie outside of the original yield surface [Perzyna, 1966]. In the inelastic regime ($Y \geq 0$), the overstress function $\psi(Y)$ is uniquely invertible. The yield function follows the inverse of the overstress function:

$$Y = \psi^{-1}(\dot{\lambda}||\boldsymbol{M}^p||\eta) = \psi^{-1}(\dot{\kappa}\eta) \tag{7.26}$$

Therefore we can define a new condition constraining the viscoplastic flow:

$$\bar{Y}(\boldsymbol{S}, \kappa, \dot{\kappa}, \dot{\epsilon^v}) = Y(\boldsymbol{S}, \kappa, \dot{\epsilon^v}) - \psi^{-1}(\dot{\kappa}\eta) = 0 \tag{7.27}$$

This condition represents a generalization of the yield condition $Y = 0$ for viscoplastic materials of the Perzyna type [Etse and Carosio, 1999, Carosio et al., 2000]. The approach is analogous to the so called consistent viscoplasticity [Wang et al., 1997] or the continuous Perzyna approach [Etse and Carosio, 1999, Ponthot, 1995] used in an earlier model for bone [Schwiedrzik and Zysset, 2013a]. It allows the use of generalized Kuhn-Tucker conditions for viscoplastic flow in the form of

$$\bar{Y} \leq 0, \qquad \dot{\kappa} \geq 0, \qquad \dot{\kappa}\bar{Y} = 0$$

which assure that the inelastic process satisfies $\bar{Y} = 0$ during viscoplastic deformation [Wang et al., 1997, Etse and Carosio, 1999]. It should be noted that in this approach the viscoplastic surface $\bar{Y}$ degenerates to the original yield surface Y for $\eta \rightarrow 0$ transforming the viscoplastic model to a rate-independent plastic one.

7.2.4 Algorithmic treatment

For simplicity's sake, all state variables at the end of the increment X_{n+1} will be called X and state variables at the beginning of the increment X_n will be called X_0 from now on. The commercial finite element solver Abaqus uses an updated Lagrangian mapping technique with the Cauchy stress tensor and an approximation of the integral of the rate of deformation $\int \boldsymbol{D}dt$ in a local corotational coordinate system as the conjugate strain tensor for simulations involving anisotropy, large deformations and rotations. These stress and strain measures were therefore used in this implementation. In principle, the algorithm is consistent for any conjugate pair of stress and strain measures, though.

Stress integration

In order to find the new state of the material, first the elastic trial stress is determined:

$$\boldsymbol{S}^{e,T} = (1 - D(\kappa_0))\mathbb{S}_0(\boldsymbol{E} - \boldsymbol{E}_0^v - \boldsymbol{E}_0^p) \tag{7.28}$$

Since viscous strains develop in both the elastic and the inelastic domain, a viscoelastic trial stress $\boldsymbol{S}^{v,T}$ is calculated by numerical time integration of the evolution equations of the viscous strains in each Kelvin element using an implicit Euler scheme. The viscous strains may then be written in incremental form as:

$$\boldsymbol{E}_m^v = \boldsymbol{E}_{0,m}^v + \Delta\boldsymbol{E}_m^v = \boldsymbol{E}_{0,m}^v + \mathbb{V}_m^{-1}(\boldsymbol{S} - (1 - D(\kappa))\mathbb{S}_{v,m}(\boldsymbol{E}_{0,m}^v + \Delta\boldsymbol{E}_m^v))\Delta t \tag{7.29}$$

When isolating $\Delta\boldsymbol{E}_m^v$, the viscous strain increment in each Kelvin element is given by

$$\Delta\boldsymbol{E}_m^v = (\mathbb{I} + (1 - D(\kappa_0 + \Delta\kappa))\Delta t\mathbb{V}_m^{-1}\mathbb{S}_{v,m})^{-1}\mathbb{V}_m^{-1}(\boldsymbol{S} - (1 - D(\kappa_0 + \Delta\kappa))\mathbb{S}_{v,m}\boldsymbol{E}_{0,m}^v)\Delta t \tag{7.30}$$

The total viscous strain increment is then

$$\Delta\boldsymbol{E}^v(\boldsymbol{S}, \Delta\kappa) = \sum_{m=1}^{n} \Delta\boldsymbol{E}_m^v(\boldsymbol{S}, \Delta\kappa) \tag{7.31}$$

The stress is linearized and expressed in incremental form as:

$$\begin{aligned}\boldsymbol{S} &= (1 - D(\kappa_0) - (D(\kappa) - D(\kappa_0)))\mathbb{S}(\boldsymbol{E}_0 + \Delta\boldsymbol{E} - \boldsymbol{E}_0^v - \Delta\boldsymbol{E}^v - \boldsymbol{E}_0^p - \Delta\boldsymbol{E}^p) \\ &= \boldsymbol{S}_T - (D(\kappa) - D(\kappa_0))\mathbb{S}(\boldsymbol{E} - \boldsymbol{E}_0^v - \boldsymbol{E}_0^p) - (1 - D(\kappa))\mathbb{S}(\Delta\boldsymbol{E}^v + \Delta\kappa\boldsymbol{N}^p)\end{aligned} \tag{7.32}$$

In order to solve for the viscoelastic trial state, a tensorial residual function $\boldsymbol{R}(\boldsymbol{S}, \Delta\kappa)$ is introduced. It is found by multiplication of the linearized incremental form of stress with $-\mathbb{E}$ and may be interpreted as a residuum of strains multiplied by $1 - D(\kappa)$.

$$\boldsymbol{R}(\boldsymbol{S}, \Delta\kappa) = \mathbb{E}_0(\boldsymbol{S}^{e,T} - \boldsymbol{S}) - (D(\kappa) - D(\kappa_0))(\boldsymbol{E} - \boldsymbol{E}_0^v - \boldsymbol{E}_0^p) - (1 - D(\kappa))(\Delta\boldsymbol{E}^v + \Delta\kappa\boldsymbol{N}^p) \tag{7.33}$$

For computation of the viscoelastic trial stress and more generally in the absence of plasticity $\Delta\kappa = 0$ and the nonlinear system of equations is linearized with respect to its remaining variable $\boldsymbol{S}$

$$\boldsymbol{R}_{i+1} = \boldsymbol{R}_i + \nabla_{\boldsymbol{S}}\boldsymbol{R}_i : \delta\boldsymbol{S} = \boldsymbol{0} \tag{7.34}$$

and solved using a Newton scheme, which gives the recursive equation:

$$\delta \boldsymbol{S} = \mathbb{S}_{a,ve} \boldsymbol{R}_i \tag{7.35}$$

with the incremental stiffness

$$\mathbb{S}_{a,ve} = -\nabla_{\boldsymbol{S}} \boldsymbol{R}_i^{-1} \tag{7.36}$$

After convergence of the algorithm, the viscoelastic trial state is obtained. Next, the yield criterion is evaluated using the viscoelastic trial stress $\boldsymbol{S}^{v,T}$ and the previous plastic state κ_0. If $Y(\boldsymbol{S}^{v,T}, \kappa_0, \dot{\epsilon}^{v,T}) < 0$, the stress increment is purely viscoelastic and no further inelastic deformation is taking place. If the yield criterion $Y(\boldsymbol{S}^{v,T}, \kappa_0, \dot{\epsilon}^{v,T}) \geq 0$, an implicit backprojection on the rate-dependent yield surface $\bar{Y}(\boldsymbol{S}, \kappa, \dot{\kappa}, \dot{\epsilon^v})$, coupled to the evolution of the viscous strains through the viscous flow rule is performed. In this case, $\dot{\kappa}$ is approximated by $\dot{\kappa} = \frac{\Delta\kappa}{\Delta t}$ and $\dot{\epsilon^v} = \frac{||\Delta \boldsymbol{E}^v||}{\Delta t}$. An incremental form of $\bar{Y}$ is added to the original system of equations $\boldsymbol{R}(\boldsymbol{S}, \Delta\kappa)$:

$$\bar{Y}(\boldsymbol{S}, \Delta\kappa) = Y(\boldsymbol{S}, \kappa_0 + \Delta\kappa, \dot{\epsilon^v}) - \psi^{-1}(\Delta\kappa) \tag{7.37}$$

The system of equations is linearized with respect to its variables $\boldsymbol{S}$ and $\Delta\kappa$ analogously to Schwiedrzik and Zysset [2013a] and solved using a Newton algorithm. The resulting recursive functions giving the state variable updates are:

$$\delta\Delta\kappa = -\frac{\bar{Y}_i + \nabla_{\boldsymbol{S}} \bar{Y}_i : \mathbb{S}_a \boldsymbol{R}_i}{\nabla_{\boldsymbol{S}} \bar{Y}_i : \mathbb{S}_a^E \frac{\partial \boldsymbol{R}_i}{\partial \Delta\kappa} + \frac{\partial \bar{Y}_i}{\partial \Delta\kappa}} \tag{7.38}$$

$$\delta \boldsymbol{S} = \mathbb{S}_a (\boldsymbol{R}_i + \frac{\partial \boldsymbol{R}_i}{\partial \Delta\kappa} \delta\Delta\kappa) \tag{7.39}$$

with the incremental stiffness

$$\mathbb{S}_{a,vp} = -(\nabla_{\boldsymbol{S}} \boldsymbol{R}_i)^{-1} \tag{7.40}$$

The gradients and derivatives used in this implementation are given in explicit form in the appendix of this chapter. After convergence of the algorithm, the coupled viscoelastic-viscoplastic damage state is obtained. In order to enlarge the region of convergence of the model, the primal Closest Point Projection Algorithm (CPPA) of Armero et al. [Armero and Pérez-Foguet, 2002, Pérez-Foguet and Armero, 2002] was implemented as a fail-safe algorithm after the standard Newton scheme in the UMAT subroutine.

Algorithmic tangent operator

The algorithmic tangent operator $\mathbb{S}_t$ relates infinitesimal changes of the strain increment $\delta\Delta\boldsymbol{E}$ to corresponding infinitesimal changes in the stress increment $\delta\Delta\boldsymbol{S}$. In order to find the tangent, a linearization of the stress-strain relationship has to be performed around the current solution. In this case, the consistency condition has to be applied to the algorithmic form of the rate equations. This was already done during the stress integration and does not need to be repeated. After convergence of the Newton scheme, the yield function $\bar{Y} \leq 0$ and the tensorial residual function $\boldsymbol{R}$ may be interpreted as an infinitesimal variation in strain multiplied by $1 - D(\kappa)$:

$$\boldsymbol{R}|_{conv} = (1 - D(\kappa))\delta\boldsymbol{E} \tag{7.41}$$

Therefore the tensor relating infinitesimal changes of strain $\frac{\delta\boldsymbol{R}}{1-D(\kappa)} = \delta\Delta\boldsymbol{E}$ to infinitesimal changes of the stress increment $\delta\Delta\boldsymbol{S}$ is the sought algorithmic tangent stiffness tensor. The algorithmic tangent stiffness operator in the case of viscoelasticity is:

$$\mathbb{S}_{t,ve} = (1 - D(\kappa))\mathbb{S}_{a,ve} \tag{7.42}$$

In the case of viscoelastic-viscoplastic deformation and damage accumulation, the algorithmic tangent operator takes the form:

$$\mathbb{S}_{t,vp} = (1 - D(\kappa))\mathbb{S}_{a,vp} - \frac{(1 - D(\kappa))\mathbb{S}_{a,vp}(\frac{\partial\boldsymbol{R}}{\partial\Delta\kappa} \otimes \boldsymbol{N}^p)\mathbb{S}_{a,vp}}{\boldsymbol{N}^p\mathbb{S}_{a,vp}\frac{\partial\boldsymbol{R}}{\partial\Delta\kappa} - \frac{1}{||\nabla_{\overline{\boldsymbol{S}}}\bar{Y}_i||}\frac{\partial\bar{Y}_i}{\partial\Delta\kappa}} \tag{7.43}$$

If viscoelasticity is turned off, the viscoelastic tangent degenerates to the damaged elastic stiffness $(1-D(\kappa))\mathbb{S}_0$ and the viscoelastic-viscoplastic damage tangent operator degenerates to an elasto-viscoplastic damage one. If the viscosity of the inelastic processes is also removed, a rate-independent elasto-plastic damage tangent is obtained (see, e.g. Schwiedrzik and Zysset [2013a]).

7.3 Verification

First, the correct implementation of the model was tested using single element tests. The viscoelastic behavior was tested using a relaxation test as shown in Fig 7.4.

The ratio of relaxed to instantaneous stiffness was found to be 0.908, which was expected and corresponds well to the experimental findings reported earlier as well as values reported in the literature [Fondrk et al., 1988, Zysset, 1994, Rincón et al., 2001]. Next, correct implementation of the yield surface and backprojection algorithm was tested. The result of

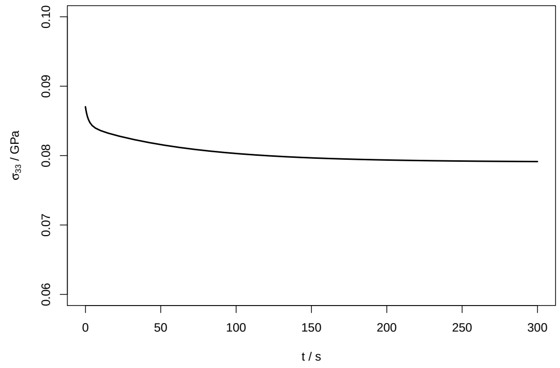

Figure 7.4: Single Element Test of a relaxation under unconfined compression in the 3-direction with an initial strain step and a 300 s holding period.

a uniaxial compression test of a linear hexahedral element at a strain rate of $0.0005\mathrm{s}^{-1}$ with a holding period at 20% nominal strain of 300 s is shown in Fig. 7.5.

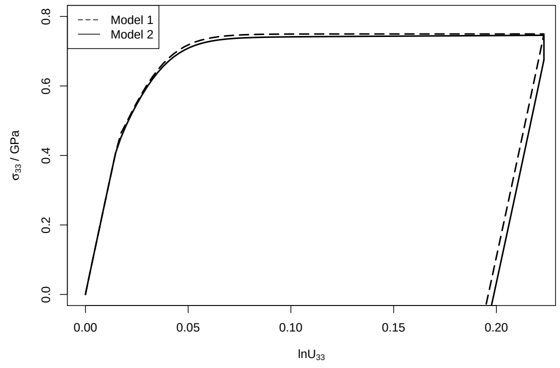

Figure 7.5: Single Element Test of a unconfined compression test in the 3-direction at $0.0005\mathrm{s}^{-1}$ followed by a 300 s holding period and unloading using the model presented above with viscoelasticity only (Model 1) and both viscoelasticity and viscoplasticity (Model 2).

The loading part of the single element test shows a behavior that corresponds well to the average response measured in the micropillar compression tests reported in Chapter 5. Almost no viscoelastic relaxation is observed for model 1, as the material has time to relax during the loading period due to the low strain rate. When introducing viscoplasticity (Model 2), a clear relaxation process becomes visible during the holding period.

7.4 Simulation of Berkovich and spherical indentations in bone

Using the above described model, indentations in bone using Berkovich and spherical indenters were simulated and the results were compared to experimental results on dry ovine bone. The finite element mesh described in detail in Chapter 3 was used and the boundary conditions of the experimental protocol (100 mN/min loading, 30 s hold period, 400 mN/min unloading) were applied on the indenter. The friction coefficient between indenter and sample was set to 0.2 following Carnelli et al. [2010]. Indentations were stopped at 1 µm depth for Berkovich indentations and 0.5 µm for spherical indentations consistent with the experimental data or alternatively at the maximum force measured during the experiments. The resulting indentation curves were greatly overestimating the hardness by a factor > 2 for both indenters when an isotropy condition was used for the shear yield strength τ_0. Therefore, both the interaction parameter and shear strength were regarded as unknown parameters. It was found that a reasonable fit could be achieved for the Berkovich indenter with $\zeta_0 = 0.3$ and $\tau_0 = 0.05$ GPa. The resulting indentation curves were analyzed using the method of Oliver and Pharr and indentation modulus, hardness, plastic and total work were compared to the experimental results.

As the creep depth using the macroscopic viscoelastic constants (Model 1) was only a small fraction of what was observed experimentally, viscoplasticity was added to the model (see Fig. 7.6, Model 2) and identified by comparison of the micropillar data with single element tests (Fig. 7.5). It was found that a reduction of the quasistatic yield properties by 10 % compensated by viscoplastic rate-dependent hardening leads to a correct uniaxial compressive strength at a strain rate of 0.0005s^{-1} (Fig. 7.5) and to realistic creep depths in Berkovich indentations (Fig. 7.6, Model 2).

However, when comparing the simulated indentation curves of the spherical indenter with a mean radius of 48 µm with the experimental ones, large differences were found (Fig. 7.6). Interestingly, the experimental moduli measured using the spherical indenter were also consistently lower compared to the measurements using the Berkovich indenter. A possible explanation for this phenomenon is that the nominal radius of the spherical indenter and the local curvature determining the indentation response at small depths can be very different [Constantinides et al., 2007]. Therefore, an effective radius of the indenter at small depths of $R = 28$ µm was determined for which the elastic moduli in transverse and axial direction correspond well to the measurements using the Berkovich tip. When using this indenter size in the Finite Element model, it was possible to obtain a reasonable correspondence of the simulated and experimental indentation curves for both Berkovich and spherical indenters in axial and transverse direction (Fig. 7.6). Tab. 7.5 summarizes the postelastic material constants used in this chapter. The identified yield surface in normal and shear stress space

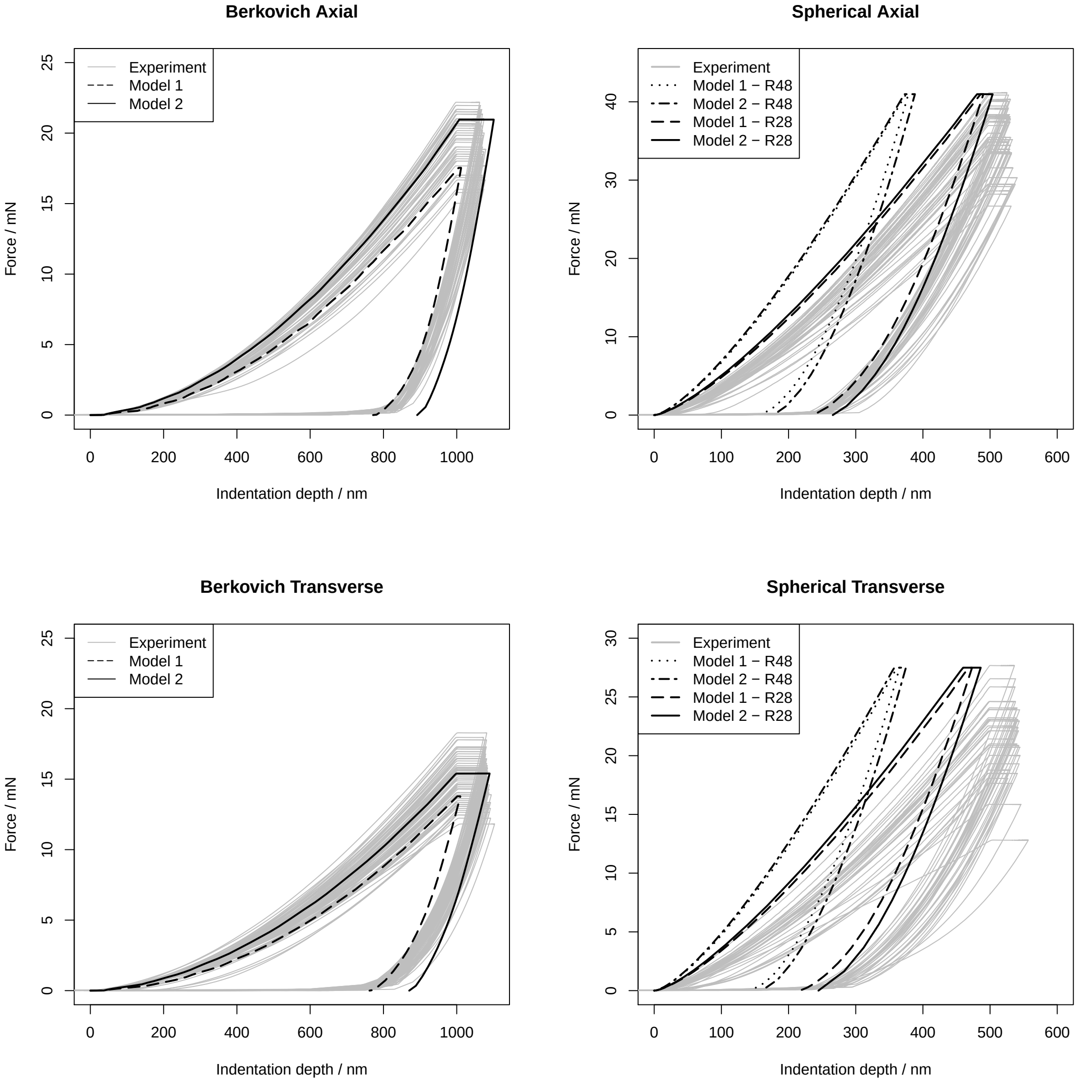

Figure 7.6: Experimental indentation curves (full grey lines) of Berkovich (left) and spherical (right) indentations in ovine bone in axial direction and FE simulations using model 1 or model 2.

is shown in Fig. 7.7.

The plastic zones under the conical and spherical indenters are shown in Fig. 7.8. Note that the maximum plastic strain under a spherical tip is an order of magnitude smaller than for the conical one. As expected [Mullins et al., 2009], no pile-up is visible in the vicinity of the indents.

Table 7.3: Comparison of experimental measurements on dry ovine bone with numerical results using viscoelasticity only (Model 1) and a combination of viscoelasticity and viscoplasticity (Model 2) using a Berkovich and a spherical (nominal radius 50µm, mean radius 48µm, effective radius 28µm) tip in axial direction.

Ind.	Dir.	Meas.	Exp. Med.	Exp. Min.	Exp. Max.	Model 1	Model 2
Berk.	Ax.	E^*/GPa	27.6	22.5	30.9	29.3	29.2
Berk.	Ax.	H_{IT}/GPa	1.025	0.768	1.182	0.828	0.839
Berk.	Ax.	h_{creep}/nm	66.8	56.3	77.6	6.8	94.1
Berk.	Ax.	h_{res}/nm	789.5	697.1	846.0	0.818	903.8
Berk.	Ax.	W_{elast}/pJ	1885.5	1173.4	2156.8	1355.45	1656.84
Berk.	Ax.	W_{total}/pJ	8332.6	5488.9	9248.9	6284.27	9496.04
Sph. 48µm	Ax.	E^*/GPa	20.4	16.8	22.7	29.8	29.6
Sph. 48µm	Ax.	H_{IT}/GPa	0.297	0.209	0.350	0.489	0.470
Sph. 48µm	Ax.	h_{creep}/nm	28.0	17.7	39.4	3.3	15.7
Sph. 48µm	Ax.	h_{res}/nm	217.3	173.1	283.0	160.5	176.4
Sph. 48µm	Ax.	W_{elast}/pJ	3960.2	2520.3	4747.2	3416.48	3344.46
Sph. 48µm	Ax.	W_{total}/pJ	8232.3	5757.9	9565.0	6635.26	7137.90
Sph. 28µm	Ax.	E^*/GPa	26.7	22.1	30.0	29.6	29.5
Sph. 28µm	Ax.	H_{IT}/GPa	0.511	0.360	0.602	0.622	0.598
Sph. 28µm	Ax.	h_{creep}/nm	28.0	17.7	39.4	4.1	23.1
Sph. 28µm	Ax.	h_{res}/nm	217.3	173.1	283.0	249.0	271.0
Sph. 28µm	Ax.	W_{elast}/pJ	3960.2	2520.3	4747.2	3885.03	3772.67
Sph. 28µm	Ax.	W_{total}/pJ	8232.3	5757.9	9565.0	8636.73	9409.12

7.5 Discussion

In this chapter, the elastic-viscoplastic damage model proposed in Chapter 2 was extended to linear viscoelasticity. The hypothesis was tested that in the presence of a dissipative process in the elastic regime it would be possible to obtain realistic indentation curves for bone when using the constitutive model governed by the uniaxial yield properties from the micropillar data. It was found that viscoelasticity alone governed by properties measured on the macroscale has very little influence on the indentation curve and results in a clear underestimation of the creep deformation. Adding viscoplasticity to the model leads to an increase in creep deformation during the hold time. However, the hardness of the material was highly overestimated when using an isotropy condition to determine the unknown shear yield strength.

In order to obtain realistic indentation curves including plasticity for both Berkovich and

Table 7.4: Comparison of experimental measurements on dry ovine bone with numerical results using viscoelasticity only (Model 1) and a combination of viscoelasticity and viscoplasticity (Model 2) using a Berkovich and a spherical (nominal radius 50µm, mean radius 48µm, effective radius 28µm) tip in transverse directions.

Ind.	Dir.	Meas.	Exp. Med.	Exp. Min.	Exp. Max.	Model 1	Model 2
Berk.	Tv.	E^*/GPa	18.9	15.5	23.1	20.5	20.0
Berk.	Tv.	H_{IT}/GPa	0.675	0.494	0.817	0.672	0.642
Berk.	Tv.	h_{creep}/nm	79.8	54.4	101.4	8.3	90.7
Berk.	Tv.	h_{res}/nm	618.3	550.4	795.8	777.7	886.1
Berk.	Tv.	W_{elast}/pJ	1647.6	1112.5	2028.7	1204.51	1312.79
Berk.	Tv.	W_{total}/pJ	6532.1	4569.6	8210.4	4746.04	6841.10
Sph. 48µm	Tv.	E^*/GPa	15.1	9.8	17.9	20.2	20.1
Sph. 48µm	Tv.	H_{IT}/GPa	0.171	0.092	0.221	0.346	0.333
Sph. 48µm	Tv.	h_{creep}/nm	38.6	25.3	55.0	4.0	17.1
Sph. 48µm	Tv.	h_{res}/nm	192.0	-	252.7	145.3	158.6
Sph. 48µm	Tv.	W_{elast}/pJ	2344.1	1402.4	3072.5	2320.79	2280.68
Sph. 48µm	Tv.	W_{total}/pJ	5385.4	3535.6	6856.8	4308.56	4658.61
Sph. 28µm	Tv.	E^*/GPa	19.9	12.9	23.5	20.3	20.1
Sph. 28µm	Tv.	H_{IT}/GPa	0.294	0.158	0.380	0.438	0.421
Sph. 28µm	Tv.	h_{creep}/nm	38.6	25.3	55.0	4.8	26.1
Sph. 28µm	Tv.	h_{res}/nm	192.0	-	252.7	228.18	247.2
Sph. 28µm	Tv.	W_{elast}/pJ	2344.1	1402.4	3072.5	2623.24	2562.36
Sph. 28µm	Tv.	W_{total}/pJ	5385.4	3535.6	6856.8	5652.86	6163.44

Table 7.5: Postelastic constants for dry ovine bone on the microscale for the viscoelastic (Model 1, top) and the viscoelastic-viscoplastic (Model 2, bottom) case.

Model	σ_0^+	σ_0^-	ζ_0	τ_0	q	r^y	η	m
1	0.644	0.429	0.3	0.05	0.407	0.6	0	0.001
2	0.580	0.386	0.3	0.045	0.407	0.6	12.0	0.001

spherical indents using the uniaxial strengths of the micropillar compressions, the assumption that shear strength is governed by an isotropy condition of the base material had to be abandoned. A set of parameters was identified that yields a reasonable fit between simulated and experimental curves. The found values for shear strength and interaction parameters of

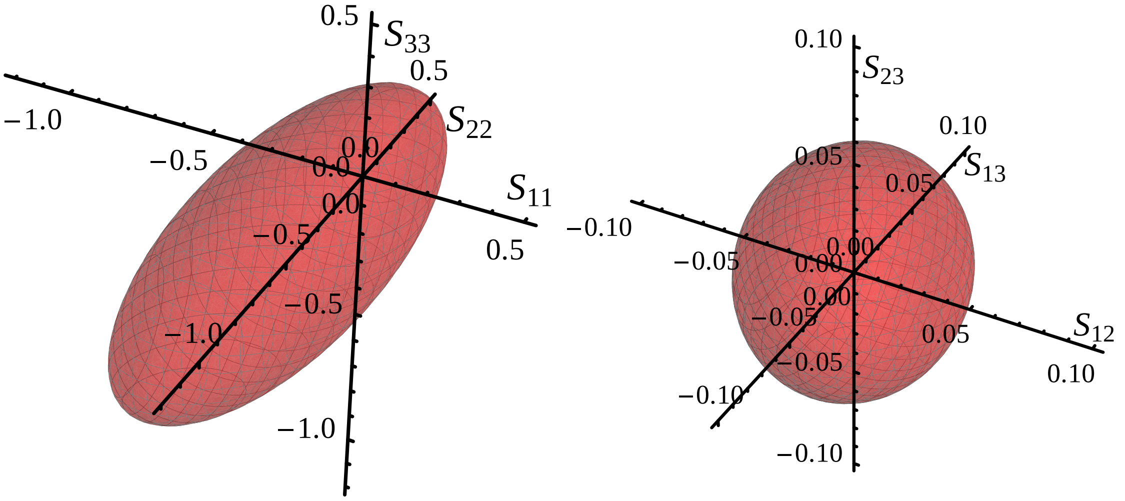

Figure 7.7: Quadric yield surface in normal (left) and shear (right) stress space governed by parameters presented in Tab. 7.5.

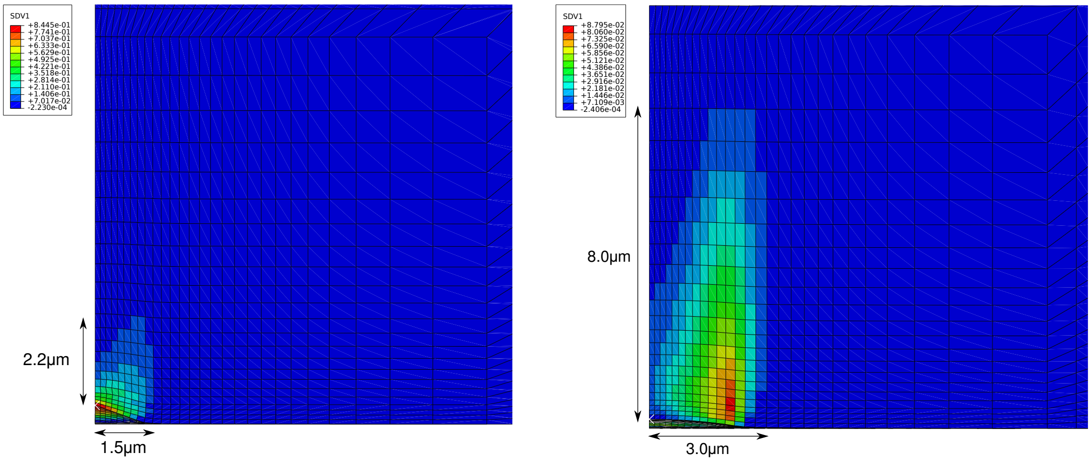

Figure 7.8: Accumulated plastic strain map of Finite Element simulations of Berkovich (left) and spherical (R = 28 μm, right) indentation in axial direction for the viscoelastic-viscoplastic material model (Model 2) at maximum indentation depth.

$\tau_0 = 0.05$ GPa and $\zeta_0 = 0.3$ remain to be verified by independent experiments. Difficulties were encountered to fit both the spherical and the Berkovich indentations. This is at least partly related to the increased uncertainty in boundary conditions for the spherical indenter. The spherical indenter had a nominal radius of 50 μm, the best fitted sphere determined from optical micrographs of the whole tip had an average radius of 48 μm. However, the exact shape function could not be determined by calibration using a fused silica sample, as Hertz indentations in brittle materials induce cone-shaped cracks that would destroy the reference sample. Therefore, the local curvature at small indentation depths was not known and was most probably understimated, as the measured indentation moduli were consistently lower than the ones measured using a Berkovich tip (Tab. 7.3,7.4). Therefore, an effective radius of the indenter at small depths of $R = 28$ µm was determined for which the measured elastic moduli in transverse and axial direction correspond well to the measurements using the Berkovich tip. Simulations using the effective indenter radius resulted in a reasonably good fit of the simulated and experimental indentation curves (Fig. 7.6, Tab. 7.3,7.4). It remains to be verified if the determined effective radius is indeed representative of the real indenter geometry. This issue could be clarified in the future by directly measuring the tip topography of the spherical indenter with an AFM as proposed by Constantinides et al. [2007].

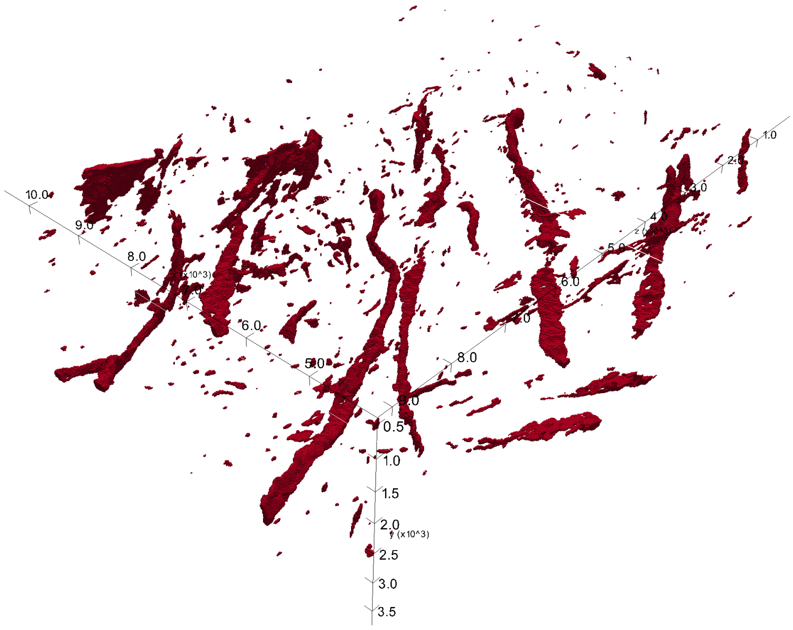

Figure 7.9: Segmented porosity from a FIB/SEM tomography of a volume of $3.5\mu m \times 5\mu m \times 10\mu m$ from a bovine cortical bone sample (by courtesy of Joan Rovira, PhD).

As Fig. 7.9 illustrates, canaliculi are present in bone with a spacing of 2 to 3 microns. It is highly probable that most of the variation in microindentation properties is related to the lacuna-canalicular porosity, as it was shown previously that neither site-matched measurements of mineralization and fibril angle [Spiesz et al., 2013] nor residual imprint shape and surface roughness (Chapter 6 of this thesis) are strongly correlated to experimental indentation results. With their diameter of $100 - 200$ nm canaliculi are small compared to the homogeneously tested volume of a micropillar or the elastically tested volume of an indentation and may be homogenized. However, they are not necessarily negligible compared to the plastically deformed volume directly under the indenter tip for microindentations to depths of $500 - 1000$ nm (Fig. 7.8). These canaliculi lead to stress concentations and may be compressed locally near the indenter tip, which would result in a lower apparent resistance of the material to plastic flow. As these structures were not modeled explicitly in the FE mesh in this study, this missing effect has to be compensated by the material model. Therefore, the plasticity of the material could be overestimated. It seems therefore reasonable to fit the stiffest curves instead of the mean ones in order to circumvent this problem. Also, it could be beneficial to clarify this issue by modeling canaliculi explicitly or using statistics based material properties when trying to identify postelastic properties of bone using microindentation in the future.

It is very probable that the response to indentation is strongly influenced by time-dependent processes near the indenter tip where the material is yielding. These are not known in detail for the microscale at the moment and not easy to identify using indentation experiments due to the heterogeneous stress state resulting in a coupled response featuring both global viscoelastic and local viscoplastic deformation. Further work is necessary to better understand the time-dependent processes governing bone at the microscale before a unique set of dissipative processes and their governing parameters can be determined from indentation curves. Especially more thorough identification strategies of the viscoelastic and viscoplastic properties on the microscale are needed in order to achieve this goal, e.g. by performing micropillar compression tests to different stress levels (both elastic and postyield) at different loading rates.

Additionally, the tensile and shear postelastic properties were not known and had to be assumed in this study. This is a severe limitation and needs to be remedied by independent experiments in the future. Another limitation of this study is that the friction coefficient between diamond and bone that has a non-negligible influence on the indentation response was taken from a microindentation study in the literature [Carnelli et al., 2010]. The reliability of the results would be greatly enhanced if nanotribologic experiments were conducted to measure the friction coefficient independently. Finally, all experiments used for the material identification were performed in dry condition, which is not the physiological state of bone. The existing methods need to be adapted to test bone in its native hydrated state in the future. While this has been achieved for microindentation, other micromechanical methods like micropillar compression have not been performed on hydrated bone yet.

In conclusion it was possible to remedy the discrepancies between indentation and micropillar data in this study by abandoning the assumption of shear strength being governed by an isotropy condition. However, additional independent measurements and a better understanding of the underlying dissipative processes and their mathematical description as well as very well defined boundary conditions regarding indenter and ultrastructure are necessary in order to verify this finding and to uniquely identify the nonlinear behaviour of bone on the microscale in the future.

7.6 Gradients and Derivatives

7.6.1 Residual of total strains

$$\boldsymbol{R}(\boldsymbol{S},\Delta\kappa) = \mathbb{E}_0(\boldsymbol{S}^{e,T}-\boldsymbol{S}) - (D(\kappa)-D(\kappa_0))(\boldsymbol{E}-\boldsymbol{E}_0^v-\boldsymbol{E}_0^p) - (1-D(\kappa))(\Delta\boldsymbol{E}^v+\Delta\kappa\boldsymbol{N}^p)$$

$$\nabla_{\boldsymbol{S}}\boldsymbol{R} = -\mathbb{E}_0 - (1-D)(\nabla_{\boldsymbol{S}}\Delta\boldsymbol{E}^v + \Delta\kappa\nabla_{\boldsymbol{S}}\boldsymbol{N}^p)$$

$$\frac{\partial\boldsymbol{R}}{\partial\Delta\kappa} = -D'(\boldsymbol{E}-\boldsymbol{E}_0^v-\Delta\boldsymbol{E}^v-\boldsymbol{E}_0^p-\Delta\kappa\boldsymbol{N}^p) - (1-D)(\frac{\partial\Delta\boldsymbol{E}^v}{\partial\Delta\kappa}+\boldsymbol{N}^p)$$

7.6.2 Viscous strain increment

General formulation

$$\Delta\boldsymbol{E}_m^v(\boldsymbol{S},\Delta\kappa) = (\mathbb{I}+(1-D(\kappa_0+\Delta\kappa))\Delta t\mathbb{V}_m^{-1}\mathbb{S}_{v,m})^{-1}\mathbb{V}_m^{-1}(\boldsymbol{S}-(1-D(\kappa_0+\Delta\kappa))\mathbb{S}_{v,m}\boldsymbol{E}_{0,m}^v)\Delta t$$

$$\nabla_{\boldsymbol{S}}\Delta\boldsymbol{E}_m^v = (\mathbb{I}+(1-D)\Delta t\mathbb{V}_m^{-1}\mathbb{S}_{v,m})^{-1}\mathbb{V}^{-1}\Delta t$$

$$\begin{aligned}\frac{\partial\Delta\boldsymbol{E}_m^v}{\partial\Delta\kappa} = \quad & (\mathbb{I}+(1-D)\Delta t\mathbb{V}_m^{-1}\mathbb{S}_{v,m})^{-2}(-D'\mathbb{V}_m^{-1}\mathbb{S}_{v,m}\Delta t)\mathbb{V}_m^{-1}(\boldsymbol{S}-(1-D)\mathbb{S}_{v,m}\boldsymbol{E}_{0,m}^v)\Delta t \\ & +(\mathbb{I}+(1-D)\Delta t\mathbb{V}_m^{-1}\mathbb{S}_{v,m})^{-1}\mathbb{V}^{-1}D'\mathbb{S}_v\boldsymbol{E}_0^v\Delta t\end{aligned}$$

Proportional viscoelasticity: $\mathbb{V}_m = \tau_m\lambda_m\mathbb{S}_0$, $\mathbb{S}_{v,m} = \lambda_m\mathbb{S}_0$

$$\Delta\boldsymbol{E}_m^v = \frac{\frac{1}{\lambda_m\tau_m}\mathbb{E}_0\boldsymbol{S}-(1-D)\frac{1}{\tau_m}\boldsymbol{E}_{0,m}^v}{1+(1-D)\frac{1}{\tau_m}\Delta t}\Delta t$$

$$\nabla_{\boldsymbol{S}}\Delta\boldsymbol{E}_m^v = \frac{\frac{1}{\lambda_m\tau_m}\mathbb{E}_0\Delta t}{1+(1-D)\frac{1}{\tau_m}\Delta t}$$

$$\frac{\partial \Delta \boldsymbol{E}^v_m}{\partial \Delta \kappa} = \frac{D' \frac{1}{\tau_m} \Delta t (\boldsymbol{E}^v_{0,m} (1 + (1-D) \frac{1}{\tau_m} \Delta t) + \Delta t (\frac{1}{\lambda_m \tau_m} \mathbb{E}_0 \boldsymbol{S} - (1-D) \frac{1}{\tau_m} \boldsymbol{E}^v_{0,m}))}{(1 + (1-D) \frac{1}{\tau_m} \Delta t)^2}$$

7.6.3 Equivalent viscous strain rate

$$\dot{\epsilon}^v(\boldsymbol{S}, \Delta\kappa) = \frac{||\Delta \boldsymbol{E}^v||}{\Delta t}$$

$$\nabla_{\boldsymbol{S}} \dot{\epsilon}^v = \frac{\Delta \boldsymbol{E}^v}{||\Delta \boldsymbol{E}^v||} \frac{\nabla_{\boldsymbol{S}} \Delta \boldsymbol{E}^v}{\Delta t}$$

$$\frac{\partial \dot{\epsilon}^v}{\partial \kappa} = \frac{\Delta \boldsymbol{E}^v}{||\Delta \boldsymbol{E}^v|| \Delta t} : \frac{\partial \Delta \boldsymbol{E}^v}{\partial \Delta \kappa}$$

7.6.4 Yield surface

$$Y(\boldsymbol{S}, \dot{\epsilon}^v, \kappa) = \sqrt{\boldsymbol{S} : \mathbb{F} \boldsymbol{S}} + \boldsymbol{F} : \boldsymbol{S} - r(\kappa) - r_v(\epsilon^v)$$

$$\nabla_{\boldsymbol{S}} Y = (\boldsymbol{S} : \mathbb{F} \boldsymbol{S})^{-\frac{1}{2}} \mathbb{F} \boldsymbol{S} + \boldsymbol{F} - r_v'(\dot{\epsilon}^v) \nabla_{\boldsymbol{S}} \dot{\epsilon}^v$$

$$\frac{\partial Y}{\partial \Delta \kappa} = -r'(\kappa) - r_v'(\dot{\epsilon}^v) \frac{\partial \dot{\epsilon}^v}{\partial \kappa}$$

7.6.5 Rate-dependent algorithmic Yield surface

$$\bar{Y}(\boldsymbol{S}, \Delta\epsilon^v, \Delta\kappa) = Y(\boldsymbol{S}, \kappa_0 + \Delta\kappa, \Delta\epsilon^v) - \psi^{-1}(\Delta\kappa)$$

$$\nabla_{\boldsymbol{S}} \bar{Y} = \nabla_{\boldsymbol{S}} Y$$

$$\frac{\partial \bar{Y}}{\partial \Delta \kappa} = \frac{\partial Y}{\partial \Delta \kappa} - \frac{\partial \psi^{-1}}{\partial \Delta \kappa}$$

7.6.6 Overstress functions

- Linear: $\Psi^{-1}(\Delta\kappa) = \eta\frac{\Delta\kappa}{\Delta t}, \qquad \frac{d\Psi^{-1}}{d\Delta\kappa} = \frac{\eta}{\Delta t}$
- Exponential: $\Psi^{-1}(\Delta\kappa) = \frac{ln(1+\eta\frac{\Delta\kappa}{\Delta t})}{m}, \qquad \frac{d\Psi^{-1}}{d\Delta\kappa} = \frac{1}{m}\frac{1}{1+\eta\frac{\Delta\kappa}{\Delta t}}\frac{\eta}{\Delta t}$
- Logarithmic: $\Psi^{-1}(\Delta\kappa) = \frac{e^{\eta\frac{\Delta\kappa}{\Delta t}}-1}{m}, \qquad \frac{d\Psi^{-1}}{d\Delta\kappa} = \frac{\frac{\eta}{\Delta t}e^{\eta\frac{\Delta\kappa}{\Delta t}}-1}{m}$
- Polynomial: $\Psi^{-1}(\Delta\kappa) = -\frac{m}{2} + \sqrt{\frac{m^2}{4} + \eta\frac{\Delta\kappa}{\Delta t}}, \qquad \frac{d\Psi^{-1}}{d\Delta\kappa} = \frac{1}{2}(\frac{m^2}{4} + \eta\frac{\Delta\kappa}{\Delta t})^{-\frac{1}{2}}\frac{\eta}{\Delta t}$
- Power law: $\Psi^{-1}(\Delta\kappa) = (\eta\frac{\Delta\kappa}{\Delta t})^{\frac{1}{m}}, \qquad \frac{d\Psi^{-1}}{d\Delta\kappa} = \frac{1}{m}(\frac{\eta}{\Delta t})^{\frac{1}{m}}\Delta\kappa^{\frac{1}{m}-1}$

7.6.7 Plastic potential

$$G(\boldsymbol{S}) = \sqrt{\boldsymbol{S} : \mathbb{G}\boldsymbol{S}} + \boldsymbol{G} : \boldsymbol{S} - 1$$

$$\nabla_{\boldsymbol{S}} G = \boldsymbol{M}^p = (\boldsymbol{S} : \mathbb{G}\boldsymbol{S})^{-\frac{1}{2}}\mathbb{G}\boldsymbol{S} + \boldsymbol{G}$$

$$\nabla^2_{\boldsymbol{S}} G = -(\boldsymbol{S} : \mathbb{G}\boldsymbol{S})^{-\frac{3}{2}}(\mathbb{G}\boldsymbol{S} \otimes \mathbb{G}\boldsymbol{S}) + (\boldsymbol{S} : \mathbb{G}\boldsymbol{S})^{-\frac{1}{2}}\mathbb{G}$$

7.6.8 Norm of the gradient on the yield surface

$$h(\boldsymbol{S}) = ||\nabla_{\boldsymbol{S}} G||$$

$$\nabla_{\boldsymbol{S}} h = (\nabla_{\boldsymbol{S}} G : \nabla_{\boldsymbol{S}} G)^{-\frac{1}{2}}\nabla_{\boldsymbol{S}} G \nabla^2_{\boldsymbol{S}} G$$

7.6.9 Direction of plastic flow

$$\boldsymbol{N}^p(\boldsymbol{S}) = \frac{\nabla_{\boldsymbol{S}} G(\boldsymbol{S})}{h(\boldsymbol{S})}$$

$$\nabla_{\boldsymbol{S}} \boldsymbol{N}^p = \frac{\nabla^2_{\boldsymbol{S}} G h - \nabla_{\boldsymbol{S}} G \otimes \nabla_{\boldsymbol{S}} h}{h^2}$$

8

Conclusion

An increase in bone fractures due to the progressive aging of societies poses a severe challenge for health care systems all over the world. As bone strength is determined by both bone mass and quality, today's treatments for osteoporosis rely on a better understanding of the mechanical behavior of bone at the microscale and its relation to adaptation processes [Bajaj et al., 2014]. A high level of predictability has been reached for elastic properties on several length scales [Fritsch and Hellmich, 2007, Reisinger et al., 2010, Spiesz et al., 2011]. However, up to now there is a lack of reliable postyield data, especially on the lower length scales. The aim of this thesis was to find the dominating deformation mechanisms and the postelastic mechanical properties on the microscale.

A common approach for identifying microscale yield properties are inverse methods based on comparison of microindentations and Finite Element simulations. In order to be able to describe the behavior of bone at the microscale, as a first step an anisotropic elastic-viscoplastic damage model was developed using an eccentric generalized Hill criterion and nonlinear isotropic hardening. Viscoplasticity was implemented using the continuous Perzyna formulation [Carosio et al., 2000, Wang et al., 1997], damage was modeled by a scalar function of the accumulated plastic strain [Charlebois et al., 2010, Zysset, 1994]. The model was implemented as a user subroutine in the commercial FE code Abaqus and correct implementation of the algorithm, convergence and accuracy of the tangent operator were tested by means of single element tests. A FE simulation of microindentation in lamellar bone showed that the constitutive model is able to reproduce the main features of force-depth curves of Berkovich indentations in bone including creep deformation at constant force.

As the generalized Hill criterion is limited to elliptical and cylindrical yield surfaces and micromechanical considerations by Maghous et al. [2009] showed that the introduction of porosity into a cohesive-frictional material like bone would lead to both a decrease in uniaxial strength properties as well as a change of the shape of the criterion from conical to elliptical, a new yield surface was proposed that can take any convex quadratic shape and that is easy to implement. The main advantage of the new formulation is that in the case of material identification the shape of the yield surface does not have to be anticipated. Instead, a minimization using the quadric criterion would result in the optimal shape among all convex quadrics. Also, the proposed criterion is a homogeneous function of degree one, which is beneficial for implementation of isotropic hardening rules in a computational mechanics framework. The convexity limits of the criterion and the transition points between the different shapes were identified. The criterion was discussed for general anisotropy as well as special cases of material symmetry such as isotropy, cubic symmetry, fabric-based orthotropy and general orthotropy. The generality of the formulation was demonstrated by showing its degeneration to several classical yield surfaces [Hill, 1951, Liu et al., 1997, von Mises, 1913, Tsai and Wu, 1971]. Finally, several existing yield criteria [Carnelli et al., 2010, Rincón-

Kohli and Zysset, 2009, Wolfram et al., 2012] were converted to the quadric formulation thus demonstrating the applicability of the new criterion to the description of bone at multiple length scales.

Postyield properties of bone may be assessed by comparison of nonlinear Finite Element simulations of microindentations using elastoplastic damage models [Lucchini et al., 2011]. So far, most of the studies assumed that bone can be approximated by a conical yield surface on the microscale [Carnelli et al., 2010, Lucchini et al., 2011, Mullins et al., 2009, Wang et al., 2008]. However, due to the presence of nanoporosity this is not verified [Maghous et al., 2009]. Therefore, a computational study was undertaken aiming at determining the influence of yield surface shape and damage on the depth dependent response of bone to microindentation using spherical and conical tips. The constitutive model developed in Chapter 2 was modified to make use of the yield criterion proposed in Chapter 3. Yield surface shape and critical damage were varied and shown to have a major impact on the indentation curves. Their influence on indentation modulus, hardness, their ratio as well as the elastic to total work ratio were found to be well described by multilinear regressions for both tip shapes. For conical tips, indentation depth was not a significant factor, while for spherical tips damage was insignificant. On the one hand, this verified the self-similarity of conical indentations in the presence of plasticity and damage. On the other hand, the fact that damage was not significantly affecting the response to spherical indentations can help to identify the two effects of plasticity and damage independently by choice of a proper identification strategy. The yield properties could be mainly identified by spherical indentations in different directions and ideally using different indentation depth to indenter radius ratios, while Berkovich indentations could serve to identify the amount of damage present under the indenter.

However, inverse methods based on microindentation suffer from a lack of uniqueness of the found material properties in the case of nonlinear material behavior. This can be overcome by using several different indenter shapes [Bocciarelli et al., 2005, Bolzon et al., 2004, Bucaille et al., 2003, Ganneau et al., 2006] if the underlying dissipative mechanisms and their mathematical description are well understood. However, some uncertainty with respect to the identified parameters remains due to the inherent non-uniqueness of parameters found using inverse methods, the necessity to choose the main dissipative mechanisms a priori, and the inhomogeneous and mostly compressive loading conditions imposed on the material. Therefore it is necessary to perform independent complementary experiments to increase the reliability of the found parameters. In order to achieve this, measurements allowing a straightforward interpretation are needed.

Therefore, monotonic and cyclic micropillar compression tests in a scanning electron microscope complemented by microindentation and macroscopic uniaxial compression tests were performed on dry ovine lamellar bone to identify elastic modulus, yield stress, plastic deformation, damage accumulation and failure mechanisms. While the elastic properties measured during micropillar compression, microindentation and macroscopic compression tests were highly consistent, the postyield deformation and failure mechanisms differed between the two length scales. A majority of the micropillars showed a highly ductile postyield behavior with continuous strain hardening until failure by localization in a slip plane, while the macroscopic samples failed in a quasi-brittle fashion with microcracks forming and coalescing into macroscopic failure surfaces. Consequently, compressive strength was 2.4 times higher on the microscale than on the macroscale, maximum plastic strain even 6 times. Also, the cyclic compression tests showed no modulus reduction in the micropillars up to 8% of plastic strain as opposed to the macroscopic samples. This is in conflict with the current literature on bone strength at the microscale, which reports uniaxial properties similar to macroscopic values and the presence of damage [Carnelli et al., 2010, Lucchini et al., 2011]. In agreement with a proposed rheological model these experiments illustrate a transition from a ductile mechanical behavior of bone at the microscale to a quasi-brittle response driven by the increased heterogeneity due to growth of preexisting cracks at the macroscale. The yield stress and ultimate plastic strain associated with the growth of pre-existing cracks near interfaces [Carter and Hayes, 1977, Martin and Burr, 1989] or pores [Currey, 1962] on the macroscale are substantially lower than the ones necessary to initiate and propagate a new crack through a micropillar made of a single osteonal lamella. This scale-effect is well known for brittle materials like ceramics [Michler et al., 2007, Östlund et al., 2009, 2011] and in line with the theory of quasi-brittle failure [Bažant, 2004] as well as earlier reports of size effects on yield and fatigue properties in equine bone on the macroscale [Bigley et al., 2007, 2008]. The data supports the thesis that, under compressive loading, multiple slip planes emerging at the weak interfaces or in the vicinity of pores in the interstitial bone coalesce into microcracks, the statistical distribution and growth of which lead to a quasi-brittle failure at the macroscopic level. These findings highlight the importance of studying interface properties of cement lines and the stress concentration effect of pores in the interstitial tissue more closely. They remain to be extended to human bone, physiological testing conditions and further loading modes.

As the analysis of microindentation data is based on assumptions on the contact between sample and surface, a study was then undertaken to quantify the topological variability of indentations in bone and examine its relationship with mechanical properties. Microindentations were performed in dry human and ovine bone in axial and transverse directions and their topography was measured by atomic force microscopy. Statistical shape modeling of the residual imprint allowed to define a mean shape and to describe the variability in terms of 21 principal components related to imprint depth, surface curvature and roughness. The indentation profile of bone was found to be highly consistent and free of any pile up, which is in line with the literature [Mullins et al., 2009] while differing mostly by depth between species and direction. A few of the topological parameters, in particular depth, showed significant correlations to variations in mechanical properties, but the correlations were not very strong or consistent and the standard errors were low, as the mechanical response of bone as well as the residual imprint shape were highly consistent within each category. It could thus be verified that bone is rather homogeneous in its micromechanical properties and that indentation results are not strongly influenced by small deviations from the ideal case if the surface is prepared well. The mean residual imprint shapes obtained in this study may be used as additional observables for comparison to Finite Element simulations in an inverse approach to identify the nonlinear mechanical properties of bone on the microscale.

As the uniaxial properties reported in Chapter 5 are in conflict with the current literature on bone indentation [Carnelli et al., 2010, Lucchini et al., 2011], it is likely that another dissipative mechanism is present influencing the response of bone to microindentations. Bone has been shown to feature a distinct time-dependent behavior in the elastic regime [Bargren et al., 1974, Fondrk et al., 1988, Lakes et al., 1979, Lakes and Katz, 1979]. Therefore the elastic-viscoplastic damage model proposed in Chapter 2 was extended to viscoelasticity. The viscoelastic properties were identified from macroscopic experiments, while the quasistatic postelastic properties were extracted from the data reported in Chapter 5. It was found that viscoelasticity alone governed by properties measured on the macroscale has very little influence on the indentation curve and results in a clear underestimation of the creep deformation. Adding viscoplasticity to the model lead to realistic values of creep. At the moment, the nature of the time-dependent deformation in bone is not well understood and cannot be identified clearly using indentation experiments, as the indentation curves are a result of a combination of global viscoelastic and local viscoplastic creep. Further independent experiments are necessary to clearly identify the time-dependent properties of bone on the microscale in both the elastic and postyield regime. It was found that maximum force for a given deformation was largely overestimated for both indenters when using an isotropy condition to determine the unknown shear strength. In order to fit the experimental data, the isotropy condition for the yield stress was abandoned. However, it was not possible to fit both the Berkovich and the spherical data using the mean indenter radius of 48 µm measured using optical micrographs. The fact that the measured indentation moduli using the spherical tip were consistently lower than the ones measured using a Berkovich tip suggested that the local curvature for small indentation depths was underestimated by the mean radius, which is a common problem for spherical indenters [Constantinides et al., 2007]. Therefore, an effective radius of the indenter at small depths of $R = 28$ µm was determined for which the measured elastic moduli in transverse and axial direction correspond well to the measurements using the Berkovich tip. Using the effective indenter radius resulted in a reasonably good fit of the simulated and experimental indentation curves for both the Berkovich and the spherical microindentations. It remains to be verified if the thus determined effective radius is indeed representative of the real indenter geometry. This issue could be clarified in the future by directly measuring the tip topography of the spherical indenter with an AFM as proposed by Constantinides et al. [2007]. It is highly likely that a high fraction of the variation in the experimental data is due to the presence of the lacuno-canalicular porosity. Lacunae have a diameter of $\sim 10\mu$m and may therefore influence the stress state if they are in close proximity of the indenter. However, the lacunar density is rather low and it is possible to avoid indenting near lacunae. Canaliculi on the other hand have diameters of $100 - 300$ nm and are therefore small compared to the homogeneously tested volume of a micropillar or the elastically tested volume of a microindentation. However, their diameter is of a similar scale as the plastic zone directly under the indenter tip for microindentations to depths of $500 - 1000$ nm and they form a relatively dense network with a spacing of only a few microns. Therefore, they cause stress concentrations under the tip and may be compressed locally, which would result in a lower apparent resistance of the material to plastic flow. As these structures are not modeled explicitly in the FE model used in this study, this missing effect has to be compensated by the material model. Therefore, the yield and postyield properties of the material may be underestimated. It would therefore be preferable to model canaliculi explicitly in the future or use statistics based material properties to compensate this effect when trying to identify postelastic properties of bone using nanoindentations. Another limitation is that the friction coefficient between diamond and bone that has a non-negligible influence on the indentation response was taken from a nanoindentation study in the literature [Carnelli et al., 2010]. The reliability of the results would be greatly enhanced if nanotribologic experiments were conducted to measure the friction coefficient independently. In conclusion, it was possible to remedy the discrepancies between indentation and micropillar data in this study by abandoning the assumption of shear strength being governed by an isotropy condition. However, additional independent measurements and a better understanding of the underlying dissipative processes and their mathematical description as well as very well defined boundary conditions regarding indenter and ultrastructure are necessary in order to verify this finding and to uniquely identify the nonlinear behaviour of bone on the microscale in the future.

In conclusion, in this thesis several theoretical, numerical and experimental approaches were developed that allow to describe the complex behavior of bone on the microscale. Experimental campaigns were launched to identify the nonlinear material properties governing the developed models. However, the complex behavior of bone leads to a need for several independent experiments allowing a straightforward interpretation in order to decouple the different effects. Micromechanical considerations about bone's viscoelastic behavior have been recently published [Eberhardsteiner et al., 2014], but additional tests are necessary to identify the time-dependent response over a large range of loading speeds as well as the postelastic properties in tension and shear. Especially experiments allowing to uniquely identify the viscoelastic and viscoplastic properties on the microscale are needed, e.g. micropillar compression tests to both elastic and postelastic stress levels at different loading rates or microscale creep/relaxation tests. Furthermore, independent tests are necessary to identify the postelastic properties in tension and shear additional to the compressive properties reported in Chapter 5. Additionally, there is a need for tests in different directions using non-proportional loading protocols in order to identify the postyield characteristics of bone. The isotropic hardening that has been assumed in this work is most probably unrealistic and was chosen for a lack of reliable knowledge on the exact nature of the postyield behavior of bone. Further work in this direction is necessary.

Knowledge of viscoelastic as well as postelastic properties would then allow to determine the yield surface shape based on indentation data using realistic models of indentations with different tip shapes. Using this strategy, it would be possible to uniquely identify the three-dimensional constitutive behavior of a specific bone on the microscale. Such a valid mechanical model for bone on the microscale could be used to obtain more reliable macroscopic material properties for bone as a function of density and structural anisotropy by means of numerical homogenization schemes using e.g. microstructural Finite Element (µFE) models. Homogenized material descriptions of bone are already used today in longitudinal clinical studies on patient data exploring e.g. influence of drug treatment or disease with comparatively small computational effort and would benefit highly from a better understanding of the underlying processes and more reliable empirical constants. Another interesting application of the model would be the development of a valid model of Reference Point Indentation (RPI), which is a method used on patients today in which a sharp tip is pressed into the outer surface of a patient's bone to measure bone quality. While certain measurements have been shown to correlate with fracture risk, a clear understanding of the processes and thus a proper interpretation of the test results has not been presented up to now. Before a translation into a clinical setting would be possible, the efficiency of the method needs to be enhanced and it has to be assessed how the variability in the postyield properties compares to the variability due to the different pores affecting the measurements at this length scale. First steps in this direction have been taken in this work but several additional experiments are yet to be performed before the final goal can be achieved. Furthermore, the existing protocols have to be adapted to test bone in its natural hydrated state in order to mimick physiological conditions more closely. This was not possible in the frame of this dissertation and remains a clear limitation of this work. Also, the micropillar compression experiments highlighted a size effect in bone due to the presence of defects like preexisting cracks and pores or interfaces such as cement lines. Identifying the exact nature of the size effect and the mechanical role of interfaces in bone will be a crucial and interesting task for future work, as this is an important point limiting the applicability of mean field methods in predicting failure properties of heterogeneous and quasi-brittle materials like bone. It seems that the statistical distribution of defects and interfaces plays a very important role in the macroscopic failure behavior of bone. Deciphering the micromechanical behavior of lamellar bone and its evolution with age, disease and treatment as well as the nature of failure on several length scales will help preventing fractures in the elderly in the future.

Bibliography

O. Akkus, F. Adar, and M. B. Schaffler. Age-related changes in physicochemical properties of mineral crystals are related to impaired mechanical function of cortical bone. *Bone*, 34 (3):443–453, 2004.

F. Armero and A. Pérez-Foguet. On the formulation of closest-point projection algorithms in elastoplasticity – part i: The variational structure. *International Journal for Numerical Methods in Engineering*, 53(2):297–329, 2002.

Y. P. Arramon, M. M. Mehrabadi, D. W. Martin, and S. C. Cowin. A multidimensional anisotropic strength criterion based on kelvin modes. *International Journal of Solids and Structures*, 37(21):2915–2935, 2000.

M. Ashby and D. Jones. *Engineering Materials*. Pergamon Press, Oxford, 1980.

D. Bajaj, J. R. Geissler, M. R. Allen, D. B. Burr, and J. Fritton. The resistance of cortical bone tissue to failure under cyclic loading is reduced with alendronate. *Bone*, 64(0):57 – 64, 2014. ISSN 8756-3282.

J. H. Bargren, C. A. L. Bassett, and A. Gjelsvik. Mechanical properties of hydrated cortical bone. *Journal of Biomechanics*, 7(3):239–245, 1974.

H. H. Bayraktar, E. F. Morgan, G. L. Niebur, G. E. Morris, E. K. Wong, and T. M. Keaveny. Comparison of the elastic and yield properties of human femoral trabecular and cortical bone tissue. *Journal of Biomechanics*, 37(1):27 – 35, 2004.

Z. P. Bažant. Scaling theory for quasibrittle structural failure. *Proceedings of the National Academy of Sciences of the United States of America*, 101(37):13400–13407, 2004.

R. Bigley, J. Gibeling, S. Stover, S. Hazelwood, D. Fyhrie, and R. Martin. Volume effects on fatigue life of equine cortical bone. *Journal of Biomechanics*, 40(16):3548–3554, 2007.

R. Bigley, J. Gibeling, S. Stover, S. Hazelwood, D. Fyhrie, and R. Martin. Volume effects on yield strength of equine cortical bone. *Journal of the Mechanical Behavior of Biomedical Materials*, 1(4):295–302, 2008.

G. Binnig, C. F. Quate, and C. Gerber. Atomic force microscope. *Physical Review Letters*, 56:930–933, 1986.

R. Blanc, M. Reyes, C. Seiler, and G. Székely. Conditional variability of statistical shape models based on surrogate variables. In *Medical Image Computing and Computer-Assisted Intervention–MICCAI 2009*, pages 84–91. Springer, 2009.

M. Bocciarelli, G. Bolzon, and G. Maier. Parameter identification in anisotropic elastoplasticity by indentation and imprint mapping. *Mechanics of Materials*, 37(8):855 – 868, 2005.

A. Bolshakov and G. Pharr. Influences of the pileup on the measurement of mechanical properties by load and depth sensing indentation techniques. *Journal of Material Research*, 13:1049–1058, 1998.

G. Bolzon, G. Maier, and M. Panico. Material model calibration by indentation, imprint mapping and inverse analysis. *International Journal of Solids and Structures*, 41(11-12): 2957 – 2975, 2004.

J. Bucaille, S. Stauss, E. Felder, and J. Michler. Determination of plastic properties of metals by instrumented indentation using different sharp indenters. *Acta Materialia*, 51 (6):1663 – 1678, 2003.

D. B. Burr, M. B. Schaffler, and R. G. Frederickson. Composition of the cement line and its possible mechanical role as a local interface in human compact bone. *Journal of Biomechanics*, 21(11):939–945, 1988.

A. J. Bushby, V. L. Ferguson, and A. Boyde. Nanoindentation of bone: Comparison of specimens tested in liquid and embedded in polymethylmethacrylate. *Journal of Materials Research*, 19:249–259, 2004.

W. E. Caler and D. R. Carter. Bone creep-fatigue damage accumulation. *Journal of Biomechanics*, 22(6):625–635, 1989.

D. Carnelli, D. Gastaldi, V. Sassi, R. Contro, C. Ortiz, and P. Vena. A finite element model for direction-dependent mechanical response to nanoindentation of cortical bone allowing for anisotropic post-yield behavior of the tissue. *Journal of Biomechanical Engineering*, 132(8):081008, 2010.

D. Carnelli, R. Lucchini, M. Ponzoni, R. Contro, and P. Vena. Nanoindentation testing and finite element simulations of cortical bone allowing for anisotropic elastic and inelastic mechanical response. *Journal of Biomechanics*, 44(10):1852 – 1858, 2011.

A. Carosio, K. Willam, and G. Etse. On the consistency of viscoplastic formulations. *International Journal of Solids and Structures*, 37(48-50):7349 – 7369, 2000.

D. R. Carter and W. C. Hayes. Compact bone fatigue damage: A microscopic examination. *Clinical Orthopaedics and Related Research*, 127:265–274, 1977.

J. Chaboche. A review of some plasticity and viscoplasticity constitutive theories. *International Journal of Plasticity*, 24(10):1642 – 1693, 2008.

A. Chamay. Mechanical and morphological aspects of experimental overload and fatigue in bone. *Journal of Biomechanics*, 3(3):263–270, 1970.

M. Charlebois, M. Jirásek, and P. Zysset. A nonlocal constitutive model for trabecular bone softening in compression. *Biomechanics and Modeling in Mechanobiology*, 9:597–611, 2010.

X. Chen, N. Ogasawara, M. Zhao, and N. Chiba. On the uniqueness of measuring elastoplastic properties from indentation: The indistinguishable mystical materials. *Journal of the Mechanics and Physics of Solids*, 55(8):1618 – 1660, 2007.

L. Cheng, X. Xia, L. Scriven, and W. Gerberich. Spherical-tip indentation of viscoelastic material. *Mechanics of Materials*, 37(1):213–226, 2005.

K. Choi and S. A. Goldstein. A comparison of the fatigue behavior of human trabecular and cortical bone tissue. *Journal of Biomechanics*, 25(12):1371–1381, 1992.

G. Constantinides, E. C. C. M. Silva, G. S. Blackman, and K. J. V. Vliet. Dealing with imperfection: quantifying potential length scale artefacts from nominally spherical indenter probes. *Nanotechnology*, 18(30):305503, 2007.

S. Cowin. Bone poroelasticity. *Journal of Biomechanics*, 32(3):217–238, 1999.

S. C. Cowin. On the strength anisotropy of bone and wood. *Journal of Applied Mechanics*, 46(4):832–838, 1979.

S. C. Cowin. The relationship between the elasticity tensor and the fabric tensor. *Mechanics of Materials*, 4(2):137 – 147, 1985.

S. C. Cowin. Fabric dependence of an anisotropic strength criterion. *Mechanics of Materials*, 5:251 – 260, 1986.

S. C. Cowin. *Bone Mechanics Handbook*. CRC Press, Boca Raton, FL, 2001.

S. C. Cowin and Q. C. He. Tensile and compressive stress yield criteria for cancellous bone. *Journal of Biomechanics*, 38(1):141–144, 2005.

S. C. Cowin and M. M. Mehrabadi. Anisotropic symmetries of linear elasticity. *Applied Mechanics Reviews*, 48:247–285, 1995.

J. Crolet, B. Aoubiza, and A. Meunier. Compact bone: Numerical simulation of mechanical characteristics. *Journal of Biomechanics*, 26(6):677–687, 1993.

A. Curnier. *Computational Methods in Solid Mechanics*. Kluwer, Dordrecht, 1994.

J. D. Currey. Stress concentrations in bone. *Quarterly Journal of Microscopical Science*, 3 (61):111–133, 1962.

J. D. Currey. The relationship between the stiffness and the mineral content of bone. *Journal of Biomechanics*, 2(4):477 – 480, 1969.

J. D. Currey. *Bones: Structure and Mechanics*. Princeton University Press, 2002.

T. Diab and D. Vashishth. Morphology, localization and accumulation of in vivo microdamage in human cortical bone. *Bone*, 40(3):612–618, 2007.

A. Dubach, R. Raghavan, J. Löffler, J. Michler, and U. Ramamurty. Micropillar compression studies on a bulk metallic glass in different structural states. *Scripta Materialia*, 60(7): 567–570, 2009.

V. Ebacher, P. Guy, T. R. Oxland, and R. Wang. Sub-lamellar microcracking and roles of canaliculi in human cortical bone. *Acta biomaterialia*, 8(3):1093–1100, 2012.

L. Eberhardsteiner, C. Hellmich, and S. Scheiner. Layered water in crystal interfaces as source for bone viscoelasticity: arguments from a multiscale approach. *Computer Methods in Biomechanics and Biomedical Engineering*, 17(1):48–63, 2014.

J. A. El-Awady, C. Woodward, D. M. Dimiduk, and N. M. Ghoniem. Effects of focused ion beam induced damage on the plasticity of micropillars. *Physical Review B*, 80(10): 104104, 2009.

G. Etse and A. Carosio. Constitutive equations and numerical approaches in rate dependent material formulations. MECOM, 1999.

G. E. Fantner, O. Rabinovych, G. Schitter, P. Thurner, J. H. Kindt, M. M. Finch, J. C. Weaver, L. S. Golde, D. E. Morse, E. A. Lipman, I. Rangelow, and P. Hansma. Hierarchical interconnections in the nano-composite material bone: Fibrillar cross-links resist fracture on several length scales. *Composites science and technology*, 66(9):1205–1211, 2006.

A. Fischer-Cripps. *Nanoindentation*. Springer, New York, 2002.

M. Fondrk, E. Bahniuk, D. Davy, and C. Michaels. Some viscoplastic characteristics of bovine and human cortical bone. *Journal of Biomechanics*, 21(8):623–630, 1988.

M. Fondrk, E. Bahniuk, and D. Davy. A damage model for nonlinear tensile behavior of cortical bone. *Journal of Biomedical Engineering*, 121:533–541, 1999.

G. Franzoso and P. K. Zysset. Elastic anisotropy of human cortical bone secondary osteons measured by nanoindentation. *Journal of Biomechanical Engineering*, 131(11):117001, 2009.

P. Fratzl and R. Weinkamer. Nature's hierarchical materials. *Progress in Materials Science*, 52(8):1263 – 1334, 2007.

A. Fritsch and C. Hellmich. Universal microstructural patterns in cortical and trabecular, extracellular and extravascular bone materials: Micromechanics-based prediction of anisotropic elasticity. *Journal of Theoretical Biology*, 244(4):597–620, 2007.

A. Fritsch, C. Hellmich, and L. Dormieux. Ductile sliding between mineral crystals followed by rupture of collagen crosslinks: Experimentally supported micromechanical explanation of bone strength. *Journal of Theoretical Biology*, 260(2):230 – 252, 2009.

F. Ganneau, G. Constantinides, and F.-J. Ulm. Dual-indentation technique for the assessment of strength properties of cohesive-frictional materials. *International Journal of Solids and Structures*, 43(6):1727 – 1745, 2006.

D. Garcia. *Elastic plastic damage laws for cortical bone*. PhD thesis, Ecole Polytechnique Federale de Lausanne, 2006.

D. Garcia, P. Zysset, M. Charlebois, and A. Curnier. A three-dimensional elastic plastic damage constitutive law for bone tissue. *Biomechanics and Modeling in Mechanobiology*, 8(2):149–165, Apr. 2009.

I. M. Gelfand, M. M. Kapranov, and A. V. Zelevinsky. *Discriminants, Resultants and Multidimensional Determinants*. Birkhäuser, 1994.

L. J. Gibson. The mechanical behaviour of cancellous bone. *Journal of Biomechanics*, 18 (5):317 – 328, 1985.

L. J. Gibson and M. F. Ashby. *Cellular solids: Structure and properties.* Cambridge University Press, 1999.

M. Giraud-Guille. Twisted plywood architecture of collagen fibrils in human compact bone osteons. *Calcified Tissue International*, 42(3):167–180, 1988.

C. Goodall. Procrustes methods in the statistical analysis of shape. *Journal of the Royal Statistical Society B*, pages 285–339, 1991.

A. E. Green and P. M. Naghdi. A general theory of an elastic-plastic continuum. *Archive for Rational Mechanics and Analysis*, 18(4):251–281, 1965.

A. Griffith. The phenomena of flow and rupture in solids. *Philosophical Transactions of the Royal Society A*, 221(582-593):163–198, 1921.

Q. Grimal, K. Raum, A. Gerisch, and P. Laugier. Derivation of the mesoscopic elasticity tensor of cortical bone from quantitative impedance images at the micron scale. *Computer Methods in Biomechanics and Biomedical Engineering*, 11(2):147–157, 2008.

T. Gross. The effects of heterogeneous mineralization on the elastic and yield properties of human cancellous bone. Master's thesis, Vienna University of Technology, 2010.

T. Gross. *Development and Application of 3D CT Image-based Micro and Macro Finite Element Models for Human Bones and Orthopedic Implant Systems.* PhD thesis, Vienna University of Technology, 2014.

H. S. Gupta and P. Zioupos. Fracture of bone tissue: The 'hows' and the 'whys'. *Medical Engineering and Physics*, 30(10):1209 – 1226, 2008.

H. S. Gupta, W. Wagermaier, G. A. Zickler, D. Raz-Ben Aroush, S. S. Funari, P. Roschger, H. D. Wagner, and P. Fratzl. Nanoscale deformation mechanisms in bone. *Nano Letters*, 5(10):2108–2111, 2005.

H. S. Gupta, W. Wagermaier, G. Zickler, J. Hartmann, S. Funari, P. Roschger, H. Wagner, and P. Fratzl. Fibrillar level fracture in bone beyond the yield point. *International Journal of Fracture*, 139:425–436, 2006.

H. S. Gupta, P. Fratzl, M. Kerschnitzki, G. Benecke, W. Wagermaier, and H. O. Kirchner. Evidence for an elementary process in bone plasticity with an activation enthalpy of 1?ev. *Journal of The Royal Society Interface*, 4(13):277–282, 2007.

H. S. Gupta, S. Krauss, M. Kerschnitzki, A. Karunaratne, J. Dunlop, A. Barber, P. Boesecke, S. Funari, and P. Fratzl. Intrafibrillar plasticity through mineral/collagen sliding is the dominant mechanism for the extreme toughness of antler bone. *Journal of the Mechanical Behavior of Biomedical Materials*, 28(0):366 – 382, 2013.

P. Hansma, G. Fantner, J. Kindt, P. Thurner, G. Schitter, P. Turner, S. Udwin, and M. Finch. Sacrificial bonds in the interfibrillar matrix of bone. *Journal of Musculoskeletal and Neuronal Interactions*, 5(4):313–315, 2005.

T. P. Harrigan and R. W. Mann. Characterisation of microstructural anisotropy in orthotropic materials using a second rank tensor. *Journal of Materials Sciences*, 19:761 – 767, 1984.

J. Hay, A. Bolshakov, and G. Pharr. A critical examination of the fundamental relations used in the analysis of nanoindentation data. *Journal of Material Research*, 14:2296–2305, 1999.

W. C. Hayes and D. R. Carter. Postyield behavior of subchondral trabecular bone. *Journal of Biomedical Materials Research*, 10(4):537–544, 1976.

O. Heeres, A. Suiker, and R. de Borst. A comparison between the Perzyna viscoplastic model and the Consistency viscoplastic model. *European Journal of Mechanics-A/Solids*, 21(1):1–12, 2002.

T. Heimann and H.-P. Meinzer. Statistical shape models for 3d medical image segmentation: A review. *Medical Image Analysis*, 13(4):543–563, 2009.

C. Hellmich and F.-J. Ulm. Are mineralized tissues open crystal foams reinforced by crosslinked collagen? Some energy arguments. *Journal of Biomechanics*, 35(9):1199 – 1212, 2002.

C. Hellmich, A. Fritsch, and L. Dormieux. Multiscale homogenization theory: An analysis tool for revealing mechanical design principles in bone and bone replacement materials. In P. Gruber, D. Bruckner, C. Hellmich, H.-B. Schmiedmayer, H. Stachelberger, and I. C. Gebeshuber, editors, *Biomimetics – Materials, Structures and Processes*, Biological and Medical Physics, Biomedical Engineering, pages 81–103. Springer Berlin Heidelberg, 2011.

S. Hengsberger, A. Kulik, and P. Zysset. A combined atomic force microscopy and nanoindentation technique to investigate the elastic properties of bone structural units. *European Cells and Materials*, 1:12–17, 2001.

S. Hengsberger, A. Kulik, and P. Zysset. Nanoindentation discriminates the elastic properties of individual human bone lamellae under dry and physiological conditions. *Bone*, 30 (1):178 – 184, 2002.

S. Hengsberger, J. Enstroem, F. Peyrin, and P. Zysset. How is the indentation modulus of bone tissue related to its macroscopic elastic response? A validation study. *Journal of Biomechanics*, 36(10):1503–1509, 2003.

E. Herbert, G. Pharr, W. Oliver, B. Lucas, and J. Hay. On the measurement of stress–strain curves by spherical indentation. *Thin Solid Films*, 398:331–335, 2001.

H. Hertz. Über die Berührung fester elastischer Körper. *Journal für die reine und angewandte Mathematik*, 92:156–171, 1881.

T. Hildebrand, A. Laib, R. Müller, J. Dequeker, and P. Rüegsegger. Direct three-dimensional morphometric analysis of human cancellous bone: Microstructural data from spine, femur, iliac crest, and calcaneus. *Journal of Bone and Mineral Research*, 14(7):1167–1174, 1999.

R. Hill. *The mathematical theory of plasticity*. Oxford University Press, 1951.

C. E. Hoffler, X. E. Guo, P. K. Zysset, and S. A. Goldstein. An application of nanoindentation technique to measure bone tissue lamellae properties. *Journal of Biomechanical Engineering*, 127(7):1046–1053, Dec. 2005.

P. R. Howie, S. Korte, and W. J. Clegg. Fracture modes in micropillar compression of brittle crystals. *Journal of Materials Research*, 27(1):141–151, 2012.

T. Iyo, Y. Maki, N. Sasaki, and M. Nakata. Anisotropic viscoelastic properties of cortical bone. *Journal of Biomechanics*, 37(9):1433–1437, 2004.

N. Jalili and K. Laxminarayana. A review of atomic force microscopy imaging systems: application to molecular metrology and biological sciences. *Mechatronics*, 14(8):907 – 945, 2004.

K.-I. Kanatani. Distribution of directional data and fabric tensors. *International Journal of Engineering Science*, 22(2):149 – 164, 1984.

T. M. Keaveny, E. F. Morgan, G. L. Niebur, and O. C. Yeh. Biomechanics of trabecular bone. *Annual Review of Biomedical Engineering*, 3(1):307–333, 2001.

T. M. Keaveny, E. Morgan, and O. Yeh. *Standard Handbook of Biomedical Engineering & Design*, chapter Bone Mechanics. McGraw Hill, 2003.

M. Kerschnitzki, W. Wagermaier, P. Roschger, J. Seto, R. Shahar, G. N. Duda, S. Mundlos, and P. Fratzl. The organization of the osteocyte network mirrors the extracellular matrix orientation in bone. *Journal of Structural Biology*, 173(2):303 – 311, 2011.

J. H. Keyak and S. A. Rossi. Prediction of femoral fracture load using finite element models: an examination of stress- and strain-based failure theories. *Journal of Biomechanics*, 33 (2):209 – 214, 2000.

K. J. Koester, J. W. Ager, and R. O. Ritchie. The true toughness of human cortical bone measured with realistically short cracks. *Nature Materials*, 7(8):672–677, Aug. 2008.

D. Krajcinovic, J. Trafimow, and D. Sumarac. Simple constitutive model for a cortical bone. *Journal of Biomechanics*, 20(8):779–784, 1987.

R. Kristic. *Human Microscopic Anatomy*. Springer, 1991.

H. W. Kuhn and A. W. Tucker. Nonlinear programming. *Proceedings of 2nd Berkeley Symposium*, pages 481–492, 1951.

R. S. Lakes and J. L. Katz. Viscoelastic properties of wet cortical bone - ii. relaxation mechanisms. *Journal of Biomechanics*, 12(9):679–687, 1979.

R. S. Lakes, J. L. Katz, and S. S. Sternstein. Viscoelastic properties of wet cortical bone - i. torsional and biaxial studies. *Journal of Biomechanics*, 12(9):657–678, 1979.

S. Lees, N.-J. Tao, and S. Lindsay. Studies of compact hard tissues and collagen by means of brillouin light scattering. *Connective Tissue Research*, 24(3-4):187–205, 1990.

G. Lewis and J. Nyman. The use of nanoindentation for characterizing the properties of mineralized hard tissues: State-of-the art review. *Journal of Biomedical Materials Research Part B: Applied Biomaterials*, 87(1):286–301, 2008.

C. Liu, Y. Huang, and M. Stout. On the asymmetric yield surface of plastically orthotropic materials: A phenomenological study. *Acta Materialia*, 45(6):2397 – 2406, 1997.

R. Lucchini, D. Carnelli, M. Ponzoni, E. Bertarelli, D. Gastaldi, and P. Vena. Role of damage mechanics in nanoindentation of lamellar bone at multiple sizes: Experiments and numerical modeling. *Journal of the Mechanical Behavior of Biomedical Materials*, 4 (8):1852 – 1863, 2011.

M. Lüthi, T. Albrecht, T. Gass, O. Goksel, M. Kistler, H. Bousleiman, M. Reyes, P. Buechler, P. Cattin, and T. Vetter. Statismo-a framework for pca based statistical models. *The Insight Journal*, 1:1–18, 2012.

S. Maghous, L. Dormieux, and J. F. Barthélémy. Micromechanical approach to the strength properties of frictional geomaterials. *European Journal of Mechanics - A/Solids*, 28(1): 179 – 188, 2009.

R. Martin. Porosity and specific surface of bone. *Critical Reviews in Biomedical Engineering*, 10(3):179–222, 1984.

R. B. Martin and D. B. Burr. *Structure, function, and adaptation of compact bone.* Raven Press, New York, 1989.

M. Matsuura, F. Eckstein, E.-M. Lochmüller, and P. Zysset. The role of fabric in the quasi-static compressive mechanical properties of human trabecular bone from various anatomical locations. *Biomechanics and Modeling in Mechanobiology*, 7:27–42, 2008.

G. Mazza. Anisotropic elastic properties of vertebral bone measured by microindentation. Master's thesis, Politecnico di Milano, 2008.

M. Mehrabadi and S. Cowin. Eigentensors of linear anisotropic elastic materials. *The Quarterly Journal of Mechanics and Applied Mathematics*, 43(1):15–41, 1990.

C. Mercer, M. He, R. Wang, and A. Evans. Mechanisms governing the inelastic deformation of cortical bone and application to trabecular bone. *Acta Biomaterialia*, 2(1):59–68, 2006.

J. Michler, K. Wasmer, S. Meier, F. Ostlund, and K. Leifer. Plastic deformation of gallium arsenide micropillars under uniaxial compression at room temperature. *Applied Physics Letters*, 90(4):043123 – 043123–3, 2007.

M. D. Morris and G. S. Mandair. Raman assessment of bone quality. *Clinical Orthopaedics and Related Research*, 469(8):2160–2169, 2011.

L. Mullins, M. Bruzzi, and P. McHugh. Calibration of a constitutive model for the post-yield behaviour of cortical bone. *Journal of the Mechanical Behavior of Biomedical Materials*, 2(5):460–470, Oct. 2009.

R. K. Nalla, J. H. Kinney, and R. O. Ritchie. Mechanistic fracture criteria for the failure of human cortical bone. *Nature Materials*, 2(3):164–168, 2003.

R. K. Nalla, J. J. Kruzic, J. H. Kinney, and R. O. Ritchie. Mechanistic aspects of fracture and R-curve behavior in human cortical bone. *Biomaterials*, 26(2):217–231, 2005.

A. N. Natali, E. L. Carniel, and P. G. Pavan. Constitutive modelling of inelastic behaviour of cortical bone. *Medical Engineering and Physics*, 30(7):905–912, 2008.

S. Nemat-Nassar and M. Mori. *Micromechanics: Overall Properties of Heterogeneous Materials*. Elsevier Science Publishers, 1993.

J. S. Nyman, A. Roy, X. Shen, R. L. Acuna, J. H. Tyler, and X. Wang. The influence of water removal on the strength and toughness of cortical bone. *Journal of Biomechanics*, 39(5):931 – 938, 2006.

F. J. O'Brien, D. Taylor, and T. C. Lee. An improved labelling technique for monitoring microcrack growth in compact bone. *Journal of Biomechanics*, 35(4):523 – 526, 2002.

S. Olesiak, M. Oyen, and V. Ferguson. Viscous-elastic-plastic behavior of bone using Berkovich nanoindentation. *Mechanics of Time-Dependent Materials*, 14:111–124, 2010.

W. Oliver and G. Pharr. An improved technique for determining hardness and elastic modulus using load and displacement sensing indentation experiments. *Journal of Materials Research*, 7:1564–1583, 1992.

W. Oliver and G. Pharr. Measurement of hardness and elastic modulus by instrumented indentation: Advances in understanding and refinements to methodology. *Journal of Materials Research*, 19(01):3–20, 2004.

F. Östlund, K. Rzepiejewska-Malyska, K. Leifer, L. M. Hale, Y. Tang, R. Ballarini, W. W. Gerberich, and J. Michler. Brittle-to-ductile transition in uniaxial compression of silicon pillars at room temperature. *Advanced Functional Materials*, 19(15):2439–2444, 2009.

F. Östlund, P. R. Howie, R. Ghisleni, S. Korte, K. Leifer, W. J. Clegg, and J. Michler. Ductile–brittle transition in micropillar compression of gaas at room temperature. *Philosophical Magazine*, 91(7-9):1190–1199, 2011.

M. L. Oyen and C.-C. Ko. Indentation variability of natural nanocomposite materials. *Journal of Materials Research*, 23(03):760–767, 2008.

A. Parfitt. Age-related structural changes in trabecular and cortical bone: Cellular mechanisms and biomechanical consequences. *Calcified Tissue International*, 36:S123–S128, 1984.

A. Pearce, R. Richards, S. Milz, E. Schneider, S. Pearce, et al. Animal models for implant biomaterial research in bone: a review. *European Cells & Materials*, 13:1–10, 2007.

K. Pearson. On lines and planes of closest fit to systems of points in space. *The London, Edinburgh, and Dublin Philosophical Magazine and Journal of Science*, 2(11):559–572, 1901.

A. Pérez-Foguet and F. Armero. On the formulation of closest-point projection algorithms in elastoplasticity – part ii: Globally convergent schemes. *International Journal for Numerical Methods in Engineering*, 53(2):331–374, 2002.

P. Perzyna. *Fundamental Problems in Viscoplasticity*, volume 9 of *Advances in Applied Mechanics*. Elsevier, 1966.

H. Peterlik, P. Roschger, K. Klaushofer, and P. Fratzl. From brittle to ductile fracture of bone. *Nature Materials*, 5(1):52–55, Jan. 2006.

J.-P. Ponthot. Radial return extensions for visco-plasticity and lubricated friction. In *SMIRT-13 International Conference on Structural Mechanics and Reactor Technology*, 1995.

B. Poon, D. Rittel, and G. Ravichandran. An analysis of nanoindentation in elasto-plastic solids. *International Journal of Solids and Structures*, 45(25-26):6399–6415, Dec. 2008a.

B. Poon, D. Rittel, and G. Ravichandran. An analysis of nanoindentation in linearly elastic solids. *International Journal of Solids and Structures*, 45(24):6018–6033, Dec. 2008b.

A. A. Poundarik, T. Diab, G. E. Sroga, A. Ural, A. L. Boskey, C. M. Gundberg, and D. Vashishth. Dilatational band formation in bone. *Proceedings of the National Academy of Sciences*, 109(47):19178–19183, 2012.

W. Prager and D. Drucker. Soil mechanics and plastic analysis or limit design. *Quarterly of Applied Mathematics*, 10(2):157–165, 1952.

R Development Core Team. *R: A Language and Environment for Statistical Computing.* R Foundation for Statistical Computing, Vienna, Austria, 2008.

R. Rabe, J.-M. Breguet, P. Schwaller, S. Stauss, F.-J. Haug, J. Patscheider, and J. Michler. Observation of fracture and plastic deformation during indentation and scratching inside the scanning electron microscope. *Thin Solid Films*, 469:206–213, 2004.

R. Rakatomanana, A. Curnier, and P. Leyvraz. An objective elastic plastic model and algorithm applicable to bone mechanics. *European Journal of Mechanics A/Solids*, 10: 327–342, 1991.

A. Ravaglioli, A. Krajewski, G. Celotti, A. Piancastelli, B. Bacchini, L. Montanari, G. Zama, and L. Piombi. Mineral evolution of bone. *Biomaterials*, 17(6):617 – 622, 1996.

D. T. Reilly and A. H. Burstein. The elastic and ultimate properties of compact bone tissue. *Journal of Biomechanics*, 8(6):393 – 405, 1975.

A. G. Reisinger. *Modeling and Validation of Multiscale Lamellar Bone Elasticity*. PhD thesis, Vienna University of Technology, 2011.

A. G. Reisinger, D. H. Pahr, and P. K. Zysset. Elastic anisotropy of bone lamellae as a function of fibril orientation pattern. *Biomechanics and Modeling in Mechanobiology*, pages 1–11, 2010.

A. G. Reisinger, D. H. Pahr, and P. K. Zysset. Principal stiffness orientation and degree of anisotropy of human osteons based on nanoindentation in three distinct planes. *Journal of the Mechanical Behavior of Biomedical Materials*, 4(8):2113 – 2127, 2011.

N. Reznikov, R. Shahar, and S. Weiner. Three-dimensional structure of human lamellar bone: The presence of two different materials and new insights into the hierarchical organization. *Bone*, 59:93 – 104, 2014.

J.-Y. Rho, L. Kuhn-Spearing, and P. Zioupos. Mechanical properties and the hierarchical structure of bone. *Medical Engineering & Physics*, 20(2):92 – 102, 1998.

L. Rincón, A. Frossard, A. Curnier, and P. K. Zysset. A rate-dependent damage model for bovine trabecular bone. In J. M. et al., editor, *Computer Methods in Biomechanics and Biomedical Engineering*, pages 161–166. Gordon & Breach, Amsterdam, 2001.

L. Rincón-Kohli and P. K. Zysset. Multi-axial mechanical properties of human trabecular bone. *Biomechanics and Modeling in Mechanobiology*, 8:195–208, 2009.

N. Sasaki, Y. Nakayama, M. Yoshikawa, and A. Enyo. Stress relaxation function of bone and bone collagen. *Journal of Biomechanics*, 26(12):1369–1376, 1993.

M. Schaffler, K. Choi, and C. Milgrom. Aging and matrix microdamage accumulation in human compact bone. *Bone*, 17(6):521–525, 1995.

J. J. Schwiedrzik and P. K. Zysset. An anisotropic elastic-viscoplastic damage model for bone tissue. *Biomechanics and Modeling in Mechanobiology*, 12(2):201–213, 2013a.

J. J. Schwiedrzik and P. K. Zysset. The influence of yield surface shape and damage in the depth-dependent response of bone tissue to nanoindentation using spherical and berkovich indenters. *Computer Methods in Biomechanics and Biomedical Engineering*, 0(0):1–14, 2013b.

J. J. Schwiedrzik, U. Wolfram, and P. K. Zysset. A generalized anisotropic quadric yield criterion and its application to bone tissue at multiple length scales. *Biomechanics and Modeling in Mechanobiology*, 2013.

J. J. Schwiedrzik, R. Raghavan, A. Bürki, V. LeNader, U. Wolfram, J. Michler, and P. K. Zysset. In situ micropillar compression reveals superior strength and ductility but an absence of damage in lamellar bone. *Nature Materials*, 13(7):740–747, 2014.

S. S. Shapiro and M. B. Wilk. An analysis of variance test for normality (complete samples). *Biometrika*, 52(3/4):591–611, 1965.

C. F. Shih and D. Lee. Further developments in anisotropic plasticity. *Journal of Engineering Materials and Technology*, 100(3):294–302, 1978.

J. Simo and J. Ju. Strain- and stress-based continuum damage models - i. formulation. *International Journal of Solids and Structures*, 23:821–840, 1987.

C. I. Smith, M. Faraldos, and Y. Fernández-Jalvo. The precision of porosity measurements: Effects of sample pre-treatment on porosity measurements of modern and archaeological bone. *Palaeogeography, Palaeoclimatology, Palaeoecology*, 266:175–182, 2008.

I. N. Sneddon. Boussinesq's problem for a rigid cone. *Mathematical Proceedings of the Cambridge Philosophical Society*, 44(04):492–507, 1948.

I. N. Sneddon. The relation between load and penetration in the axisymmetric boussinesq problem for a punch of arbitrary profile. *International Journal of Engineering Science*, 3 (1):47–57, May 1965.

T. Spampatti. Influence of hydration on mechanical properties of bone measured by nanoindentation. Master's thesis, Politechnico di Milano, 2013.

E. M. Spiesz. *Experimental and computational micromechanics of mineralized tendon and bone*. PhD thesis, Vienna University of Technology, 2011.

E. M. Spiesz, A. G. Reisinger, P. Roschger, and P. K. Zysset. Experimental validation of a multiscale model of mineralized collagen fibers at two levels of hierarchy. *Osteoporosis International*, 22:561–666, 2011.

E. M. Spiesz, P. Roschger, and P. K. Zysset. Elastic anisotropy of uniaxial mineralized collagen fibers measured using two-directional indentation. Effects of hydration state and indentation depth. *Journal of the Mechanical Behavior of Biomedical Materials*, 12:20–28, 2012.

E. M. Spiesz, A. G. Reisinger, W. Kaminsky, P. Roschger, D. H. Pahr, and P. K. Zysset. Computational and experimental methodology for site-matched investigations of the influence of mineral mass fraction and collagen orientation on the axial indentation modulus of lamellar bone. *Journal of the Mechanical Behavior of Biomedical Materials*, 28:195 – 205, 2013.

Y. Sugawara, H. Kamioka, T. Honjo, K. K. Tezuka, and T. Takano-Yamamoto. Three-dimensional reconstruction of chick calvarial osteocytes and their cell processes using confocal microscopy. *Bone*, 36(5):877 – 883, 2005.

X. Sun, J. H. Jeon, J. Blendell, and O. Akkus. Visualization of a phantom post-yield deformation process in cortical bone. *Journal of Biomechanics*, 43(10):1989 – 1996, 2010.

J. G. Swadener and G. M. Pharr. Indentation of elastically anisotropic half-spaces by cones and parabolae of revolution. *Philosophical Magazine A*, 81(2):447–466, 2001.

K. Tai, F.-J. Ulm, and C. Ortiz. Nanogranular origins of the strength of bone. *Nano Letters*, 6(11):2520–2525, 2006.

S. Tsai and E. Wu. A general theory of strength for anisotropic materials. *Journal of Composite Materials*, 5(1):58–80, 1971.

M. D. Uchic and D. M. Dimiduk. A methodology to investigate size scale effects in crystalline plasticity using uniaxial compression testing. *Materials Science and Engineering: A*, 400: 268 – 278, 2005.

F.-J. Ulm, M. Vandamme, C. Bobko, J. Alberto Ortega, K. Tai, and C. Ortiz. Statistical indentation techniques for hydrated nanocomposites: Concrete, bone, and shale. *Journal of the American Ceramic Society*, 90(9):2677–2692, 2007.

M. Vandamme and F.-J. Ulm. Viscoelastic solutions for conical indentation. *International Journal of Solids and Structures*, 43(10):3142 – 3165, 2006.

P. Varga. *Prediction of Distal Radius Fracture Load Using HR?pQCT?based Finite Element Analysis*. PhD thesis, Vienna University of Technology, 2009.

P. Varga, A. Pacureanu, M. Langer, H. Suhonen, B. Hesse, Q. Grimal, P. Cloetens, K. Raum, and F. Peyrin. Investigation of the three-dimensional orientation of mineralized collagen fibrils in human lamellar bone using synchrotron x-ray phase nano-tomography. *Acta biomaterialia*, 9(9):8118–8127, 2013.

R. von Mises. Mechanik der festen Körper im plastisch deformablen Zustand. *Göttin. Nachr. Math. Phys.*, 1:582–592, 1913.

G. Voyiadjis and R. Peters. Size effects in nanoindentation: an experimental and analytical study. *Acta Mechanica*, 211:131–153, 2010.

H. D. Wagner and S. Weiner. On the relationship between the microstructure of bone and its mechanical stiffness. *Journal of Biomechanics*, 25(11):1311–1320, 1992.

R. Wang and H. S. Gupta. Deformation and fracture mechanisms of bone and nacre. *Annual Review of Materials Research*, 41:41–73, 2011.

W. Wang, L. Sluys, and R. De Borst. Viscoplasticity for instabilities due to strain softening and strain-rate softening. *International Journal for Numerical Methods in Engineering*, 40(20):3839–3864, 1997.

X. Wang, M. R. Allen, D. B. Burr, E. J. Lavernia, B. Jeremic, and D. P. Fyhrie. Identification of material parameters based on Mohr-Coulomb failure criterion for bisphosphonate treated canine vertebral cancellous bone. *Bone*, 43(4):775 – 780, 2008.

S. Weiner and H. D. Wagner. The material bone: Structure-mechanical function relations. *Annual Review of Materials Science*, 28(1):271–298, 1998.

S. Weiner, T. Arad, I. Sabanay, and W. Traub. Rotated plywood structure of primary lamellar bone in the rat: Orientations of the collagen fibril arrays. *Bone*, 20(6):509 – 514, 1997.

S. Weiner, W. Traub, and H. D. Wagner. Lamellar bone: Structure-function relations. *Journal of Structural Biology*, 126(3):241 – 255, 1999.

W. Whitehouse. The quantitative morphology of anisotropic trabecular bone. *Journal of Microscopy*, 101:153–68, 1974.

U. Wolfram, H.-J. Wilke, and P. K. Zysset. Rehydration of vertebral trabecular bone: Influences on its anisotropy, its stiffness and the indentation work with a view to age, gender and vertebral level. *Bone*, 46(2):348 – 354, 2010a.

U. Wolfram, H.-J. Wilke, and P. K. Zysset. Valid μ finite element models of vertebral trabecular bone can be obtained using tissue properties measured with nanoindentation under wet conditions. *Journal of Biomechanics*, 43(9):1731–1737, 2010b.

U. Wolfram, T. Gross, D. Pahr, J. J. Schwiedrzik, H.-J. Wilke, and P. K. Zysset. Fabric based Tsai-Wu yield criteria for vertebral trabecular bone in stress and strain space. *Journal of the Mechanical Behaviour of Biomedical Materials*, 15:218–228, 2012.

Y. Yeni, X. Dong, D. Fyhrie, and C. Les. The dependence between the strength and stiffness of cancellous and cortical bone tissue for tension and compression: Extension of a unifying principle. *Bio-Medical Materials and Engineering*, 14(3):303–310, 2004.

J. S. Yerramshetty, C. Lind, and O. Akkus. The compositional and physicochemical homogeneity of male femoral cortex increases after the sixth decade. *Bone*, 39(6):1236–1243, 2006.

H. Zhang, B. E. Schuster, Q. Wei, and K. T. Ramesh. The design of accurate microcompression experiments. *Scripta Materialia*, 54(2):181–186, 2006.

J. Zhang, G. L. Niebur, and T. C. Ovaert. Mechanical property determination of bone through nano- and micro-indentation testing and finite element simulation. *Journal of Biomechanics*, 41(2):267–275, Jan. 2008.

J. Zhang, M. M. Michalenko, E. Kuhl, and T. C. Ovaert. Characterization of indentation response and stiffness reduction of bone using a continuum damage model. *Journal of the Mechanical Behavior of Biomedical Materials*, 3(2):189–202, Feb. 2010.

J. F. Ziegler and J. P. Biersack. *The stopping and range of ions in matter*. Springer, 1985.

O. Zinkiewicz, S. Valliapan, and I. King. Elastoplastic solutions of engineering problems initial stress, finite element approach. *International Journal for Numerical Methods in Engineering*, pages 75–100, 1969.

P. Zioupos, U. Hansen, and J. D. Currey. Microcracking damage and the fracture process in relation to strain rate in human cortical bone tensile failure. *Journal of Biomechanics*, 41(14):2932 – 2939, 2008.

P. K. Zysset. *A Constitutive Law for Trabecular Bone*. PhD thesis, Ecole Polytechnique Federale de Lausanne, 1994.

P. K. Zysset. A review of morphology-elasticity relationships in human trabecular bone: theories and experiments. *Journal of Biomechanics*, 36(10):1469 – 1485, 2003.

P. K. Zysset. Indentation of bone: A short review. *Osteoporosis International*, 20:1049–1055, 2009.

P. K. Zysset and A. Curnier. An alternative model for anisotropic elasticity based on fabric tensors. *Mechanics of Materials*, 21(4):243 – 250, 1995.

P. K. Zysset and L. Rincón. An alternative fabric-based yield and failure criterion for trabecular bone. *Mechanics of Biological Tissue*, pages 457–470, 2006.

P. K. Zysset, X. Edward Guo, C. Edward Hoffler, K. E. Moore, and S. A. Goldstein. Elastic modulus and hardness of cortical and trabecular bone lamellae measured by nanoindentation in the human femur. *Journal of Biomechanics*, 32(10):1005–1012, Oct. 1999.

Acknowledgements

First of all, I would like to thank my supervisor Prof. Philippe Zysset. He has been a great and constant support during the whole time of my PhD. I have learned a lot from him during these last years and am still always amazed by his patience, extensive knowledge and the active part and interest he takes in the projects of his students. I will miss our weekly meetings and am sorry they usually took much longer than expected!

I would also like to thank my second supervisor Prof. Edoardo Mazza, GCB mentor PD Dr. Nyffeler, and external referee Prof. Franz-Josef Ulm for their time and effort.

I gratefully acknowledge the support of the German National Academic Foundation by means of a PhD scholarship from January 2011 to June 2013.

Many thanks go to all the colleagues, both at the ISTB and the ILSB. Especially, I would like to thank the two lab managers Enrico Dall'Ara and Uwe Wolfram for teaching me how to work properly in a biomechanics lab! Also, I want to thank Ghislain Maquer, Hadi Hosseini, Thomas Gross, Uwe Wolfram, and Alexander Bürki for the great discussions and collaborations we had throughout the last years.

I would like to express my deep gratitude to the external collaborators with whom I had the pleasure to work during the last years. Especially, I would like to thank Rejin Raghavan, Victor LeNader, and Johann Michler of EMPA. The collaboration with the Laboratory of Mechanics of Materials and Nanostructures was very inspiring and definitely a highlight of my PhD. I would also like to thank Joan Josep Roa Rovira and Peter Varga for the very interesting collaboration regarding FIB/SEM tomography of bone and Prof. Stefan Hengsberger for the introduction to and collaboration on atomic force microscopy.

Finally, I would like to thank my wife Barbara Haidmayer for her support and love in both good and hard times, especially when moving from Vienna to Bern. I am very happy to have you by my side. Furthermore, I want to thank my parents Wolfgang and Susanne for providing a safe haven and an intellectually inspiring environment for their children as well as my brothers Caspar and Ludwig for setting the standards high and always being there for each other.

Curriculum Vitae

Personal Data	Johann Jakob Schwiedrzik January 8th, 1986, Köln (Germany) married to Barbara Haidmayer German
Career Progression	
11/2011 – today	PhD student, Institute for Surgical Technology and Biomechanics, University of Bern, Switzerland
12/2010 – 10/2011	PhD student, Institute of Lightweight Design and Structural Biomechanics, Vienna University of Technology, Austria
Academic Background	
01/2012 – today	PhD program in Biomedical Engineering, Graduate School for Cellular and Biomedical Sciences, University of Bern, Switzerland
09/2010 – 01/2012	PhD program in Mechanical Engineering, Vienna University of Technology, Austria
09/2008 – 07/2009	Exchange student in Biomedical Engineering, University of Michigan, Ann Arbor, USA
10/2004 – 08/2010	Diploma program in Mechanical Engineering, Vienna University of Technology, Austria
Matura	
07/2004	Bundesgymnasium 18 Klostergasse, Vienna, Austria

Publications in scientific journals related to this thesis

- J.J. Schwiedrzik, R. Raghavan, A. Bürki, V. LeNader, U. Wolfram, J. Michler, P.K. Zysset: *In situ micropillar compression reveals superior strength and ductility but an absence of damage in lamellar bone.* Nature Materials 13, 740–747, 2014
- J.J. Schwiedrzik, P.K. Zysset: *The influence of yield surface shape and damage in the depth-dependent response of bone tissue to nanoindentation using spherical and Berkovich indenters.* Computer Methods in Biomechanics and Biomedical Eng., 2013
- J.J. Schwiedrzik, U. Wolfram, P.K. Zysset: *A generalized anisotropic quadric yield criterion and its application to bone tissue on multiple length scales.* Biomechanics and Modeling in Mechanobiology, 12(6), 1155–1168, 2013
- J.J. Schwiedrzik, P.K. Zysset: *An Anisotropic Elastic Viscoplastic Damage Model for Bone Tissue.* Biomechanics and Modeling in Mechanobiology, 12(2), 201–213, 2013

Conference contributions related to this thesis

- J.J. Schwiedrzik: *Experimental, theoretical and numerical investigation of the non-linear micromechanical properties of bone.* Presentation, Research Award Session, Swiss Society of Biomedical Engineering Annual Meeting, 2014
- J.J. Schwiedrzik, R. Raghavan, A. Bürki, U. Wolfram, J. Michler, P.K. Zysset: *In situ micropillar compression tests of lamellar bone show a remarkable strength and ductility but no damage on the microscale.* Poster, 7th World Congress of Biomechanics, 2014
- J.J. Schwiedrzik, U. Wolfram, P.K. Zysset: *A generalized anisotropic quadric yield criterion and its application to bone tissue on multiple length scales.* Presentation, 19th Congress of the European Society of Biomechanics, 2013
- J.J. Schwiedrzik, P.K. Zysset: *The influence of the yield surface shape and damage on the depth-dependent response of bone to nanoindentation using spherical and Berkovich tips.* Presentation, 11th International Symposium on Computer Methods in Biomechanics and Biomedical Engineering, 2013
- J.J. Schwiedrzik, P.K. Zysset: *Depth-dependent response of bone tissue to nanoindentation as a function of yield surface shape and damage accumulation.* Presentation, CSM User Meeting, 2012
- J.J. Schwiedrzik, P.K. Zysset: *Anisotropic Elastic Viscoplastic Damage Model for Simulation of Nanoindentation in Bone Tissue.* Presentation, 8th European Solid Mechanics Conference, 2012

Declaration of Originality

Last name, first name:

Matriculation number:

I hereby declare that this thesis represents my original work and that I have used no other sources except as noted by citations.
All data tables, figures and text citations which have been reproduced from any other source, including the internet, have been explicitly acknowledged as such.
I am aware that in case of non-compliance, the Senate is entitled to withdraw the doctorate degree awarded to me on the basis of the present thesis in accordance with the "Statut der Universität Bern (Universitätsstatut; UniSt)", Art. 69, of 7 June 2011.

Place, date

Signature